

# Experimental study into the dependence of ice-induced vibrations on dynamic structural properties

Nick Ebben

Master of Science Thesis

**TU Delft** Delft University of Technology

**A!** Aalto University School of Engineering

**SIEMENS Gamesa**  
RENEWABLE ENERGY



# Experimental study into the dependence of ice-induced vibrations on dynamic structural properties

MASTER OF SCIENCE THESIS

For the degree of Master of Science in Offshore and Dredging Engineering at Delft University of Technology

Nick Ebben

22 October 2021

Supervisors:	Dr. ir. H. Hendrikse Ir. T.C. Hammer	Delft University of Technology Delft University of Technology
Thesis committee	Dr. ir. H. Hendrikse Ir. T.C. Hammer Dr. ir. M.A. van der Berg Prof. dr. ir. A. Metrikine	Delft University of Technology Delft University of Technology Delft University of Technology Delft University of Technology



---

## Abstract

Arctic and sub-arctic regions are more and more used to build offshore wind farms. There is a lack of model-scale tests where dynamic structural properties were systematically varied to derive the influence of these properties on boundaries of the three crushing regimes. Those regimes are intermittent crushing, where both the ice load and displacement signal have a sawtooth pattern, frequency lock-in, with its characteristic sinusoidal displacement signal and continuous brittle crushing with smaller random ice loads and structural displacements compared to the two previously mentioned regimes. The first goal of this thesis is to test if an error in the dynamic structural properties (mass, stiffness and damping) has an effect on the transition velocities of the crushing regimes. Secondly, a parameter study has been done to derive trends in the transition velocities when changing dynamic structural properties. Ultimately, in literature proposed dimensionless numbers, which are particularly only taking linear elastic ice parameters into account, have been checked for rightness.

To be able to achieve the above mentioned goals of the thesis, a model-scale test campaign has been performed at the Aalto Ice Tank as part of the SHIVER test campaign. 36 unique single degree of freedom configurations have been tested to derive trends in ice-structure interaction when changing dynamic structural parameters. The most notable element of this test campaign was the usage of a real-time hybrid test setup, which allowed the testing of multiple sets of structural parameters while only one physical structure was used.

Those tests signify that there is a relation between mass, stiffness, natural frequency and damping and transition velocities in between the three crushing regimes. When mass, stiffness and natural frequency increase, the boundaries of those regimes shift to lower velocities. An increase in damping caused the velocity of the boundary between frequency lock-in and continuous brittle crushing to go up, while the boundary between intermittent crushing and frequency lock-in was not influenced by the change in damping. Furthermore, from the tests it could be concluded that dimensionless numbers based on only linear elastic parameters are not correct and more parameters should be taken into account as well.

The thesis is a stepping stone into more research into the dependency of ice-induced vibrations on dynamic structural properties with different initial conditions or structural properties. Furthermore in future test campaigns other dimensionless groups could be proposed and validated.

---

# Table of contents

<b>List of Figures</b>	<b>7</b>
<b>List of Tables</b>	<b>10</b>
<b>Acknowledgements</b>	<b>11</b>
<b>1 Introduction</b>	<b>12</b>
1-1 Model-scale experiments.....	13
1-2 Thesis objective and outline.....	13
<b>2 Ice induced vibrations</b>	<b>15</b>
2-1 Ice-structure interaction. ....	15
2-1-1 Intermittent crushing.....	15
2-1-2 Frequency lock-in.....	16
2-1-3 Continuous brittle crushing.....	17
2-2 Previous experiments.....	18
2-2-1 Toyama (1983) .....	18
2-2-2 Tsuchiya (1985) .....	18
2-2-3 Sodhi (1991) .....	18
2-2-4 Izumiyama et al. (1994).....	19
2-2-5 Kärnä et al. (2003).....	19
2-2-6 Huang et al. (2007).....	19
2-2-7 Guo et al. (2009).....	20
2-2-8 Yap (2011).....	20
2-2-9 Ziemer & Hinse (2017).....	20
2-2-10 Other reports.....	20
2-3 Influence of dynamic structural properties .....	21
2-4 Aspect ratio.....	21
2-5 Base case.....	22
<b>3 Scaling</b>	<b>24</b>
3-1 Literature proposals.....	24
3-1-1 First scaling laws.....	24
3-1-2 Reduced velocity.....	25
3-1-3 Strouhal number.....	26
3-1-4 Interaction coefficient.....	27
3-2 Viscoelastic deformation.....	28

<b>4</b>	<b>Test campaign</b>	<b>31</b>
4-1	Ice tan.....	31
4-2	Experimental setup – Hardware.....	32
4-3	Experimental setup – Software.....	33
4-4	Workflow.....	35
4-5	Test overview.....	36
4-6	Test matrix.....	39
<b>5</b>	<b>Results and conclusions</b>	<b>41</b>
5-1	Boundary identification.....	41
5-1-1	ICR to FLI.....	41
5-1-2	FLI to CBC.....	44
5-1-3	Linear anomaly.....	46
5-2	Scaling.....	47
5-3	Mass.....	48
5-4	Stiffness.....	50
5-5	Mass & Stiffness.....	52
5-6	Damping.....	54
5-7	Conclusion.....	56
<b>6</b>	<b>Discussion and recommendations</b>	<b>59</b>
6-1	Bigger pile.....	59
6-2	Boundary identification.....	60
6-3	Ice properties.....	60
6-4	Carriage velocity.....	61
6-5	Carriage vibrations.....	63
6-6	Velocity profiles.....	63
6-7	Further research.....	64
<b>A</b>	<b>Summary of previous experiments</b>	<b>65</b>
<b>B</b>	<b>Graphs of parameters from previous experiments</b>	<b>69</b>
<b>C</b>	<b>TU Delft model simulations</b>	<b>77</b>
<b>D</b>	<b>Ice thickness plots</b>	<b>79</b>
<b>E</b>	<b>Time series test campaign</b>	<b>81</b>
	<b>Bibliography</b>	<b>225</b>

---

## List of Figures

1-1	Locations of offshore wind turbines in the Baltic Sea which are fully commissioned by February 2015 [5].....	12
2-1	Maximum velocity of structural oscillation versus ice sheet velocity during frequency lock-in. Results from several experimental campaigns are plotted [8].....	16
2-2	An overview of typical structural responses and global ice loads when loaded by ice crushing forces [8].....	17
3-1	Relation between $U/Nt$ and failure mode [12].....	25
3-2	Critical Strouhal Number against damping ratio [10].....	27
4-1	The ice tank at the Aalto University.....	31
4-2	On the left the pile used during the SHIVER test campaign on its side. On the right the inside of the pile with at 1 the potentiometer, at 2 the accelerometer and at 3 the strain gauges.....	32
4-3	On the top plate with the first rails attached to it. On the right all three plates with rails in two directions to allow movement in x- and y-direction.....	32
4-4	On the left the bottom of the pile which is bolted in the lower frame. On the right the three aluminium plates with the milled honeycomb pattern.....	33
4-5	On the left the side of the setup which stands upside down, with two actuator, load cell and displacement sensor. On the right the total setup combined.....	33
4-6	The workflow of the test setup. A single degree of freedom model is uploaded from a laptop to the software in the control box in the top middle. This control box gives a displacement input to the power boxes on the bottom right and those power boxes give a voltage input to the circled actuator to move to that position. In the pile on the bottom left strain gauges are placed with measure the strain. This strain signal is send to the control box again, which converts it based on the model input from the laptop to a force and thereafter to a displacement, after which the cycle continues.....	35
4-7	On the left side the trial test day ice and on the right side non-brittle ice during the second test day.....	36
4-8	Two views of the tests at the 15 <sup>th</sup> of June with brittle ice characteristics.....	36
5-1	Typical intermittent crushing signal. The signal is from test SDOF-25 with a natural frequency of 2.0 Hz.....	42
5-2	Typical frequency lock-in signal. The signal is from test SDOF-26 with a natural frequency of 0.444 Hz.....	42

5-3	Relative velocity signal of a test which is close to the transition velocity between intermittent crushing and frequency lock-in. The signal is from test SDOF-24 with a natural frequency of 0.889 Hz.....	43
5-4	Phase plane plot of a test which is close to the transition velocity between intermittent crushing and frequency lock-in. The signal is from test SDOF-24 with a natural frequency of 0.889 Hz.....	43
5-5	Typical transition from continuous brittle crushing to frequency lock-in using a downward velocity ramp. The signal is from test SDOF-26 with a natural frequency of 0.444 Hz.....	44
5-6	The relative velocity and displacement of a signal in which frequency lock-in and continuous brittle crushing take turns. The signal is from test SDOF-25 with a natural frequency of 2.0 Hz.....	45
5-7	The pile approaching the anomaly during test SDOF-21.....	46
5-8	Relative velocity, displacement and pressure force signals of test SDOF-21 where the pile went through the anomaly.....	46
5-9	Maximum structural velocity plotted against penetration rate for tests SDOF-2 (2.0 Hz) and SDOF-3 (1.0 Hz).....	48
5-10	Maximum structural velocity plotted against penetration rate for tests SDOF-7 (2.0 Hz), SDOF-8 (1.0 Hz) and SDOF-9 (1.5 Hz).....	49
5-11	Maximum structural velocity plotted against penetration rate for tests SDOF-10 (2.0 Hz) and SDOF-11 (0.5 Hz).....	49
5-12	Velocities at which each crushing regime occurred during test SDOF-32, SDOF-33, SDOF-34 and SDOF-38 with varying stiffness.....	50
5-13	Transition from CBC to ICR without going into FLI for test SDOF-33.....	51
5-14	Test with a rigid pile where only CBC occurred during test SDOF-34.....	51
5-15	Velocities at which each crushing regime occurred during test SDOF-24, SDOF-27 and SDOF-28 with varying mass and stiffness.....	52
5-16	Maximum structural velocity plotted against penetration rate for tests SDOF-14 (base case) and SDOF-15 (four times higher mass and stiffness).....	53
5-17	Velocities at which each crushing regime occurred during test SDOF-17, SDOF-18 and SDOF-19 with varying damping.....	54
5-18	Velocities at which each crushing regime occurred during test SDOF-24, SDOF-29 and SDOF-30 with varying damping.....	55
5-19	Simulations in the TU Delft model for a structure with low stiffness. On top a plot of ice drift speed against global ice loads, below ice drift speed against maximum structural velocity, on the third row the drift speed against structural displacement and at bottom the drift speed against structural displacement frequency wavelets.....	57
5-20	: Phase plane plots (structural displacement against velocity) simulated with the TU Delft model for the structure with a low stiffness.....	57
6-1	At the left the measurement method of the ice thickness and on the right a piece from the ice where the variety in ice thickness is clearly visible.....	61
6-2	A carriage velocity signal before changing PID settings for low velocities with velocity peak during ice failures. The signal is from test SDOF-17.....	62
6-3	A carriage velocity signal after changing PID settings for low velocities with a smoother almost linear velocity signal. The signal is from test SDOF-32.....	62
6-4	Accelerations in X, Y and Z direction for the accelerometer that is fixed to the non-moving plate during test SDOF-38.....	63
B-1	Scatterplot of the stiffness against mass used during 21 model-test campaigns.	69
B-2	Scatterplot of the natural frequency against stiffness used during 21 model-test campaigns.....	70

B-3	Scatterplot of the natural frequency against mass used during 21 model-test campaigns.....	70
B-4	Scatterplot of the damping ratio against natural frequency used during 21 model-test campaigns.....	71
B-5	Scatterplot of the natural frequency against the maximum ice load divided by mass during intermittent crushing retrieved during 21 model-test campaigns....	71
B-6	Scatterplot of the natural frequency against the mean ice load divided by mass during frequency lock-in retrieved during 21 model-test campaigns.....	72
B-7	Scatterplot of the natural frequency against the maximum ice load divided by mass during frequency lock-in retrieved during 21 model-test campaigns.....	72
B-8	Scatterplot of the natural frequency against the mean ice load divided by mass during continuous brittle crushing retrieved during 21 model-test campaigns.....	73
B-9	Scatterplot of the aspect ratio against the maximum ice load divided by mass during intermittent crushing retrieved during 21 model-test campaigns.....	73
B-10	Scatterplot of the aspect ratio against the mean ice load divided by mass during frequency lock-in retrieved during 21 model-test campaigns.....	74
B-11	Scatterplot of the aspect ratio against the mean ice load divided by mass during continuous brittle crushing retrieved during 21 model-test campaigns.....	74
B-12	Scatterplot of the ice velocity against the natural frequency for which intermittent crushing occurred during 21 model-test campaigns.....	75
B-13	Scatterplot of the ice velocity against the natural frequency for which frequency lock-in occurred during 21 model-test campaigns.....	75
B-14	Scatterplot of the ice velocity against the natural frequency for which continuous brittle crushing occurred during 21 model-test campaigns.....	76
C-1	Simulations in the TU Delft model for the base case proposed in Table 3-2. On top a plot of ice drift speed against global ice loads, below ice drift speed against maximum structural velocity, on the third row the drift speed against structural displacement and at bottom the drift speed against structural displacement frequency wavelets.....	77
C-2	Phase plane plots (structural displacement against velocity) simulated with the TU Delft model for the base case in Table 3-2.....	78
D-1	Colourmap of ice thicknesses measured in the ice tank at the 17 <sup>th</sup> of June. Numbers above indicate the order and location of test channels.....	79
D-2	Plot of the ice thicknesses over time in the ice tank at the 17 <sup>th</sup> of June.....	79
D-3	Colourmap of ice thicknesses measured in the ice tank at the 21 <sup>st</sup> of June. Numbers above indicate the order and location of test channels.....	80
D-4	Plot of ice thicknesses over time in the ice tank at the 21 <sup>st</sup> of June.....	80
E	All single degree of freedom timeseries of the test campaign.....	82

---

## List of Tables

2-1	Variation of failure modes with aspect ratios [28].....	22
2-2	Base case based on the literature study.....	23
3-1	Matrix with dimensions of all relevant parameters if ice-structure interaction is assumed to be only linear elastic.....	28
3-2	Variations on base case for the study into scaling in a linear brittle manner only.....	29
4-1	Ice thicknesses, compressive strengths, bending strengths and submerged bending strengths during all SDOF tests performed at the SHIVER test campaign.....	38
4-2	Test matrix used during the SHIVER test campaign.....	39
5-1	Results of tests with varying mass and equal stiffness and damping.....	47
5-2	Results of the tests with a varying stiffness and equal mass and damping.....	50
5-3	Results of the tests with an equal natural frequency, but changing mass and stiffness.....	52
5-4	Results of the first tests with a varying damping.....	54
5-5	Results of the second tests with a varying damping.....	55
6-1	The boundary velocities from intermittent crushing to frequency lock-in and from frequency lock-in to continuous brittle crushing for test SDOF-20, SDOF-21 and SDOF-22 with a upward and downward velocity ramp.....	64
A-1	Overview of dynamic structural parameters and ice thicknesses derived from 21 reports about model-scale experiments.....	65

---

## Acknowledgments

Finding a graduation topic at a company was really difficult during the COVID-19 pandemic. Therefore I was really happy to receive the opportunity to do an experimental test campaign in Espoo. I want to thank Hayo, Tim, Cody, Marnix and Tom, not only for their help and advice with my thesis and experiments, but also for an amazing trip to Finland. I will never forget the 'ice wars', the fanatic board games, the sauna sessions after a long and cold day in the ice tank, the outings we made in the weekend and I won't be able to say the word 'finish' or 'perfect' normally again without remembering the test campaign.

Besides this, I am really thankful for my daily supervisors Hayo and Tim, who were always there to help me further with the research during the weekly meetings and gave their helpful feedback to the report, for which I want to thank Marnix as well.

Furthermore I would like to thank Hayo, Tim, Marnix and Andrei for being in the graduation committee. Also special thanks to Teemu, Lasse, Sampo and Otto for their hospitality and excellent help in the ice tank.

Without my friends and family, I would not have been able to go through the last 6 years of studying, so I would like to thank my parents, sister and brother, my girlfriend Joyce, my friends from Link and all the friends I made at the badminton association DSBA-USSR in the past few years. Lastly, I am really grateful for the collaboration in the group assignments with Jan and Tijs during the master, but also as friends next to the assignments.

Delft, October 19, 2021

Nick Ebben

---

# Chapter 1

---

## Introduction

Since countries are increasingly targeting a predominantly renewable energy production, more and more wind farms are being built in sub-arctic regions. In Europe eight countries will cooperate to accelerate the building of offshore wind turbines in the Baltic Sea. While nowadays the energy production is 2.2 GW at this location, there is a capacity of 93 GW by 2050 [1]. In Figure 1-1 a map of the Baltic Sea can be seen in which all operable offshore and nearshore wind farms in 2015 are designated, but in the coming years this will be expanded by multiple wind farms from among others Poland [2], Denmark [3], Latvia and Estonia [4]. Those windfarms are respectively marked with purple, orange and black dots in Figure 1-1.

In those sub-artic regions, an ice feature can push against the offshore wind turbines. There are multiple ways in which the ice can fail during this interaction with the turbine. This research focusses on one of the failure modes, being the crushing failure mode. During crushing, in-plane brittle failure or ductile deformation of the ice occurs while there is a non-uniform contact between ice and structure over the width of the structure [9]. Some understanding of the interaction between ice and structures exists, but up to today it is not possible to predict the exact ice-structure interaction regimes and the influence of dynamic structural parameters on those interaction regimes.



**Figure 1-1:** Locations of offshore wind turbines in the Baltic Sea which are fully commissioned by February 2015 [5].

There are three crushing regimes with each its own characteristics with respect to ice load and displacement. The prediction of the three crushing regimes is needed to perform accurate load analyses to build these wind farms in sub-arctic regions safely. The first of the three crushing regimes is intermittent crushing (ICR) which, with its high peak forces, sudden load drops and large displacements, is important for all the limit state analyses, being ultimate limit state (ULS), fatigue limit state (FLS) and serviceability limit state (SLS). Structures during frequency lock-in (FLI) have a relatively large harmonic displacement, so this should be taken into account in the FLS and SLS analysis. The last crushing regime, continuous brittle crushing (CBC) has only relatively small loads and displacements compared to intermittent crushing and frequency lock-in and is therefore only important in the FLS analysis [6].

Designers of wind turbines estimate the natural frequency of a wind turbine during those analyses, but this estimation can always have a deviation from the real value when the structure has been built. Therefore the question arises to what extent an insufficient stiffness or mass estimation influences the development of ice-structure interaction regimes, their boundary velocities and corresponding ice loads.

## **1-1 Model-scale experiments**

In the past there have been studies into the way ice is failing against structures and there are some reports which show a variation in structural properties, as further discussed in Chapter 2, but there has not been a systematic study into the dependency of ice-induced vibrations on dynamic structural properties. The main reason for this is that testing different structural properties requires multiple structures, which is very costly. Therefore for this test campaign, an experimental setup has been developed in which the structural properties can be controlled using a real-time hybrid setup, so only one physical setup is needed to simulate multiple structures. This flexibility in dynamic structural parameters gave the opportunity of doing research into the influence of mass, stiffness and damping on ice-induced vibrations and in particular to discover trends on changing velocity regimes for which the three crushing regimes occur. The test setup also gave the opportunity to test low natural frequencies. Up to this test campaign, only model-scale tests on structures of 1.27 Hz or higher have been conducted, while typical first modes of an offshore wind turbine are in the range of 0.1 to 0.2 Hz [7].

## **1-2 Thesis objective and outline**

The target of this thesis is to get an understanding of the influence of mass, stiffness and damping on the dynamic response at certain velocities of a structure subjected to ice loads. To achieve this understanding the following three sub-questions have been conceived.

- Does an error in estimation of mass, stiffness and damping have a significant effect on boundary velocities of the crushing regimes?
- What are the trends of ice-induced vibrations derived from an experimental study when changing dynamic structural properties?
- What is the predictive value of the in literature proposed dimensionless numbers for changes in dynamic properties?

The above mentioned questions have been investigated by carrying out a test campaign with a model-scale test setup in the Aalto Ice Tank in Finland.

In Chapter 2 the background information about the three different ice crushing regimes is elaborated. Afterwards an overview is given on the performed experiments in literature and the influence of dynamic structural properties on ice-induced vibrations is explained. In Section 2-3 the influence of dynamic structural parameters on ice induced vibrations is explained. The influence of the aspect ratio on the failure mode of ice is elaborated in Section 2-4. Based on the overview of the performed literature a test matrix has been developed for the SHIVER test campaign in Section 2-5. Chapter 3 contains proposed dimensionless numbers from literature which will be tested during the test campaign. In Chapter 4 the experimental setup that has been used in the test campaign in Finland is described and an overview of the campaign is given. All the elaborated results of this test campaign and associated conclusions can be found in Chapter 5. The discussion and recommendations subsequently can be found in Chapter 6.

---

## Chapter 2

---

# Ice-induced vibrations

Ice acting on a vertically sided structure can fail in multiple ways, for instance splitting, buckling, circumferential cracks, creep or crushing [8]. In this test campaign, the focus lays on the crushing failure mode. For a flexible structure, ice-induced vibrations during crushing will be generated by ice failing at the structures surface because of the compression force [9]. Within this failure mode, there are three regimes in which different structural vibrations occur, namely intermittent crushing, frequency lock-in and continuous brittle crushing [8].

In this chapter first the three crushing regimes are listed. Furthermore a test matrix for the test campaign in Finland has been developed after a literature study has been done on existing test campaigns. In this chapter the most important reports about model-scale tests are summarised and at the end graphs are shown which include relevant structural parameters and ice thicknesses based on the presented literature. In Section 2-3 the aspect ratio, the ratio between pile diameter and ice thickness is analysed and in Section 2-4 the eventually acquired base case is given. The base case is a set of parameters wherefrom variations will be conceived to investigate trends in ice-induced vibrations.

## 2-1 Ice-structure interaction

In this section the three crushing regimes, intermittent crushing, frequency lock-in and continuous brittle crushing are explained and typical characteristics of those regimes are mentioned.

### 2-1-1 Intermittent crushing

The first regime, which generally occurs at lower ice velocities for flexible structures is intermittent crushing, in some articles classified as quasi-static vibration [10], [11], [12], [13], [14]. When ice hits the structure at a low velocity, the structure will start to deflect in the direction of the ice motion. The ice load will increase gradually until it's above the compressive strength of the ice and the ice will fail. The structure will return to its initial position with a high velocity and will have some cycles of free vibration before the next loading phase begins [15]. This gradual load build up and sudden load drop creates the typical saw-tooth shape of both the displacement as the force over time, as shown on the left-hand side of Figure 2-2. In this regime the peak ice loads are significantly higher than for the other two regimes, which is

caused by the low relative velocity between ice and structure during load build-up. Because of this low relative velocity, the contact area increases and the global load on the structure increases therefore as well. At higher relative velocities during frequency lock-in and continuous brittle crushing, the global load is mainly created by small contact areas with a high pressure and therefore the forces are lower [2].

### 2-1-2 Frequency lock-in

The second regime is frequency lock-in, also referred to as steady-state vibration. The cycle of the displacement in frequency lock-in is described by Ziemer [16]. The cycle starts when the structure is moving in the opposite direction of the movement of the ice. At this position the relative velocity is high and the structure crushes into the ice sheet and the ice fails in crushing. The structure velocity reduces as energy is dissipated by crushing processes. After some time, the structure moves in the same direction as the ice. When the ice and the structure have around the same velocity, the build-up phase begins and the ice load will start to grow until the ice fails and the structure starts to deflect to its initial position and the cycle will start again. The frequency with which the structure oscillates is 1 to 10 percent below the natural frequency.

During this lock-in there is also a relation between the maximum velocity of the structure and the velocity of the ice which is given in Equation 2.1 [10],

$$\dot{U}_{max} = \beta \cdot V \tag{2-1}$$

where  $\dot{U}_{max}$  is the maximum structural velocity at waterline in the direction of the ice movement,  $\beta$  is a constant and  $V$  is the ice velocity. For frequency lock-in to occur, the value of  $\beta$  should be between 0.9 and  $\pi/2$  according to Ziemer [16], while other reports acquired different trends with a  $\beta$  between 1 and 1.5 and they point out that the physical mechanism which justifies the value of  $\beta$  for which frequency lock-in occurs is not yet understood enough to draw conclusions on those trends [8]. In Figure 2-1 the results from multiple campaigns [10], [17], [18], [19], [20] can be seen, which shows this trend between ice velocity and structural velocity.

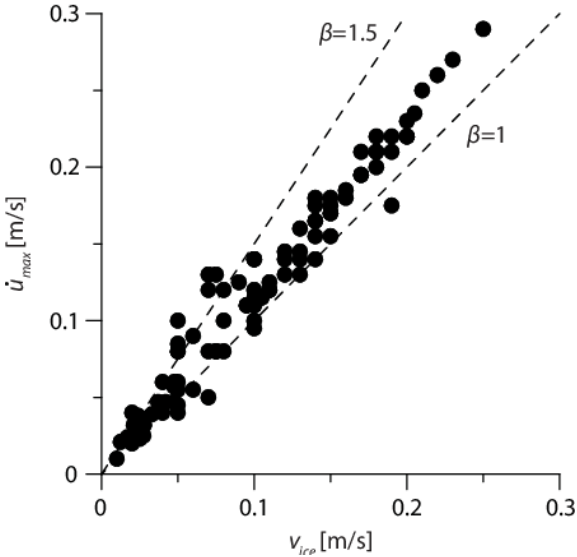


**Figure 2-1:** Maximum velocity of structural oscillation versus ice sheet velocity during frequency lock-in. Results from several experimental campaigns are plotted [8].

### 2-1-3 Continuous brittle crushing

When the ice velocity is further increased, the frequency lock-in will change into continuous brittle crushing, in literature also called random vibration [11], [14], [15], [21]. The structural displacements and ice loads at continuous brittle crushing are much smaller than at frequency lock-in. The load has a mean value around which the load randomly fluctuates. In Figure 2-2 an overview can be found of the three crushing regimes and their typical ice loads and structural displacements for a single degree of freedom structure.

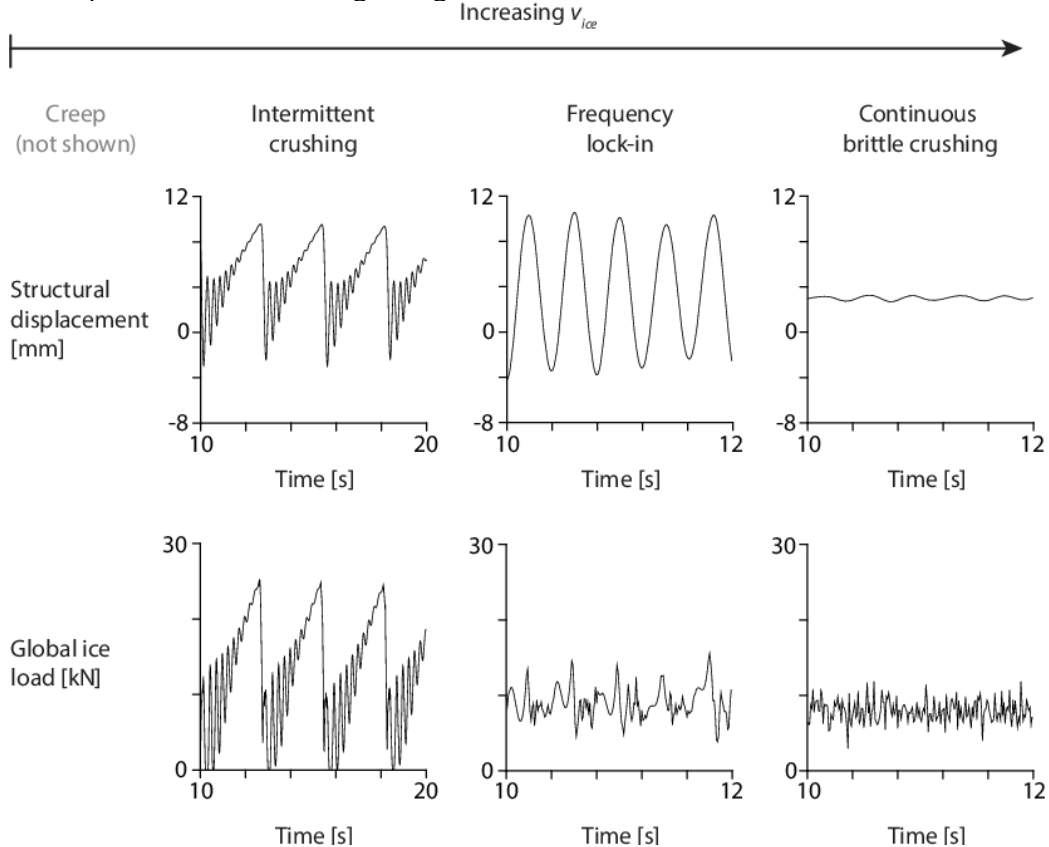


**Figure 2-2:** An overview of typical structural responses and global ice loads when loaded by ice crushing forces [8].

## **2-2 Previous experiments**

Below the nine most important previously performed model-scale experiments are listed and summarised, by explaining the experiments and writing down the most important conclusions from those experiments. The remaining experiments which are not summarised are mentioned in the end of this section. In Appendix A a table is given with an overview of the structural properties, the pile diameters and ice thicknesses of 21 model-scale experiments.

### **2-2-1 Toyama (1983)**

One of the first model tests were performed by Toyama, Sensu, Minami and Yashima in 1980, 1981 and 1982 in Hokkaido in Japan [19]. Monopiles and two-legged structures have been tested, but only monopiles have been taken into account in this report. The natural saline ice had uniform ice thicknesses between 30 and 80 mm, because it had been cut by a chainsaw. Those pieces have been pushed against the structure, from which the natural frequency could be adapted to 1.27, 4.02 and 16.00 Hz by changing the mass of the test piles. The mass and stiffness were not given, but are derived by Yap [21]. No water was involved during this experiment, which explains the low damping ratios. For low ice velocities and rigid structures, the failure mode was intermittent crushing, while for higher velocities and flexible structures frequency lock-in was observed as well. Unfortunately, for the monopiles only one time series have been plotted, so a comparison between multiple natural frequencies is difficult to make. From this test campaign it can be concluded that frequency lock-in takes some time to develop after initial contact between structure and ice. Furthermore, the research demonstrates that the stiffness of a structure influences the critical velocities between different crushing regimes.

### **2-2-2 Tsuchiya (1985)**

Tsuchiya performed his research with the same test setup as Toyama did [23]. He used three monopiles with different natural frequencies. One rigid structure with infinite stiffness and two piles with a natural frequency of 2.90 and 4.66 Hz. The main useful conclusion drawn from this report is that the natural frequency has an influence on the ice force and structural response, but it was only a slight influence. It should be noted that the natural frequencies of 2.90 and 4.66 Hz of the flexible piles are close to each other and could therefore explain the small influence. Furthermore, it turned out that the relative velocity between structure and ice sheet, the strain rate, had an interrelation with the frequencies of ice force and structural response.

### **2-2-3 Sodhi (1991)**

Sodhi [24] used a single degree of freedom system with seeded freshwater ice to identify the effect of changes in stiffness on the dynamic ice-structure interaction under different ice velocities. The mass of 600 kg has been kept the same during all tests, so changing the stiffness resulted in a changing natural frequency. It is unclear which natural frequencies have exactly been used. In the report only four of the natural frequencies that were used have been

given, but even these are estimations. Creep, intermittent crushing and continuous brittle crushing were observed during this test campaign, but frequency lock-in wasn't. With his research, Sodhi proved that stiffness plays an important role in the identification of the regions in which certain crushing regimes occur.

#### **2-2-4 Izumiyama et al. (1994)**

Izumiyama, Irani and Timco [18] performed their tests in 1984 in Canada. The ice used in this study was Propylene Glycol ice, which has the same properties as Ethylene Glycol ice. The freshwater seeded ice layer was grown at an ambience temperature of minus 20 degrees Celsius. The used structure is a model scale of a bridge pier with a scaling factor of 30. Although the stiffness of the structure is adaptable, during the campaign only a stiffness of 301 kN/m was used in the direction of the ice force, with a corresponding natural frequency of 5.86 Hz in the before mentioned direction.

According to the text, buckling, continuous crushing and a mixture of those two have been found. It is not given which crushing regimes occur, nevertheless, from the maximum force and the beta ratio between ice speed and structural response, an estimation can be made of the regimes and this indicates that all three crushing regimes have occurred.

#### **2-2-5 Kärnä et al. (2003)**

The experiments in "Ice action on compliant structures; Laboratory indentation tests" have been performed in the ARCTECLAB, operated by the HSVA. This test set-up was a multi degree of freedom set-up with an indenter with a width of 114 mm. The ice velocity is varied between 10 and 600 mm/s. The ice thickness was adjusted after the ice turned out to be too weak from 40 mm to be around 80 mm. Stiffness and mass were not given in this report. Furthermore, all three ice crushing regimes have been seen [25].

#### **2-2-6 Huang et al. (2007)**

In "Model test study of the interaction between ice and a compliant vertical narrow structure" 121 tests have been performed at the Ice Engineering Laboratory of Tianjin University [17]. The model has a high rigidity in vertical direction and complete freedom in horizontal direction, so it is assumed to be single degree of freedom. Stiffness could be adapted by changing bar diameter and length and the desired natural frequency could be obtained by changing the mass of the table.

The ice used here was urea ice with a compressive strength between 55 and 210 kPa and an ice thickness between 26 and 48 mm. The cylinder used has a diameter of 76 mm. The velocity is varied between 5 and 450 mm/s. In this report the boundary velocities between intermittent crushing (ICR) and frequency lock-in (FLI) and between frequency lock-in and continuous brittle crushing (CBC) have been found, so all three crushing regimes have been seen. The conclusion indicated a dependency off transition speeds on the stiffness value. Furthermore, three different dimensionless numbers are presented.

## **2-2-7 Guo et al. (2009)**

“Model test of ice-structure interaction” [13] scales a jacket platform in the Bohai Sea with a scaling factor of  $\lambda=10$  according to the scaling laws of Määttänen [26]. The model top mass could be varied between 1000, 2000 and 3000 kg and this resulted in natural frequencies of respectively 4.12, 2.91 and 2.38 Hz. The target ice thickness was 40 mm and the indenter had a diameter of 120 mm. Continuous brittle crushing has not been seen in this test campaign, but both intermittent crushing and frequency lock-in have been obtained.

## **2-2-8 Yap (2011)**

“Level ice-vertical structure interaction: steady-state self-excited vibration of structures” [21] and the following conference paper in 2013 [27] describe a test campaign in cooperation between the National University of Singapore (NUS) and the Dalian University of Technology (DUT) in 2010. No basin was used during this campaign, but a non-floating ice sheet was pushed against the indenter, so added mass and hydrodynamic damping of the water is not taken into account. The lowest natural frequency was 2.3 Hz with a corresponding modal stiffness of 690 kN/m and a damping ratio of 0.01. Two indenters were used, the first one with a diameter of 80 mm and the second one with 120 mm. With ice thicknesses between 25 and 50 mm, aspect ratios between 1.6 and 4.8 have been tested. All crushing regimes have been found in this study. Crushing regimes were not indicated in the report, but are derived from the structure displacement time histories and relative velocity time histories in the appendices.

## **2-2-9 Ziemer & Hinse (2017)**

In "Relation of Maximum Structural Velocity and Ice Drift Speed during Frequency Lock-In" [16] test are described which are performed in 2015 and 2016 in HSVA's Large Ice Basin as part of the IVOS project. First a bottom found cylinder with a diameter of 830 mm was used and ice was pushed against the structure, but among other things the high aspect ratio caused the ice to fail in downward buckling. Therefore a new model with a higher flexibility was designed which was then pushed through the ice. This was a single degree of freedom test set up where the diameter could be varied between 120, 200 and 500 mm.

The ice velocity was varied between 5 and 200 mm/s and the ice had a thickness between 31 and 50 mm and a compressive strength between 72 and 135 kPa. The natural frequency varied between 2.65 Hz and 7.6 Hz. In this report the boundary velocities for the crushing regimes have been given, so for almost all structural configurations all three crushing regimes have been seen. An important note has been made that ice conditions, ice thickness and strength, vary along the basin and acquired boundary velocities could be distorted because of this.

## **2-2-10 Other reports**

Not all used reports are summarised above, but they are included in Appendix A. Some of those reports were not representative for the planned experiments, because of a natural frequency above 10 Hz, a large pile diameter or higher ice thicknesses, while other reports lacked a lot of information, so it was difficult to analyse them or draw a conclusion from the reports.

## 2-3 Influence of dynamic structural properties

Boundaries of the three different regimes are dependent on dynamic structural properties. In this study mass, stiffness and damping are varied and the diameter of the structure has been kept the same over the whole test campaign. Natural frequency also has an influence on the boundaries, but this variable is fully dependent on mass and stiffness. Ice velocity is next to the structural properties also of a big influence on the boundaries.

From previous research some predictions on the influence of dynamic structural properties on ice induced vibrations on dynamic could be drawn. The first is that mass is negatively correlated with the boundary velocity of the crushing regimes. Tsuchiya [23] was the first to alter the natural frequency by changing the mass of the setup. He defined the strain rate as the ice velocity divided by four times the structural diameter. For higher masses, the critical strain rate, the strain rate for which the crushing regimes changed, went down while the pile diameter remained equal. Therefore the critical ice velocity went down as well for a larger mass.

A change in stiffness has the same negative correlation between stiffness and the boundaries. Huang used four different stiffnesses and natural frequencies and found that for every increase in stiffness, the transition speed went down [17]. Owen found the same conclusion during the experiments in the IVOS test campaign [22].

Owen also did research into the dependency on the damping ratio and a change in mass and stiffness, whilst keeping the natural frequency the same. For the first, the lower boundary of FLI was not influenced by an increasing or decreasing damping ratio. The upper boundary had a negative correlation between damping ratio and transition velocity. The latter had a negative correlation between mass and stiffness and both the lower and upper boundary of FLI [22].

It should be noted that all above predictions are based on one or a few experiments. Different initial structural properties could have different influence on the crushing regimes.

## 2-4 Aspect ratio

One of the most important parameters which defines the occurring failure or deformation mode during a test campaign is the aspect ratio, the ratio between the pile diameter and ice thickness [28]. This research focusses on crushing mainly, neglecting radial or circumferential cracking, bending, buckling or splitting. In the paper of Blanchet a theoretical model is proposed which failure mode occurs at different ice thicknesses and aspect ratios. This model is later verified by using previous full- and small-scale experiments [28]. In the SHIVER test campaign, the diameter of the two piles are 200 and 300 mm. According to Blanchet, structures below a diameter of 750 mm will only fail in pure crushing for aspect ratios below 5, while for aspect ratios between five and 20 the failure mode will change mostly to bending and above 20 only to buckling. The experiments Blanchet compared showed similar results. Table 2-1 gives the aspect ratios for which certain failure modes have been found by Blanchet. Pure crushing occurs at aspect ratios up to five, as predicted by theory. Crushing with radial cracking will occur for higher aspect ratios as well. Bending will be found for aspect ratios between 2.5 and 12 instead of the expected 5 and 20 while for higher ratios buckling will be the main failure mode. During the SHIVER test campaign the ice thickness is expected to be around 50 mm. Combined with the two fixed pile diameters of 200 and 300, this will result in aspect ratios of

respectively 4 and 6. For the thinner pile, it is expected to see pure crushing failure, nonetheless, for the thicker pile there is a possibility of not seeing pure crushing, but only crushing with radial cracking, bending and buckling. This should be analysed closely during the test campaign to avoid not getting crushing failure and only receiving undesirable results.

Previous mentioned report [28] moreover points out that below penetration rates of 0.1 mm/s, only creep will appear and between 0.1 and 1 mm/s a transition between brittle and ductile failure modes will show up. During the test campaign the minimum carriage velocity should be above 1 mm/s.

**Table 2-1:** Variation of failure modes with aspect ratios [28].

<b>Failure mode</b>	<b>Range of aspect Ratios</b>
Pure crushing	0.3 – 5
Crushing with Flaking	0.35 – 4
Crushing with Radial Cracking	0.8 – 13
Bending	2.5 – 12
Radial and circumferential cracking	3.5 – 40
Buckling	2.5 – 90

## 2-5 Base case

A base case has been chosen based on previous test campaigns and their reported parameters. Those parameters can be seen in Appendix A and Appendix B shows graph which illustrate the in Appendix A given parameters. The base case is thereafter evaluated in the TU Delft model to predict which crushing regimes will occur for which indenter velocities. The TU Delft model is a phenomenological model from Hendrikse [8], which predicts ice-structure interaction based on local contact, elastic, visco-elastic and visco-plastic ice deformation, so that the contact area between ice and structure is taken into account. In the first three graphs of Appendix B, the mass, stiffness and natural frequency have been compared. Most model-scale tests have been done with a mass between 100 and 3000 kg, with a natural frequency between 2 and 11 Hz and the stiffness between  $10^4$  and  $10^7$  N/m. Since the peak frequency of the actuators is around 5 Hz, as mentioned in Section 4-2, the natural frequency of the base case is chosen a bit below this value, so a value below 5 Hz, namely 3 Hz, is chosen so a parameter study with increasing natural frequency is still possible. In Figure B-4 the natural frequency is plotted against the damping ratio as fraction of critical damping, where the damping ratio varies between close to zero and 0.12. For low natural frequencies, it is mostly between 0 and 0.04, so a damping ratio of 0.02 has been chosen.

In Figures B-5 till B-8 the natural frequency is compared with the ice load divided by mass. During intermittent crushing the peak forces are the most important, while during frequency lock-in and continuous brittle crushing those are the mean forces. Since there was insufficient data available for the mean force during frequency lock-in to draw conclusions, a plot with the maximum force is given as well. Simulations demonstrated that the peak forces during intermittent crushing would be around 8 kN, the maximum force during frequency lock-in around 4 kN and average force during FLI and CBC around 2.5 kN. During ICR, the ratio between ice load and mass is between 6 and 10 for low frequencies, which would result in a

mass between 750 and 1250 kg for our tests. For the maximum force during FLI the ratio is around 4, resulting in a desired mass of 1000 kg. A ratio between 2 and 4 has been found for the average force during FLI, which results in a mass between 625 and 1250 kg. For CBC there is only one datapoint for a relatively low natural frequency, with a ratio of 3, which would result in a mass of around 800 kg. Considering all these findings, a base case with 1000 kg is chosen, which is also in line with the earlier found most used masses during test campaigns between 100 and 3000 kg.

An attempt has been made to plot the aspect ratios against the ice load divided by mass in Figures B-9, B-10 and B-11, but not enough data was available for high aspect ratios to draw a conclusion from this. The complete base case could be found in Table 2-2.

**Table 2-2:** Base case based on the literature study

Natural frequency [Hz]	Mass [kg]	Stiffness [kN/m]	Damping ratio [-]	Pile diameter [mm]	Ice thickness [mm]
3.0	1000	355	0.02	300	50

This base case is simulated in the TU Delft Model and the statistics of these simulation have been plotted (Figure C-1) together with the phase plane plots (Figure C-2). The transition from intermittent crushing to frequency lock-in is around 50 mm/s. This can be derived from the developing circular shape of the phase plane plot, the increasing frequency of the displacement which gets close to the natural frequency, the value of  $\beta$  which approaches 1.5 and from the decreasing difference between minimum and maximum load and displacement. Around 120 mm/s the failure mode shifts from frequency lock-in to continuous brittle crushing. The main indicators for this shift are that the difference between mean and maximum displacement is approaching zero and the  $\beta$  value which declines to far below 1. In the phase-plane plot the circular shape narrows during continuous brittle crushing. Around 130 mm/s there are a few cycles of lock-in. The range of velocities for which the carriage is able to keep its velocity accurately during the SHIVER test campaign is between 10 mm/s and 150 mm/s, which is in line with the transition velocities.

Furthermore, Figures B-12 till B-14 show for which velocities for a given natural frequency which crushing regime occurs. ICR occurs mostly between 1 and 80 mm/s, FLI between 20 and 200 mm/s and CBC above indentation speeds of 50 mm/s. The boundary velocity between ICR and FLI of 50 mm/s is in this regimes and the boundary velocity of 120 mm/s between FLI and CBC as well. These velocities are dependent on more than only natural frequency, but could be used as an indication.

---

# Chapter 3

---

## Scaling

If no full-scale data is available, model-scale data should be used to predict the behaviour of the structure. The information of model-scale data is only useful when dimensionless numbers are known which can convert the data into full-scale data. In other fields of mechanics, for example fluid mechanics, these numbers are already known, for example the Froude number and the Reynold's number [12]. Research into scaling of structural properties when loaded by ice crushing has been performed in the past, but up till now, no clear conclusions can be drawn from these studies. Several scaling laws and dimensionless numbers have been proposed, but no one is proved completely true yet.

### 3-1 Literature proposals

In this section multiple in literature proposed dimensionless numbers are listed and an explanation is given on how they are derived.

#### 3-1-1 First scaling laws

In 1984, Timco started with investigating first scaling laws to know the desired model test values for a certain full scale structure [29]. According to Timco, two structures should have the following compared to each other:

- Geometric similitude
- Kinematic similitude
- Dynamic similitude

Geometric similitude can be achieved scaling all linear dimensions with the same factor. For our test setup this would mean that both the shape of the structure and the aspect ratio, the ratio between ice thickness and diameter, should remain the same.

Kinematic similitude will be achieved when the velocity of the structure is scaled with a certain factor for all velocities. Dynamic similitude will be achieved when the forces between prototype and model-scale are directly proportional for all forces.

### 3-1-2 Reduced velocity

In “Ice-induced vibrations and scaling” [12] a dimensionless number is proposed that is based on ice velocity, ice thickness and the first natural frequency of the structure.

The analysis starts by looking at vortex-induced vibrations when a cylinder is subjected to a flow of a fluid. The vortex-shedding frequency is  $U$  over  $L$ , with  $L$  being the length between two vortices on one side of the structure, which is assumed to be equal to the cylinders diameter  $D$  for simplicity. If the damping is low, this frequency will be close to the natural frequency. The dimensionless group which results from the terms is the reduced velocity  $V_R$ . The formula for reduced velocity has been given in Formula 3-1.

$$V_R = \frac{U}{ND} \tag{3-1}$$

For ice induced vibrations they propose a dimensionless number that is almost similar. Ice fails by a formation a of transverse cracks at a distance  $L$  from the structure. The frequency of the force is then equal to  $U$  over  $L$  and again we expect vibrations when  $U/L$  equal to the first natural frequency. The most relevant natural frequency is assumed to be the lowest natural frequency, which corresponds to translation at waterline height. To determine if  $L$  is dependent on ice thickness  $t$  or diameter  $D$  a literature study has been done into 5 reports on full-scale tests and 6 reporters on model scale structures. Representing  $L$  by the ice thickness shows a higher consistency than representing it by its diameter. The other conclusion that could be drawn is that the distance  $U/N$  lies between 0.01 and 0.4 times the ice thickness during lock-in. The writers already predicted, based on “Model based on high-pressure zones” [30] [31] [32], that ice thickness would be the controlling factor for high pressure zones formation, instability and collapse. This results in the dimensionless number shown in Equation 3-2.

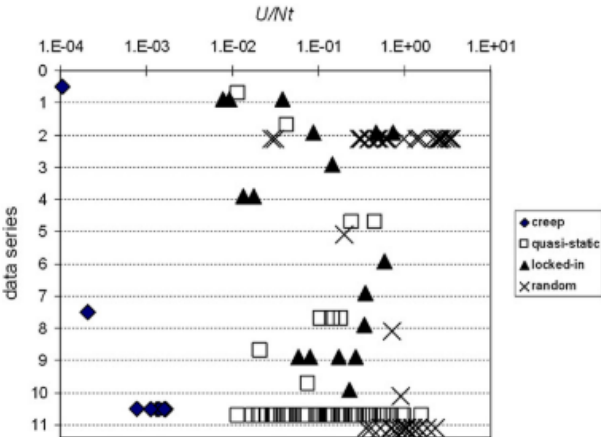


Figure 3-1: Relation between U/Nt and failure mode [12].

$$V_R = \frac{U}{Nt} \tag{3-2}$$

with  $U$  the ice velocity,  $N$  the first natural frequency and  $t$  the ice thickness.

In Figure 3-1, the results of the literature study from Palmer et al. are shown. It can indeed be seen that per data sets intermittent crushing occurs at lower number of reduced velocity than frequency lock-in and latter at lower reduced velocities than continuous brittle crushing. Comparing all data sets together, there is no clear relation between the dimensionless number and the failure modes. This suggests that more parameters are needed to scale ice-induced vibrations.

During our test campaign it is possible to check if this dimensionless number is true. The ice thickness is targeted to be kept constant at the ice basin, but the penetration rate could be changed up to 0.15 m/s and the natural frequency can be scaled up to 5 Hz. Multiple combinations with a constant U/N can be tested to check if the failure mode remains the same.

### 3-1-3 Strouhal number

In “Ice loading on a compliant indenter” [10] the analysis starts again with vortex induced vibrations. If the natural frequency in lateral direction is equal to the vortex shedding frequency, resonance of the structure can occur. The ratio of U over D to the natural frequency is the Strouhal number.

During intermittent crushing, the maximum displacement can be derived by dividing the maximum failure force of ice by the structural stiffness. The frequency of ice failure is then given by Formula 3-3.

$$f = \frac{V}{\delta_c} = \frac{KV}{F_c} \quad (3-3)$$

with  $V$  the ice indentation speed,  $\delta_c$  the maximum displacement of the structure,  $K$  the structural stiffness and  $F_c$  the maximum ice failure force.

The Strouhal number for quasi-static response is given in Formula 3-4.

$$S_I = \frac{f_N}{f} = \frac{f_N F_c}{KV} \quad (3-4)$$

Transition between intermittent crushing and frequency lock-in takes places between Strouhal numbers of 0.6 to 0.8 based on Formula 3-4. During frequency lock-in the Strouhal number reaches a value close to 1, because the structure vibrates with a frequency close to its natural frequency. Due to elastic deformation of the ice, the displacement in Formula 3-3 will be slightly higher than in reality. This means the Strouhal number calculated in Formula 3-4 is a bit lower than in reality.

When looking to the transition between frequency lock-in and continuous brittle crushing, the critical Strouhal number is the Strouhal number at which the structural response will change into CBC [19]. The critical Strouhal number is positively correlated with the damping ratio, as can be seen in Figure 3-2.

The conclusion of this report is that the Strouhal number alone is not enough to scale from model-scale to full scale. At least ice thickness is of importance here, because higher thicknesses will result in a transition at higher Strouhal numbers.

In our test campaign, the maximum failure force remained constant, if the pile geometry and ice properties are kept constant. In that case the variables of the Strouhal number are stiffness, natural frequency and ice velocity, which can be rewritten in the only variables being mass and ice velocity. The findings of Section 2-3 and Figure 3-2 about the boundary velocity between frequency lock-in and continuous brittle crushing, which will decrease for higher damping ratios or lower Strouhal numbers, correspond with each other.

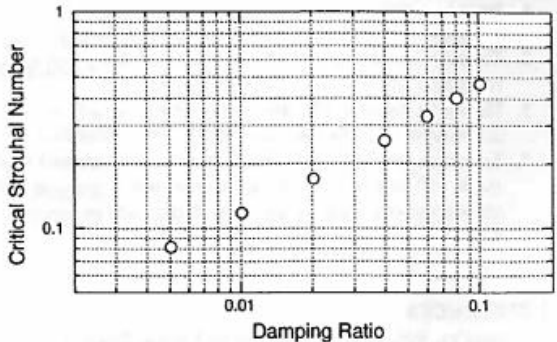


**Figure 3-2:** Critical Strouhal Number against damping ratio [10].

### 3-1-4 Interaction coefficient

In “Model test study of the interaction between ice and a compliant vertical narrow structure” [17] the thought is brought up that not only one dimensionless group is of importance during scaling, but as many as three. The first one is based on the structural stiffness, which determines the elastic deformation of the ice, resulting in the elasticity factor  $\frac{K}{Eh}$ . The second group is based on the thought that the strain rate controls the failure mode and since the natural frequency has an influence on the strain rate as well for compliant structures, resulting in the rate control factor  $\frac{Df_0}{v}$ . Lastly, linear dimensions should be kept constant, as already stated by Timco [29] and therefore the diameter of the structure and the ice thickness should be scaled with the same ratio and therefore dimension control factor  $\frac{D}{h}$  can be found.

## 3-2 Viscoelastic deformation

Hammer et al. proposes 11 dimensionless numbers which can be found by using the Buckingham Pi theorem [33] on 14 relevant parameters [34]. The three used repeating variables are  $\sigma_c$ ,  $\omega$  and  $d$ . For a single degree of freedom structure, this will result in the in Formula 3-5 mentioned groups.

$$\boldsymbol{\pi} = \left[ \frac{\sigma_c d}{m\omega^2} \zeta \frac{\ddot{x}}{d\omega^2} \frac{\dot{x}}{d\omega} \frac{x}{d} \frac{w}{d} \frac{h}{d} \frac{v_{ice}}{d\omega} \frac{E_1 \eta \omega}{\sigma_c} \frac{E_2}{\sigma_c} \right] \quad (3-5)$$

, with the ice properties being  $\sigma_c$  the crushing strength,  $d$  the average grain size,  $v_{ice}$  the drift speed,  $\eta$  the material coefficient of viscosity,  $E_1$  an elasticity modulus which defines elastic deformation and  $E_2$  an elasticity modulus which defines viscoelastic deformations. The used structural properties  $m$  the mass,  $\omega$  the natural frequency,  $\zeta$  the damping ratio as fraction of critical damping and  $x$ ,  $\dot{x}$  and  $\ddot{x}$  respectively the displacement, velocity and acceleration at the point of ice-structure interaction.

The main difference between these dimensionless numbers and the in literature proposed numbers is that the viscoelastic parameters of the ice  $\eta$  and  $E_2$  and the grain size have been taken into account. To check if those parameters could indeed be neglected, it will be studied what the effect is of taking them out of the relevant dimensionless numbers.

If ice will only deform in a linear elastic manner, there is a set of 11 variables. Using again the Buckingham Pi theorem [33], with three dimensions, the problem can be written in the form of 8 dimensionless numbers, the  $\pi$ -groups. The chosen repeating variables are natural frequency, compressive strength and ice thickness. In Table 3-1 all dimensions of the relevant parameters are given and in Formula 3-6 the subsequent  $\pi$ -groups derived from these parameters.

**Table 3-1:** Matrix with dimensions of all relevant parameters if ice-structure interaction is assumed to be only linear elastic.

Dim	$m$	$\zeta$	$\omega$	$\ddot{x}$	$\dot{x}$	$x$	$w$	$h$	$v_{ice}$	$E_1$	$\sigma_c$
M	1	0	0	0	0	0	0	0	0	1	1
L	0	0	0	1	1	1	1	1	1	-1	-1
T	0	0	-1	-2	-1	0	0	0	-1	-2	-2

$$\boldsymbol{\pi} = \left[ \frac{\sigma_c h}{m\omega^2} \zeta \frac{\ddot{x}}{h\omega^2} \frac{\dot{x}}{h\omega} \frac{x}{h} \frac{w}{h} \frac{v_{ice}}{h\omega} \frac{E_1}{\sigma_c} \right] \quad (3-6)$$

There is a lot of similarity when comparing those  $\pi$ -groups with earlier literature study. Group  $\pi_7$ ,  $\frac{v_{ice}}{h\omega}$ , can be recognised from “Ice-induced vibrations and scaling” [12]. “Ice loading on a compliant indenter” [10] derived the Strouhal number of  $S_l = \frac{f_N F_C}{KV}$  which can be rewritten to

$S_I = \frac{f_N \sigma_c w h}{KV}$  and this is equal to  $\frac{\pi_1 \pi_6}{\pi_7}$ . In “Model test study of the interaction between ice and a compliant vertical narrow structure” [17] three dimensionless groups are proposed,  $\frac{1}{\pi_1 \pi_8}$  is the so-called elasticity control factor,  $\frac{\pi_6}{\pi_7}$  is the rate control factor and  $\pi_6$  is called the dimension control factor.

Parameters  $\pi_3$ ,  $\pi_4$  and  $\pi_5$  are not relevant in our study, since those are outputs of the system and cannot be scaled beforehand. Since  $\pi_2$  only depends on the damping ratio, this has to be kept the same during scaling, if the same interaction is desired. Since the ice parameters during the test campaign are not easily controllable, those will be tried to be kept constant. Therefore it won't be possible to change the compressive strength or the elastic modulus and  $\pi_8$  will remain the same.

$\pi_1$ ,  $\pi_6$  and  $\pi_7$  are the variables which could be adapted during the campaign to check if the theory that ice only fails in a linear elastic way holds. If the diameter of the cylinder is kept the same, the only variables which could be changed are the ice velocity and the mass. Next to the cylinder with a diameter of 300 mm, a second pile will be brought with a diameter of 200 mm. The ice thickness should be changed with the same ratio to keep  $\pi_6$  constant. There are three possibilities to change the variables, without adjusting the value of the dimensionless group, being a change in stiffness and ice velocity, a change in stiffness and mass and the last is an adjustment in stiffness, mass and ice velocity. The input values can be found in the table below, wherein the values altered with respect to the base case are marked in grey. Note that for variation 1 all other variations are possible, as long as the natural frequency and ice velocity scale with the same ratio and mass with the negative value of that ratio squared. All other variations are fixed, since the pile diameter is fixed

**Table 3-2:** Variations on base case for the study into scaling in a linear brittle manner only.

	<b>m</b> [kg]	<b>F<sub>n</sub></b> [Hz]	<b>K</b> [kN/m]	<b>ζ</b> [-]	<b>Ice thickness</b> [mm]	<b>Structure width</b> [mm]	<b>Ice velocity</b> [mm/s]
<b>Base case</b>	1000	3.00	355	0.02	50	300	60.0
<b>Variation 1</b>	2250	2.00	355	0.02	50	300	40.0
<b>Variation 2</b>	1000	2.45	237	0.02	33.3	200	32.7
<b>Variation 3</b>	296	4.50	237	0.02	33.3	200	60.0
<b>Variation 4</b>	667	3.00	237	0.02	33.3	200	40.0

If all four variations give the same output as the base case, we can assume that ice fails in a purely linear elastic brittle manner, but if the output is different we have to include the viscoelastic parameters as well and we get three extra dimensionless groups. Those groups are  $\frac{h}{a}$ ,  $\frac{\eta \omega}{\sigma_c}$  and  $\frac{E_2}{\sigma_c}$ . The latter can't be changed since we can't change the parameters of the ice precisely. In variation 4 the natural frequency is kept the same as in the base case, so  $\frac{\eta \omega}{\sigma_c}$  will

remain constant. If the output of variation 4 is different from the base case, we know that there is still another parameter which should be constant. This could be the parameter including the grain size, but this is not controllable or measurable for us.

A follow-up test campaign could validate or reject the predicted visco-elastic parameters. The grain size could be measured after the test runs by taking thin sections at various locations along the channels and analysing those under a microscope. The elasticity modulus which defines viscoelastic deformations and the material coefficient of viscosity could not be measured directly, but effects of those parameters could be derived from the data. First of all a measurement could be done where the structure is pushed into the ice and before the ice fails, the structure stops pushing. If the ice load remains equal, only linear elastic parameters could be taken into account, but if the ice load shows relaxations over time, viscoelastic parameters will have an influence as well. A possible influence could also be retrieved from plotting the ice speed against the ice failure frequency over ice thickness. If this is a linear trend, the ice is purely linear elastic, while if this ratio is lower at lower speeds, viscoelastic parameters should be taken into account.

---

# Chapter 4

---

## Test campaign

In this chapter information about the ice tank where the experimental tests were conducted is presented. Furthermore a description of the hardware and software of the experimental setup is given.

### 4-1 Ice tank

The tests are conducted at the Ice tank from the Aalto University. The tank is 40 by 40 metres and 2.8 metres deep (Figure 4-1). During the experiments a mixture of ethanol and water was frozen. During the first tests, the ice turned out to be too slushy, while brittle ice was desired to measure all three crushing regimes, so the freezing temperature was decreased and the freezing degree hours were increased. The freezing temperature was between -10 and -18 degrees Celsius. The tests were conducted at air temperatures between -10 degrees Celsius and -12 degrees Celsius and the water temperature was varying just below zero, namely between -0.10 and -0.40 degrees Celsius.



**Figure 4-1:** The ice tank at the Aalto University.

## 4-2 Experimental setup - Hardware

During the SHIVER test campaign a cylindrical pile with a diameter of 200 mm was used. A second pile with a diameter of 300 mm was brought, but as discussed in Chapter 6, not used. In Figure 4-2 on the left the pile is shown on its side with two notches around the whole diameter. These notches were created to improve the accuracy of the strain gauges on the inside of the pile. These strain gauges, which can be seen at the right side of the figure at number 3, are installed in pairs at four sides of the pile to measure the strain. At the top of the pile, an accelerometer was attached, which can be seen at number 2. At number 1 one of the two potentiometers is presented which detect the deflection of the pile in x- and y- direction.

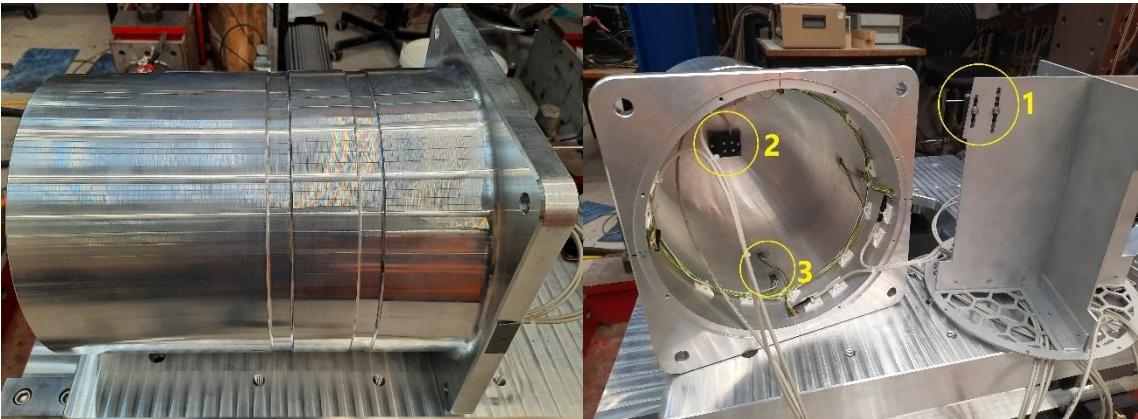


**Figure 4-2:** On the left the pile used during the SHIVER test campaign on its side. On the right the inside of the pile with at 1 the potentiometer, at 2 the accelerometer and at 3 the strain gauges.

The pile was mounted with 4 bolts to an aluminium plate. The plate provides a honeycomb pattern for reasons of weight reduction. With a railing system on both ends of the plate, it is attached to a top plate with the similar honeycomb pattern. This plate is again connected with a railing system, but perpendicular to the first one, to another aluminium frame, which is clamped and screwed between the railings of the carriage from the ice tank. On the right of Figure 4-3, the two aluminium plates with the railing system and the top frame are shown. In Figure 4-4 the honeycomb pattern and the attachment of the pile in the plates are presented. On both of the plates another accelerometer is pasted to measure carriage vibrations and providing the availability to calculate inertial forces.



**Figure 4-3:** On the top plate with the first rails attached to it. On the right all three plates with rails in two directions to allow movement in x- and y-direction.

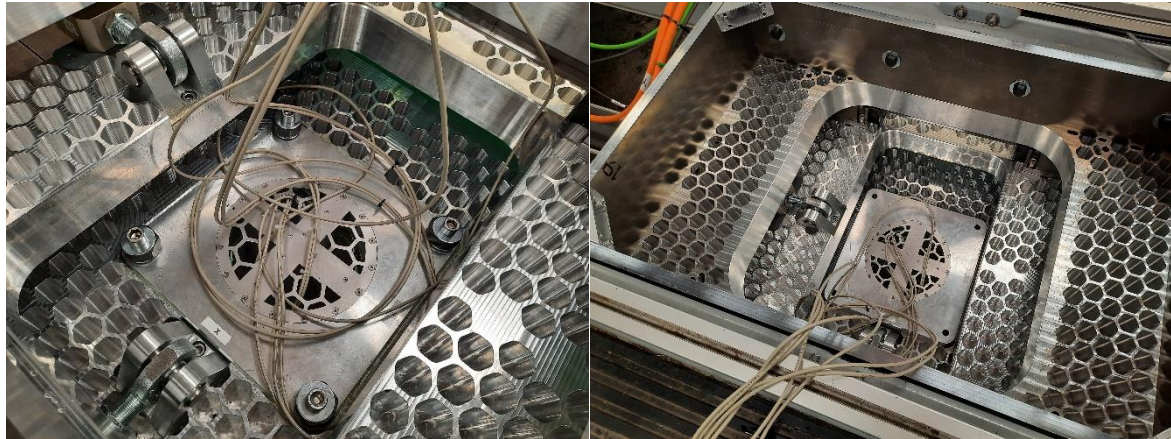


**Figure 4-4:** On the left the bottom of the pile which is bolted in the lower frame. On the right the three aluminium plates with the milled honeycomb pattern.

The two plates were pushed with a linear actuator to provide the correct displacement. The maximum design frequency of those actuators is 5 Hz, which should be taken into account when performing tests with higher natural frequencies. Those actuators were fixed to the plate above the one being pushed. Next to the strain gauges, the ice load was also measured by two load cells to provide redundancy in measurement and inertial load. The displacement of the pile was measured by two displacement sensors attached to the plates. On the left of Figure 4-5 the black actuator which is attached to the load cell is depicted. Next to the actuator, the displacement sensor could be seen. A complete overview of all the hardware is shown on the right of Figure 4-5.



**Figure 4-5:** On the left the side of the setup which stands upside down, with two actuator, load cell and displacement sensor. On the right the total setup combined.

### 4-3 Experimental setup - Software

To provide the correct displacement for the actuators, a real-time numerical model is used. The problem is solved in the modal domain. The equation of motion of a damped system in the modal domain is given by Equation 4-1 which can be rewritten into Equation 4-2.

$$\mathbf{M}^* \ddot{\mathbf{u}} + \mathbf{C}^* \dot{\mathbf{u}} + \mathbf{K}^* \mathbf{u} = \mathbf{E}^T \mathbf{f} \quad (4-1)$$

, with  $M^*$  the modal mass matrix,  $C^*$  the modal damping matrix,  $K^*$  the modal stiffness matrix,  $u$ ,  $\dot{u}$ ,  $\ddot{u}$  respectively the displacement, velocity and acceleration of the structure at a certain time and  $f$  the ice force.

$$\ddot{u}_i + \frac{c_{ii}^*}{m_{ii}^*} \cdot \dot{u}_i + \omega_i^2 \cdot u_i = \frac{F_i^*(t)}{m_{ii}^*} \quad (4-2)$$

In Equation 4-3 and 4-4 above equation is rewritten by replacing the modal damping matrix by the ratio of critical damping.

$$c_{ii}^* = \zeta_i \cdot 2 \cdot m_{ii}^* \cdot \omega_i \quad (4-3)$$

$$\ddot{u}_i(t) + 2 \cdot \zeta_i \cdot \omega_i \cdot \dot{u}_i(t) + \omega_i^2 \cdot u_i(t) = \frac{\Phi_{ice}}{m^*} \cdot F_{ice}(t) \quad (4-4)$$

, with  $u$ ,  $\dot{u}$ ,  $\ddot{u}$  respectively the displacement, velocity and acceleration of the structure at a certain time,  $\zeta_i$  the damping coefficient as fraction of critical damping,  $\omega_i$  the natural frequency,  $F_{ice}$  the ice load,  $\Phi_{ice}$  the amplitude at ice-structure interaction point and  $m^*$  the model amplitude at ice action point, but since it is mass-normalised with the eigenmodes, it is in this case always equal to 1. The subscript  $i$  denotes the mode, but since it is a single degree of freedom system,  $i$  is always equal to 1.

To derive the displacement and velocity of the next time step  $t_{i+1}$ , the Euler-Cromer Method is used [35]. This method uses the velocity at a certain time  $t_i$  and adds up the acceleration at  $t_i$  times the time step to determine the velocity for the next time step at  $t_{i+1}$ . This velocity for time  $t_{i+1}$  is multiplied with the timestep and added to the displacement at time  $t_i$  to determine the displacement at  $t_{i+1}$ . Formulas 4-5 and 4-6 show the Euler-Cromer Method applied on Formula 4-4.

$$\dot{u}(t_{i+1}) = \dot{u}(t_i) + \left( \frac{\Phi_{ice}}{m^*} \cdot F_{ice}(t) - 2 \cdot \zeta \cdot \omega \cdot \dot{u}(t_i) + \omega^2 \cdot u(t_i) \right) \cdot \Delta t \quad (4-5)$$

$$u(t_{i+1}) = u(t_i) + \dot{u}(t_{i+1}) \cdot \Delta t \quad (4-6)$$

### 4-4 Workflow

A structural model of a single degree of freedom structure is used as input for the test setup. In this structural model, the natural frequency, the mass in the form of modal amplitude ( $1/\sqrt{m}$ ) and damping in the form of logarithmic decrement were used as input. This model was uploaded to a Teensy board in the control box. The control box gives a displacement in y-direction to one of the power boxes as input and this power box directs the actuator to the correct displacement in y-direction. During this research only single degree of freedom structures were tested, so the actuator in x-direction was not used. On the inside of the pile, as can be seen in Figure 4-2, there are eight strain gauges, of which four measured the strain in the pile in the direction of the ice and four in the direction perpendicular to the ice. This strain was sent to the control box, which converts it to a force via a calibration factor which is determined during calibration prior to the testing days. This force is then used as input of the control box in Formula 4-5 and the displacement of the next time step is calculated and the cycle starts over. At the same time the acquired data is sent to the laptop to have a real-time overview of the tests. This workflow is visualised in Figure 4-6.

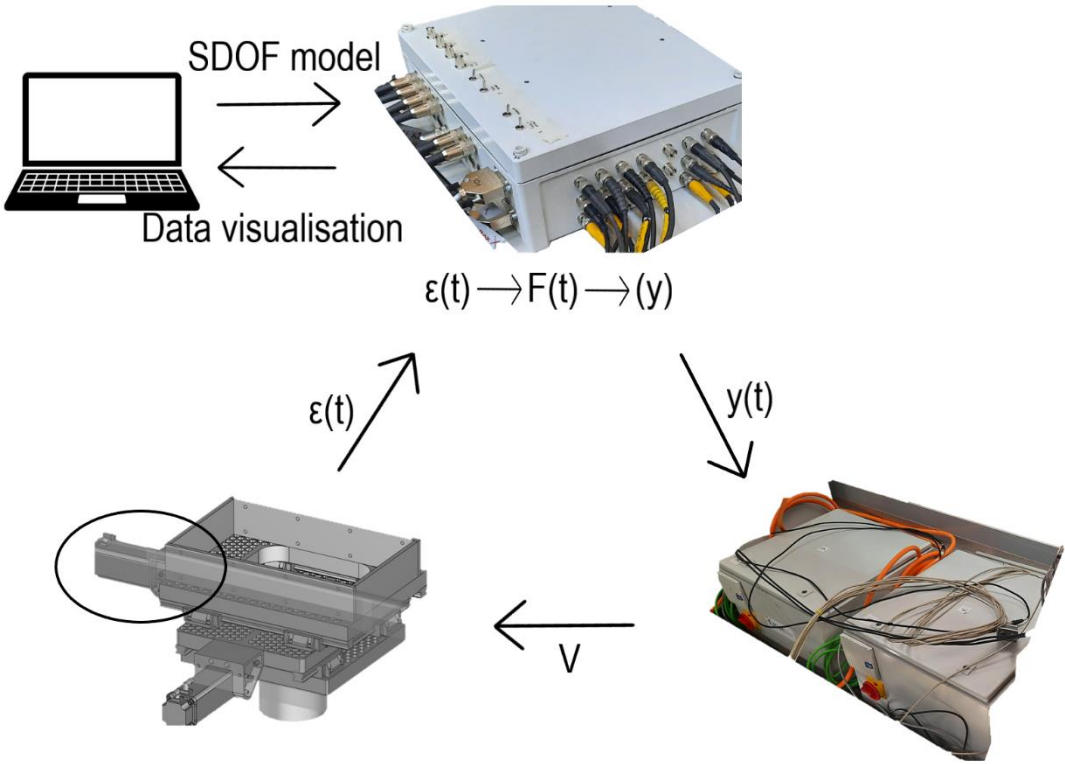


**Figure 4-6:** The workflow of the test setup. A single degree of freedom model is uploaded from a laptop to the software in the control box in the top middle. This control box gives a displacement input to the power boxes on the bottom right and those power boxes give a voltage input to the circled actuator to move to that position. In the pile on the bottom left strain gauges are placed with measure the strain. This strain signal is send to the control box again, which converts it based on the model input from the laptop to a force and thereafter to a displacement, after which the cycle continues.

## 4-5 Test overview

During some open water tests, the discovery has been made that the natural frequency of the carriage was at 3 Hz. Unfortunately this was at the natural frequency of the base case, so it was decided to lower the natural frequency of the base case to two Hz and increase the mass to 2000 kg, because the TU Delft model simulations showed equal boundary velocities for the old and new base case. The first tests were performed with the new base case, where the mass and stiffness were scaled according to the measured ice loads, to keep the natural frequency equal. The first test day at the 28<sup>th</sup> of May was a trial test day with thin ice to ensure that the test setup was working (left-hand of Figure 4-7). The next testing day the ice was thicker, but the desired brittle characteristics were not achieved as can be seen on the right side of Figure 4-7. On top of that, the peak loads were below 1.8 kN, while peak loads of seven to eight kN were expected.

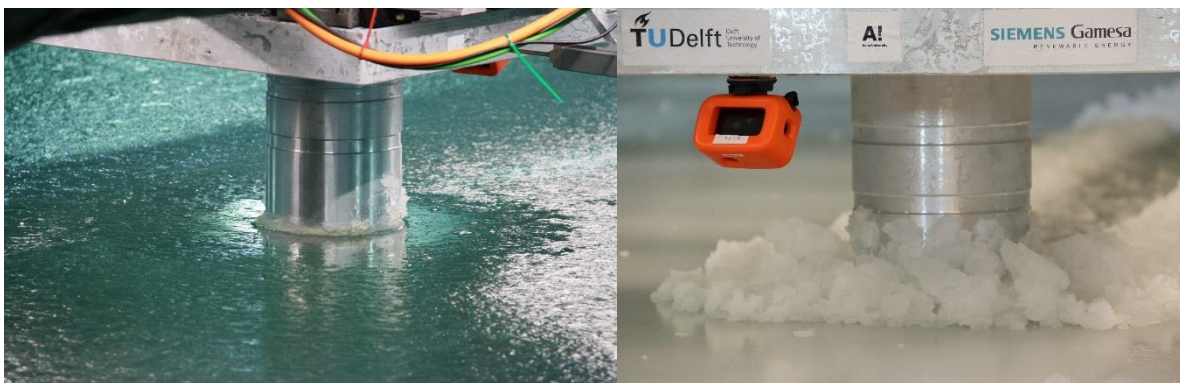


**Figure 4-7:** On the left side the trial test day ice and on the right side non-brittle ice during the second test day.

In the beginning of the third testing day at the 4<sup>th</sup> of June the ice the ice was better, but it quickly degraded over time to the same properties as the day before, so further tests were stopped that day. At the 8<sup>th</sup> of June the freezing degree hours were increased and peak loads of almost 10 kN were achieved, but for low velocities the carriage motor gave an error because it did not have enough power to push through the ice. Therefore the freezing degree hours were decreased the next three testing days. After the 15<sup>th</sup> of June the carriage PID controller was adapted, as discussed in Section 6-4 and the last two testing days have been done with the new PID controls. In Figure 4-8 the brittle ice failure could be seen at the 15<sup>th</sup> of June.



**Figure 4-8:** Two views of the tests at the 15<sup>th</sup> of June with brittle ice characteristics.

During the test campaign it has been discovered that crushing regimes were better definable for lower frequencies, so a new base case have been chosen at the 17<sup>th</sup> of June, which would be tested at the last two test days. The decision has been made to pick the second mode of an offshore wind turbine of 0.889 Hz, to have a possibility to also compare single degree of freedom structures with multi degree of freedom structures during the same test campaign. Furthermore the first and third mode have been tested as well as single degree of freedom structure.

Some tests were initially performed with a really low mass, but it turned out that the actuators could not follow the required accelerations, because of the limit of 4.9 m/s<sup>2</sup>. For tests with a mass of 250 kg, this would mean that the load drop could maximum be 1,23 kN, which was reached in most of the tests. Therefore all tests with a mass below 990 kg gave 'following errors' on the actuators or data which is unusable.

During all tests the ice thickness is measured at four locations in the channel and at the end of the day the flexural, submerged flexural and compressive strength have been measured. Those are listed in Table 4-1.

**Table 4-1:** Ice thicknesses, compressive strengths, bending strengths and submerged bending strengths during all SDOF tests performed at the SHIVER test campaign.

Test ID	Ice thickness [mm]				Compressive strength [kPa]	Bending Strength [kPa]	Bending strength sub [kPa]
	0 m	10 m	20 m	30 m			
SDOF-01	-	-	-	-	-	-	-
SDOF-02	48	49	49	53	123.6	144.5	135.5
SDOF-03							
SDOF-04							
SDOF-05	45	50	50	45	345.6	269.7	256.1
SDOF-06							
SDOF-07							
SDOF-08							
SDOF-09	43	46	44	45	487.2	444.8	434.8
SDOF-10							
SDOF-11							
SDOF-12							
SDOF-13							
SDOF-14	41	45	49	49	501.6	483.8	469.5
SDOF-15							
SDOF-16							
SDOF-17	32	35	34	38	597.0	390.4	374.4
SDOF-18							
SDOF-19							
SDOF-20	32	37	31	31	563.4	548.8	521.2
SDOF-21							
SDOF-22							
SDOF-23							
SDOF-24							
SDOF-25							
SDOF-26							
SDOF-27	33	29	36	30	579.4	500.4	526.6
SDOF-28							
SDOF-29							
SDOF-30	25	33	34	31	579.4	500.4	526.6
SDOF-31							
SDOF-32	27	26	29	26	579.4	500.4	526.6
SDOF-33							
SDOF-34	26	27	24	26	579.4	500.4	526.6
SDOF-35							
SDOF-36							
SDOF-37	28	24	29	26	579.4	500.4	526.6
SDOF-38							

## 4-6 Test matrix

In Table 4-2 the test matrix is given where all single degree of freedom tests of the SHIVER test campaign have been listed. The white rows are the base cases, the blue rows the tests where only mass is varied, the orange rows where mass and stiffness are varied, the yellow rows where damping was the variable and the grey lines are the tests where stiffness is varied. The two green lines are the first and third mode of the offshore wind turbine. The tests that are compared with each other and the base case are framed by thicker lines.

SDOF-01 is the first base case, which is used for the first tests, but the base case was changed depending on the ice properties. Therefore up to test SDOF-19, the base case was tested as well every day. Tests 20, 21 and 22 were tested without one of the base cases, to find out the behaviour at low frequencies. As explained in Section 4-4, at the 17<sup>th</sup> of June the new base case SDOF-24 has been chosen, which is thereafter varied with mass (25 and 26), mass and stiffness combined (27 and 28), damping ratio (29 and 30) and stiffness (32, 33 and 34). Since the mass variation could not go to a higher frequency because of the accelerations becoming too high for the actuators as explained in Section 4-4, a higher stiffness structure has been tested with varying mass as well to include higher frequencies (test 35, 36 and 37).

**Table 4-2:** Test matrix used during the SHIVER test campaign.

Test ID	Date	Natural Frequency [Hz]	Mass [kg]	Stiffness [kN/m]	Damping [-]
SDOF-01	28-05	2.0	2000	316	0.02
SDOF-02	01-06	2.0	1000	158	0.02
SDOF-03	01-06	1.0	4000	158	0.02
SDOF-04	01-06	4.0	250	158	0.02
SDOF-05	04-06	2.0	3000	474	0.02
SDOF-06	04-06	2.0	2500	395	0.02
SDOF-07	04-06	2.0	1500	237	0.02
SDOF-08	04-06	1.0	6000	237	0.02
SDOF-09	04-06	1.5	2667	237	0.02
SDOF-10	08-06	2.0	1500	237	0.02
SDOF-11	08-06	0.5	24000	237	0.02
SDOF-12	08-06	8.0	94	237	0.02
SDOF-13	08-06	6.0	167	237	0.02
SDOF-14	08-06	2.0	1500	237	0.02
SDOF-15	08-06	2.0	6000	947	0.02
SDOF-16	08-06	2.0	375	59	0.02
SDOF-17	11-06	2.0	3000	474	0.02
SDOF-18	11-06	2.0	3000	474	0.01
SDOF-19	11-06	2.0	3000	474	0.005
SDOF-20	15-06	0.408	15000	99	0.02
SDOF-21	15-06	0.75	4444	99	0.02
SDOF-22	15-06	0.5	10000	99	0.02
SDOF-23	17-06	0.154	308616	288	0.008
SDOF-24	17-06	0.889	5016	156	0.0133
SDOF-25	17-06	2.0	990	156	0.0133
SDOF-26	17-06	0.444	20063	156	0.0133

Test ID	Date	Natural Frequency [Hz]	Mass [kg]	Stiffness [kN/m]	Damping [-]
SDOF-27	17-06	0.889	1254	39	0.0133
SDOF-28	17-06	0.889	20063	625	0.0133
SDOF-29	17-06	0.889	5016	156	0.10626
SDOF-30	17-06	0.889	5016	156	0.00166
SDOF-31	21-06	1.663	3144	343	0.0188
SDOF-32	21-06	2.0	5016	792	0.0133
SDOF-33	21-06	0.444	5016	39	0.0133
SDOF-34	21-06	6.0	5016	7129	0.0133
SDOF-35	21-06	6.0	1100	1563	0.0133
SDOF-36	21-06	0.444	200632	1563	0.0133
SDOF-37	21-06	2.0	9900	1563	0.0133
SDOF-38	21-06	0.889	5016	156	0.0133

---

## Chapter 5

---

# Results and conclusions

### 5-1 Boundary identification

In the following section the criteria are given to determine the transition speed from ICR to FLI and from FLI to CBC.

#### 5-1-1 ICR to FLI

It can sometimes be difficult to identify if the ice fails in ICR or FLI. When the ice speed increases, the sawtooth displacement signal will turn into a sinusoidal displacement signal, but this will happen gradually, which makes it difficult to label the crushing regimes around the boundary velocity. There are multiple ways to still make a difference between those regimes. Since tests have been performed with both a ramp velocity profile and a constant velocity, multiple identification methods have been used. For both velocity profiles, it was possible to look at the above mentioned sawtooth displacement signal for ICR and sinusoidal signal for FLI, which can be seen on the middle row of Figure 5-1 and 5-2. For both signals it was also possible to distinguish the regimes by the relative velocity between carriage and structure. During intermittent crushing a high peak is observed at first after which the relative velocity drops below zero and continues with a decaying oscillation before staying just above zero during load build up, while for frequency lock-in the relative velocity has a sinusoidal shape with the minimum relative velocity at or just below zero. A third way to distinguish the boundaries is the force signal which changes from a sawtooth pattern during ICR to a signal with significantly lower peaks during FLI, which can be seen at the bottom row of Figure 5-1 and 5-2.

Test: SDOF-15. Fn: 2 Hz. V = 20 mm/s

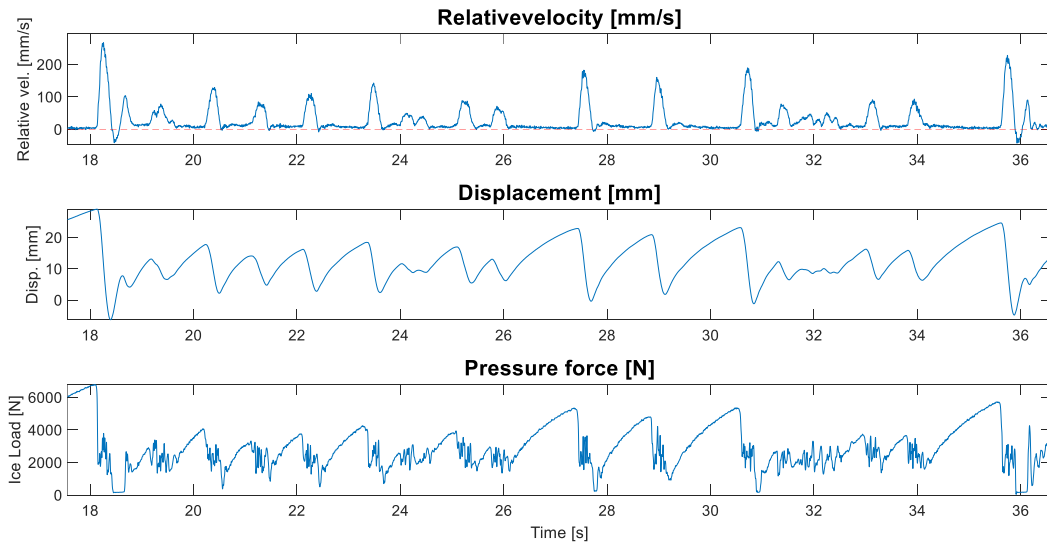


**Figure 5-1:** Typical intermittent crushing signal. The signal is from test SDOF-25 with a natural frequency of 2.0 Hz.

Test: SDOF-26. Fn: 0.444 Hz. V = 25 mm/s

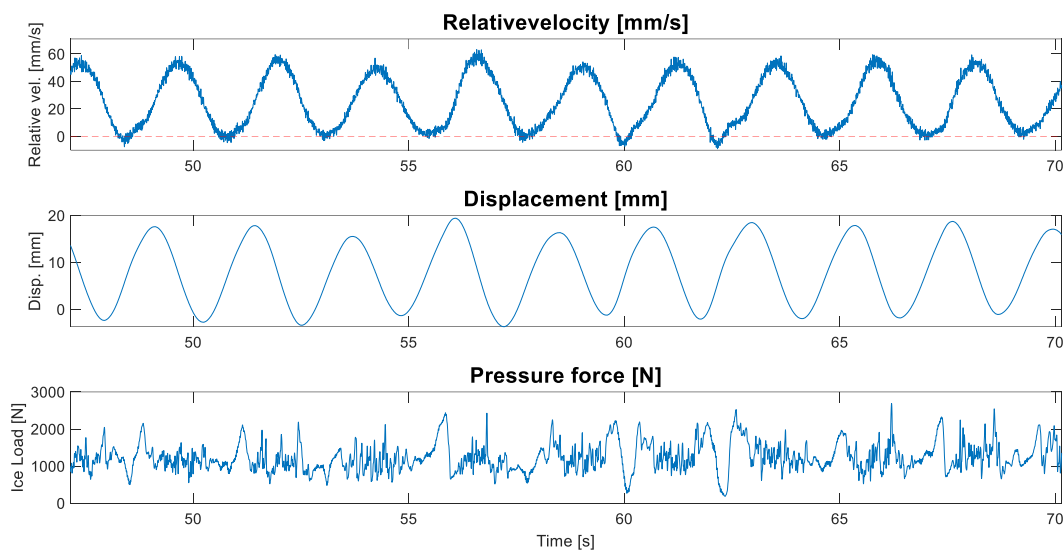


**Figure 5-2:** Typical frequency lock-in signal. The signal is from test SDOF-26 with a natural frequency of 0.444 Hz.

Besides that, during ICR, the frequency for both the displacement and ice load is relatively low and for FLI the frequency gets close to the natural frequency. With the constant velocity profile, a frequency density spectrum has been plotted, while for the velocity ramp a continuous 1D wavelet function in MATLAB is used [36]. Since the wavelet function for the ice load did not give accurate plots and the computational time for plots with a higher resolution was extremely high, a script has been used which compares the 10 seconds before and after a certain time and determines the average frequency spectrum of that time range. It should be noted that it compares 20 seconds of data and the exact velocity at which the boundary is could therefore

be a bit lower, since the velocity dropped already before the effect could be seen in the frequency response plot. For comparing multiple data sets this won't be a problem since this method is still accurate.

For the constant velocity profile, the beta-ratio, the ratio between maximum structural velocity and penetration rate could be used. For ICR this value is above 1.5, while for FLI this value is between 1.0 and 1.5. Since there is sometimes one cycle with a higher velocity, which would influence the beta value, the 99.8% highest structural velocity has been taken. Furthermore the phase plane plots have been studied. During FLI this profile is circular, while for ICR the shape changes to a spiral with a horizontal line on the right, as could be seen in Figure C-2. For the sloping velocity profile those values could not be used since the velocity is constantly changing and there is only one cycle per velocity.

The first method used to distinguish between the regimes was the frequency of the displacement. If this frequency was approaching the natural frequency, but did not have the exact value yet, the shape of the force and displacement signal was looked into. If no conclusions could be drawn from the shape, for a constant velocity profile, the beta ratio has been checked. As last option the relative velocity and the shape of the phase plane plot were analysed. Those were not used in an earlier stage, because the shapes are not easy to distinguish anymore close to transition velocities. In Figure 5-3 it can be seen that the relative velocity starts to take a sinusoidal shape which would indicate FLI being the failure mode, but there is still a period of a relative velocity close to zero which would indicate the failure mode being ICR. In Figure 5-4 the phase plane plot is starting to become circular, but there is still a horizontal line at the right top, which would indicate ICR.

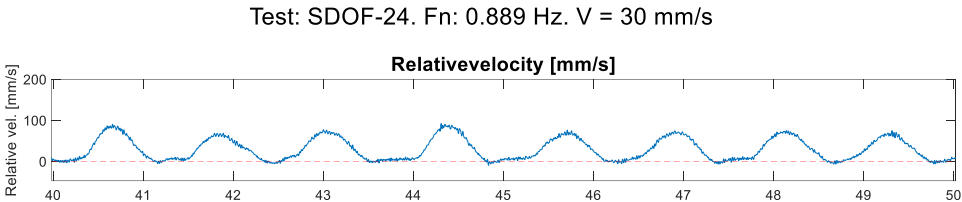


**Figure 5-3:** Relative velocity signal of a test which is close to the transition velocity between intermittent crushing and frequency lock-in. The signal is from test SDOF-24 with a natural frequency of 0.889 Hz.

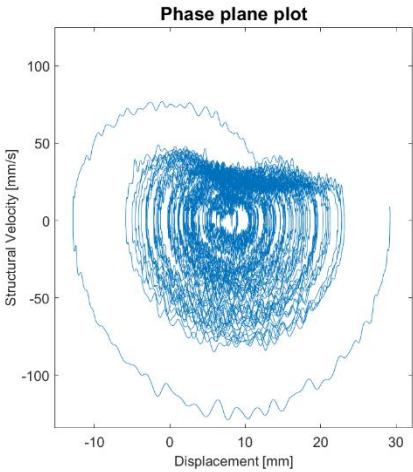


**Figure 5-4:** Phase plane plot of a test which is close to the transition velocity between intermittent crushing and frequency lock-in. The signal is from test SDOF-24 with a natural frequency of 0.889 Hz.

## 5-1-2 FLI to CBC

The boundary between frequency lock-in and continuous brittle crushing is generally easier to define. Displacements during CBC are much smaller, as can be seen in Figure 5-5, where a signal is shown around the transition velocity between FLI and CBC. After the red dashed line, the amplitude increases from 2 mm to circa 7 mm. Furthermore the force signal develops into a completely random signal, while for FLI the frequency spectrum of the force shows that the ice load fails with the same frequency as the displacement of the pile or a multiple of this frequency. Besides the small displacements and the random force signal, the relative velocity will also increase during CBC. While during FLI the relative velocity decreases to just below zero, during CBC it will always be positive. Figure 5-5 indicates this clearly. After 302 seconds, when FLI becomes the crushing regime, the relative velocity drops just below zero as the structure moves in the same direction as the ice. The relative velocity signal is rather noisy. This is mainly because of the velocity signal of the structure which is derived from the displacement signal, but to a lesser extent from the velocity signal of the carriage as well.

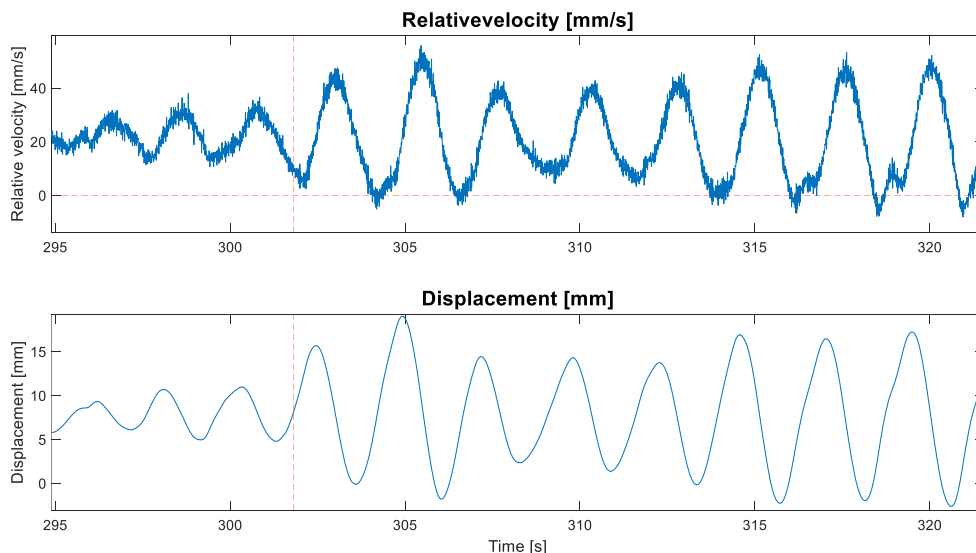


**Figure 5-5:** Typical transition from continuous brittle crushing to frequency lock-in using a downward velocity ramp. The signal is from test SDOF-26 with a natural frequency of 0.444 Hz.

The challenge with assessing the precise boundary velocity between FLI and CBC is that the structure could go into lock-in, but also gets back to continuous crushing multiple times. In Figure 5-6 this is clearly visible. A downward ramping velocity profile is used, so it is expected that once the structure gets into lock-in, it will stay there until ICR occurs at low velocities. At 73 seconds the structure gets back into CBC and around 85 seconds there are a few cycles of FLI before going back into CBC. In cases where this effect took place, the highest velocity where FLI took place is being used as transition velocity, since a small change in energy can take the structure out of lock-in and with the non-uniformity of the ice this is realistic to expect. However, the lock-in at higher velocities proves that it is possible to occur, also for lower velocities.

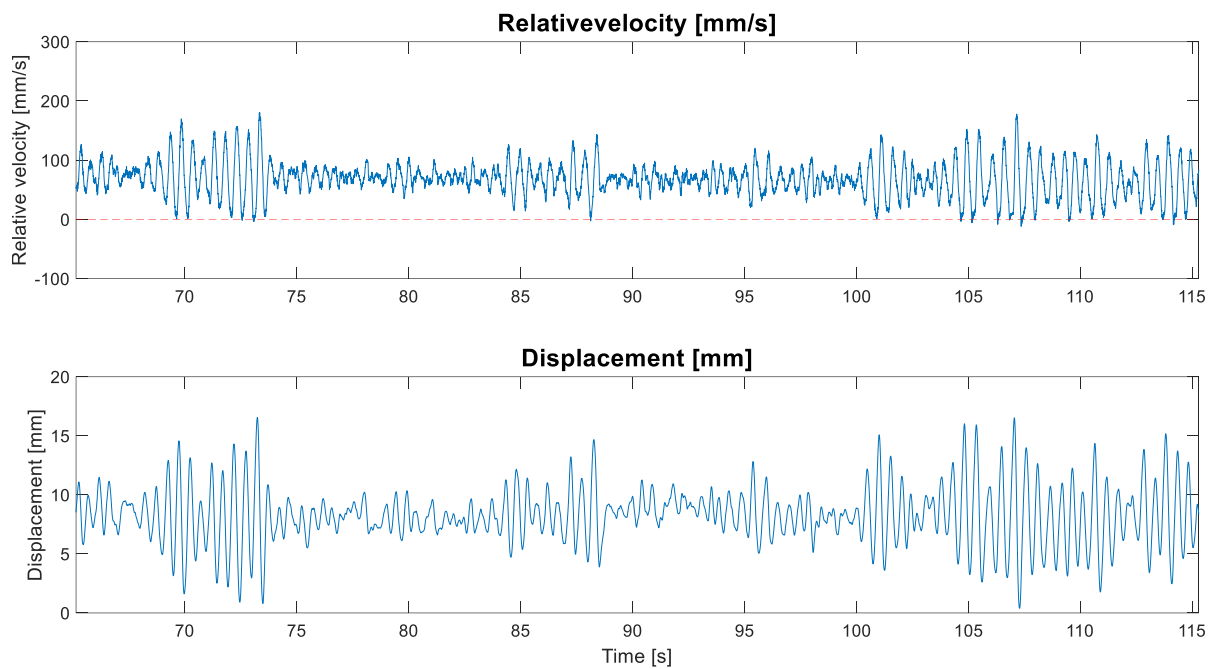


**Figure 5-6:** The relative velocity and displacement of a signal in which frequency lock-in and continuous brittle crushing take turns. The signal is from test SDOF-25 with a natural frequency of 2.0 Hz.

To determine the boundary between FLI and CBC, first the relative velocity is analysed. In most tests a conclusion could be drawn from this. Also the displacement signal gave a clear indication where FLI began, because of the higher displacements. At structures with a high rigidity, sometimes the relative velocity dropped below zero, but since it became a rigid structure instead of a flexible structure, the failure mode was CBC. Therefore the force and displacement signals have always been checked as well around the transition velocity.

### 5-1-3 Linear anomaly

During some tests there was a linear anomaly in the model ice, where the ice was stronger. This was caused by a defect in one of the spray nozzles used for seeding the ice. In Figure 5-7 the pile is approaching the 'ice ridge' on the left side. This moment is at the time of 460 seconds in Figure 5.8. First a load build-up takes place, where the force increases from just above 1 kN to peaks of almost 3 kN. This increase of force adds energy to the system and therefore the structure gets into a few lock-in cycles around 465 seconds, before returning to continuous brittle crushing. For the tests in which this scenario appeared, those frequency lock-in cycles have been neglected, because the ice conditions were totally different.

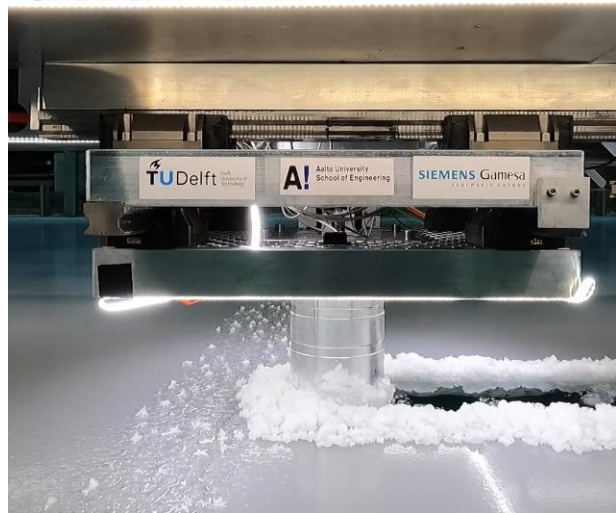


Figure 5-7: The pile approaching the anomaly during test SDOF-21.

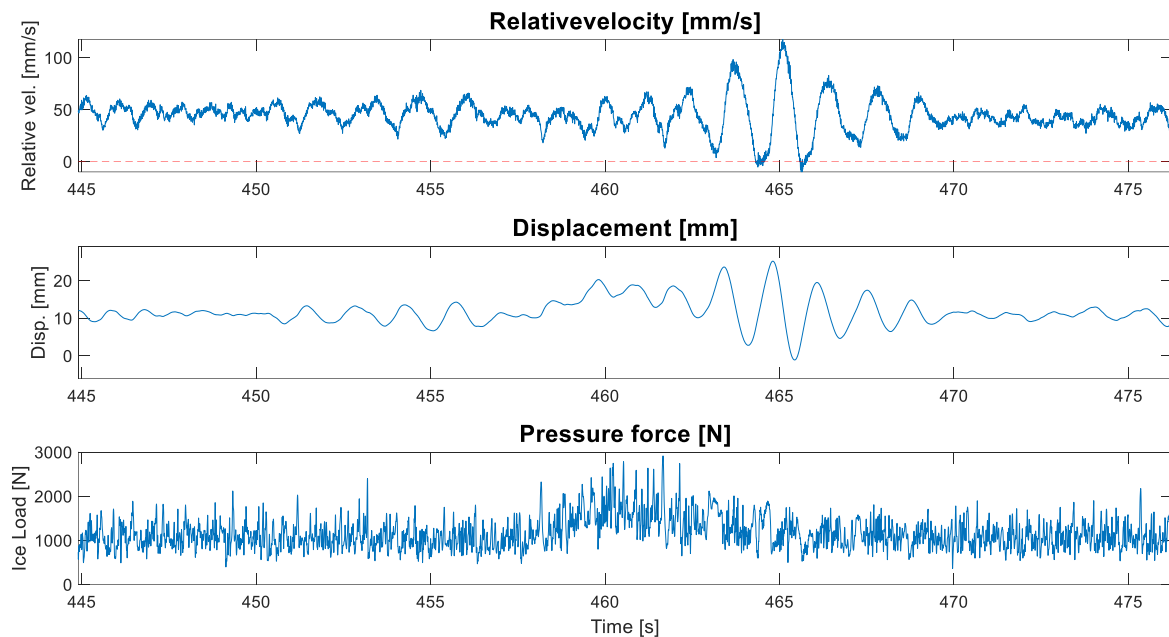


Figure 5-8: Relative velocity, displacement and pressure force signals of test SDOF-21 where the pile went through the anomaly.

## 5-2 Scaling

As explained in more detail in Section 6-1, only one pile has been used during the test campaign and therefore only variation 1 from Section 3-2 could be tested. If ice fails only in a linear elastic manner, the ice velocity should scale with the same ratio as the natural frequency when keeping the stiffness equally. Multiple tests have been performed to check these scaling laws, being 02-04, 07-09, 10-13, 20-22, 24-26 and 35-37. The first three have been performed with a constant velocity profile, while the last three have been tested with a decaying velocity profile. In Table 5-1 the boundary velocity between intermittent crushing and frequency lock-in  $v_I$  and the boundary velocity between frequency lock-in and continuous brittle crushing  $v_{II}$  are given for each test where mass was varied. The two columns on the right show the transition velocities divided by the natural frequency, which should remain equal in between compared tests if only linear elastic dimensionless numbers are needed. In Table 5-1 each box of three or four tests with the same colour has the same damping and stiffness, but they are not equal to other sets of tests.

**Table 5-1:** Results of tests with varying mass and equal stiffness and damping.

Test	Mass [kg]	$F_n$ [Hz]	$v_I$ [mm/s]	$v_{II}$ [mm/s]	$v_I/F_n$	$v_{II}/F_n$
SDOF-02	1000	2.0	40	60	20	30
SDOF-03	4000	1.0	15	30	15	30
SDOF-04	250	4.0	-	-	-	-
SDOF-07	1500	2.0	40	80	20	40
SDOF-08	6000	1.0	20	40	20	40
SDOF-09	2667	1.5	30	60	20	40
SDOF-10	1500	2.0	40	60	20	30
SDOF-11	24000	0.5	25	30	50	60
SDOF-12	94	8.0	-	-	-	-
SDOF-13	167	6.0	-	-	-	-
SDOF-20	15000	0.408	19	26	46.6	63.7
SDOF-21	4444	0.75	27	36	36.0	48.0
SDOF-22	10000	0.5	17	26	34.0	52.0
SDOF-24	5016	0.889	27	44	30.4	49.5
SDOF-25	990	2.0	52	77	26.0	38.5
SDOF-26	20063	0.444	20	23	45.0	51.8
SDOF-35	1100	6.0	16	>50	2.7	>8.3
SDOF-36	200632	0.444	-	7	-	15.8
SDOF-37	9900	2.0	8	28	4	14.0

During the first test day for this topic, the mass was too low in test SDOF-04, so only two tests have been performed. The ratio between boundary velocities and natural frequency seems to remain equal. The same holds for test day 2, with SDOF-07 till SDOF-09. However, it should be noted that the changes in frequency are only small and a constant velocity profile has been used with steps of at least 10 mm/s, so the exact transition velocity has not been found.

In tests SDOF-10 till SDOF-13 the higher natural frequency tests gave following errors on the actuators, so again only two plots could be compared, but from these results it could be derived that for larger changes in mass, the theory of linear elastic failure only is not correct.

This could also be derived from tests 20 until 22 and 24 until 26. The higher the mass and therefore lower the natural frequency, the higher the ratio between transition velocity and

natural frequency becomes. Therefore  $\pi_7$  is not constant, but increases with decreasing natural frequencies.

Tests 35 till 37 were thereafter done with a high stiffness, to verify if this theory still applies for high rigidities, however the maximum velocity at Test 35 with a high natural frequency was chosen at 50 mm/s, but even though there was a lot of alternation between FLI and CBC, at 50 mm/s FLI was still observed and the boundary velocity could not be determined. The test with a low natural frequency (SDOF-36) only showed FLI and CBC and ICR has not been seen. This is probably because the stiffness and especially mass were so high that it almost got a rigid structure, for which CBC is the only failure mode during crushing. For the upper boundary of FLI, the same trend as found before has been found, but the difference is only 10%, so no conclusions for high stiffnesses could be drawn. Altogether, it can be concluded that ice could not be assumed to be linear elastic only for low natural frequencies and more research is needed to ascertain if for example viscoelastic parameters or inertia play a role as well.

### 5-3 Mass

In the scaling tests, the mass has been varied and stiffness and damping has been kept equal, resulting in the fact that the same tests are usable to derive trends in mass changes. Figure 5-9 shows the results of test SDOF-2 and SDOF-3 where the penetration rate is plotted against the maximum structural velocity as discussed in Section 5-3. In this figure beta values of 1.0 and 1.5 are depicted in the dotted red lines, as explained in Section 2-1-2. The differences are small, but the structure with the lower frequency and accordingly higher mass, has slightly lower boundaries between the three crushing regimes. Figure 5-10 depicts the same trend, even though the difference are still small. The high-mass structure is the first to go from ICR to lock-in, while the low-mass structure has the highest boundary velocity to go from FLI into CBC. It should be noted that the white dot on the left bottom was ICR, despite of the low value of beta.

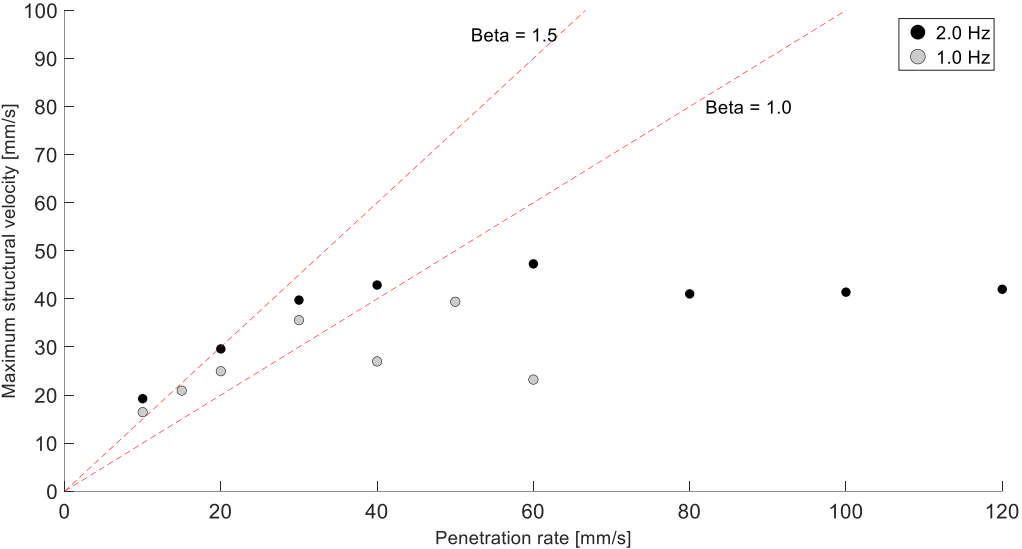


**Figure 5-9:** Maximum structural velocity plotted against penetration rate for tests SDOF-2 (2.0 Hz) and SDOF-3 (1.0 Hz).

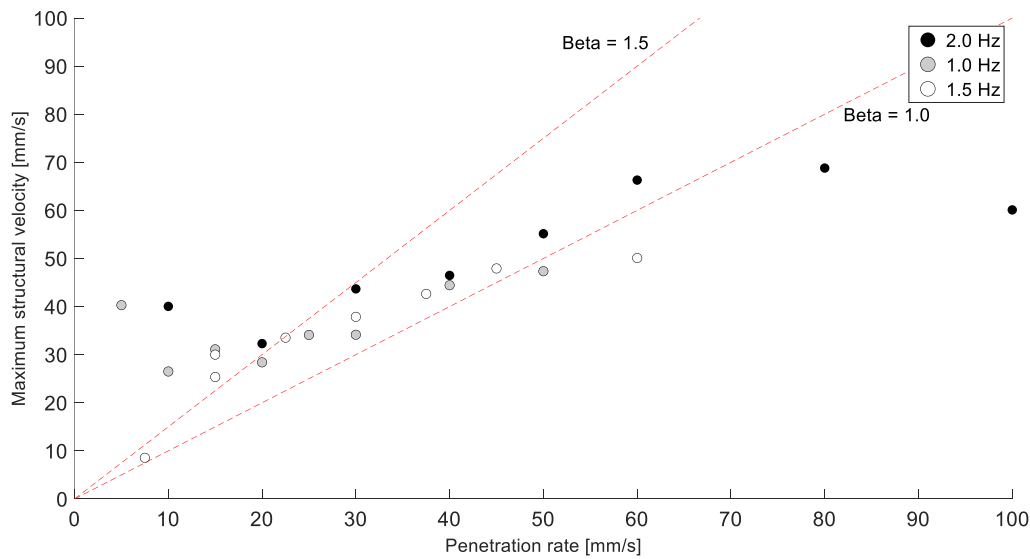


**Figure 5-10:** Maximum structural velocity plotted against penetration rate for tests SDOF-7 (2.0 Hz), SDOF-8 (1.0 Hz) and SDOF-9 (1.5 Hz).

In Figure 5-11 tests SDOF-10 and SDOF-11 are illustrated. In these tests the difference in mass and natural frequency were higher and a trend could be seen. For the high-mass structure with a natural frequency of 0.5 Hz, the transition velocities are lower than for the structure with a lower mass. All other tests from Table 5-1 confirm the findings that a higher mass results in a lower boundary velocity for both ICR to FLI as FLI to CBC. Only SDOF-20 and SDOF-22 contradict with this theory, but the differences in natural frequency and transition velocities are small during those tests.

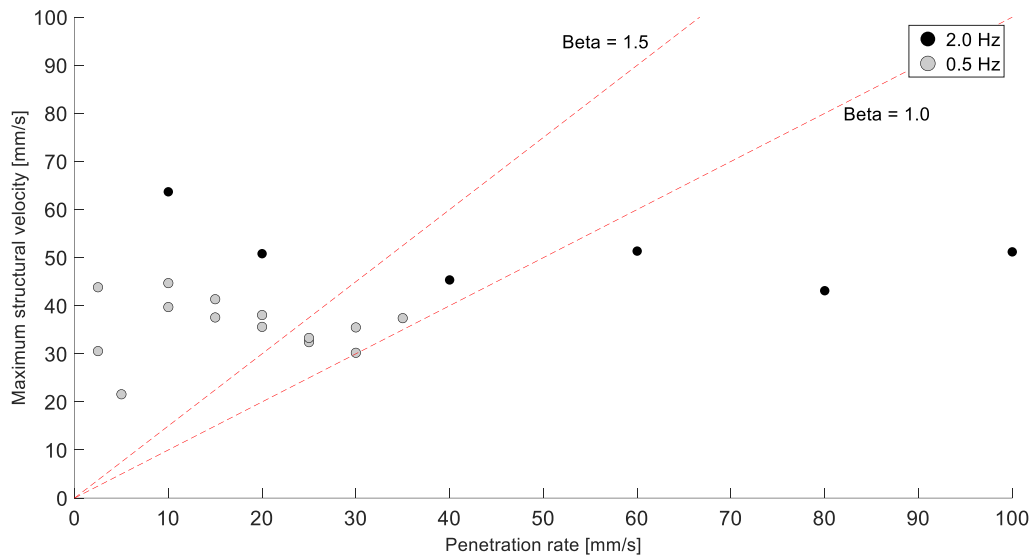


**Figure 5-11:** Maximum structural velocity plotted against penetration rate for tests SDOF-10 (2.0 Hz) and SDOF-11 (0.5 Hz).

# 5-4 Stiffness

Four test runs have been performed in which the mass and damping remained equal, but the stiffness was varied. The results could be found in Table 5-2 and they are visualised in Figure 5-12. The lower boundary velocity between ICR and FLI is negatively correlated with structural stiffness; the higher the stiffness, the lower the boundary velocity. For the upper boundary velocity between FLI and CBC the same trend could be found when comparing test SDOF-32, SDOF-34 and SDOF-38, but SDOF-33 gives a velocity which is not in line. This could be explained by the lowness of the stiffness, which results in transitioning from ICR to CBC and not having any frequency lock-in during the test, as can be seen in Figure 5-13 around 205 seconds. It is assumed that the negative correlation for boundary velocity and stiffness applies for a certain range of stiffnesses, but when the stiffness becomes too small, no lock-in can occur.

In test SDOF-34 no ICR and FLI have been seen, but only CBC, which can be explained by the high stiffness. At low ice velocities, the relative velocity dropped below zero, but the force and displacement signal did not look like ICR nor FLI. In Figure 5-14 it can be seen that the ice and structure do not have an interaction anymore, but the ice force only follows the displacement of the structure. With the high mass and stiffness, the pile became a rigid structure and therefore only CBC could occur.

**Table 5-2:** Results of the tests with a varying stiffness and equal mass and damping.

Test	Stiffness [kN/m]	$v_I$ [mm/s]	$v_{II}$ [mm/s]
SDOF-32	792	14	35
SDOF-33	39	33	33
SDOF-34	7129	-	25
SDOF-38	156	27	41

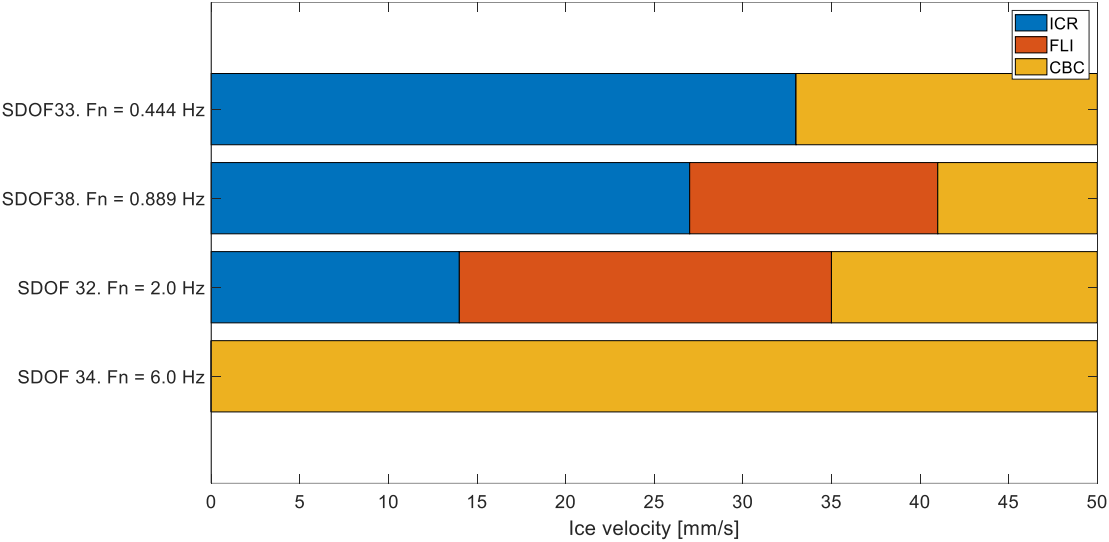


**Figure 5-12:** Velocities at which each crushing regime occurred during test SDOF-32, SDOF-33, SDOF-34 and SDOF-38 with varying stiffness.

Test: SDOF-33. Fn: 0.444 Hz.

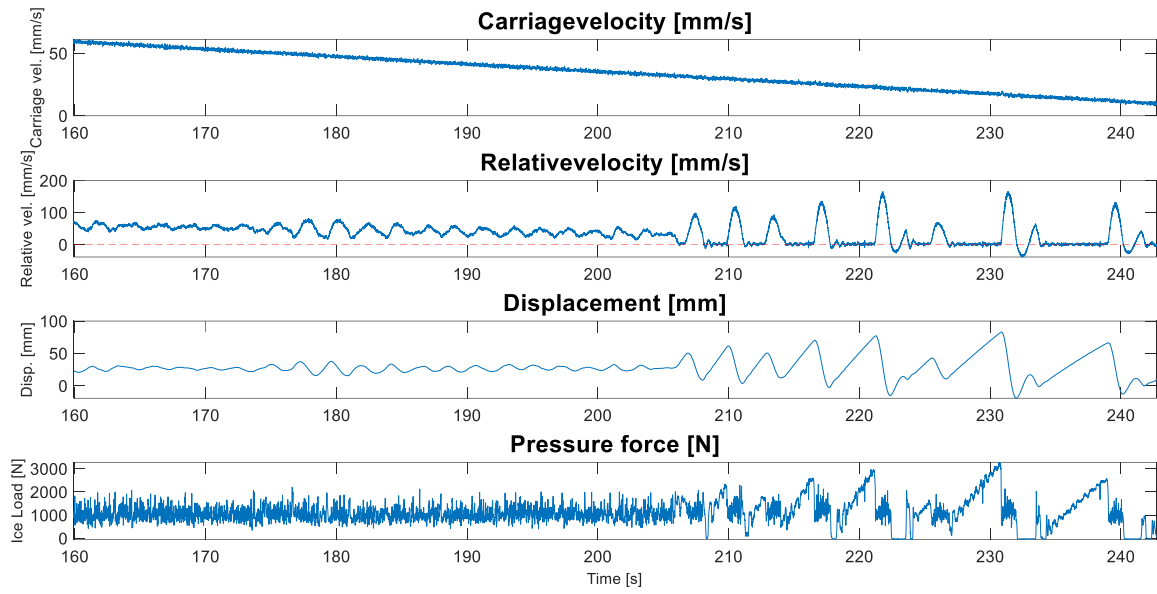


Figure 5-13: Transition from CBC to ICR without going into FLI for test SDOF-33.

Test: SDOF-34. Fn: 6 Hz.

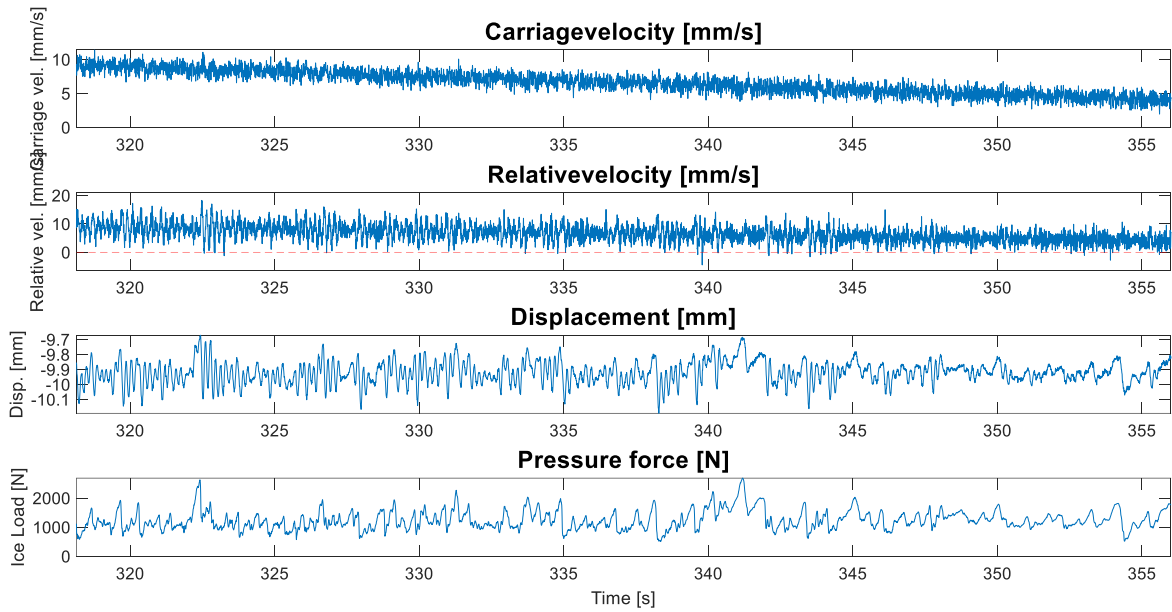


Figure 5-14: Test with a rigid pile where only CBC occurred during test SDOF-34.

# 5-5 Mass & Stiffness

Not only mass and stiffness have been compared independent from each other, also both mass and stiffness have been varied to keep the natural frequency equal. During test SDOF-14 till 16, a constant velocity profile has been used and for tests 24, 27 and 28 a velocity ramp is used. The results are shown in Table 5-3 and visualised in Figure 5-15 and 5-16. Both testing days clearly indicate that a change in both mass and stiffness is negatively correlated with the boundary velocities. Test setup SDOF-14 just gets into FLI from ICR at speeds of 40 mm/s, while setup SDOF-15 is already at CBC at that particular velocity. The same applies for the second test day. When SDOF-24 just goes from ICR to FLI at 27 mm/s, SDOF-28 is almost going in CBC. Furthermore it can be seen that during tests with setup SDOF-27, frequency lock-in almost completely disappears with a low stiffness, as also observed in Section 5-4.

**Table 5-3:** Results of the tests with an equal natural frequency, but changing mass and stiffness.

Test	Natural frequency [Hz]	Stiffness [kN/m]	Mass [kg]	$v_I$ [mm/s]	$v_{II}$ [mm/s]
SDOF-14	2.0	237	1500	40	100
SDOF-15	2.0	947	6000	20	40
SDOF-16	2.0	59	375	-	-
SDOF-24	0.889	156	5016	27	44
SDOF-27	0.889	39	1254	61	67
SDOF-28	0.889	625	20063	11	32

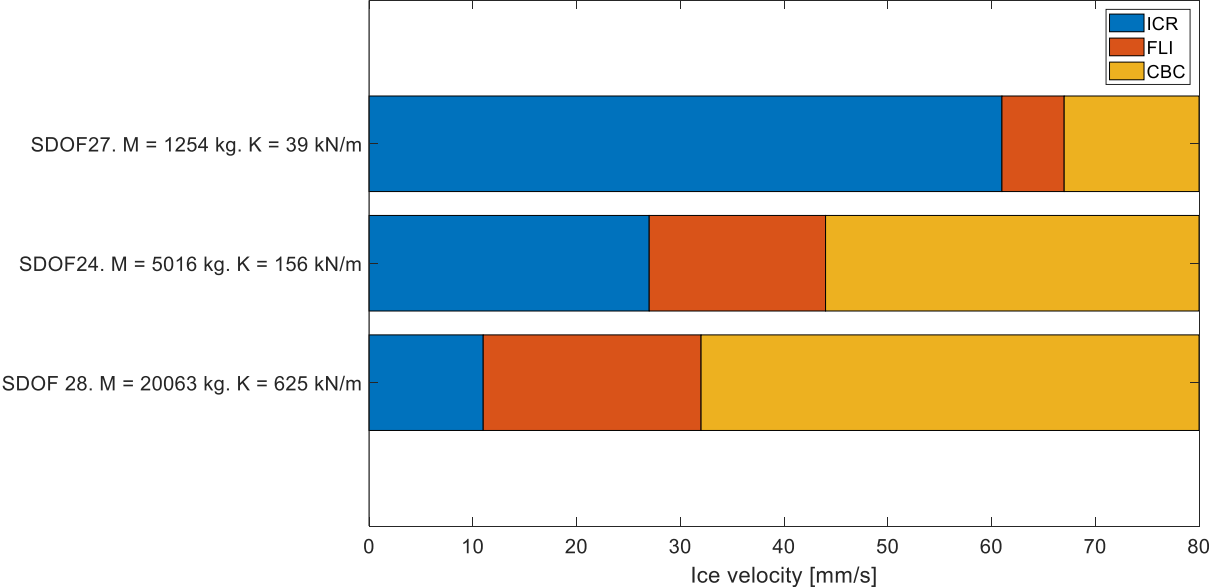


**Figure 5-15:** Velocities at which each crushing regime occurred during test SDOF-24, SDOF-27 and SDOF-28 with varying mass and stiffness.

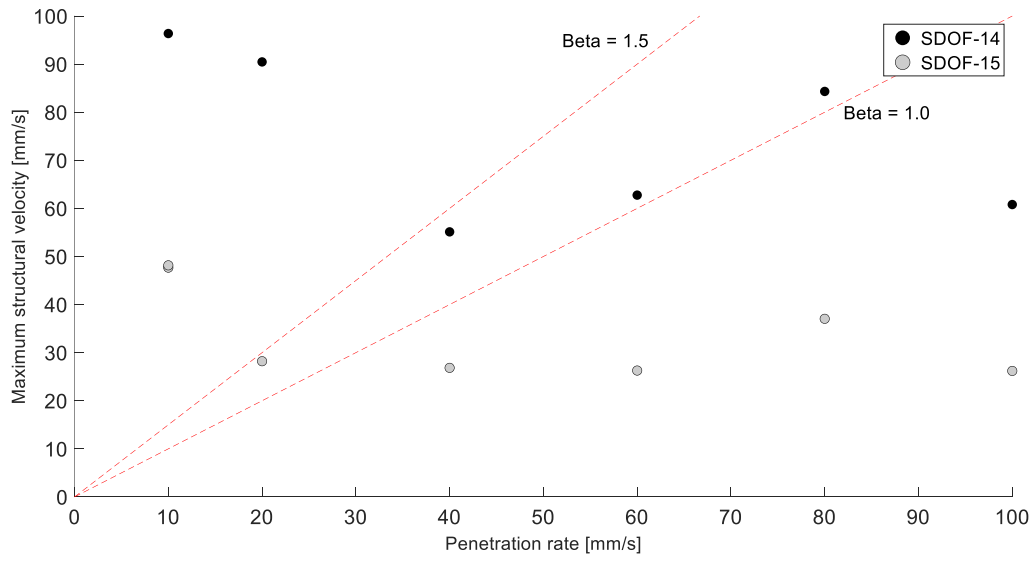


**Figure 5-16:** Maximum structural velocity plotted against penetration rate for tests SDOF-14 (base case) and SDOF-15 (four times higher mass and stiffness).

# 5-6 Damping

During the campaign the damping has been varied two times. First in test SDOF-17, 18 and 19 and later in SDOF-24, 29 and 30. Both test series have been performed with a downward velocity ramp. The lower and upper boundary velocity for frequency lock-in have been given in Table 5-4 and in Figure 5-17 the boundary velocities are visualised.

**Table 5-4:** Results of the first tests with a varying damping.

Test	Damping [%]	$v_I$ [mm/s]	$v_{II}$ [mm/s]
SDOF-17	2	16	47
SDOF-18	1	22	40
SDOF-19	0.5	22	46

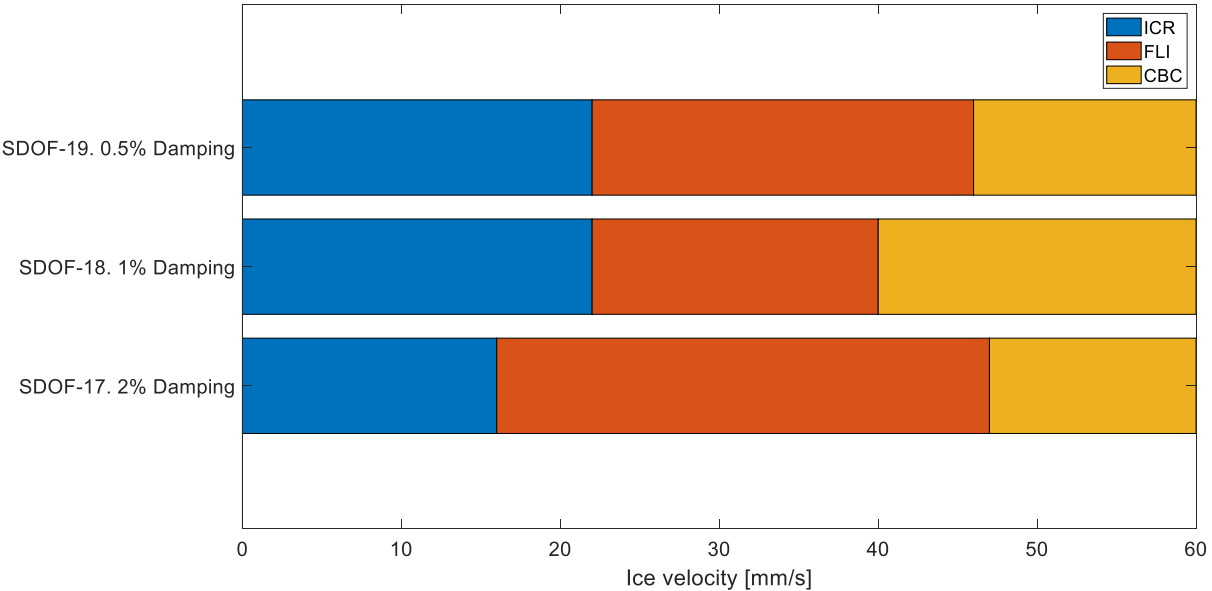


**Figure 5-17:** Velocities at which each crushing regime occurred during test SDOF-17, SDOF-18 and SDOF-19 with varying damping.

No logic conclusions could be drawn from this test series, since the lower boundary velocity goes first up for higher damping, but then down and the upper boundary first down and then up again. Those tests are still performed with the carriage which couldn't keep its velocity as explained in Section 6-4, which could devalue the results. Moreover, it could be that the change in damping is too small to really have an effect on the boundary velocity. Therefore the test is again performed with higher changes in damping. The base case is hereby the second mode of the wind turbine, compared with a damping eight times higher and lower than its damping. The results are shown in Table 5-5 and Figure 5-18.

**Table 5-5:** Results of the second tests with a varying damping.

Test	Damping [%]	$v_I$ [mm/s]	$v_{II}$ [mm/s]
SDOF-24	1.33	27	44
SDOF-29	10.64	29	33
SDOF-30	0.166	29	47

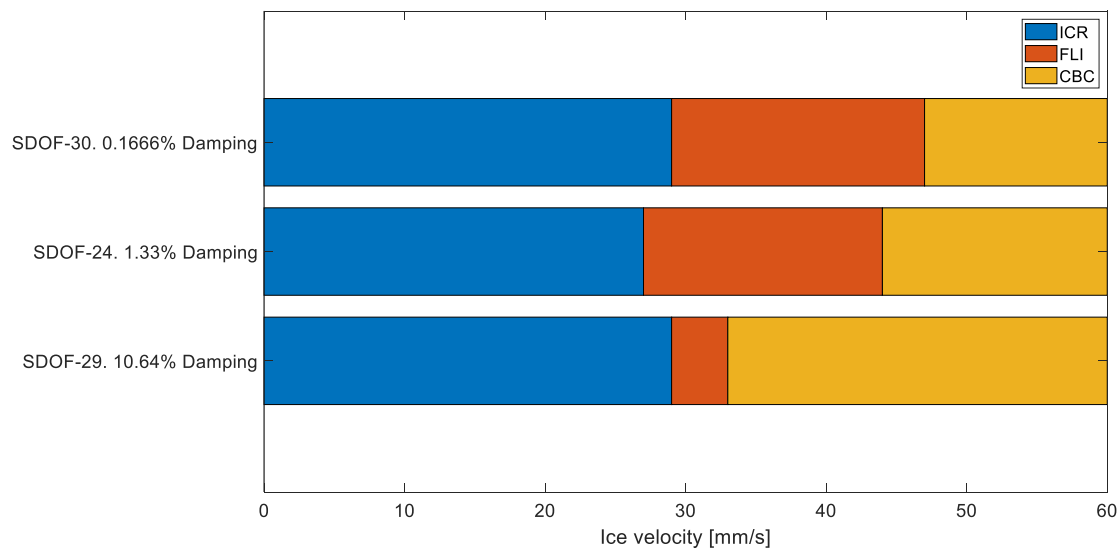


**Figure 5-18:** Velocities at which each crushing regime occurred during test SDOF-24, SDOF-29 and SDOF-30 with varying damping.

It seems like the lower boundary of FLI is not influenced by the damping ratio. For the upper boundary a negative correlation have been found between transition velocity and damping ratio. This can be explained by the fact that a lot of energy is dissipated by the damping and therefore the structure will go quicker to CBC than a structure with a lower damping. Both conclusions about the upper and lower boundary velocity of FLI are in line with the findings in Section 2-3.

## 5-7 Conclusion

A total of 37 unique single degree of freedom test setups have been tested during the SHIVER test campaign, to achieve a better understanding of the influence of dynamic structural properties on boundary velocities of the three crushing regimes. Three sub-questions have been formulated to achieve this understanding.

The first one is: “Does an error in estimation of mass, stiffness and damping have a significant effect on boundary velocities of the crushing regimes?”. During design there is always a possibility of having an error in the estimation of mass, stiffness or damping. After the PID controller of the carriage was fixed, the decision has been made to use the remaining tests to look into trends only and not vary small changes, since it was expected to not find big differences in boundary velocities for small changes in structural properties. Test 20, 21 and 22 have a offset of 50% from each other with respect to mass. From this test it could be concluded that a small error in the estimation does have some effect on the boundary velocities, but this effect is relatively small. Explicit changes do only occur for different structures with completely different structural properties. More research is needed to test small errors of for example 10%.

The second question was: “What are the trends of ice-induced vibrations derived from a parameter study when changing dynamic structural properties?”. In Section 2-3 some assumptions have been made based on the literature study. The first assumption was that mass and boundary velocities were negatively correlated. The findings of this thesis validate this assumption. When structures with equal stiffness and damping and increasing mass were tested, the boundary velocities went down and the other way around as well. It should be taken into account that no low-mass structures with masses below 990 kg could be tested, since the accelerations became too high for the actuators. The second assumption was that stiffness and boundary velocities were negatively correlated too. This assumption is confirmed by the tests as well, with a sidenote that a low stiffness could result in non-existence of the boundaries, because of not having frequency lock-in. This finding was also noticed during simulations with the TU Delft model. In Figure 5-15 and 5-16 a model was simulated with a natural frequency of 0.5 Hz, a stiffness of 39 kN/m, a mass of 5000 kg and a damping ratio of 2% of critical damping. Only at 90 mm/s there is some FLI, but even at this velocity some cycles of ICR occurred and besides that only ICR and CBC. Furthermore the tests showed that the shifts of the regimes because of stiffness, were smaller in relation to shifts because of changing mass.

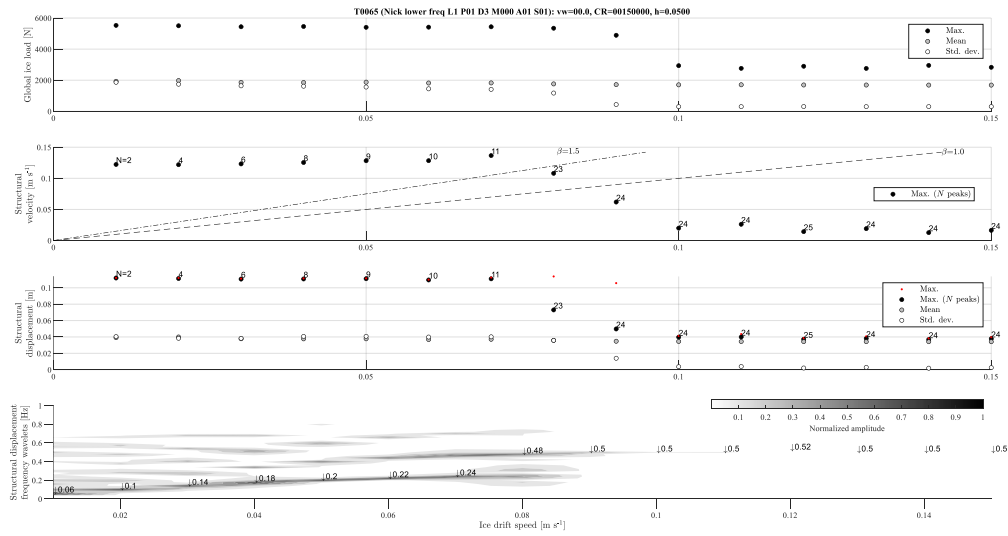


**Figure 5-15:** Simulations in the TU Delft model for a structure with low stiffness. On top a plot of ice drift speed against global ice loads, below ice drift speed against maximum structural velocity, on the third row the drift speed against structural displacement and at bottom the drift speed against structural displacement frequency wavelets.

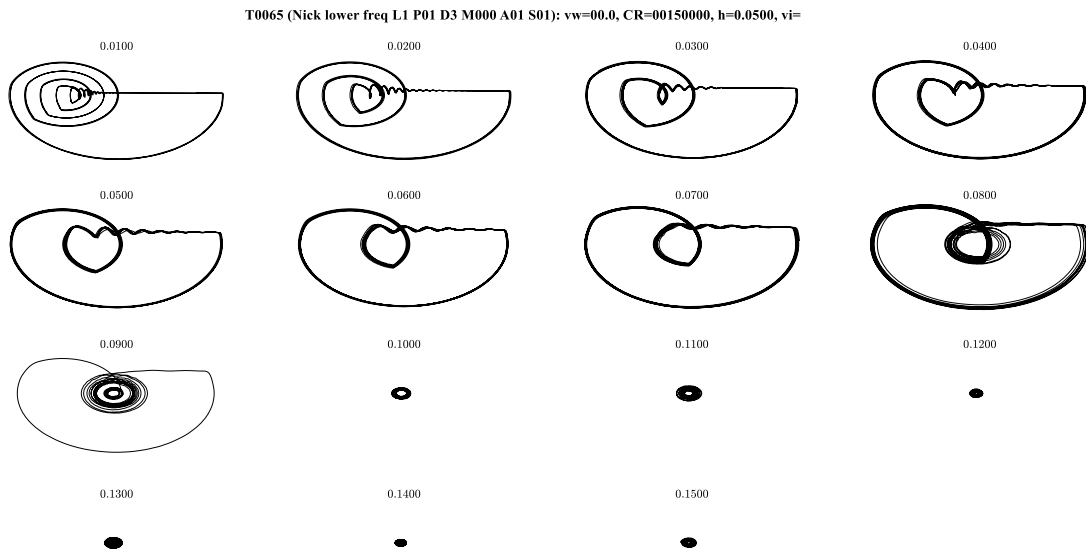


**Figure 5-16:** Phase plane plots (structural displacement against velocity) simulated with the TU Delft model for the structure with a low stiffness.

Research to consistent natural frequencies and changing mass and stiffness has not been performed yet, however from the two assumptions above, where both mass and stiffness were negatively correlated with the boundary velocities, it could be assumed that changing them both simultaneously would result in the same negative correlation. This trend has also been found during the test campaign. Higher masses and stiffnesses resulted in lower transition velocities.

Lastly damping has been studied during this campaign. From Section 2-3 the prediction was that the boundary velocity between intermittent crushing and frequency lock-in would not be influenced by damping, while the upper boundary would have a negative correlation with the damping ratio. This trend has also been seen during the SHIVER test campaign, however, only for large changes in damping ratio. For small changes in damping ratio, the differences were too small to draw conclusions or find a trend.

The last sub-question was: "What is the predictive value of the in literature proposed dimensionless numbers for changes in dynamic properties?". In literature only linear elastic dimensionless numbers have been proposed. Only one of the four variations to keep the linear elastic dimensionless numbers equal could be tested during the SHIVER test campaign, but from this variation (Section 5-2) it is concluded that this approach is not correct and more parameters should be included in the dimensionless numbers. Further research is needed to validate if the proposed viscous dimensionless numbers by Hammer et al. [34] are correct.

---

## Chapter 6

---

# Discussion and recommendations

### 6-1 Bigger pile

During the SHIVER test campaign, only one pile has been used with a fixed diameter of 200 mm. A second pile with a diameter of 300 mm has been brought, but the strain gauges did not give accurate results. Because the rigidness of the thicker pile was higher, the deformations were smaller and the calibration factor of the strain gauges was extremely high. This caused large errors in the force measurement, which was the input for the analytical model and therefore it has been decided not to use this extra pile. In case of a following test campaign in which the assumption of only having to use linear elastic dimensionless parameters is tried to be rejected, piles with multiple diameters should be used. A new force measurement method could be used which is not effected by the rigidness of the pile, but together with that does not measure the inertial forces of the moving tables either. On the occasion that the inertial forces could be calculated real-time, for example a load cell could be used which is connected to the actuators.

## 6-2 Boundary identification

The identification of the boundaries is a manual process, which makes it difficult to exactly choose the velocity. Multiple techniques to identify the boundary velocities are used, as explained in Section 5-1, but not always all different techniques gave the same crushing regime for certain velocities. It sometimes occurred that for example the beta-value indicated frequency lock-in, while the frequency spectrum clearly showed intermittent crushing. Since there is no absolutely clear definition of intermittent crushing, frequency lock-in and continuous brittle crushing, someone else could interpret the data differently. Boundary velocities could thus be different when someone else has a look at the data. However, since the same approach is used for every data set, trends obtained from these datasets are still valuable.

Moreover, the signal of the carriage velocity was not a completely straight line. Especially with the first PID settings (see Section 6-4), there were drops in the velocity profile. A straight line has been drawn through the velocity profile to determine the transition velocity, but the real velocity at that moment could be different. Even after the PID settings were changed, there were still fluctuations in the signal, which could result in an offset of maximum 1 mm/s. Therefore velocities are round up to an integer, because at one decimal would be more accurate than the actual measurement was.

## 6-3 Ice properties

A typical test day lasted from nine o'clock in the morning till five in the afternoon. Keeping the ice properties constant for more than eight hours turned out to be challenging. First of all the perfect air temperature had to be found, to make sure the ice didn't melt, but didn't grow either. As can be concluded from Appendix D, keeping the ice thickness constant failed at those tests dates. The ice thickness was measured at four equally spaced locations in the channels. Figure D-2 and D-4 show that the average ice thickness over those four locations decreased over time, at the former, the ice thickness dropped over 60 mm in the first three hours and therefore it was decided to decrease the temperature and take a break to let the ice grow before continuing with testing. This explains the increase in average ice thickness after 13:00 in Figure D-2. In Figure D-1 it is clearly visible that the ice thickness during run four, five and six, just before the break, had a much lower ice thickness than the tests after the break. Tests that were compared with each other have been conducted as close as possible to each other with regards to time, but it can be concluded that the ice thickness is not equal for all tests.

Furthermore, the measurement of the ice thicknesses itself had some difficulties. On the left of Figure 6-1 the remaining rubble from the tests is frozen to the ice layer, which increases the ice thickness. On the right the bottom of the ice layer is presented, but it is no longer a uniform thickness, but a lot of water froze to the bottom. During the measurements of the ice thickness, both the upper and lower layer of extra added ice are being scraped off, but this probably still influenced some measurements.



**Figure 6-1:** At the left the measurement method of the ice thickness and on the right a piece from the ice where the variety in ice thickness is clearly visible.

The other ice properties, flexural and compressive strength have only been measured once a day, after the last test was conducted. Only on the 8<sup>th</sup> of June those strengths have been measured twice, once in the morning and once in the afternoon. The compressive strength increase from 426 kPa to 487 kPa, the bending strength from 311 to 445 kPa and the submerged bending strength from 300 to 435 kPa. It can be concluded that this strength was not uniform over the day as well, but effects on other days are not known.

## 6-4 Carriage velocity

For the tests until the 15<sup>th</sup> of June, until test SDOF-23, the carriage had trouble keeping its velocity for low carriage velocities and higher forces. During the load build-ups the velocity dropped and during a failure event of the ice, a velocity peak could be seen in Figure 6-2. At the 15<sup>th</sup> of June the settings of the PID controller were adapted to make its movement to the desired position more instantaneous by increasing the frequency at which the position is checked and therefore the velocity profile becomes more linear, which could be seen at Figure 6-3. Still the velocity fluctuates around the desired velocity, but with an amplitude of 1 mm/s, while before sometimes velocity peaks of 20 mm/s above desired velocity were measured.

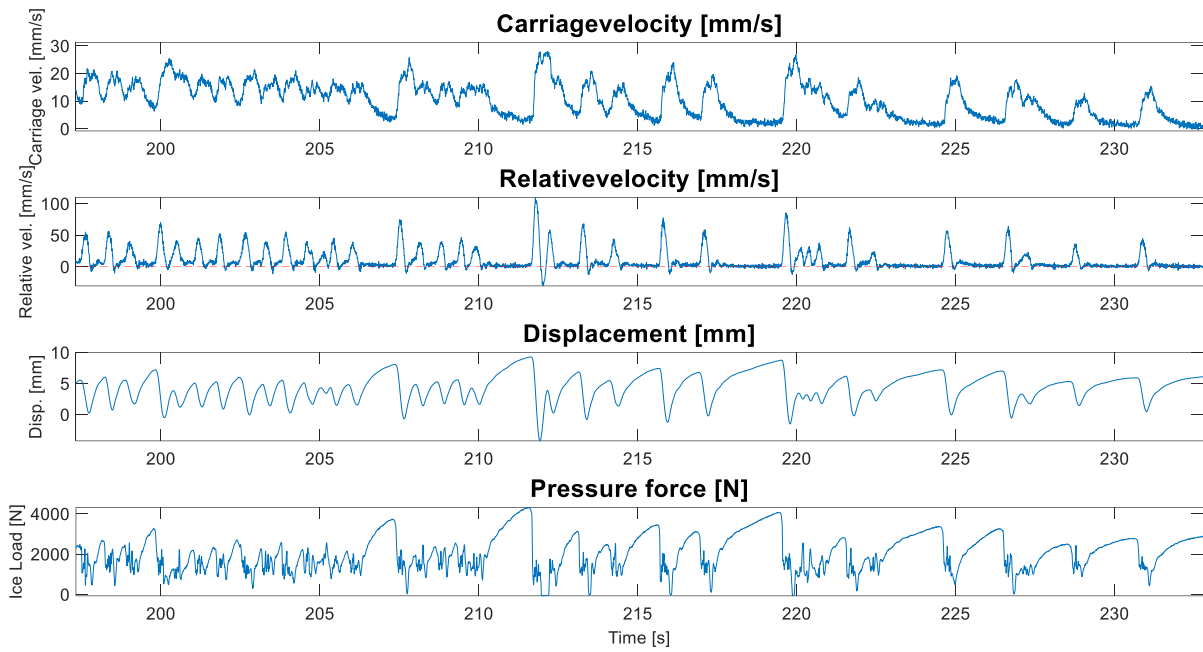


**Figure 6-2:** A carriage velocity signal before changing PID settings for low velocities with velocity peak during ice failures. The signal is from test SDOF-17.

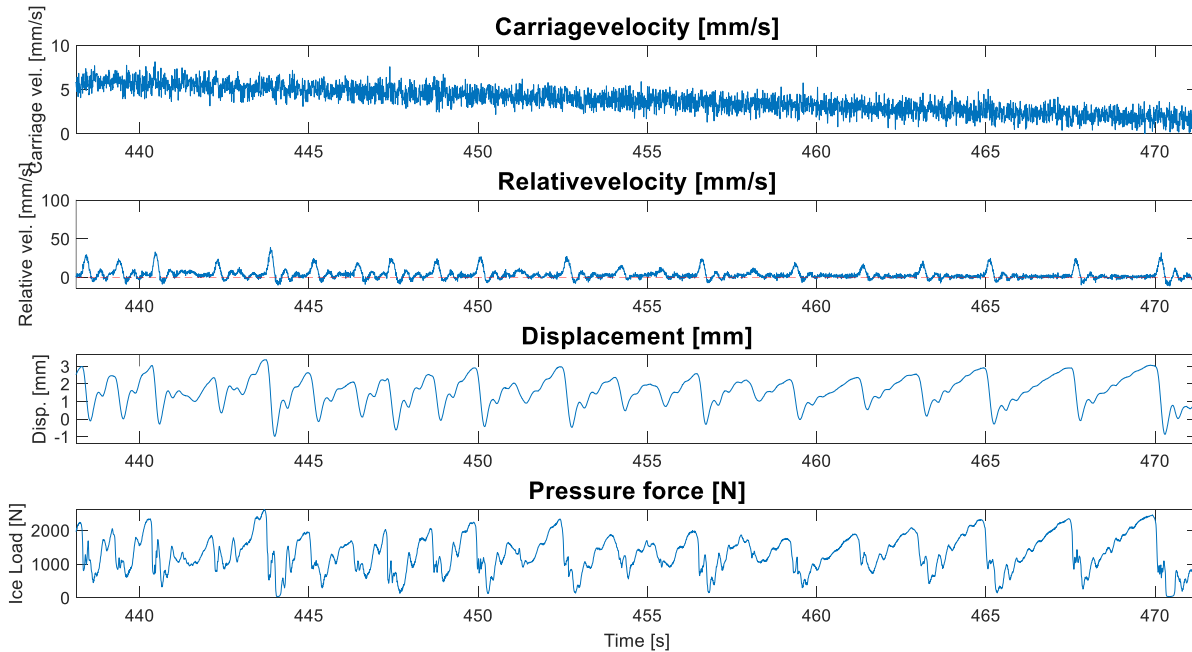


**Figure 6-3:** A carriage velocity signal after changing PID settings for low velocities with a smoother almost linear velocity signal. The signal is from test SDOF-32.

## 6-5 Carriage vibrations

The carriage is assumed to be completely stiff compared to the rails where it is hanging onto, but in reality this is not true. Two accelerometers have been placed on the plates above the pile and one accelerometer to the body which is not moving and fixed directly to the carriage. The accelerations which occur at this location of up to  $0.5 \text{ mm/s}^2$ , as can be seen in Figure 6-4, are relatively small compared to the accelerations of the pile, which are in the range up to  $5 \text{ mm/s}^2$ , but the displacements induced by carriage vibrations would still influence the test results. For following test campaigns it is recommended to stiffen the connection between carriage and rails, to prevent carriage vibrations to occur.

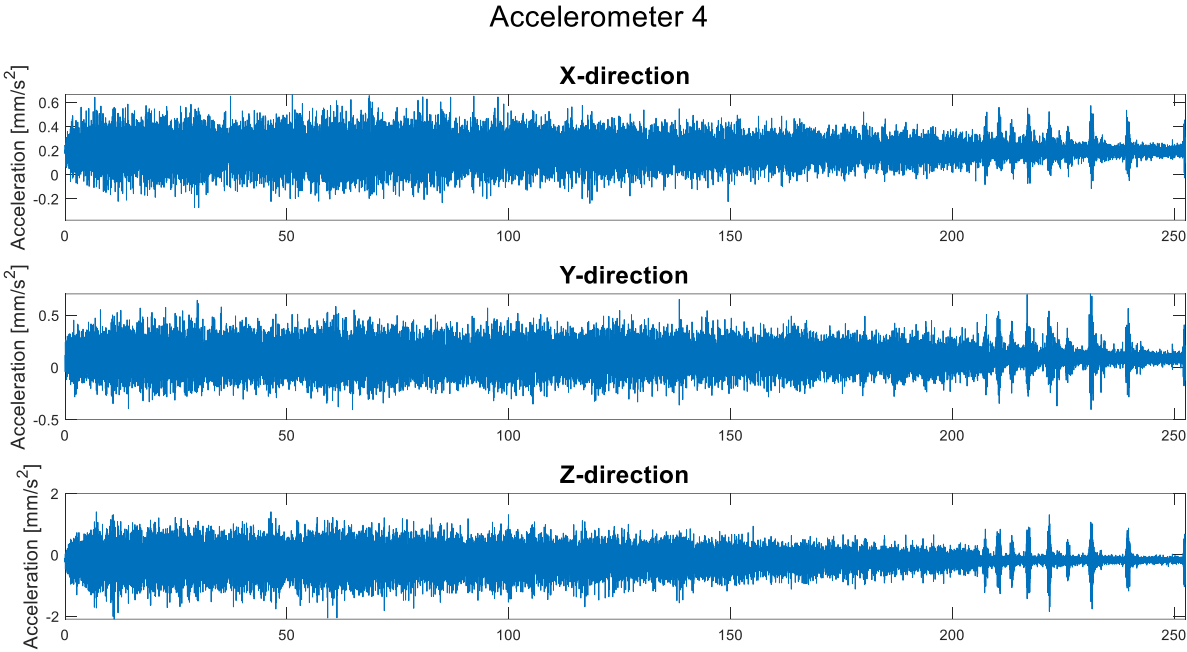


**Figure 6-4:** Accelerations in X, Y and Z direction for the accelerometer that is fixed to the non-moving plate during test SDOF-38.

## 6-6 Velocity profiles

An nonlinear dynamic problem is always dependent on the initial conditions. There are multiple velocity profiles which are used during this test campaign, being a constant indentation speed, an upward velocity ramp and a downward velocity ramp. A peak force could be seen during at initial contact between structure and ice which resulted in different regimes at the start of the measurement than at the end of the measurement. Therefore some tests have been done with a high initial damping to temper the effect of the initial impact.

Tests SDOF-20, SDOF-21 and SDOF-22 have been done with a linear upward velocity ramp to  $80 \text{ mm/s}$  of 325 seconds and afterwards a linear velocity ramp downwards with an equal duration. The results of the boundaries are given in Table 6-1. It can be concluded that for all tests, the boundary velocities were between  $2$  and  $10 \text{ mm/s}$  higher for the upward velocity profile. This can be explained, because the initial conditions are different and there is less energy in the system when coming from continuous brittle crushing at higher velocities then when staying in frequency lock-in at the upper boundary. At the lower boundary, there is also

less energy in the system when coming from intermittent crushing, so a higher velocity is needed with an upward ramp to get into frequency lock-in.

**Table 6-1:** The boundary velocities from intermittent crushing to frequency lock-in and from frequency lock-in to continuous brittle crushing for test SDOF-20, SDOF-21 and SDOF-22 with a upward and downward velocity ramp.

Test	Ramp direction	$v_I$ [mm/s]	$v_{II}$ [mm/s]
SDOF-20	Upward	23	35
	Downward	19	26
SDOF-21	Upward	29	38
	Downward	27	36
SDOF-22	Upward	23	36
	Downward	17	26

### 6-7 Further research

All conclusions drawn in Chapter 5 have been done by comparing several model-scale tests from this test campaign. Tests conducted with different initial conditions could result in different trends and therefore further research is needed to verify those results. The further research should not only be done with dynamic parameters in the range of this thesis, but also with for example high frequencies and low masses, to check if the same trends apply for those parameters.

## Appendix A

# Summary of previous experiments

**Table A-1:** Overview of dynamic structural parameters and ice thicknesses derived from 21 reports about model-scale experiments.

#	Year	Authors	Article	Fn [Hz]	M [kg]	K [kN/m]	$\zeta$ [-]	d [mm]	h [mm]
1	1983	Y. Toyama T. Sensu M. Minami Et al.	Model tests on ice-induced self-excited vibration of cylindrical structures [19]	1.27	3769	240	0.0023	76	39
2	1984	D. Sodhi C. Morris	Ice Forces on Rigid, Vertical, Cylindrical Structures [37]	60	-	5700	-	500	50 - 55
				81	-	5700	-	50	54 - 80
3	1985	M. Tsuchiya S. Kanie K. Ikejiri	An Experimental Study on Ice-Structure Interaction [23]	2.90	1060	3200	0.001	76	50
				4.66	1060	1235	0.0012		
4	1990	S. Singh G. Timco R. Frederking Et al.	Tests of ice crushing on a flexible structure [9]	17.6	20.5	250	0.045	60	34 - 41
							0.038		
				55.7	-	-	0.08		
				10.7	-	-	0.045		
						0.057			
5	1991	D. Sodhi	Ice - Structure Interaction During Indentation Tests [24]	8.50	600	1710	-	50	24 - 28
				6.91	600	1130	-		
				11.68	600	3230	-		
				6.13	600	890	-		

#	Year	Authors	Article	Fn [Hz]	M [kg]	K [kN/m]	$\zeta$ [-]	d [mm]	h [mm]
6	1992	A. Muhonen T. Kärnä E. Erantie Et al.	Laboratory indentation tests with thick freshwater ice [38]	2	15000	2400	0.1	100	100
				4.1	15000	10000	0.1	100	95 – 112
								300	105 - 110
								900	51 - 70
				26.4	2000	55000	0.05	100	110
								200	55
								300	108 - 115
								400	55
				27.6	2000	60000	0.05	100	110
								200	55 - 100
								300	108 – 125
								400	54
								900	80
				28.7	2000	65000	0.05	200	55 - 100
300	110 - 125								
400	54								
900	80								
29.8	2000	70000	0.05	300	125				
				900	80				
7	1993	D. Finn S. Jones I. Jordaan	Vertical and inclined edge-indentation of freshwater ice sheets [39]	63	60	9400	0.046	80 100 120	26 - 46
8	1994	K. Izumiyama M. Irani G. Timco	Influence of compliance of structure on ice load [18]	5.86	222	301	-	167	20 - 39
9	1996	K. Kamesaki Y. Yamauchi T. Kärnä	Ice force as a function of structural compliance [40]	3.91	421	254	-	-	90
				6.87	660	1230			-
				10.9	524	2460			-
10	1997	K. Izumiyama S. Uto	Ice loading on a compliant indenter [10]	5.73	117	151	-	-	30
				3.88	255	151			18 – 45
11	2003	T. Kärnä K. Kolari P. Jochmann	Ice action on compliant structures: Laboratory indentation tests [25]	6.0	-	-	-	114	77 - 96
				5.3			0.12		95 – 98
				6.7			0.007		73 – 81
				6.6			0.05		-
12	2005	A. Barker G. Timco H. Gravesen	Ice loading on Danish wind turbines. Part 1: Dynamic model tests [41]	1.9	14	74	0.059	192	22 – 25
				9.2	5	172	0.08		15 - 25

#	Year	Authors	Article	Fn [Hz]	M [kg]	K [kN/m]	$\zeta$ [-]	d [mm]	h [mm]
13	2006	Y. Qianjin G. Fengwei S. Chu	Laboratory tests of ice induced structure vibrations [42]	3.9	3000	1000	-	120	40
14	2007	Y. Huang Q. Shi A. Song	Model test study of the interaction between ice and a compliant vertical narrow structure [17]	4.29	33	24	-	76	35 - 41
				6.25	18	27			
				6.64	21	36			
				12.5	41	255			
15	2009	F. Guo Q. Yue X. Bi Y. Liu	Model test of ice-structure interaction [13]	4.12	1000	670	-	120	40
				2.91	2000				
				2.38	3000				
16	2012	T. Nord	Deciphering of Ice Induced Vibration (DIIV); Data storage report* [43]	10.4	480	-	-	220	72
				10.3	480			220	91
				10.7	480			100	46.6
				10.5	480			100	46.6
				9.2	480			220	46.6
				9.1	480			220	46.6
				9.5	360			220	57.5
				9.4	360			220	57.5
				7.8	360			220	57.5
				10.2	240			220	57.5
				10.1	240			400	57.5
				10.4	240			220	60.4
				12.2	240			220	60.4
28	-	220	60.5						
17	2013	K. Yap A. Palmer	A model test on ice-induced vibrations: structure response characteristics and scaling of the lock-in phenomenon [27]	2.3	2319	690	0.01	80	25
									50
								120	25
									50
18	2015	T. Nord E. Lourens M. Määttänen Et al.	Laboratory experiments to study ice-induced vibrations of scaled model structures during their interaction with level ice at different ice velocities [44]	7.8	360	-	-	220	58
				9.4	360				58
				10.2	240				58
				10.4	240				60
				12.2	240				60

\* Data storage report from "Novel ice induced vibration testing in a large-scale facility: Deciphering ice induced vibrations, part 1" [45].

#	Year	Authors	Article	$F_n$ [Hz]	$M$ [kg]	$K$ [kN/m]	$\zeta$ [-]	$d$ [mm]	$h$ [mm]
19	2016	B. O' Rourke I. Jordaan R. Taylor A. Gürtner	Experimental investigation of oscillation of loads in ice high-pressure zones, part 1: single indenter system [46]	205	-	53100	-	20	-
				209		16600			
20	2016	B. O' Rourke I. Jordaan R. Taylor A. Gürtner	Experimental investigation of oscillation of loads in ice high-pressure zones, part 2: double indenter system - coupling and synchronization of high-pressure zones [47]	183	-	61900	-	305	-
						17800			
21	2017	G. Ziemer P. Hinse	Relation of maximum structural velocity and ice drift speed during frequency lock-in [16]	2.65	1591	490	0.030	830	46
				5.40	1513	1935	0.023	120	41
				5.45	1712	2230	0.015	830	48
				5.47	1547	2030	0.031	500	43
				5.80	1308	1930	0.023	200	42
				7.60	1192	3020	0.027	500	31

---

# Appendix B

---

## Graphs of parameters from previous experiments

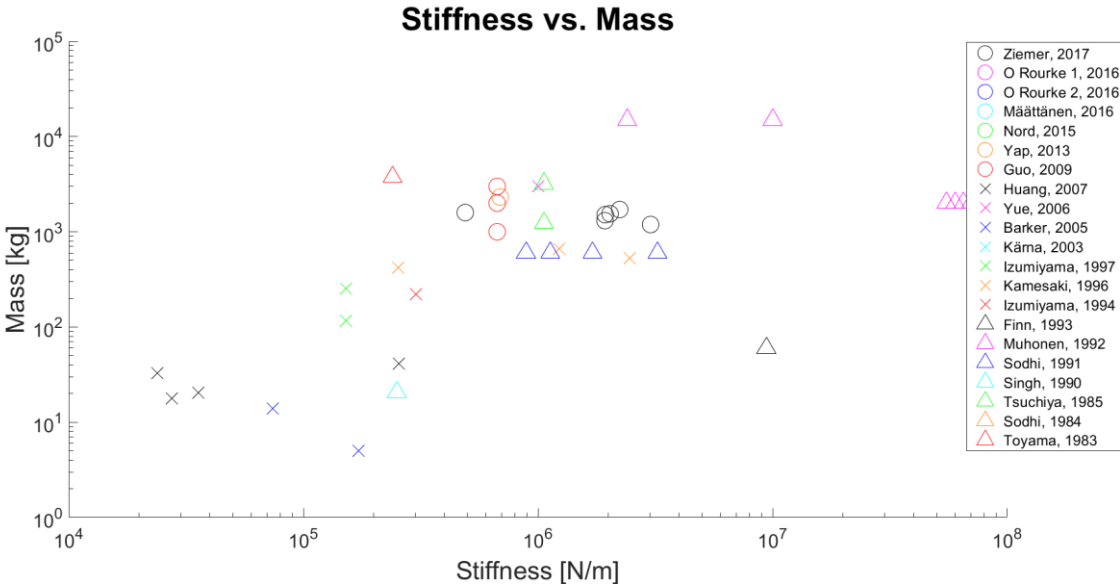
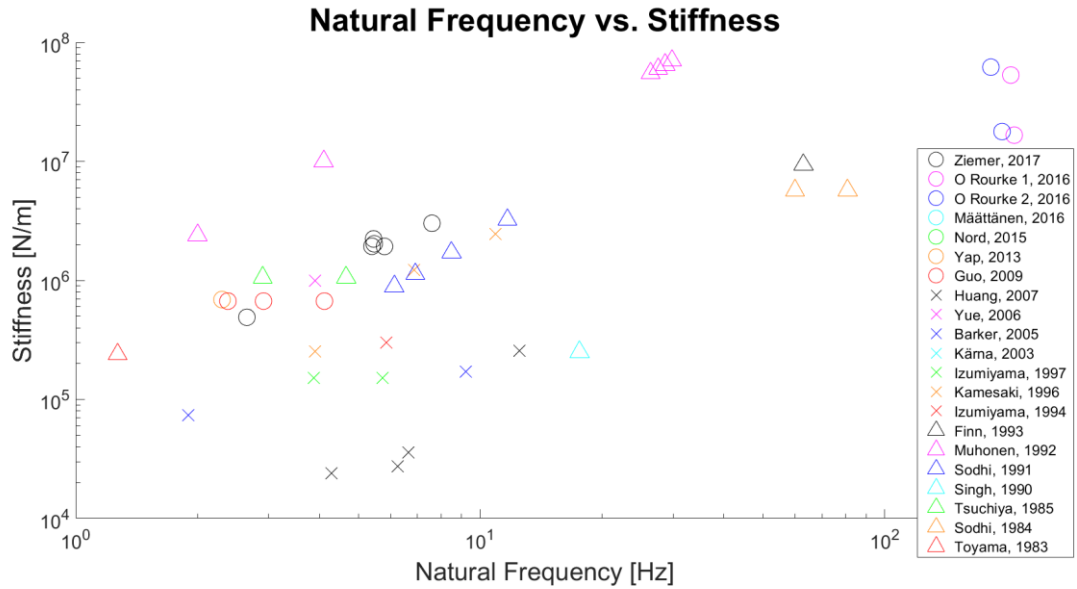
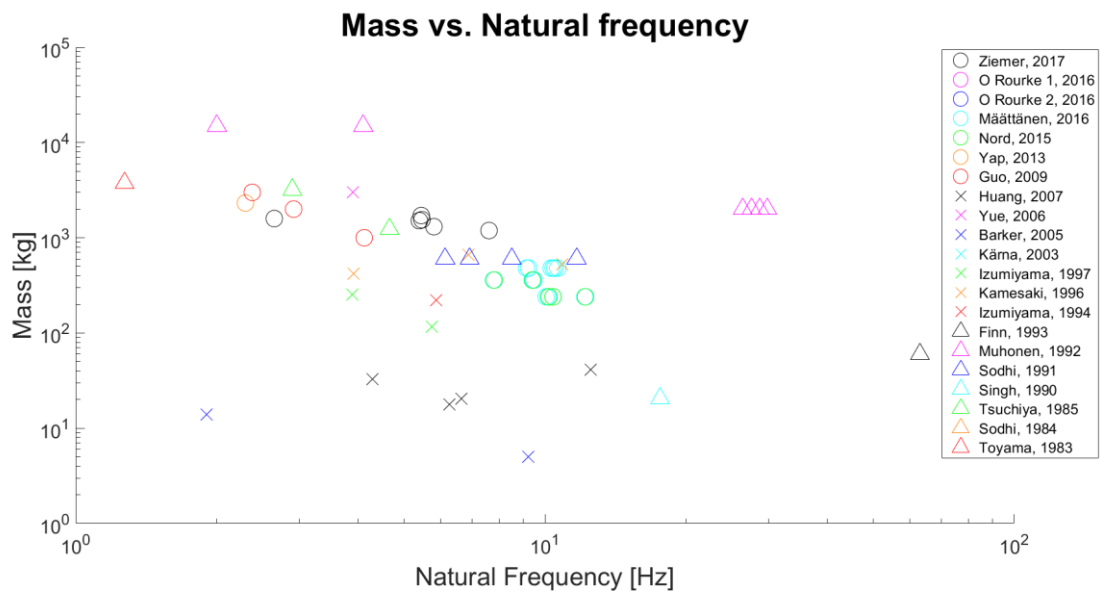


Figure B-1: Scatterplot of the stiffness against mass used during 21 model-test campaigns.



**Figure B-2:** Scatterplot of the natural frequency against stiffness used during 21 model-test campaigns.



**Figure B-3:** Scatterplot of the natural frequency against mass used during 21 model-test campaigns.

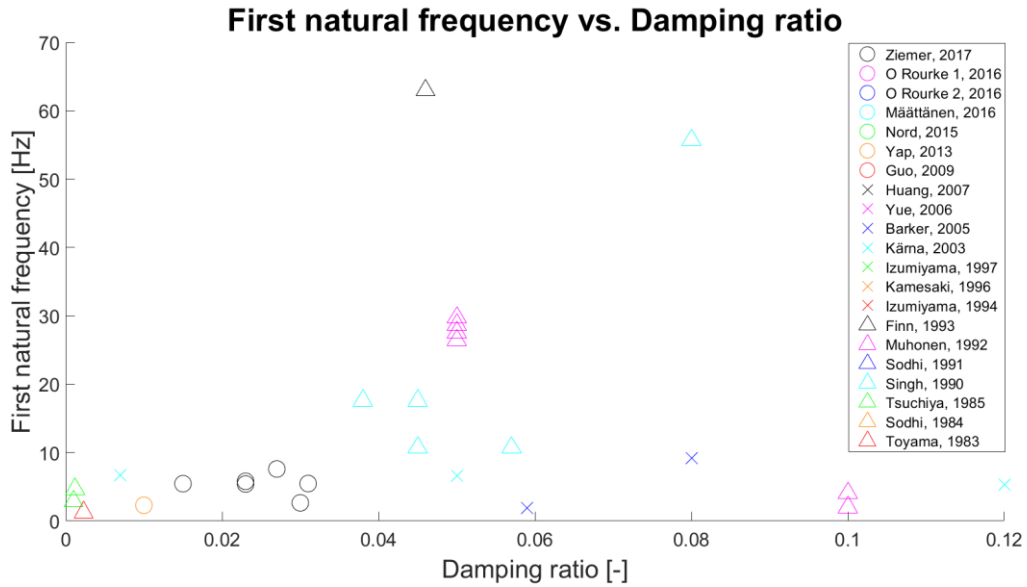


**Figure B-4:** Scatterplot of the damping ratio against natural frequency used during 21 model-test campaigns.

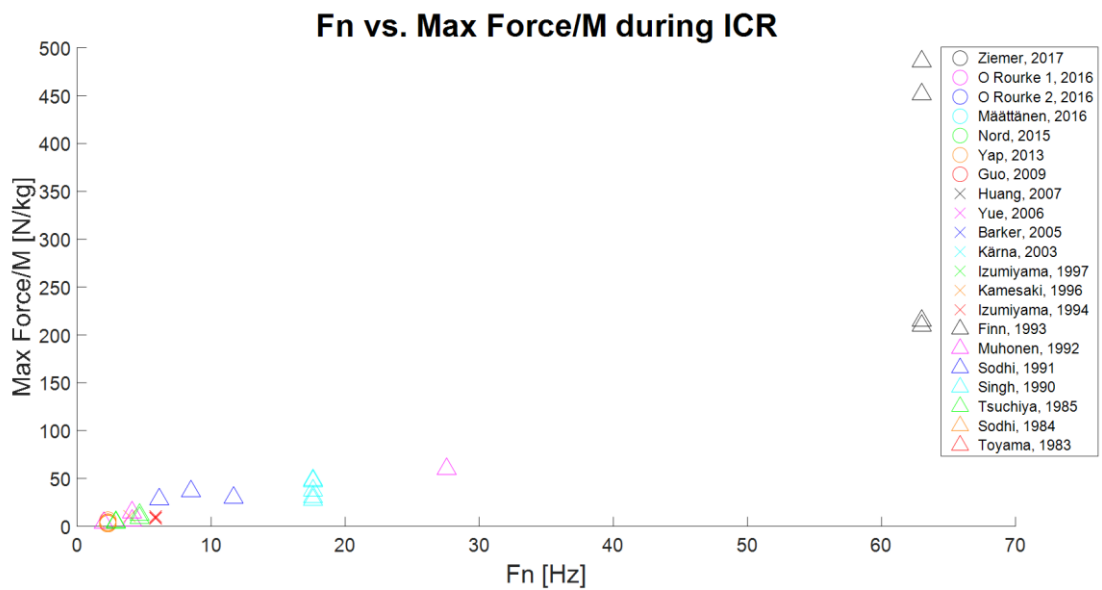


**Figure B-5:** Scatterplot of the natural frequency against the maximum ice load divided by mass during intermittent crushing retrieved during 21 model-test campaigns.

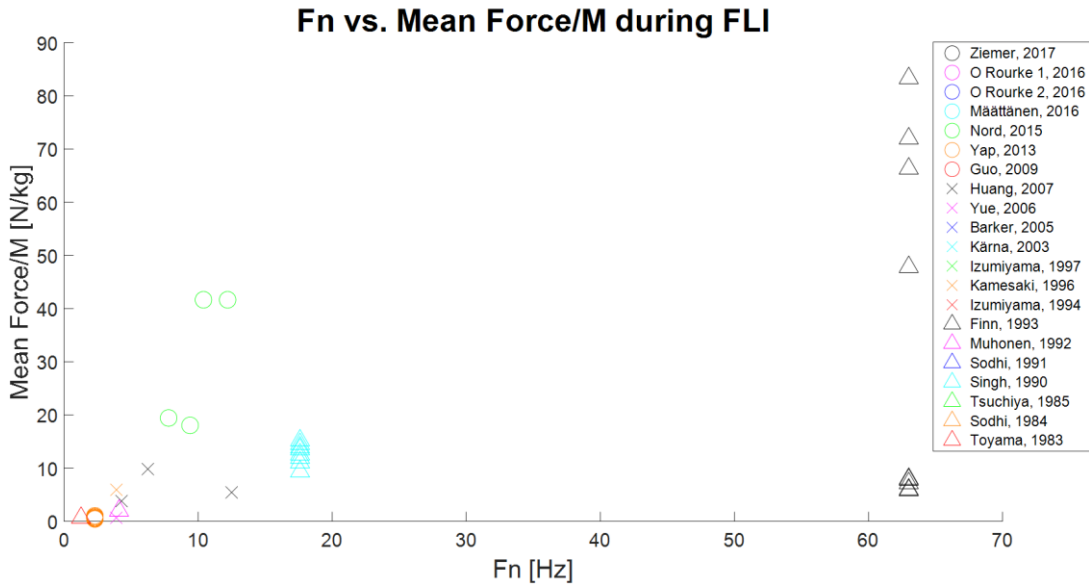


**Figure B-6:** Scatterplot of the natural frequency against the mean ice load divided by mass during frequency lock-in retrieved during 21 model-test campaigns.

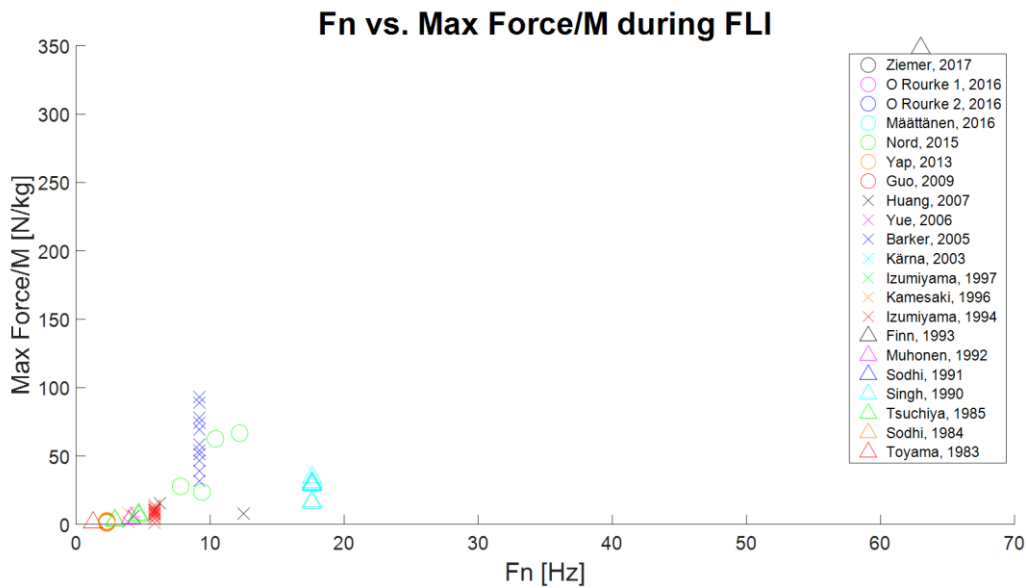


**Figure B-7:** Scatterplot of the natural frequency against the maximum ice load divided by mass during frequency lock-in retrieved during 21 model-test campaigns.

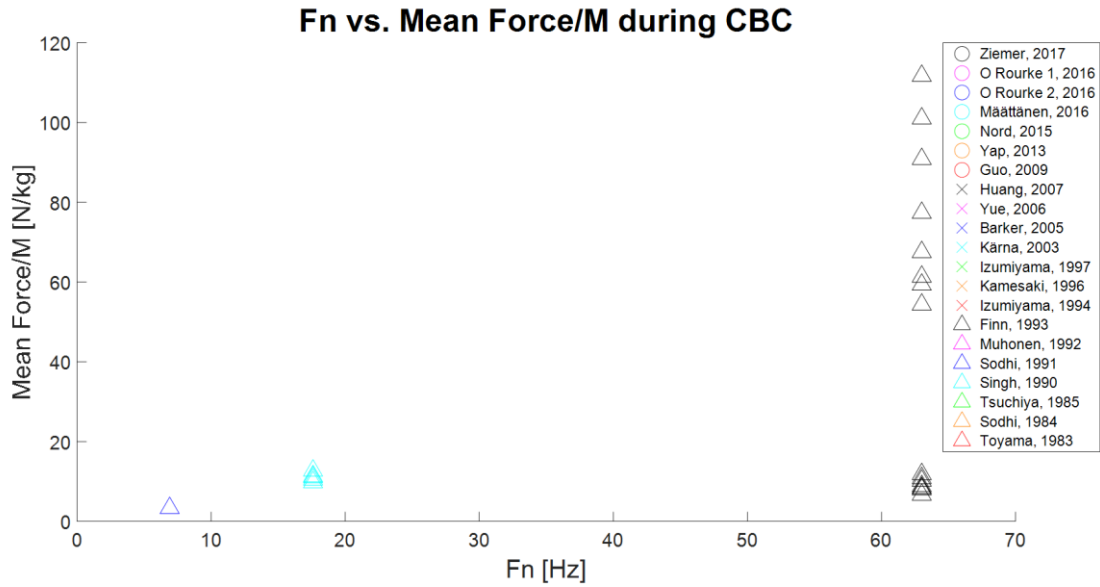


**Figure B-8:** Scatterplot of the natural frequency against the mean ice load divided by mass during continuous brittle crushing retrieved during 21 model-test campaigns.

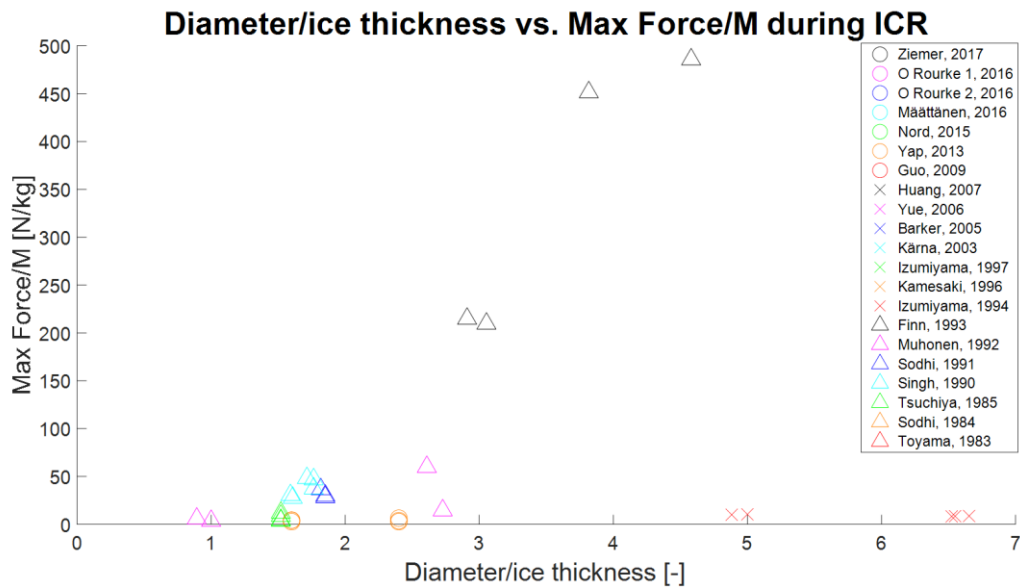


**Figure B-9:** Scatterplot of the aspect ratio against the maximum ice load divided by mass during intermittent crushing retrieved during 21 model-test campaigns.

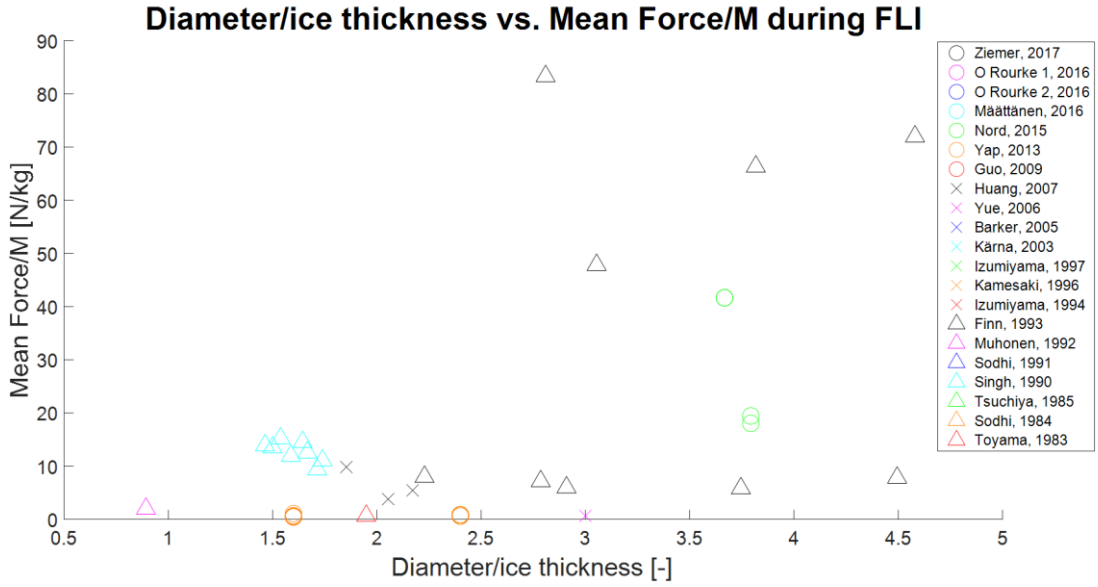


**Figure B-10:** Scatterplot of the aspect ratio against the mean ice load divided by mass during frequency lock-in retrieved during 21 model-test campaigns.

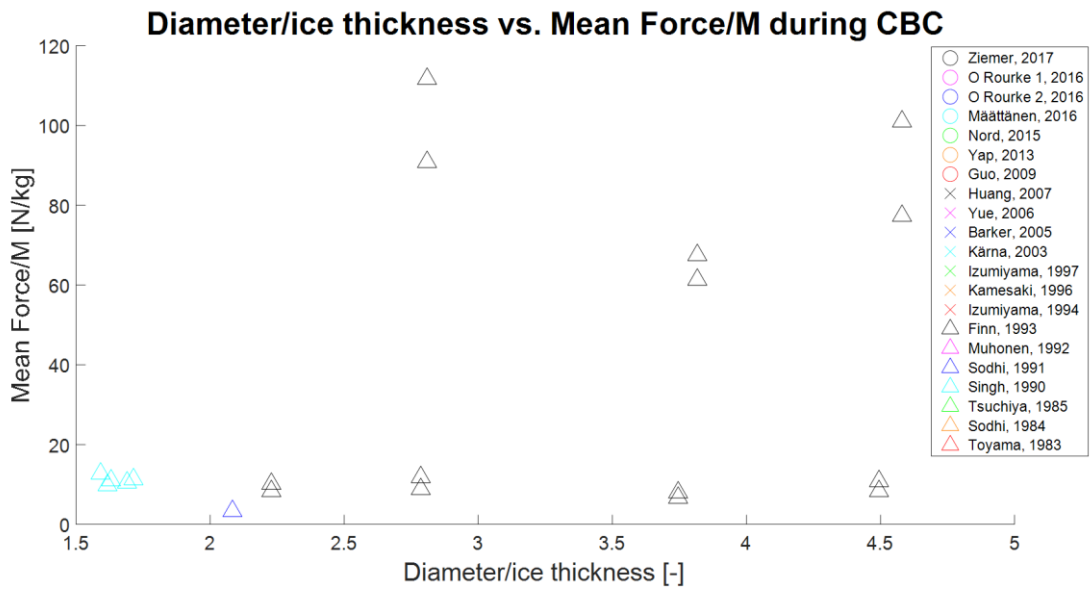


**Figure B-11:** Scatterplot of the aspect ratio against the mean ice load divided by mass during continuous brittle crushing retrieved during 21 model-test campaigns.

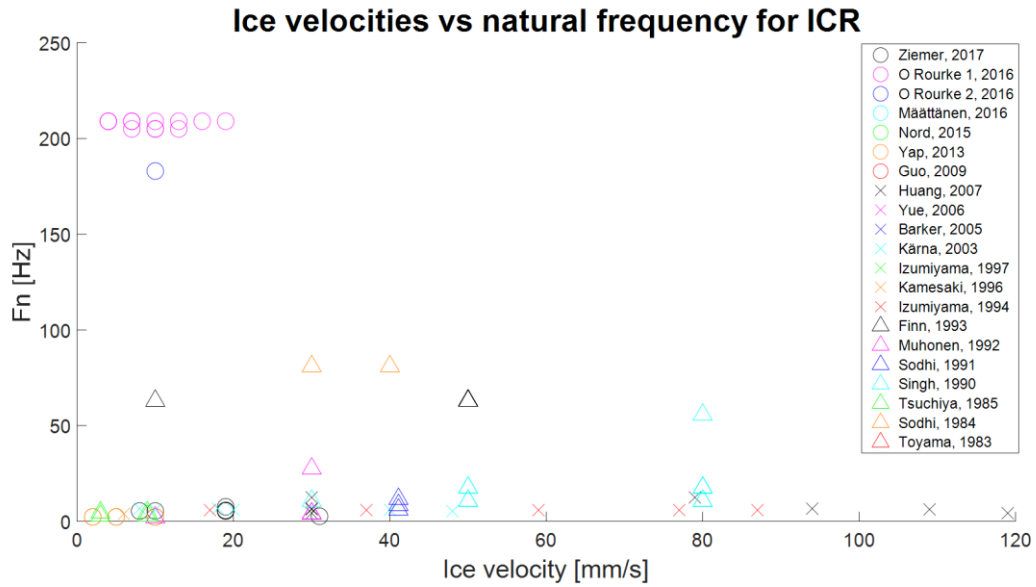


**Figure B-12:** Scatterplot of the ice velocity against the natural frequency for which intermittent crushing occurred during 21 model-test campaigns.

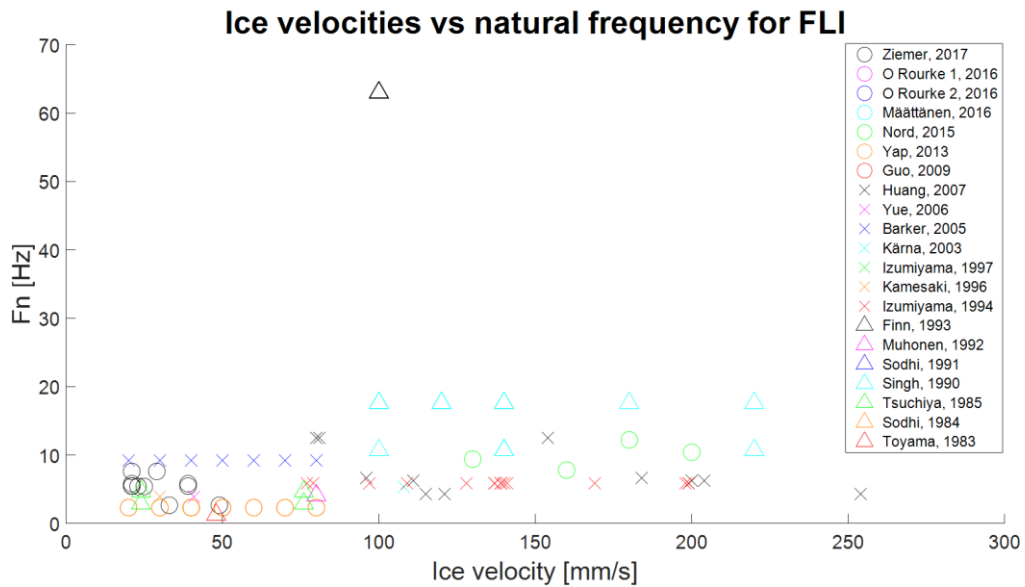


**Figure B-13:** Scatterplot of the ice velocity against the natural frequency for which frequency lock-in occurred during 21 model-test campaigns.

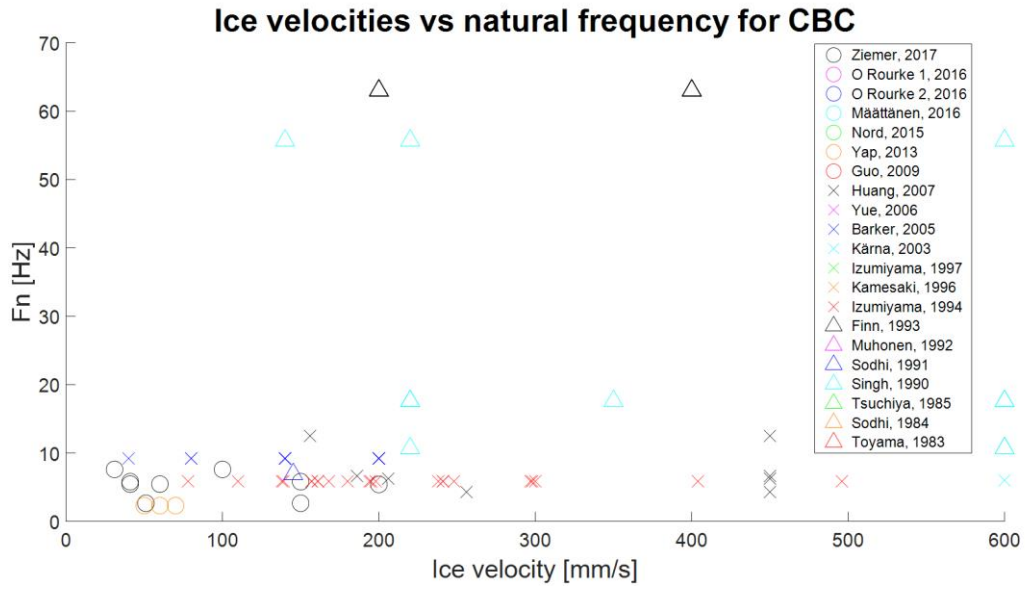


**Figure B-14:** Scatterplot of the ice velocity against the natural frequency for which continuous brittle crushing occurred during 21 model-test campaigns.

# Appendix C

## TU Delft model Simulations

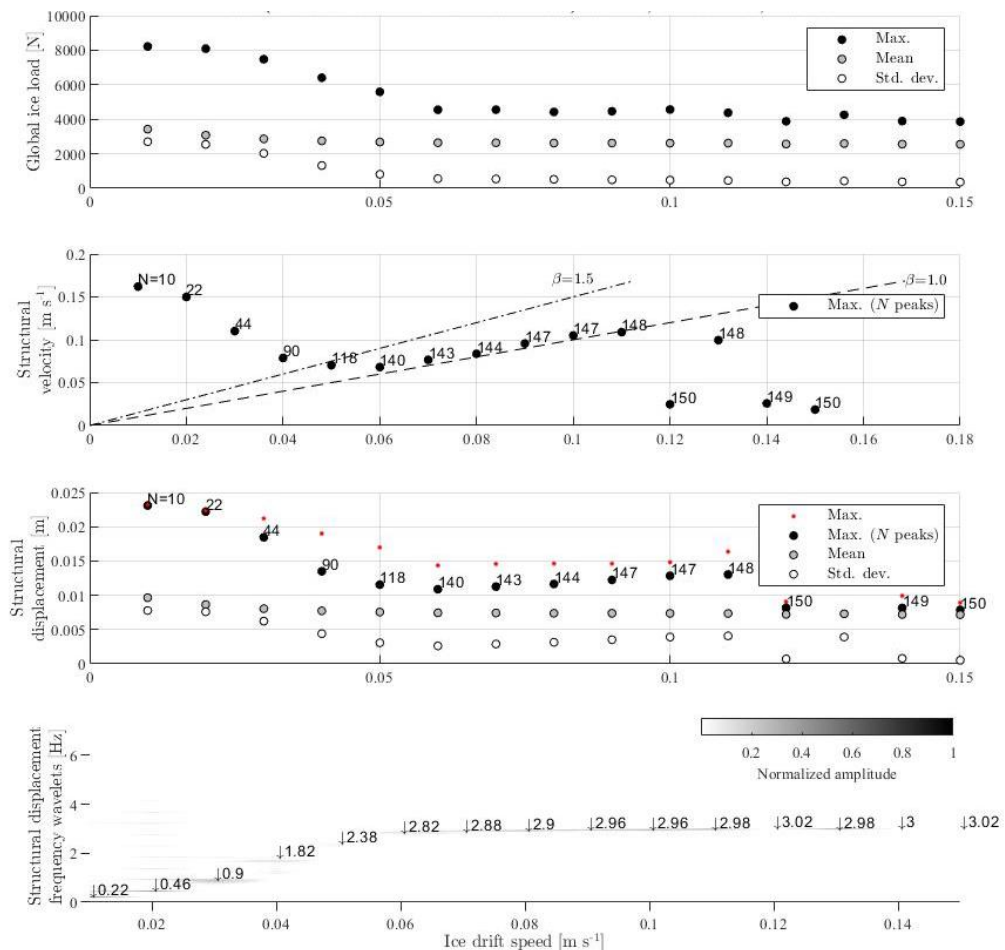


**Figure C-1:** Simulations in the TU Delft model for the base case proposed in Table 3-2. On top a plot of ice drift speed against global ice loads, below ice drift speed against maximum structural velocity, on the third row the drift speed against structural displacement and at bottom the drift speed against structural displacement frequency wavelets.

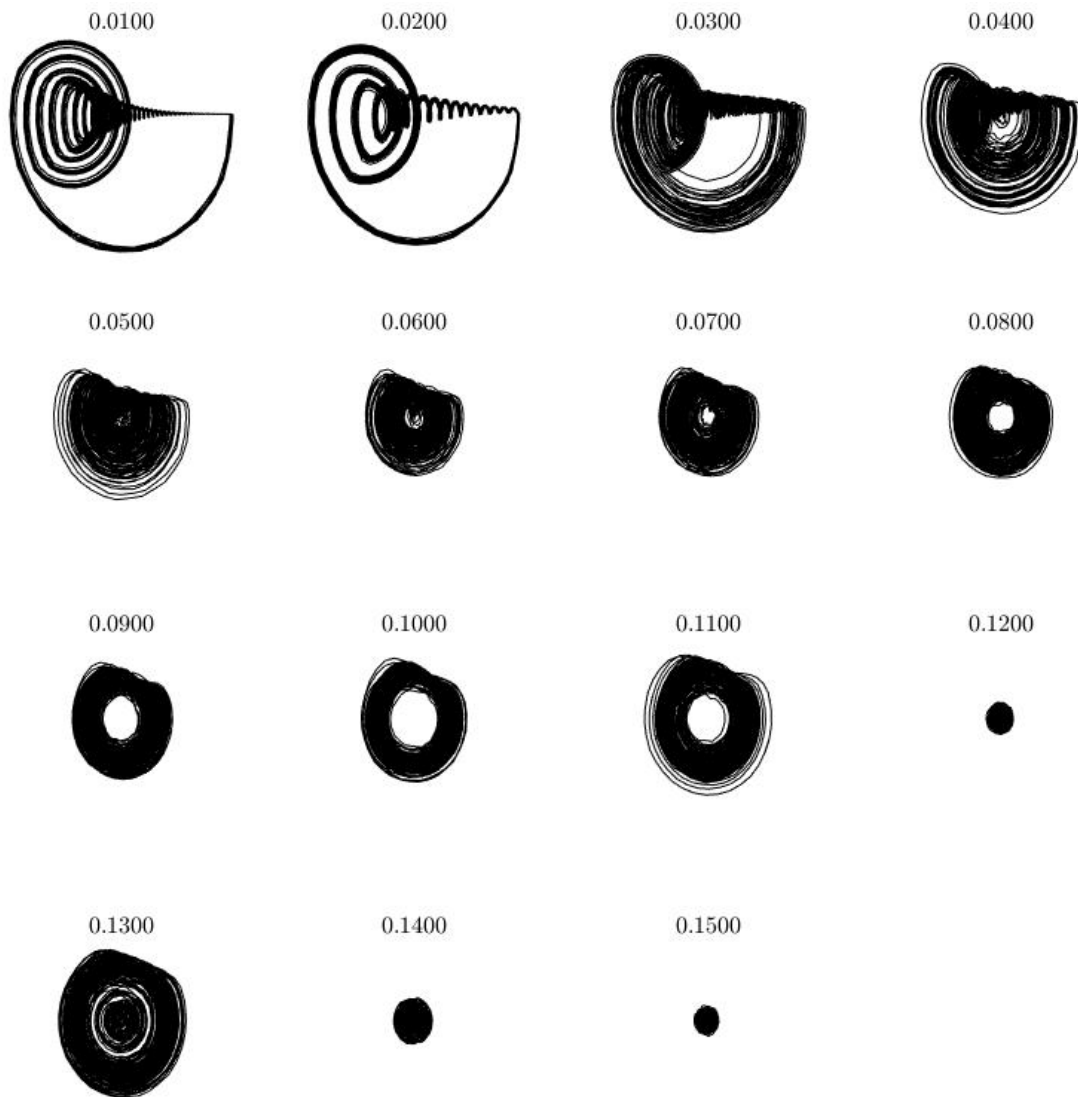


**Figure C-2:** Phase plane plots (structural displacement against velocity) simulated with the TU Delft model for the base case in Table 3-2.

---

## Appendix D

---

### Ice thickness plots

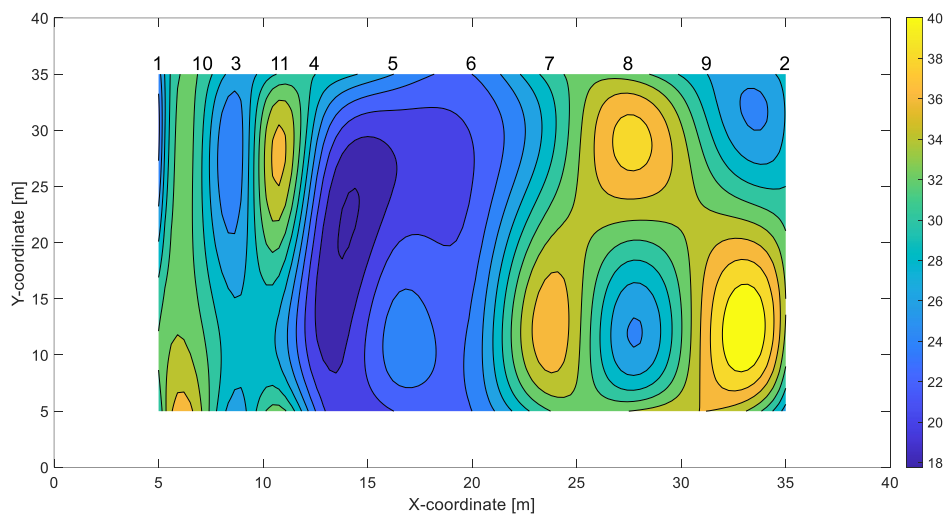


**Figure D-1:** Colourmap of ice thicknesses measured in the ice tank at the 17<sup>th</sup> of June. Numbers above indicate the order and location of test channels.

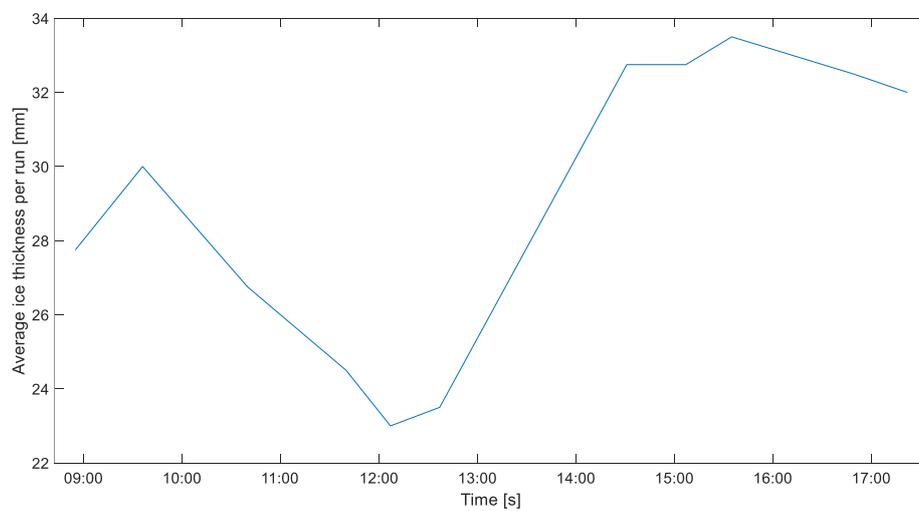


**Figure D-2:** Plot of ice thicknesses over time in the ice tank at the 17<sup>th</sup> of June.

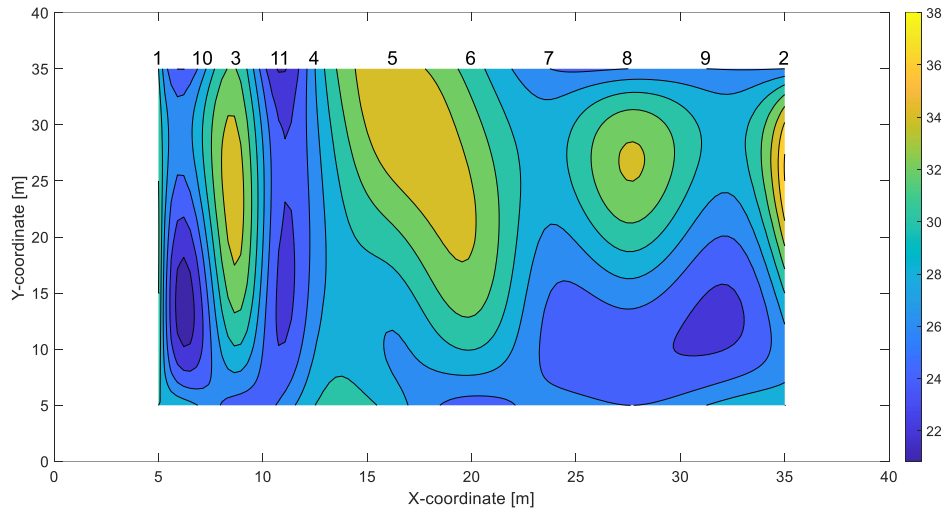


**Figure D-3:** Colourmap of ice thicknesses measured in the ice tank at the 21<sup>st</sup> of June. Numbers above indicate the order and location of test channels.

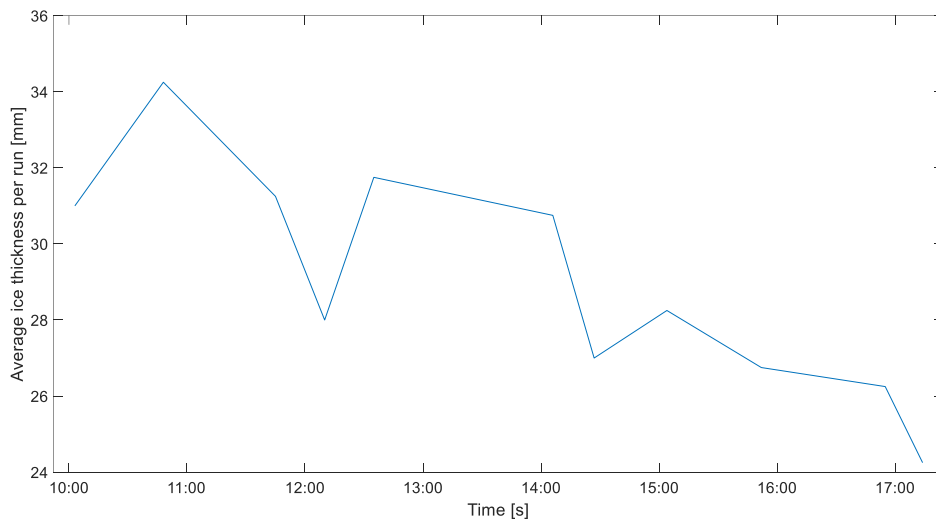


**Figure D-4:** Plot of ice thicknesses over time in the ice tank at the 21<sup>st</sup> of June.

---

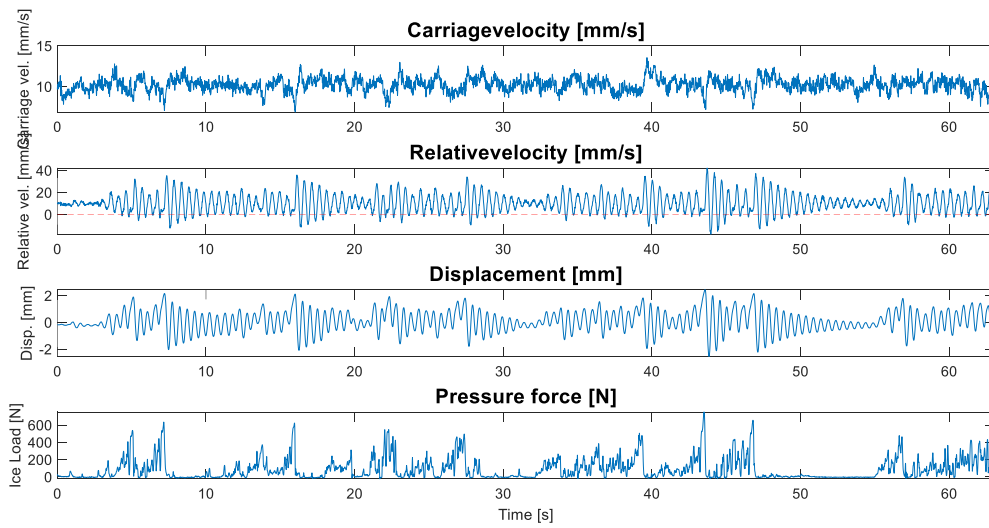
## Appendix E

---

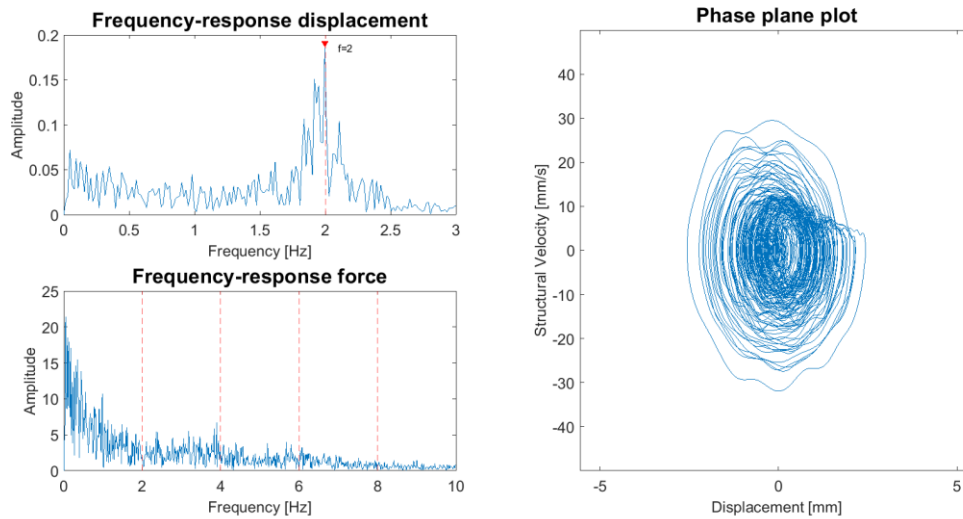
# Time series test campaign

In this Appendix all the time series from single degree of freedom tests can be found. On top of the figure the structural model name, the natural frequency and the velocity can be found. If a ramp function has been used, no velocity is given.

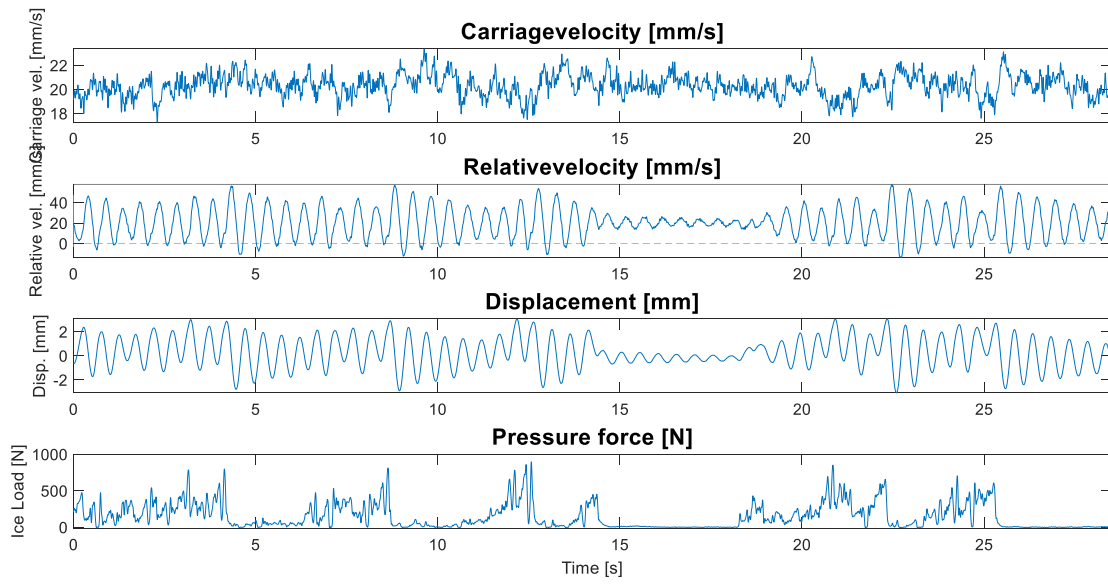
Test: SDOF-1. Fn: 2 Hz. V = 10 mm/s



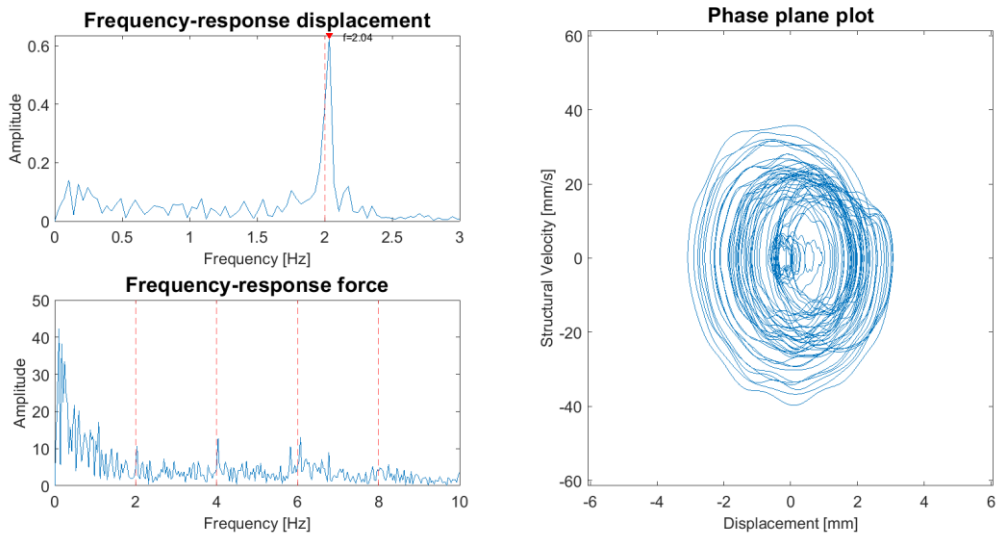
Test: SDOF-1. Fn: 2 Hz. V = 10 mm/s



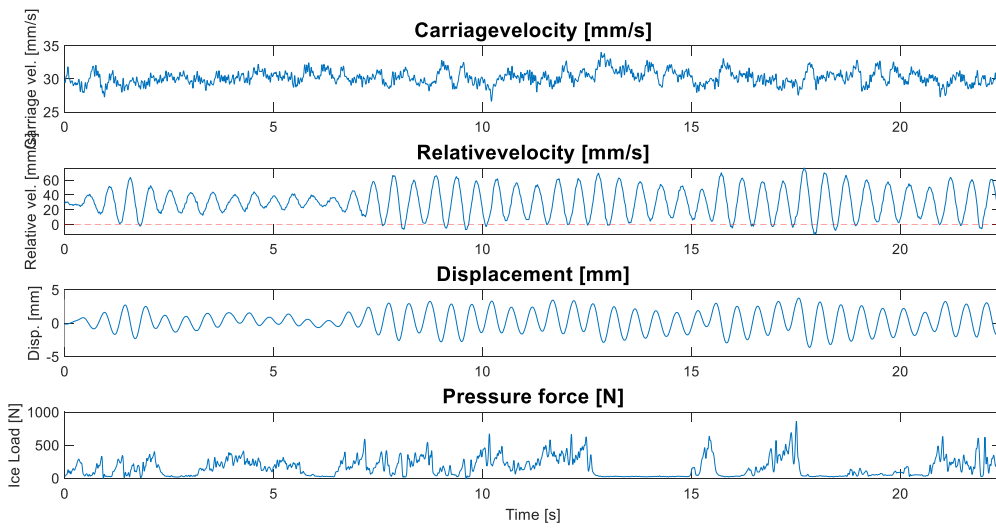
Test: SDOF-1. Fn: 2 Hz. V = 20 mm/s



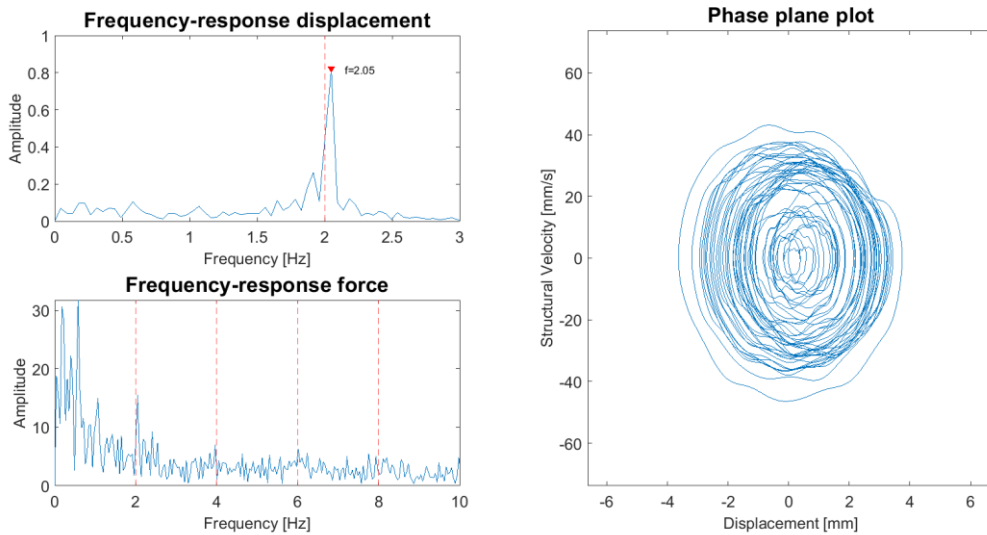
Test: SDOF-1. Fn: 2 Hz. V = 20 mm/s



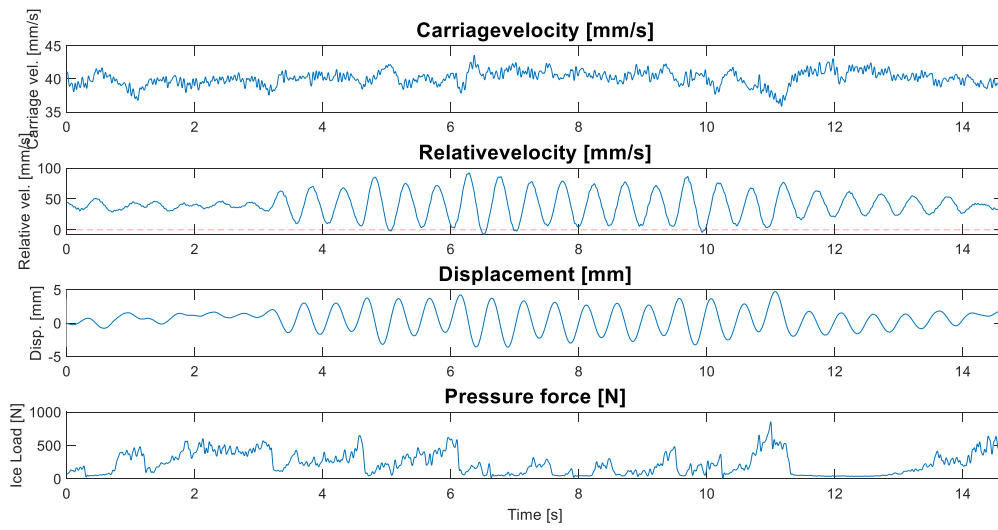
Test: SDOF-1. Fn: 2 Hz. V = 30 mm/s



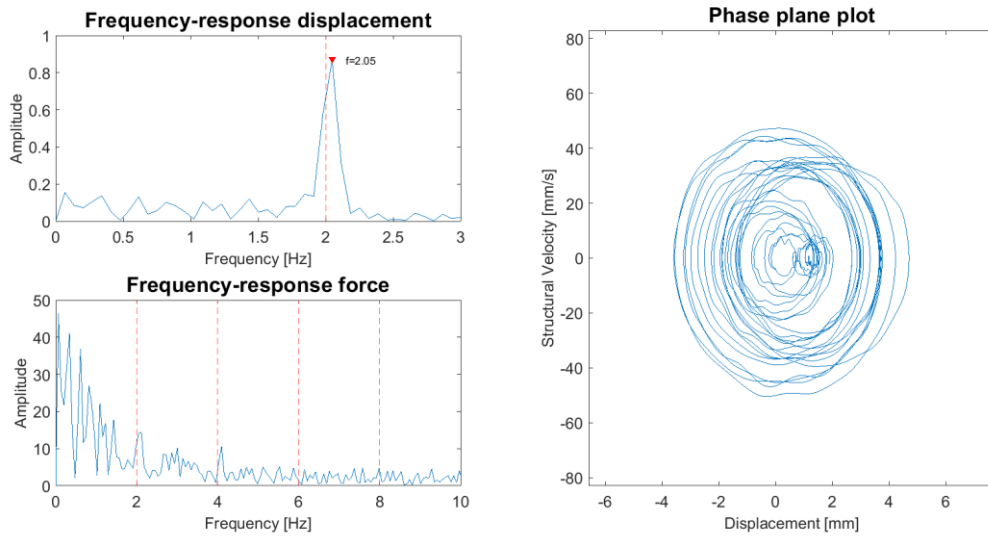
Test: SDOF-1. Fn: 2 Hz. V = 30 mm/s



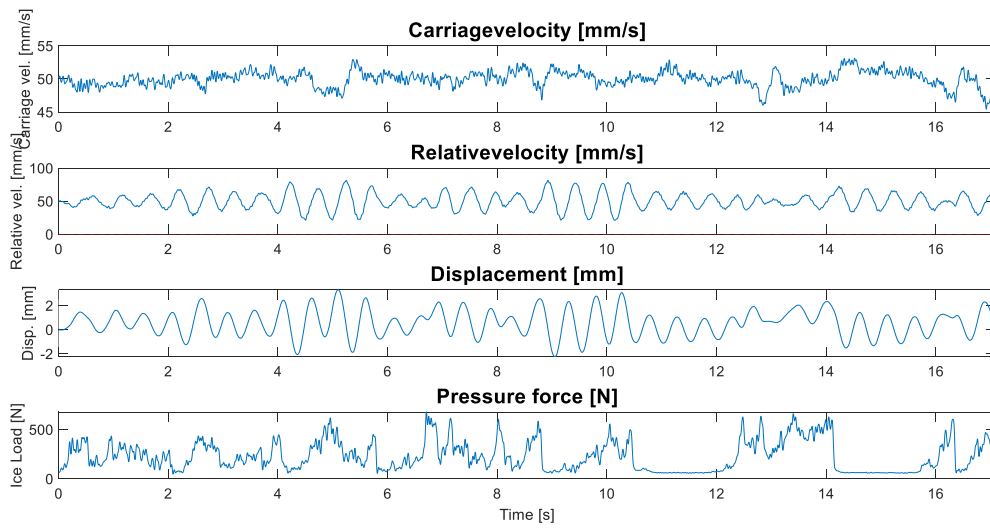
Test: SDOF-1. Fn: 2 Hz. V = 40 mm/s



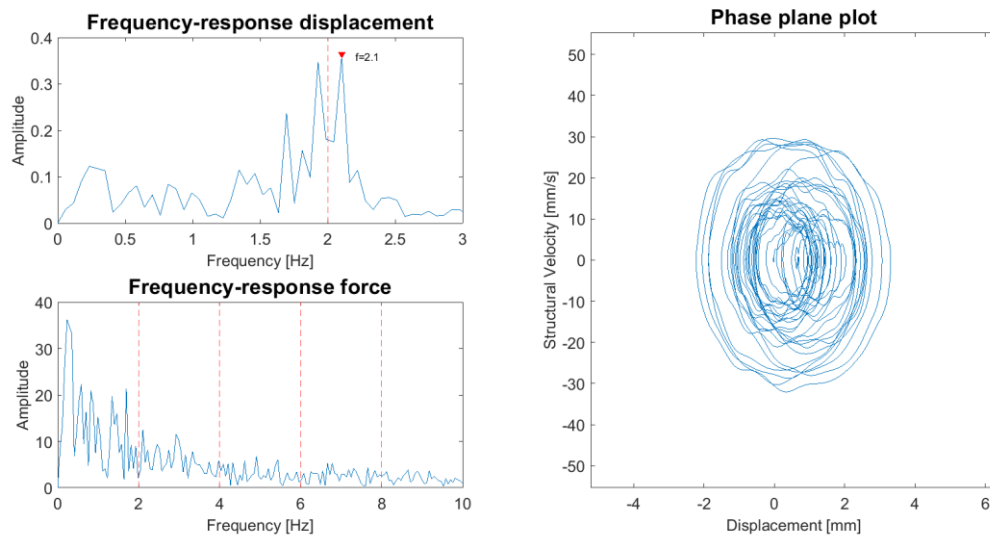
Test: SDOF-1. Fn: 2 Hz. V = 40 mm/s



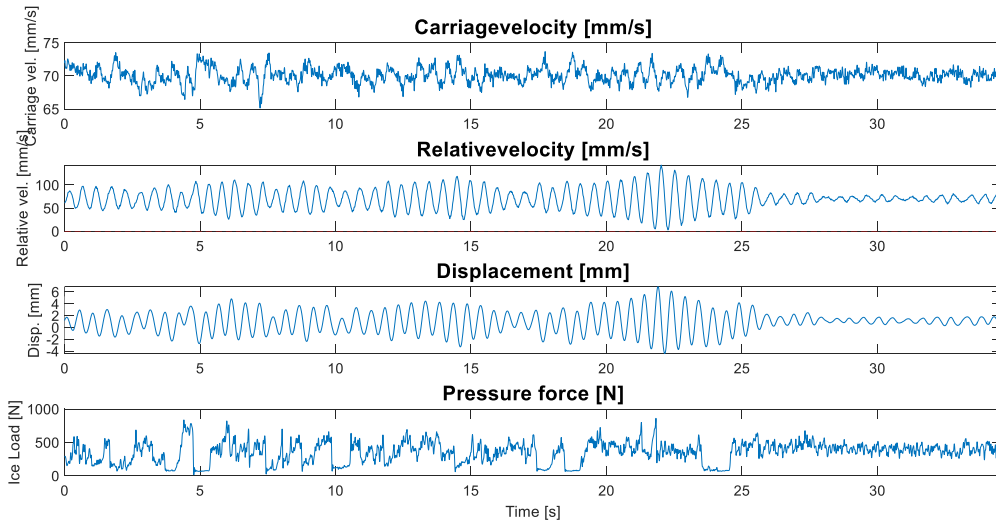
Test: SDOF-1. Fn: 2 Hz. V = 50 mm/s



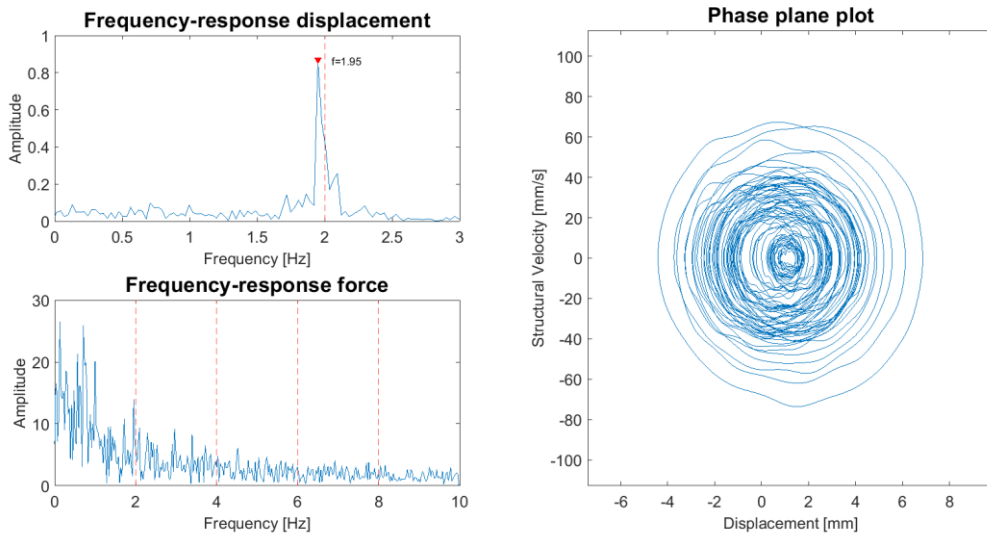
Test: SDOF-1. Fn: 2 Hz. V = 50 mm/s



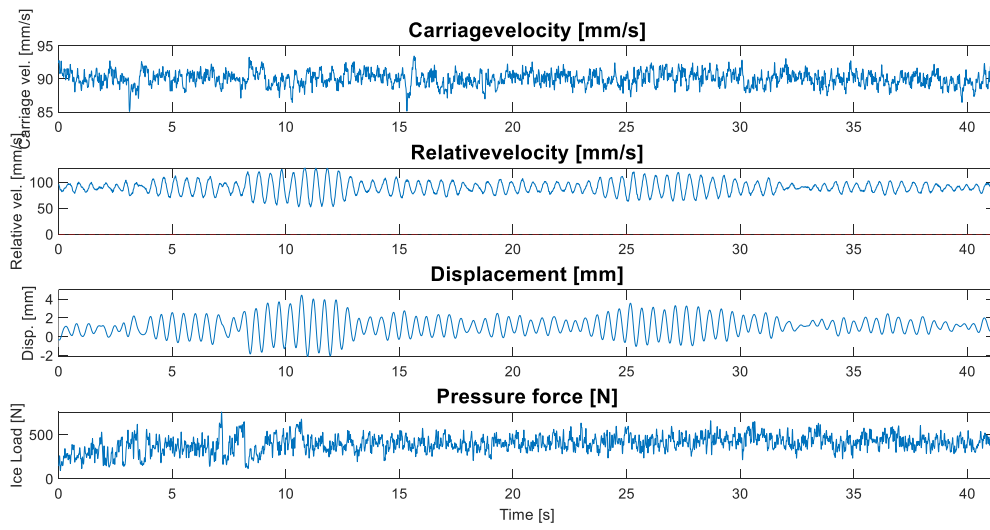
Test: SDOF-1. Fn: 2 Hz. V = 70 mm/s



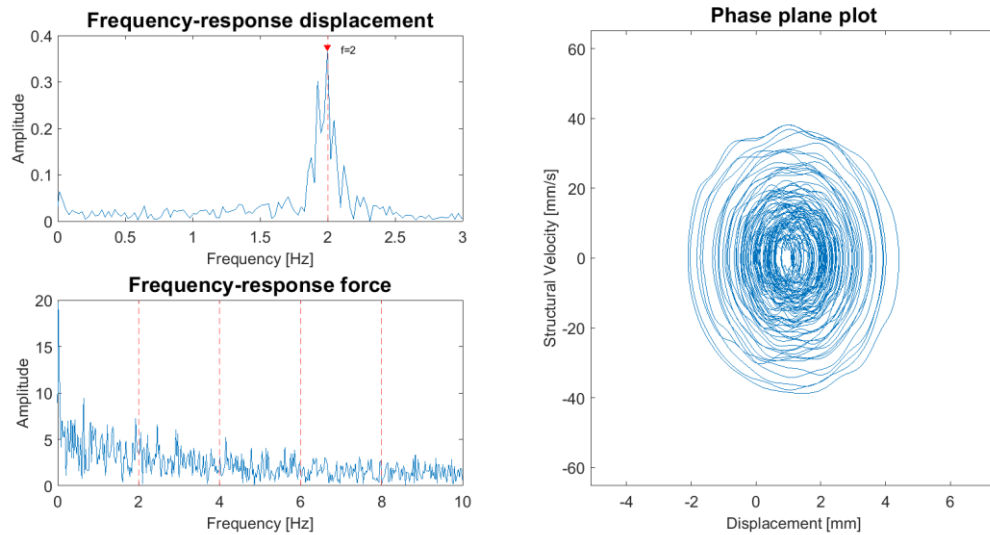
Test: SDOF-1. Fn: 2 Hz. V = 70 mm/s



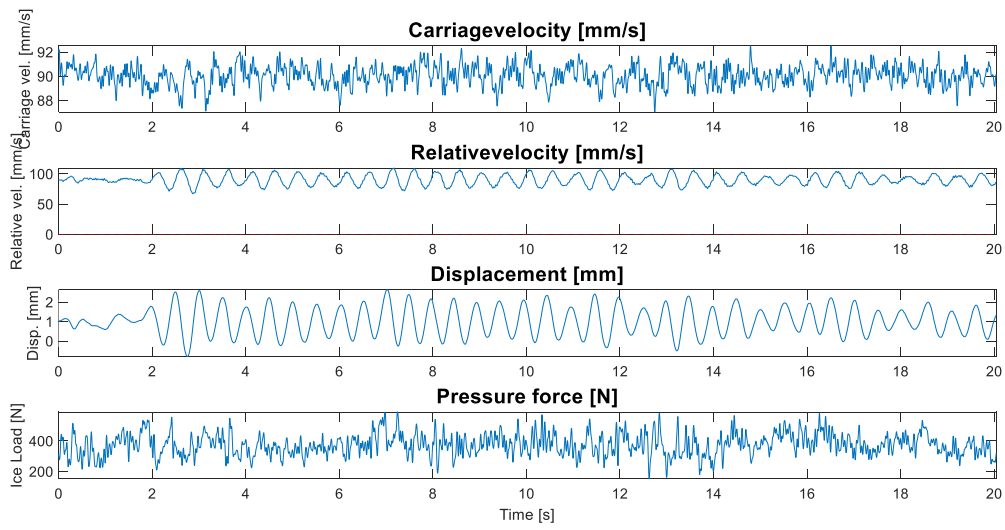
Test: SDOF-1. Fn: 2 Hz. V = 90 mm/s



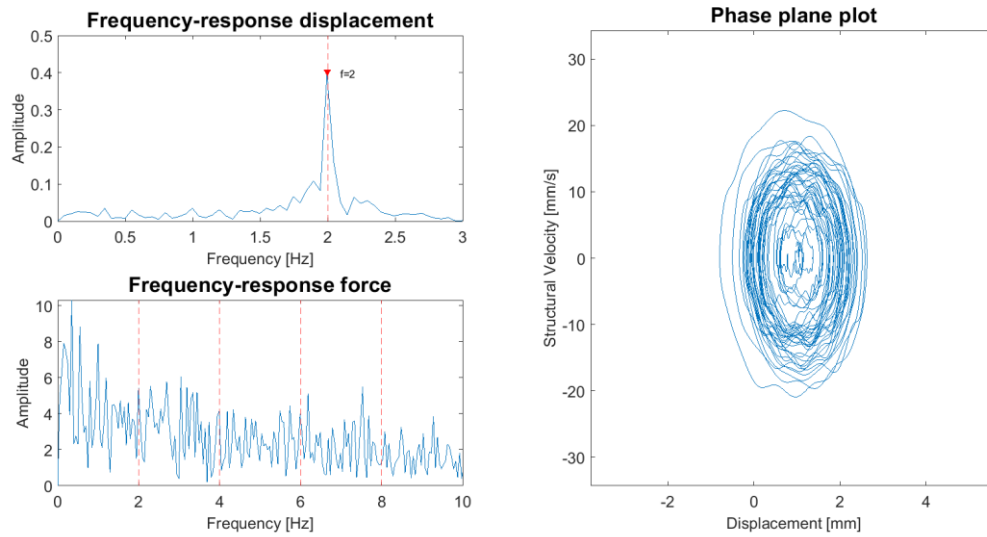
Test: SDOF-1. Fn: 2 Hz. V = 90 mm/s



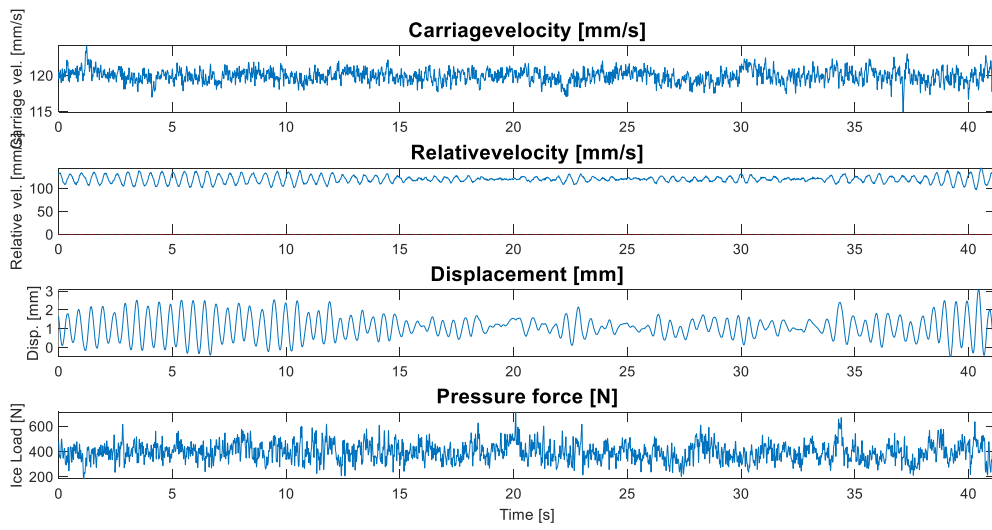
Test: SDOF-1. Fn: 2 Hz. V = 90 mm/s



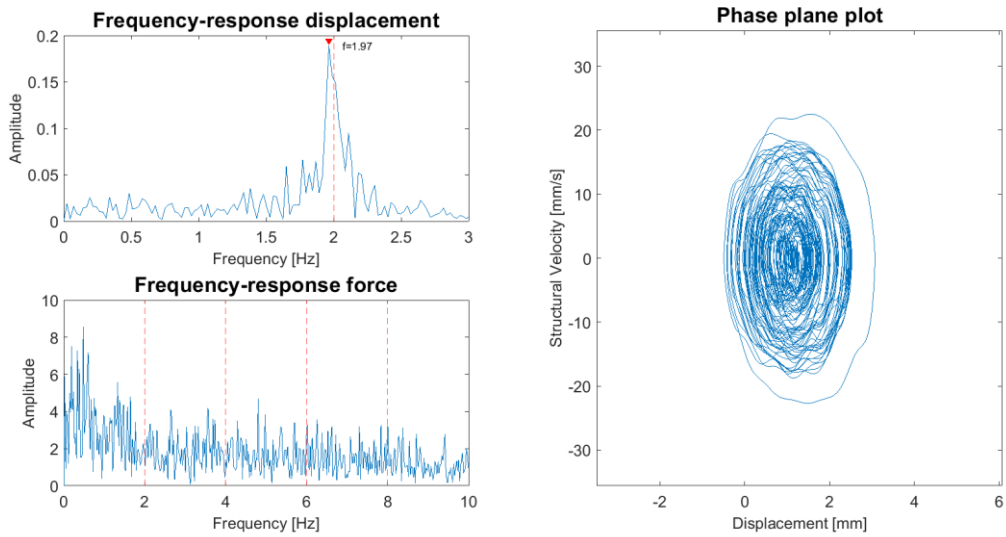
Test: SDOF-1. Fn: 2 Hz. V = 90 mm/s



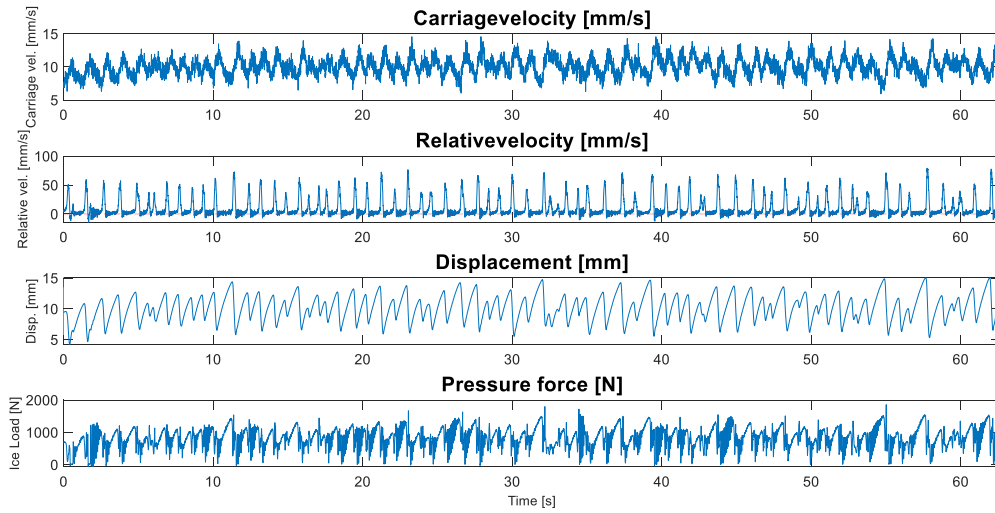
Test: SDOF-1. Fn: 2 Hz. V = 120 mm/s



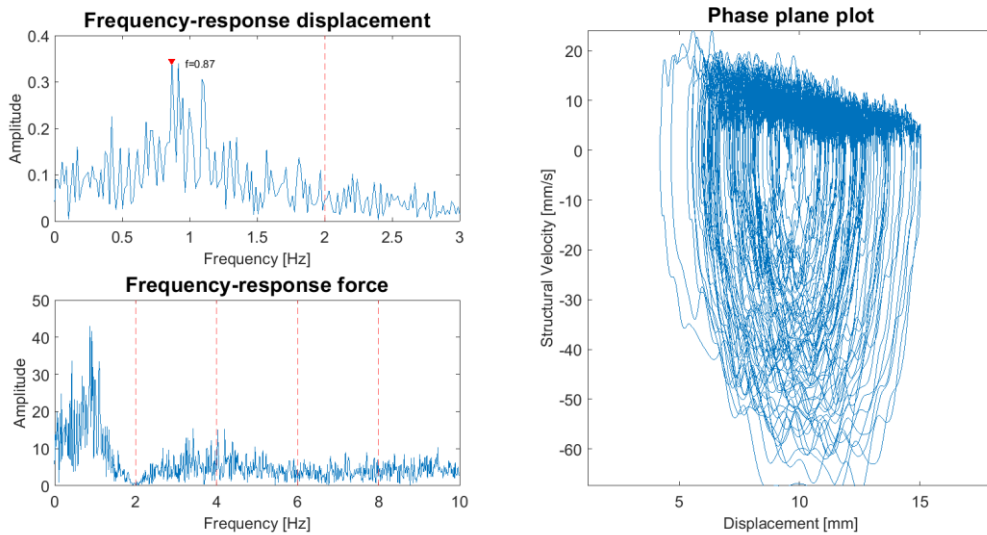
Test: SDOF-1. Fn: 2 Hz. V = 120 mm/s



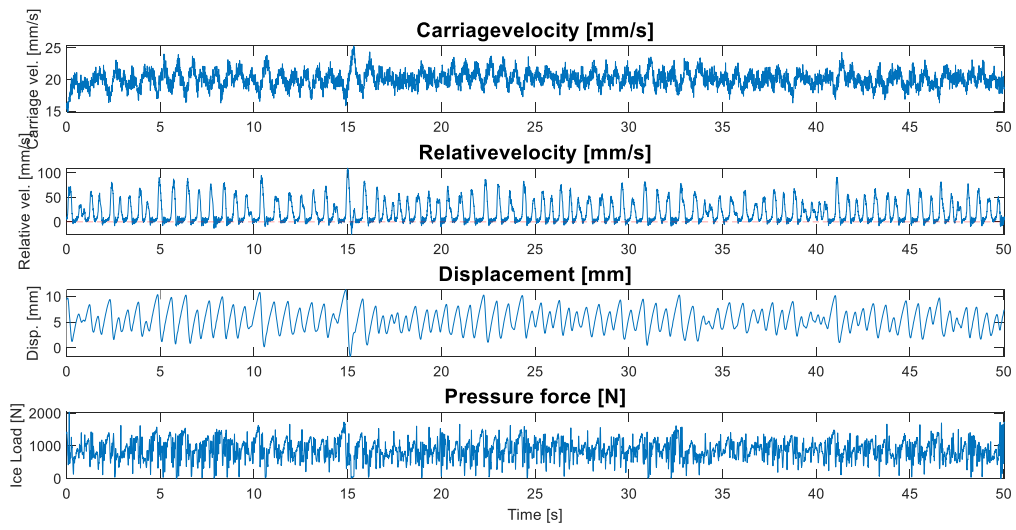
Test: SDOF-2. Fn: 2 Hz. V = 10 mm/s



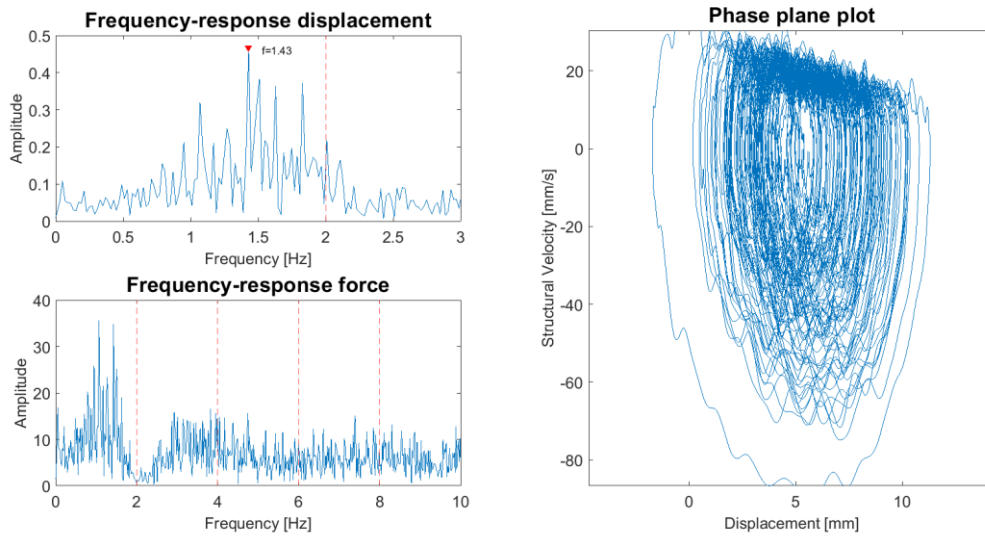
Test: SDOF-2. Fn: 2 Hz. V = 10 mm/s



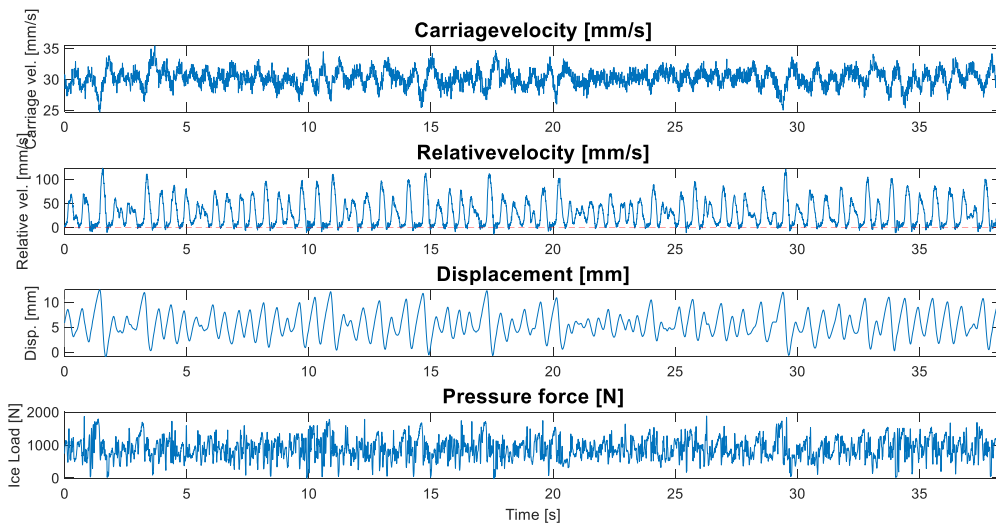
Test: SDOF-2. Fn: 2 Hz. V = 20 mm/s



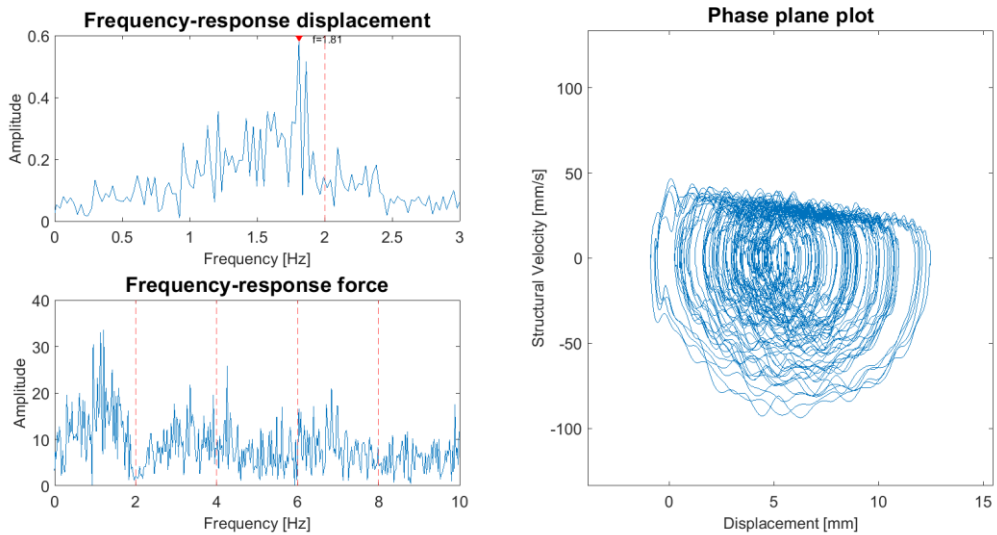
Test: SDOF-2. Fn: 2 Hz. V = 20 mm/s



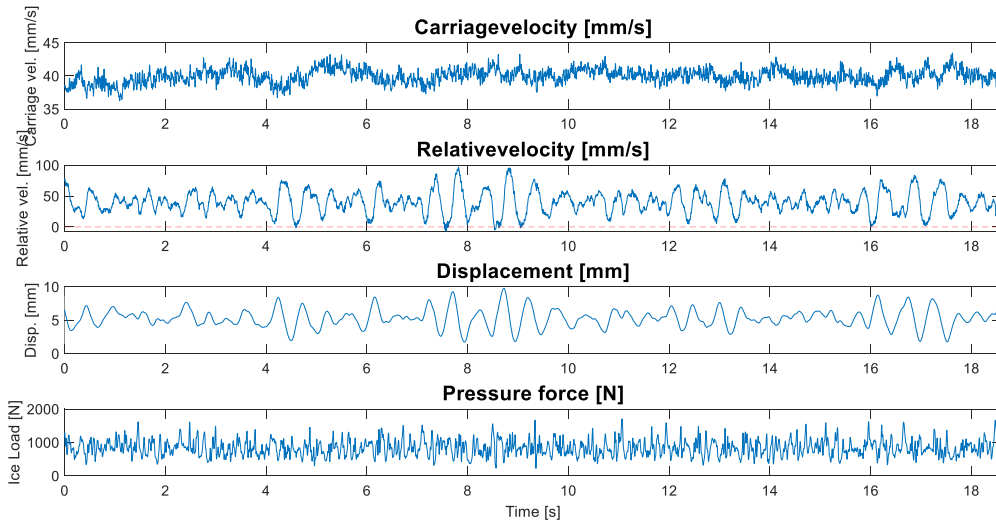
Test: SDOF-2. Fn: 2 Hz. V = 30 mm/s



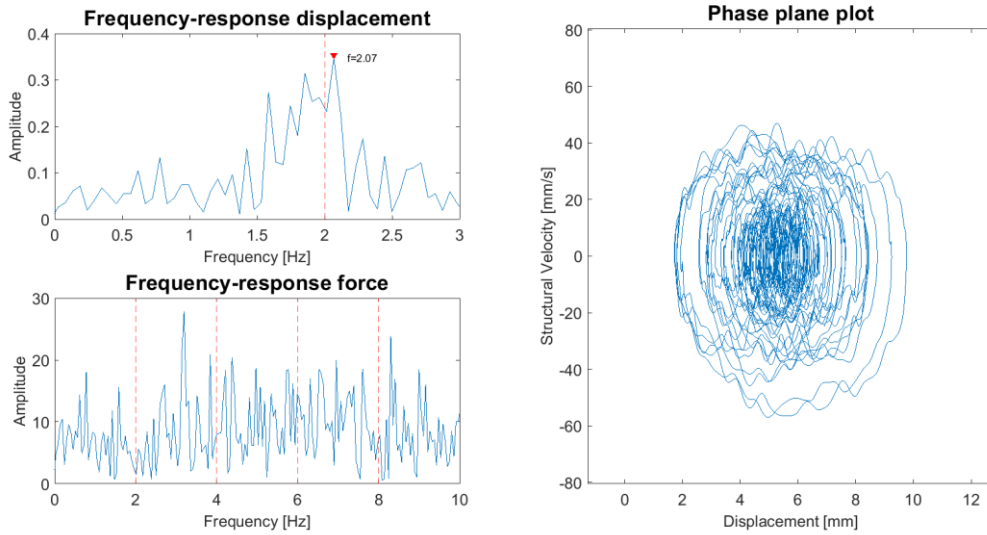
Test: SDOF-2. Fn: 2 Hz. V = 30 mm/s



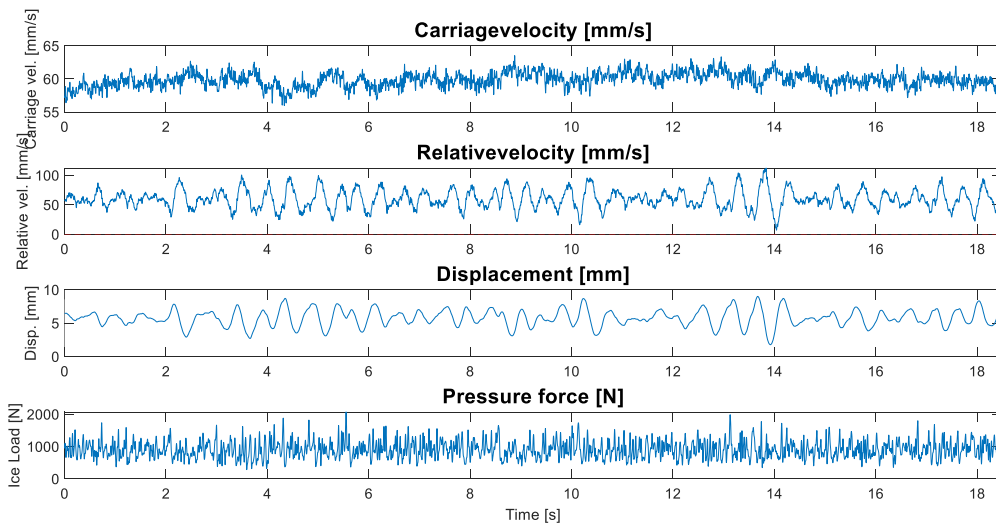
Test: SDOF-2. Fn: 2 Hz. V = 40 mm/s



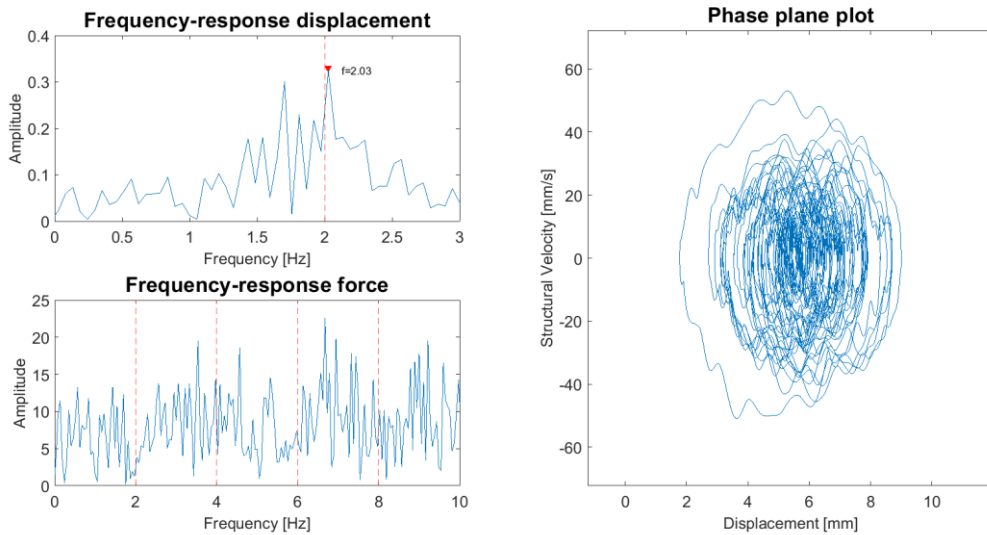
Test: SDOF-2. Fn: 2 Hz. V = 40 mm/s



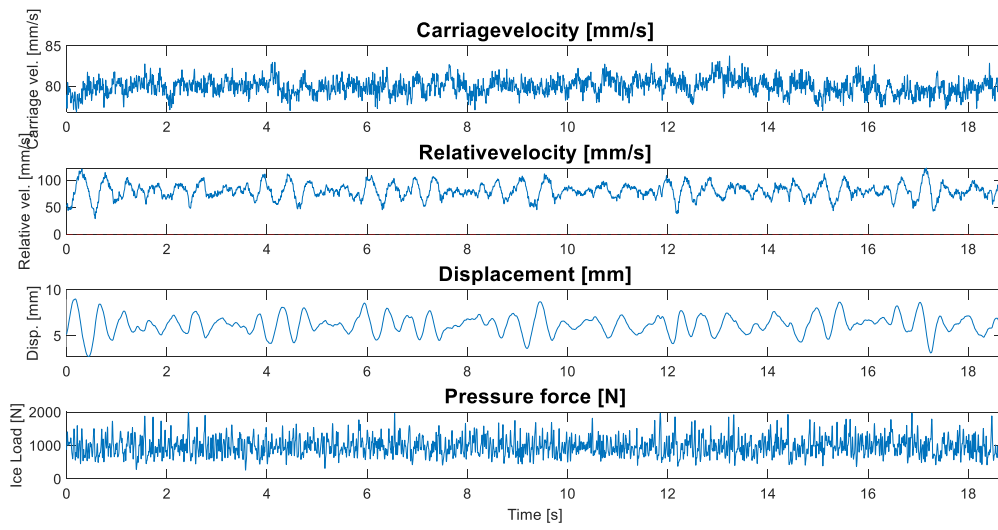
Test: SDOF-2. Fn: 2 Hz. V = 60 mm/s



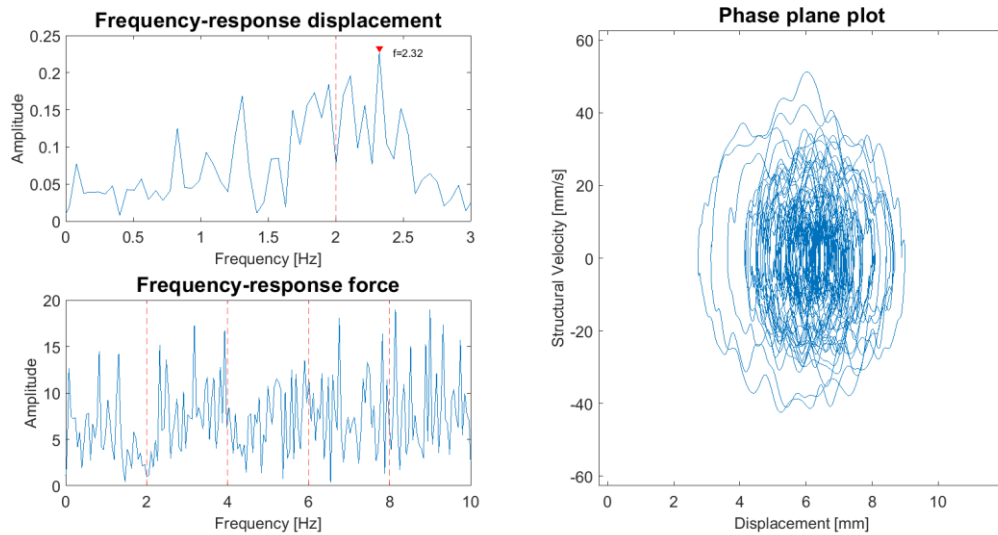
Test: SDOF-2. Fn: 2 Hz. V = 60 mm/s



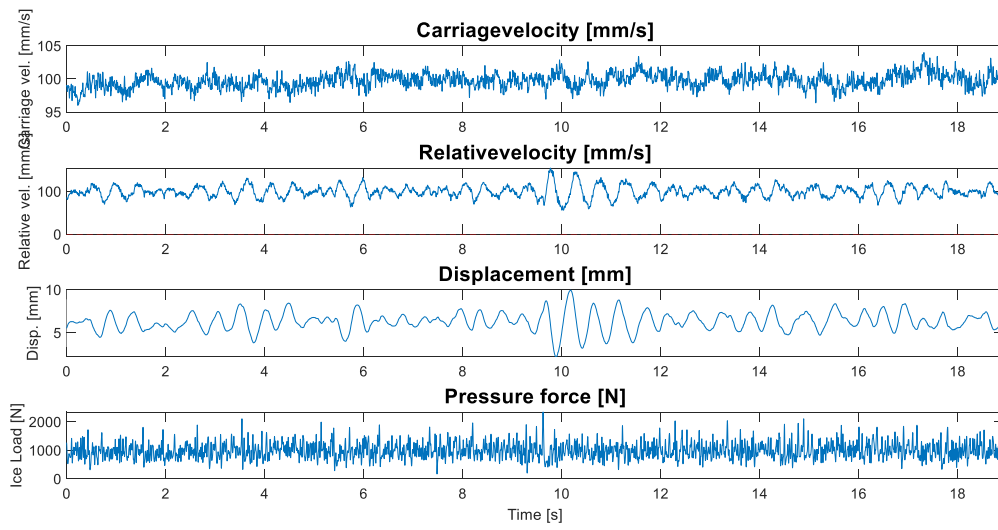
Test: SDOF-2. Fn: 2 Hz. V = 80 mm/s



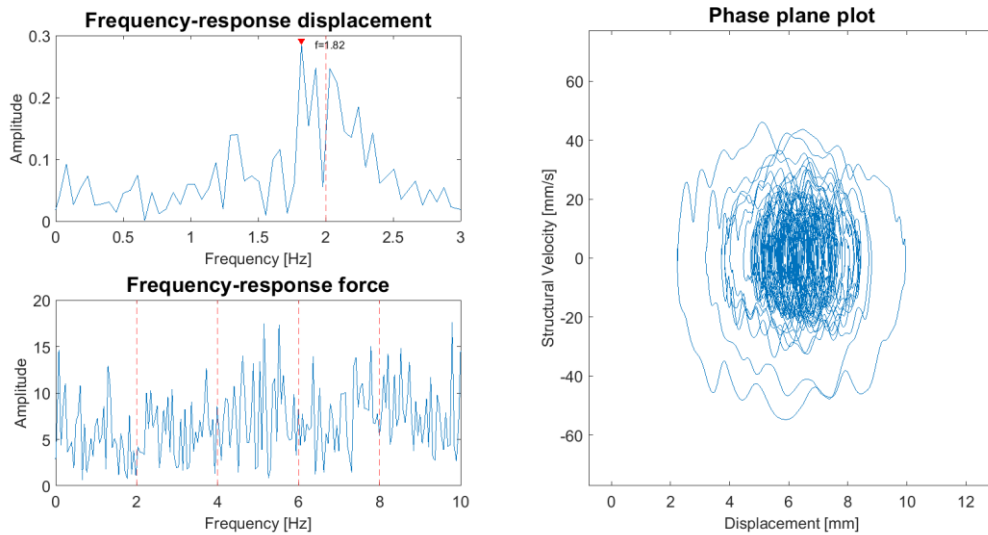
Test: SDOF-2. Fn: 2 Hz. V = 80 mm/s



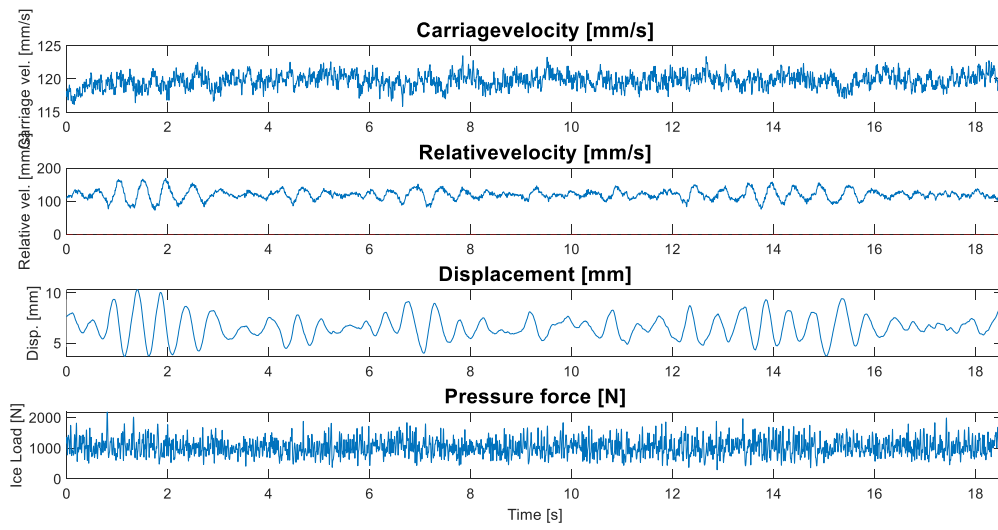
Test: SDOF-2. Fn: 2 Hz. V = 100 mm/s



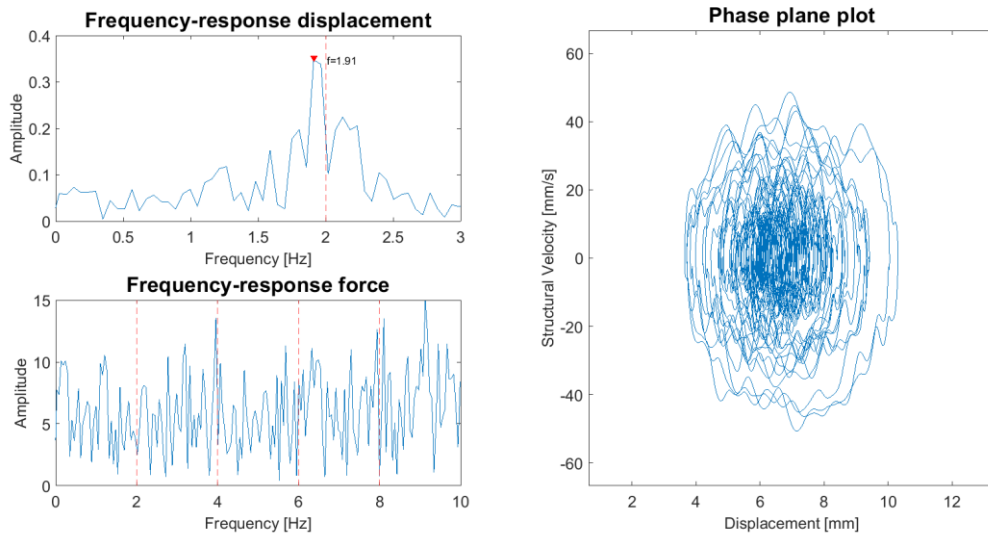
Test: SDOF-2. Fn: 2 Hz. V = 100 mm/s



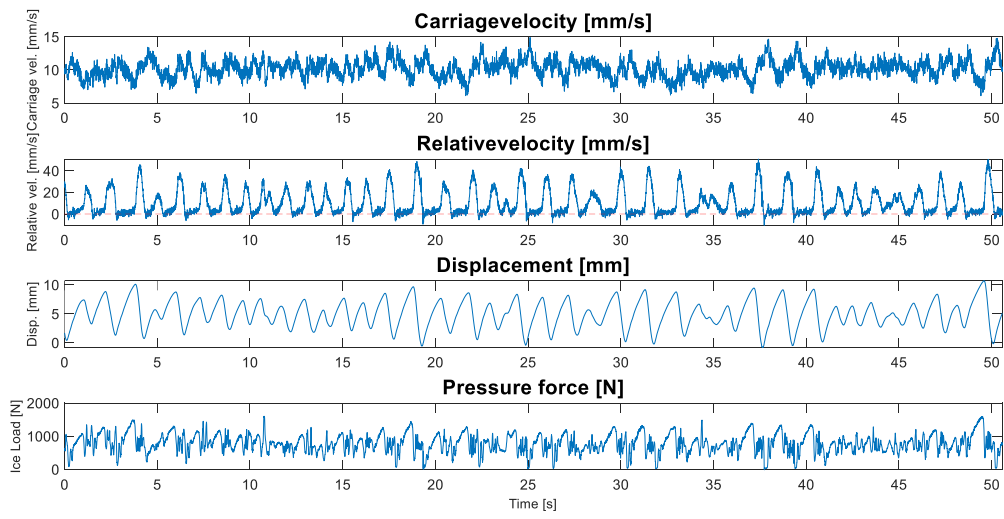
Test: SDOF-2. Fn: 2 Hz. V = 120 mm/s



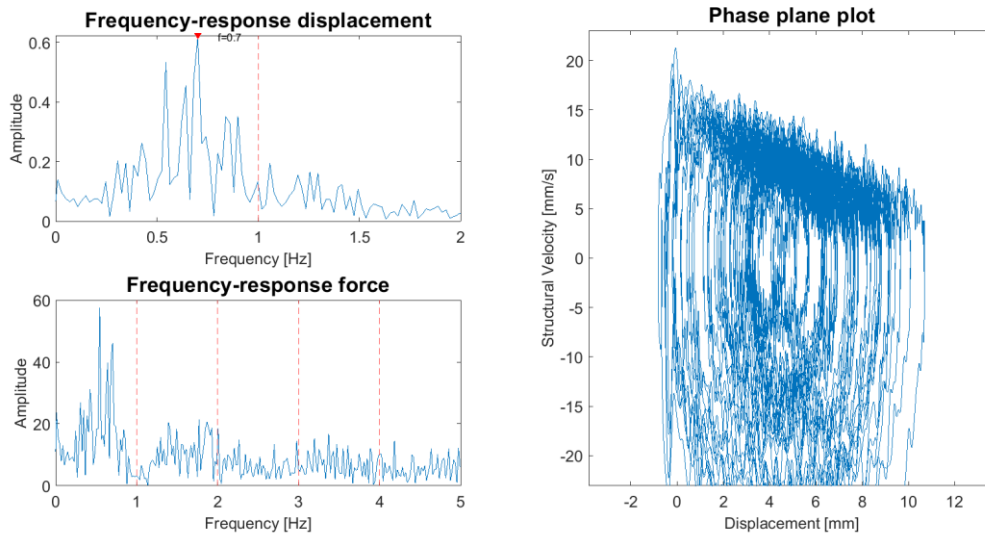
Test: SDOF-2. Fn: 2 Hz. V = 120 mm/s



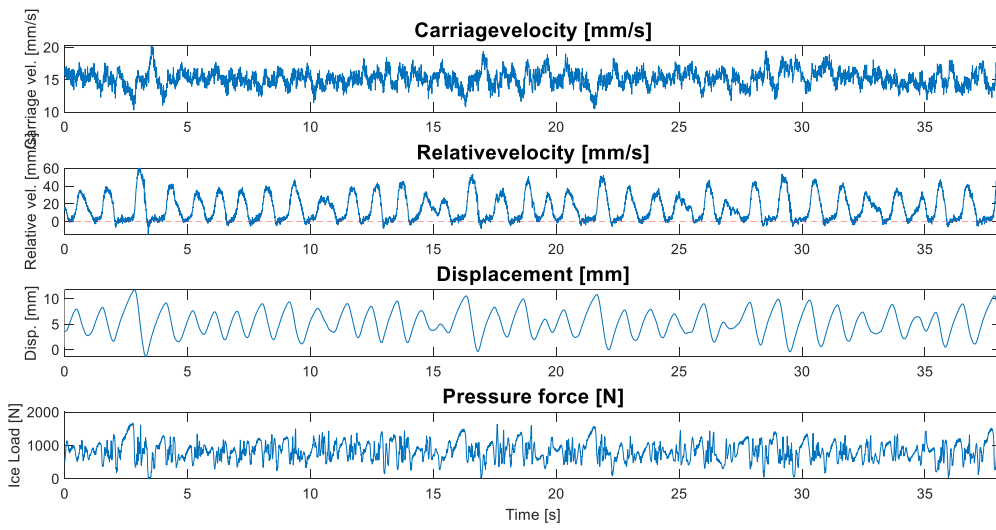
Test: SDOF-3. Fn: 1 Hz. V = 10 mm/s



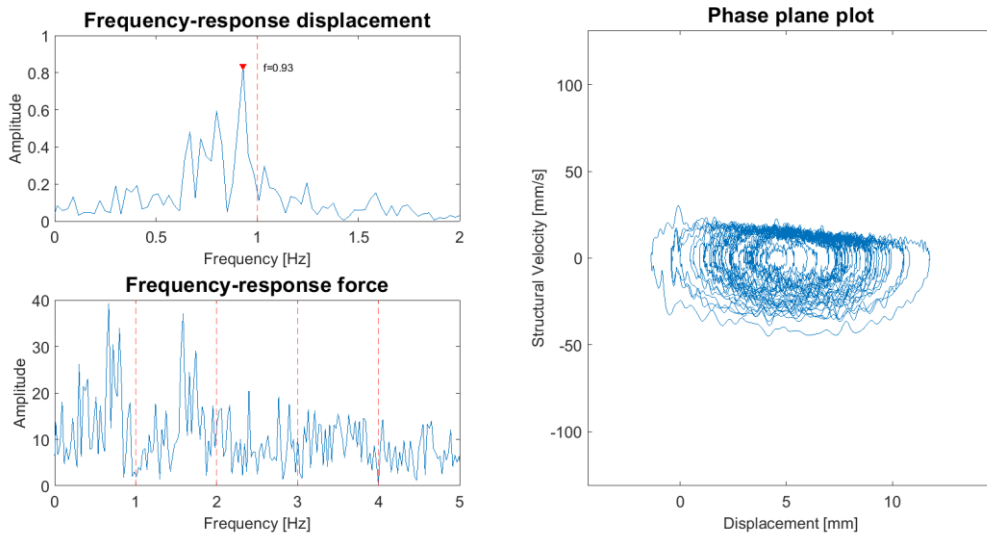
Test: SDOF-3. Fn: 1 Hz. V = 10 mm/s



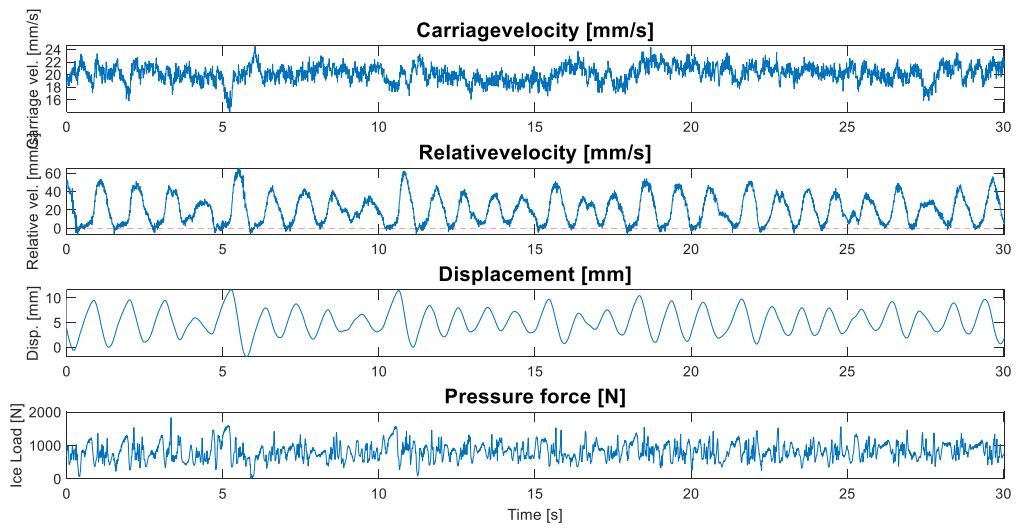
Test: SDOF-3. Fn: 1 Hz. V = 15 mm/s



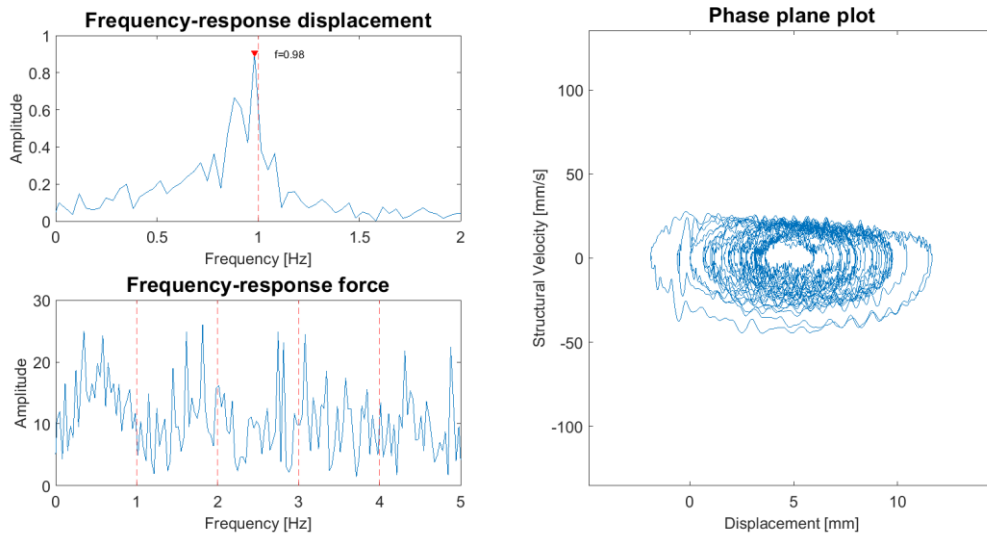
Test: SDOF-3. Fn: 1 Hz. V = 15 mm/s



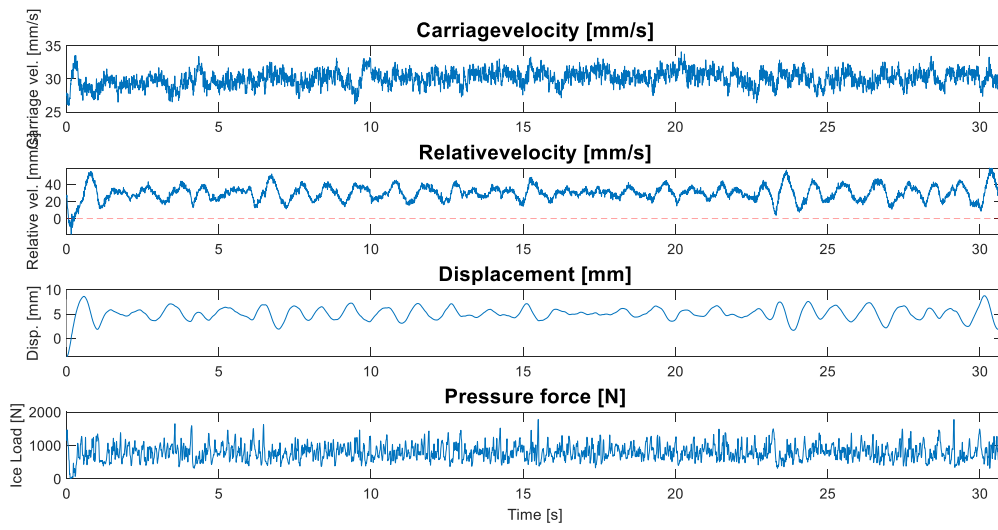
Test: SDOF-3. Fn: 1 Hz. V = 20 mm/s



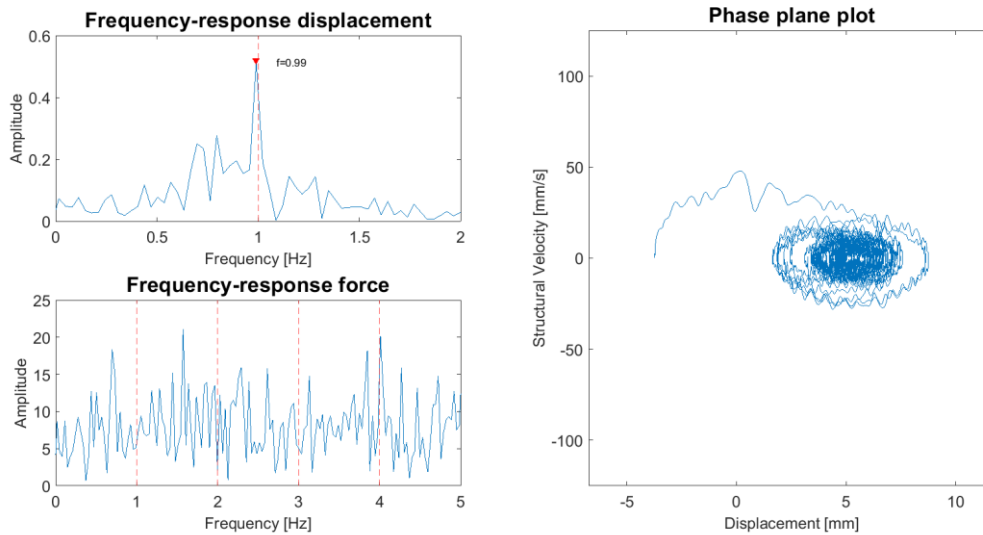
Test: SDOF-3. Fn: 1 Hz. V = 20 mm/s



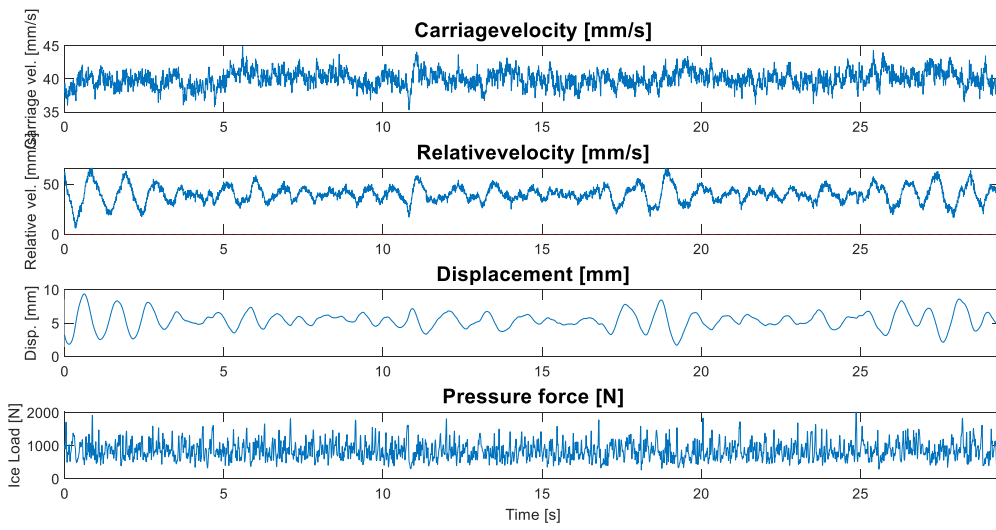
Test: SDOF-3. Fn: 1 Hz. V = 30 mm/s



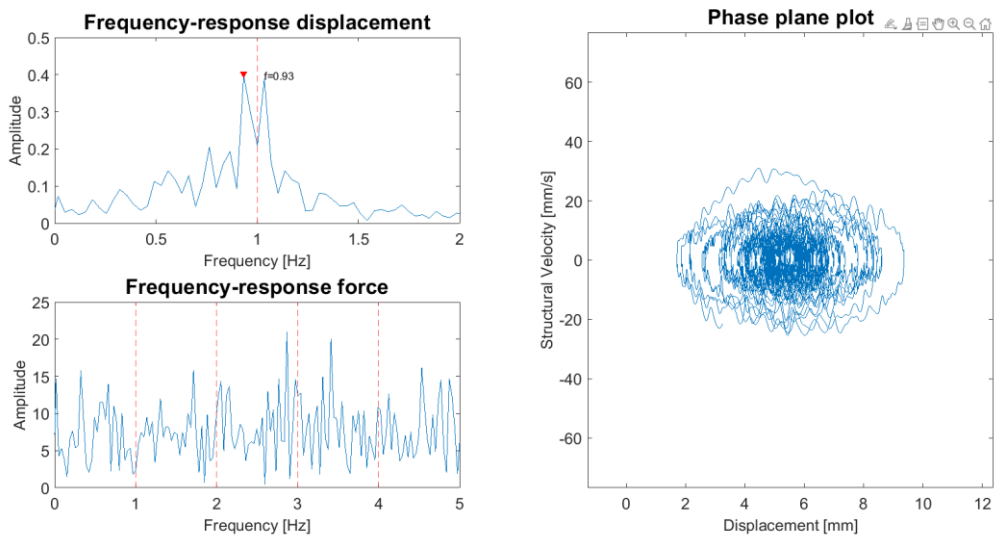
Test: SDOF-3. Fn: 1 Hz. V = 30 mm/s



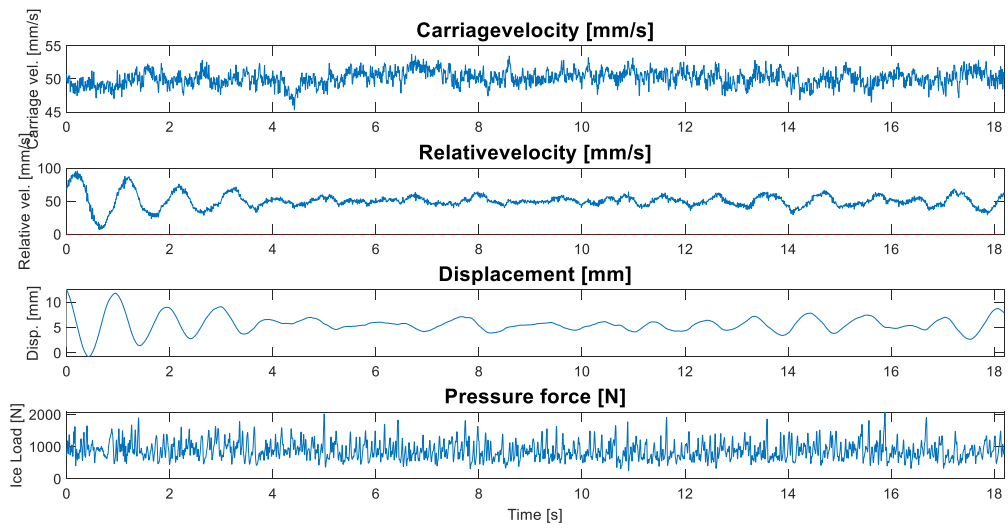
Test: SDOF-3. Fn: 1 Hz. V = 40 mm/s



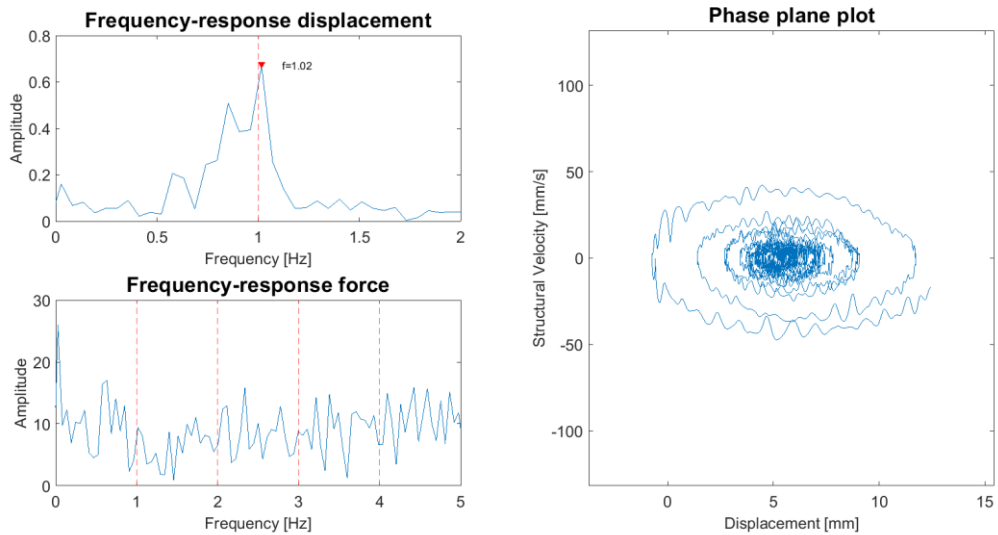
Test: SDOF-3. Fn: 1 Hz. V = 40 mm/s



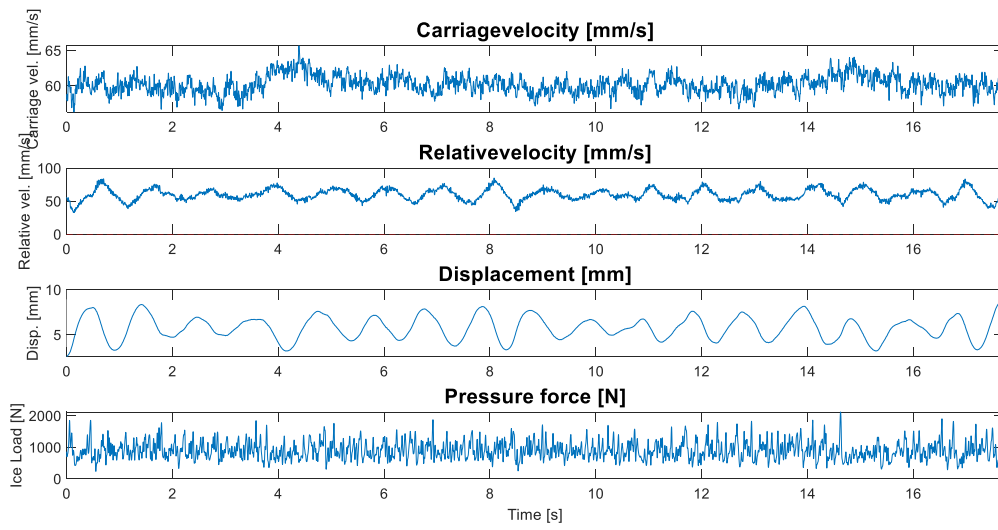
Test: SDOF-3. Fn: 1 Hz. V = 50 mm/s



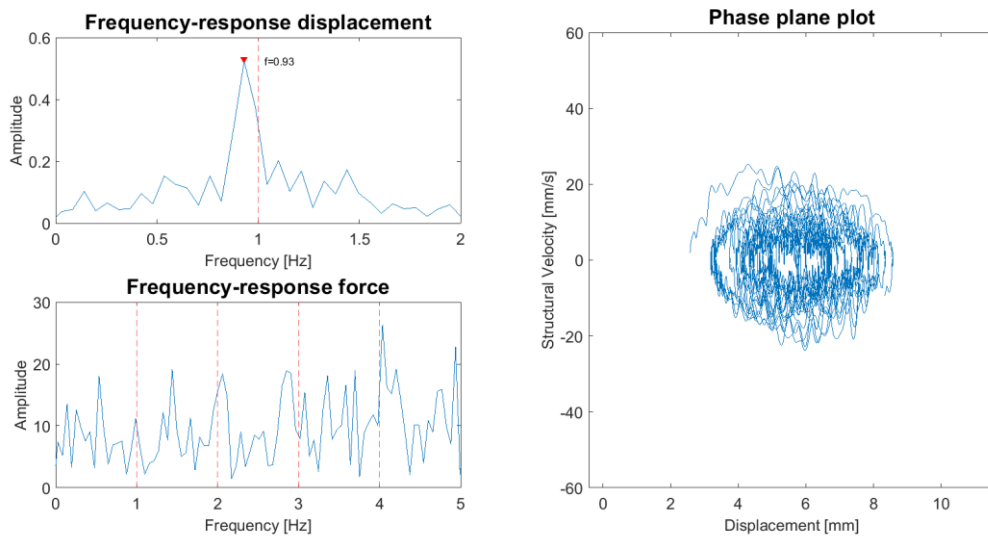
Test: SDOF-3. Fn: 1 Hz. V = 50 mm/s



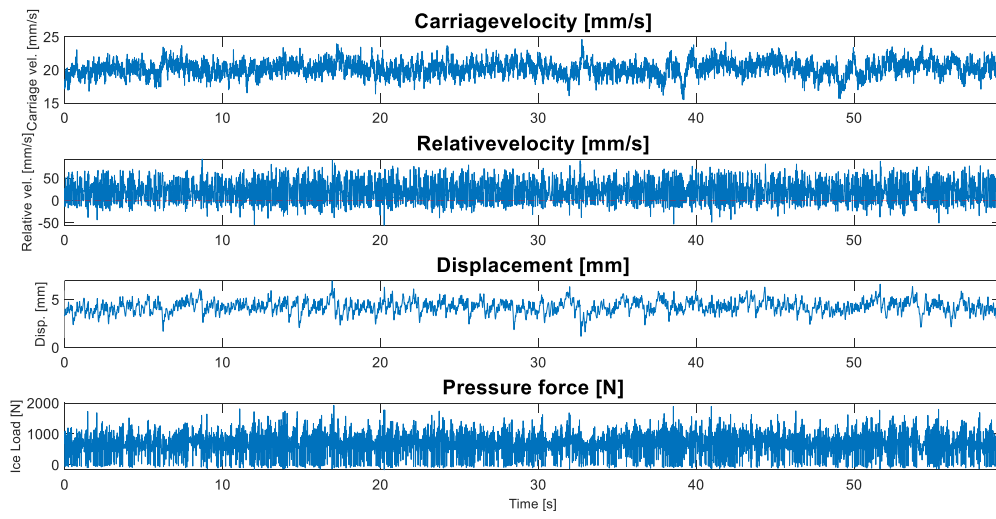
Test: SDOF-3. Fn: 1 Hz. V = 60 mm/s



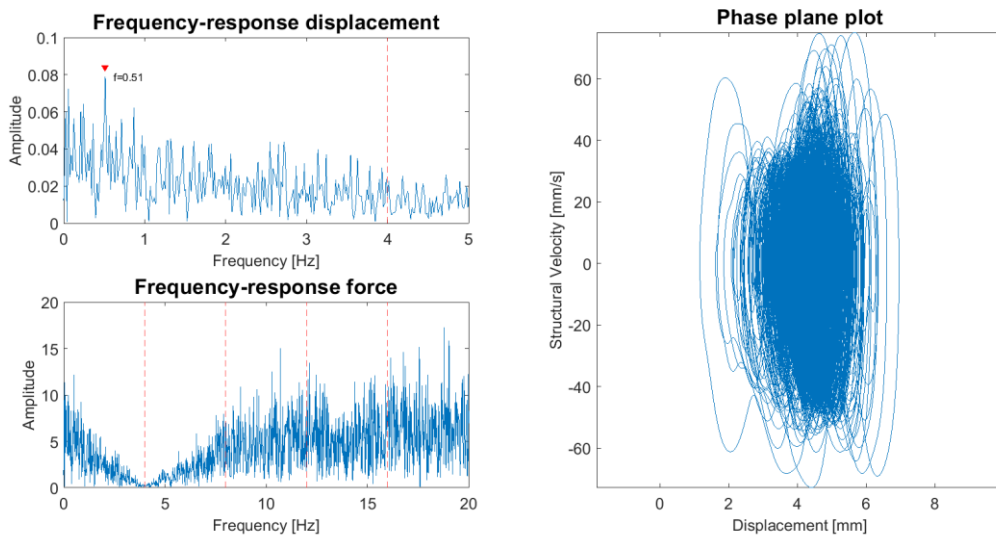
Test: SDOF-3. Fn: 1 Hz. V = 60 mm/s



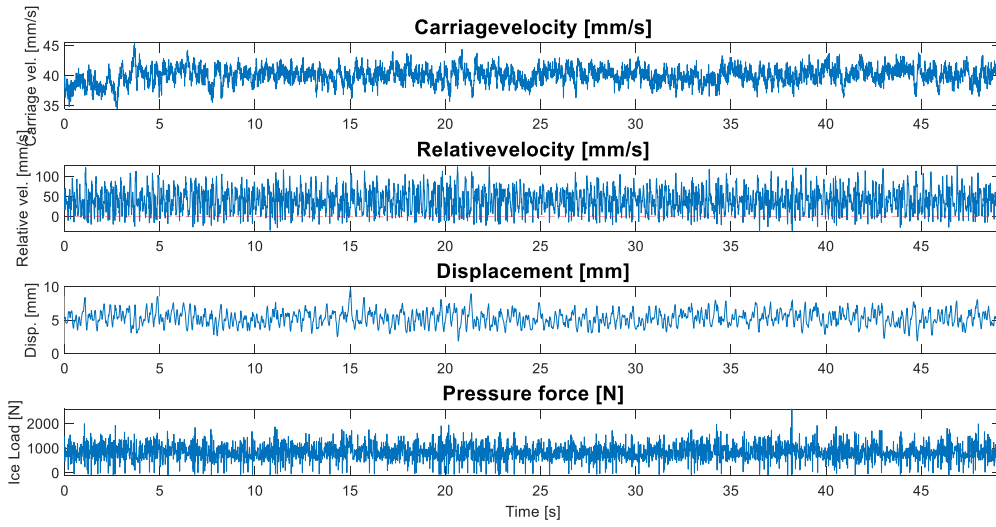
Test: SDOF-4. Fn: 4 Hz. V = 20 mm/s



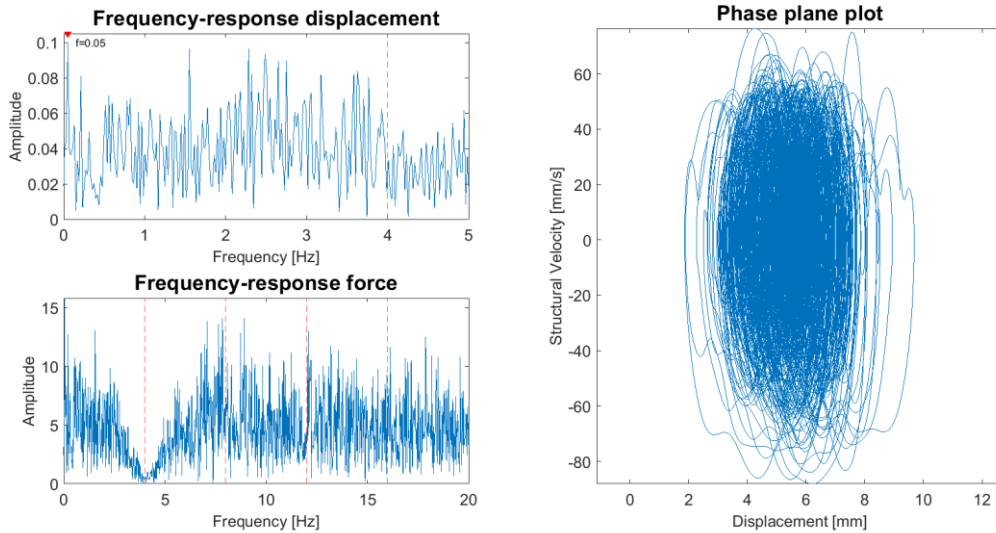
Test: SDOF-4. Fn: 4 Hz. V = 20 mm/s



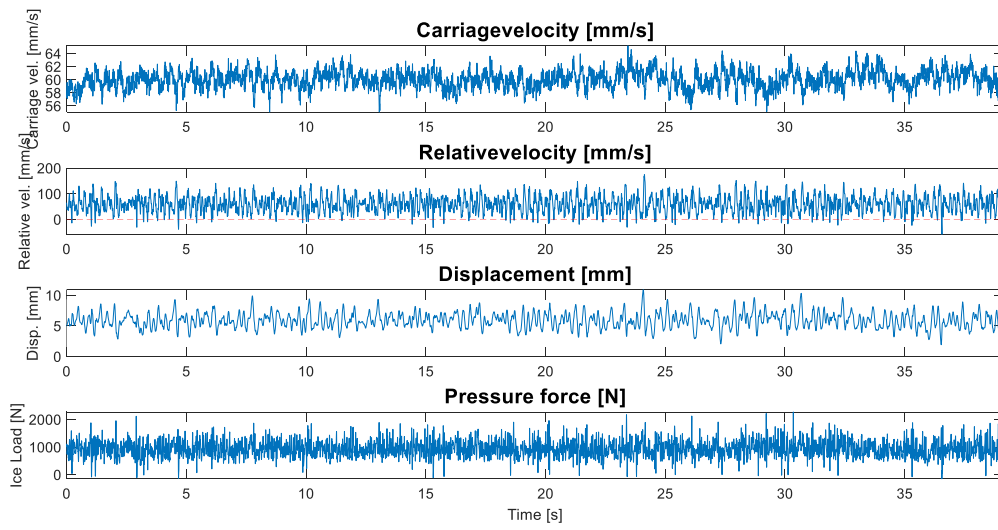
Test: SDOF-4. Fn: 4 Hz. V = 40 mm/s



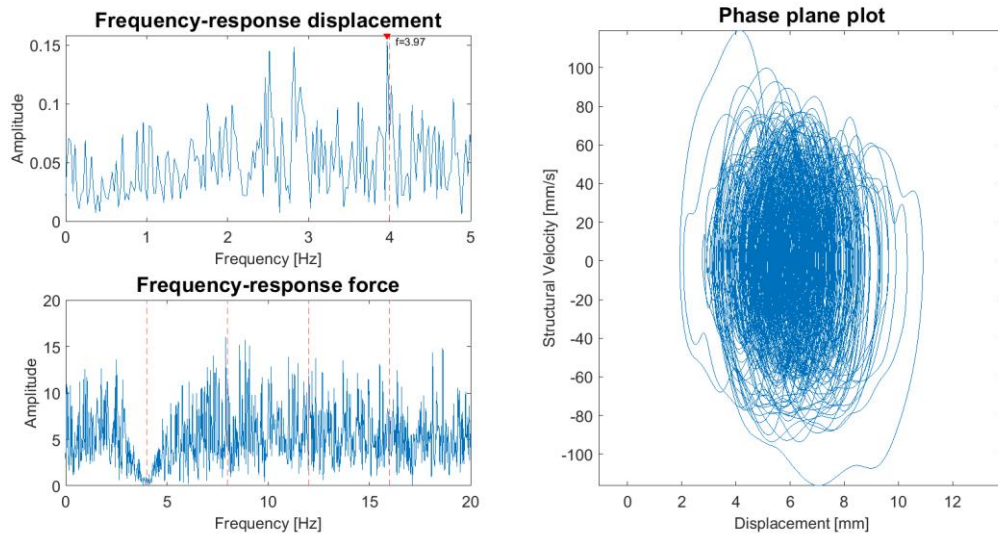
Test: SDOF-4. Fn: 4 Hz. V = 40 mm/s



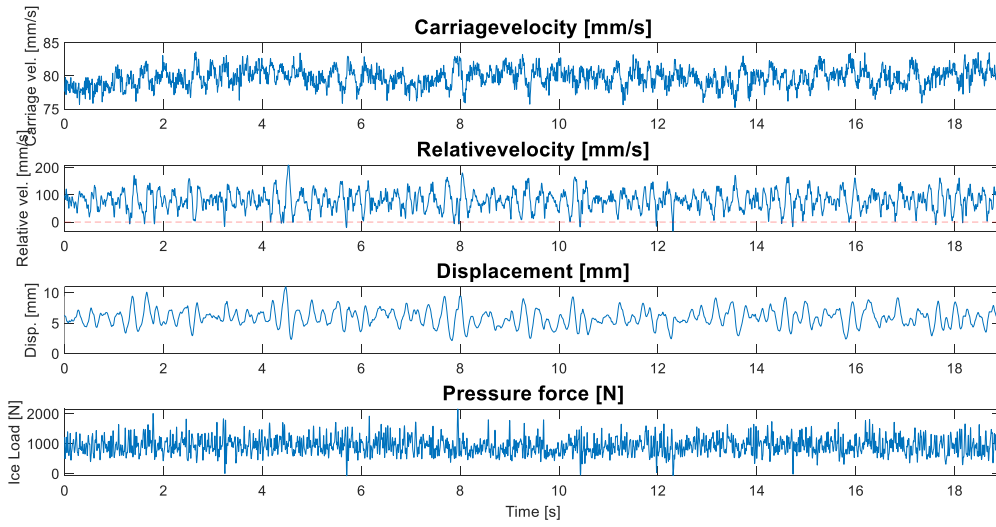
Test: SDOF-4. Fn: 4 Hz. V = 60 mm/s



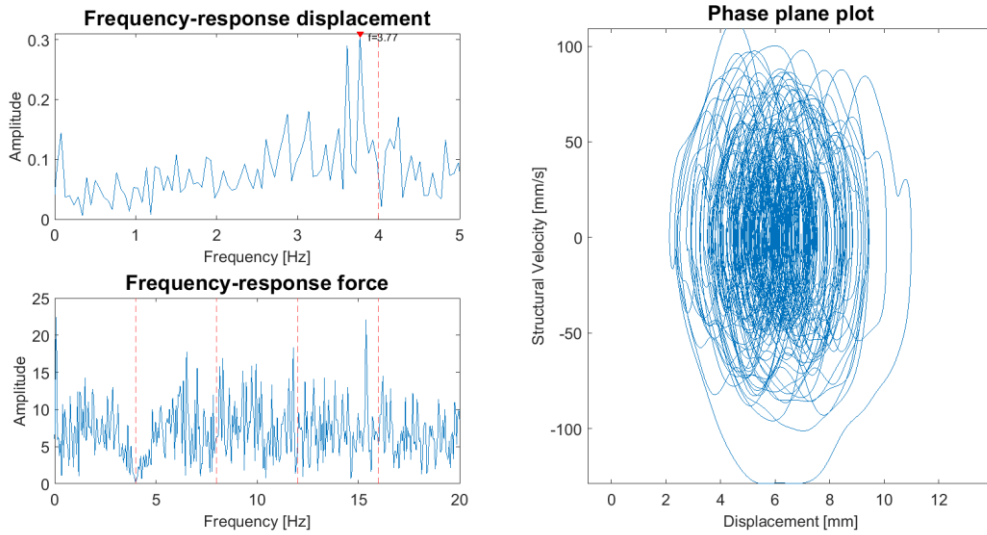
Test: SDOF-4. Fn: 4 Hz. V = 60 mm/s



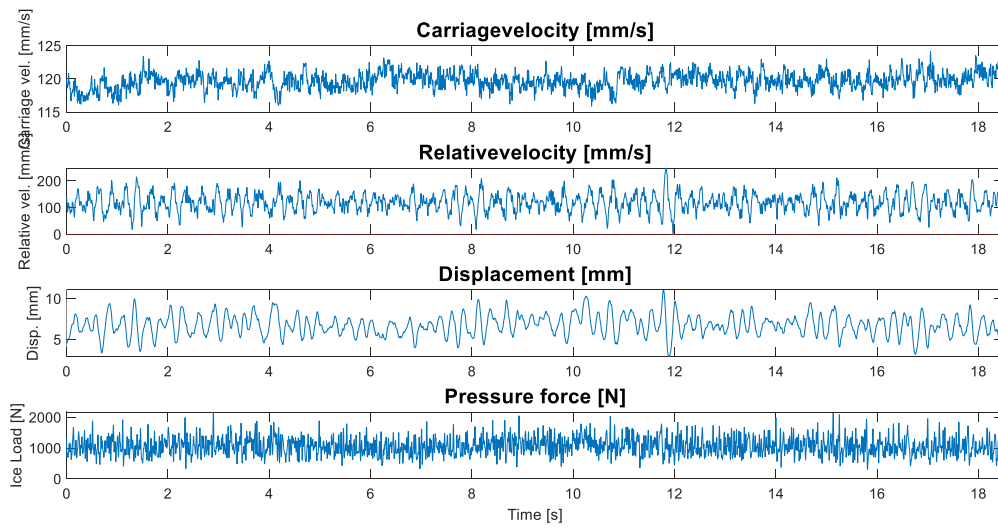
Test: SDOF-4. Fn: 4 Hz. V = 80 mm/s



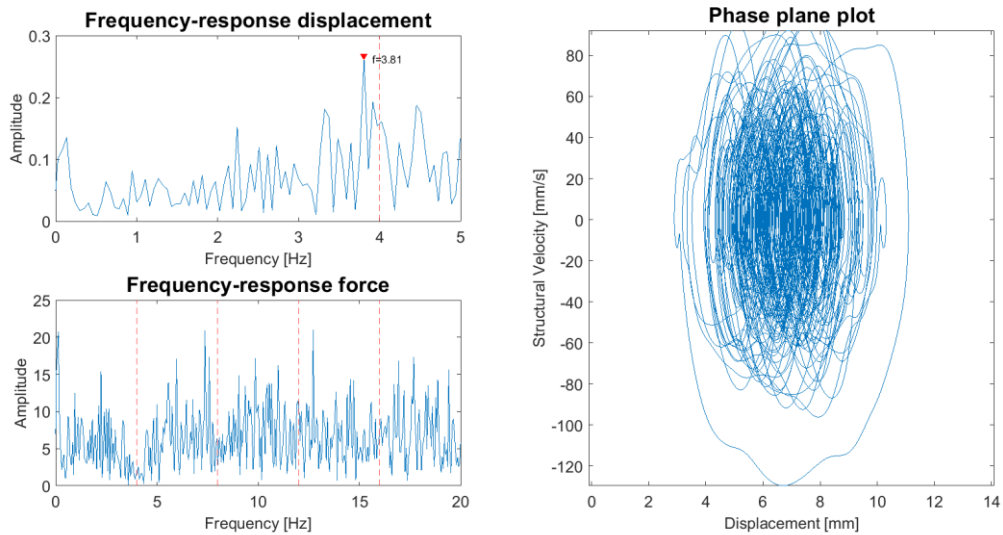
Test: SDOF-4. Fn: 4 Hz. V = 80 mm/s



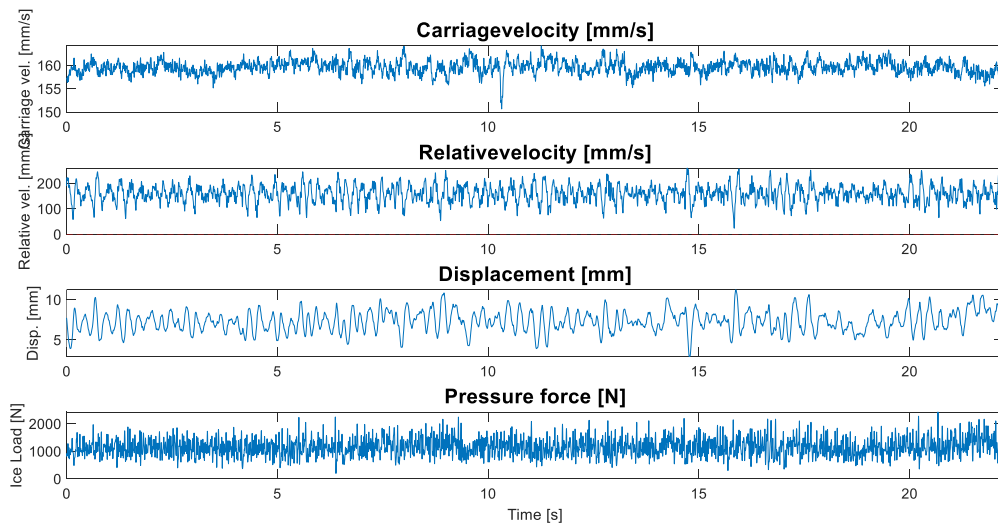
Test: SDOF-4. Fn: 4 Hz. V = 120 mm/s



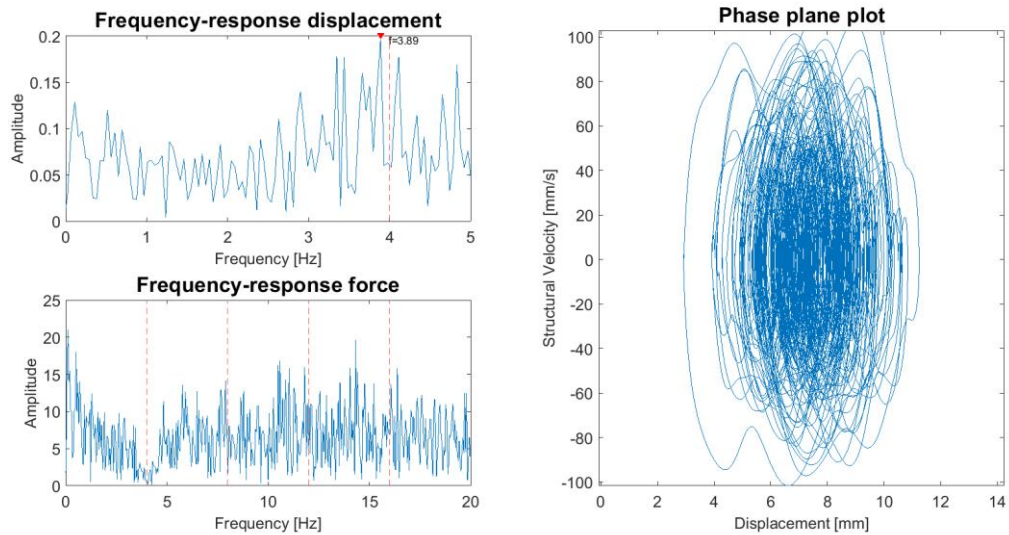
Test: SDOF-4. Fn: 4 Hz. V = 120 mm/s



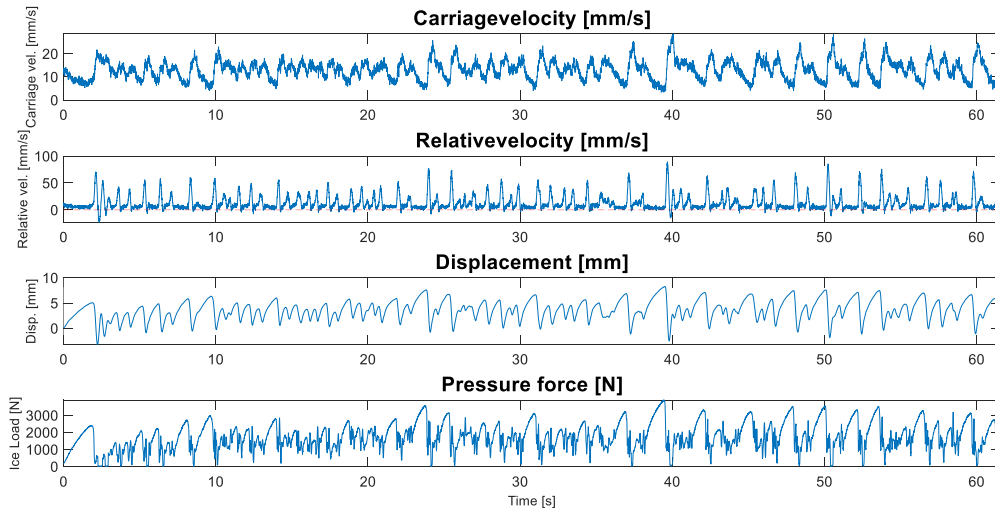
Test: SDOF-4. Fn: 4 Hz. V = 160 mm/s



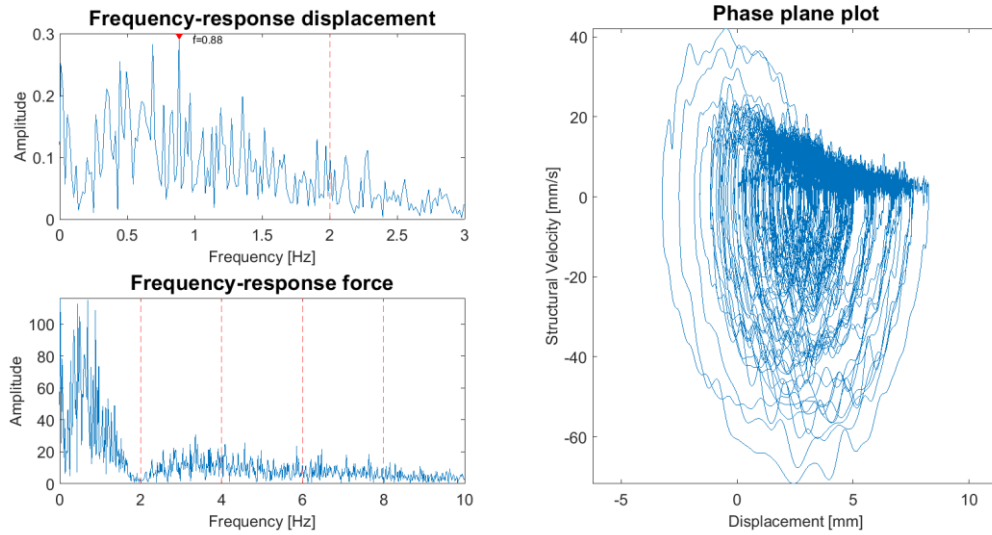
Test: SDOF-4. Fn: 4 Hz. V = 160 mm/s



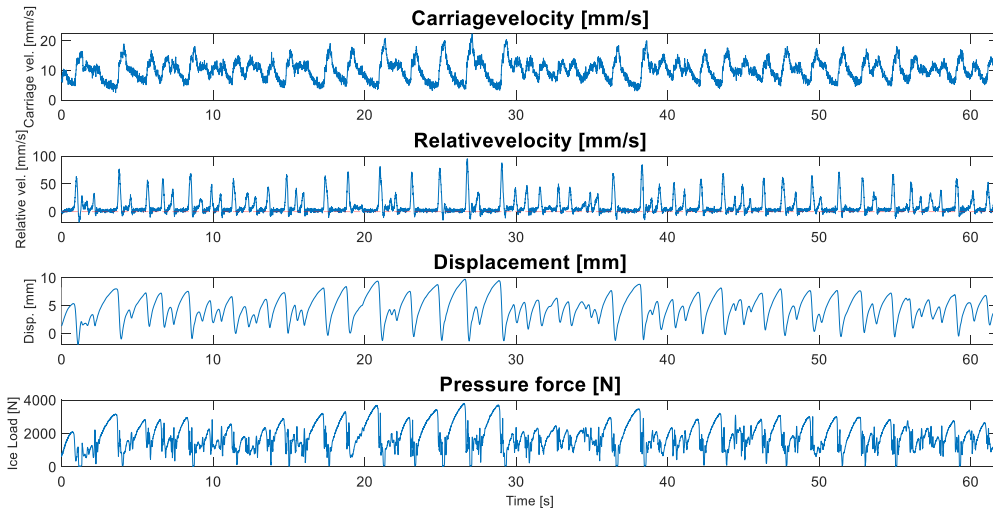
Test: SDOF-5. Fn: 2 Hz. V = 10 mm/s



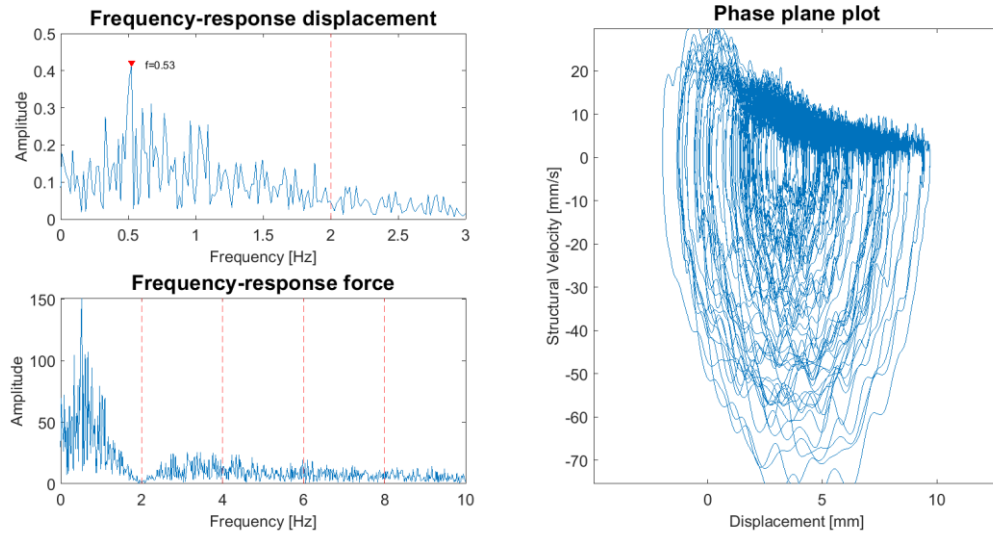
Test: SDOF-5. Fn: 2 Hz. V = 10 mm/s



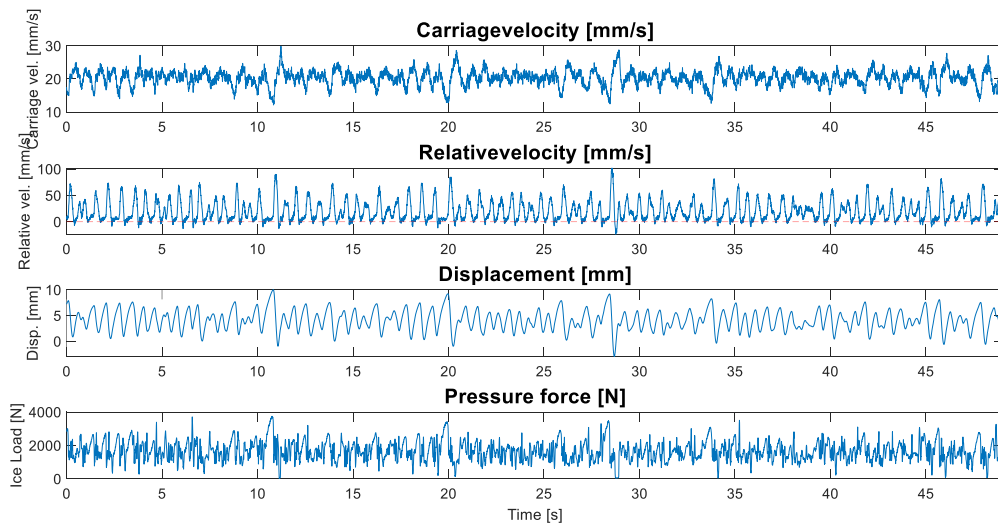
Test: SDOF-6. Fn: 2 Hz. V = 10 mm/s



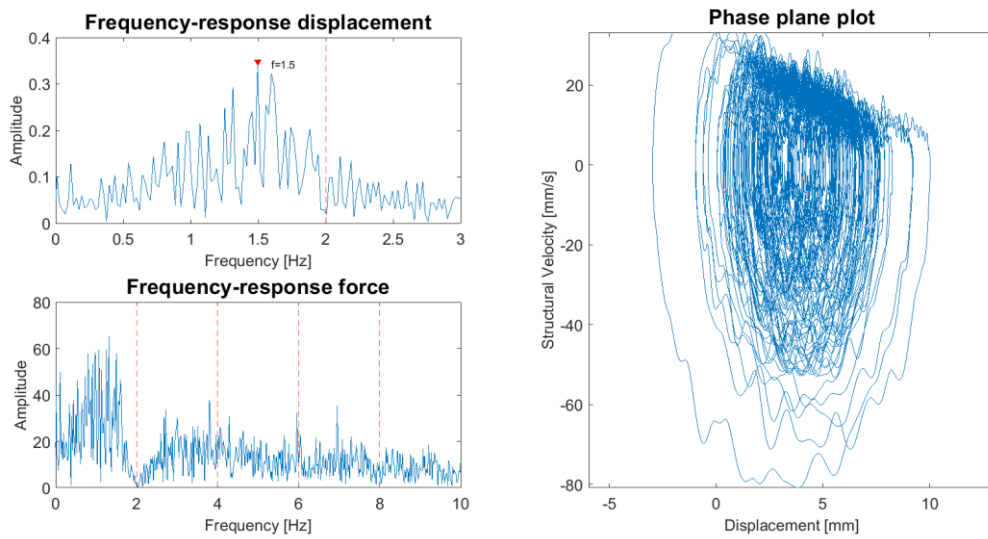
Test: SDOF-6. Fn: 2 Hz. V = 10 mm/s



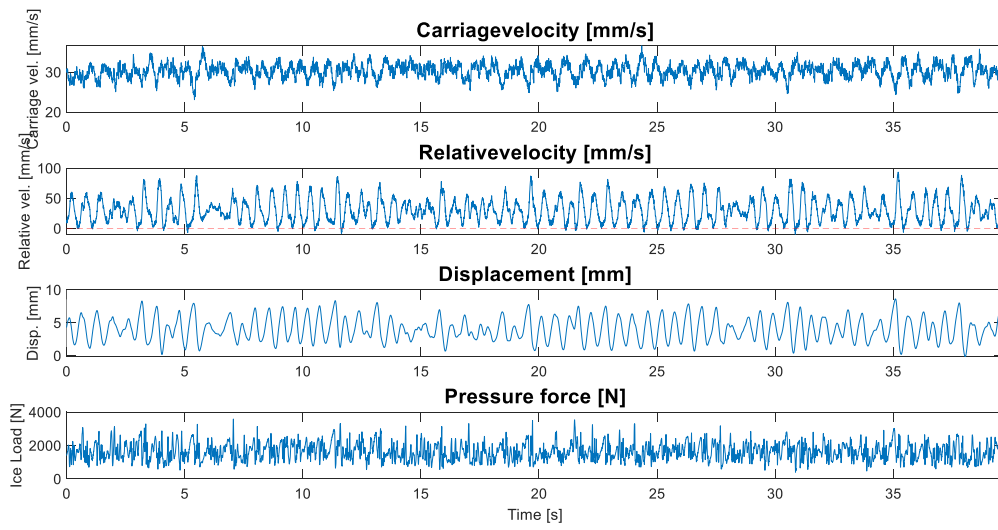
Test: SDOF-6. Fn: 2 Hz. V = 20 mm/s



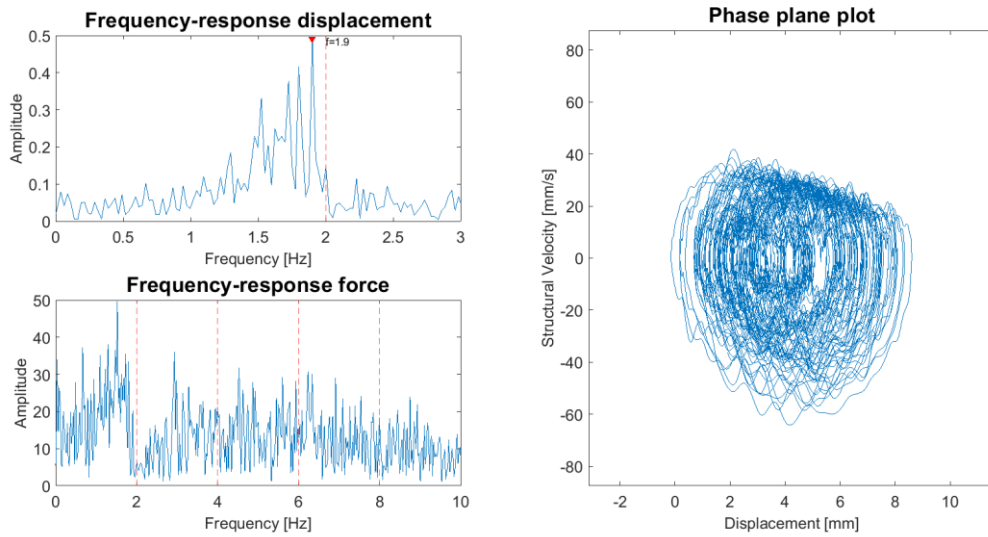
Test: SDOF-6. Fn: 2 Hz. V = 20 mm/s



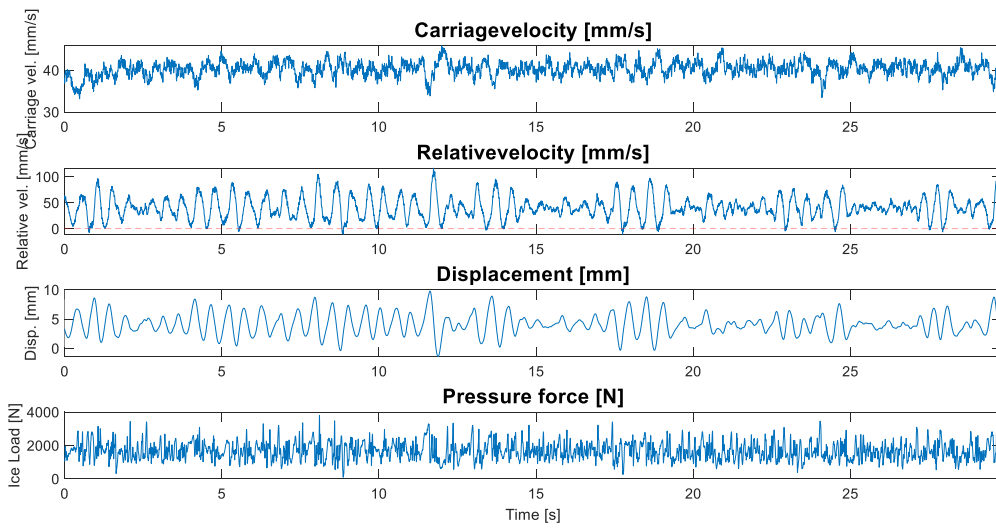
Test: SDOF-6. Fn: 2 Hz. V = 30 mm/s



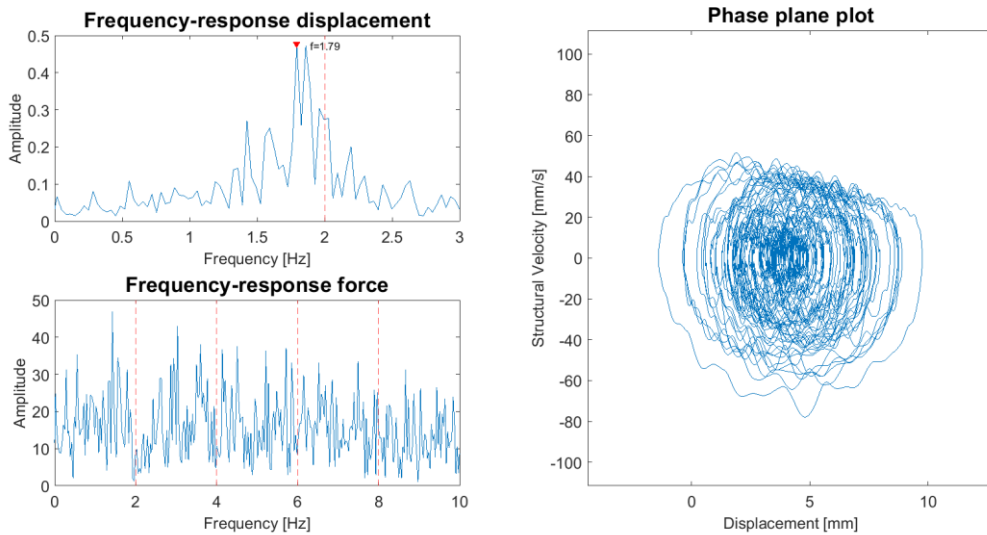
Test: SDOF-6. Fn: 2 Hz. V = 30 mm/s



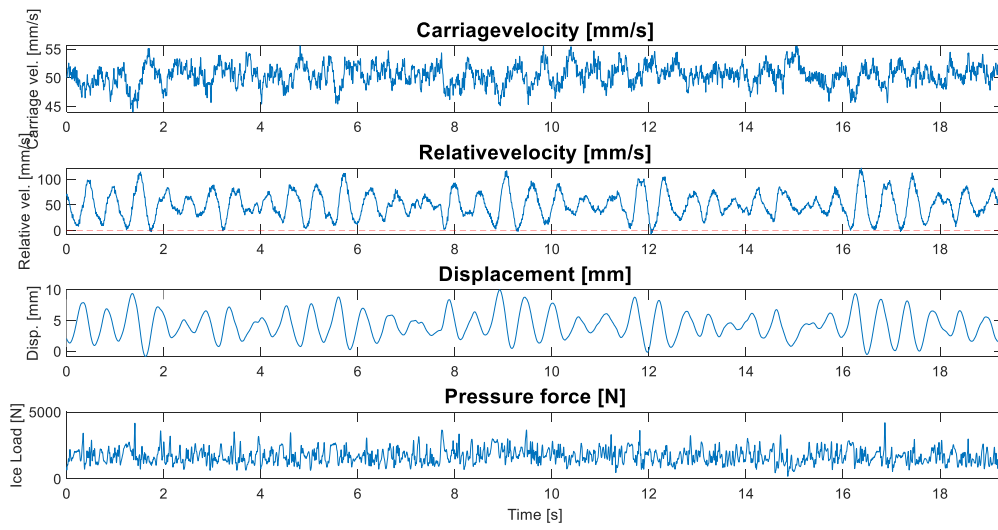
Test: SDOF-6. Fn: 2 Hz. V = 40 mm/s



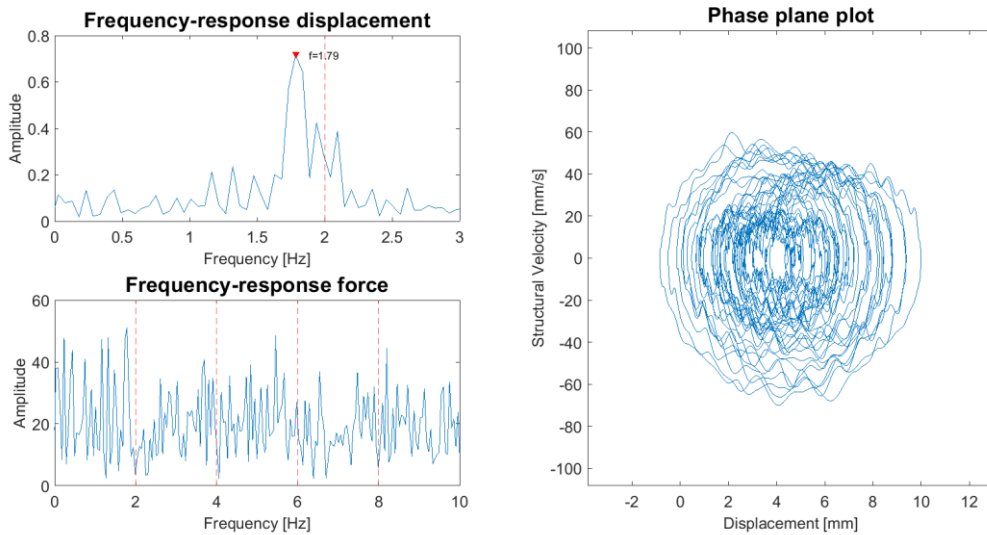
Test: SDOF-6. Fn: 2 Hz. V = 40 mm/s



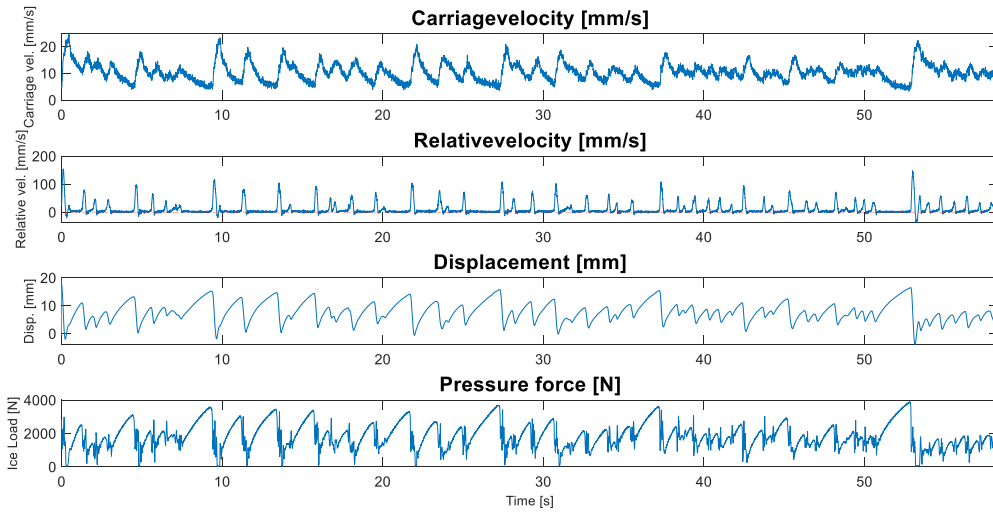
Test: SDOF-6. Fn: 2 Hz. V = 50 mm/s



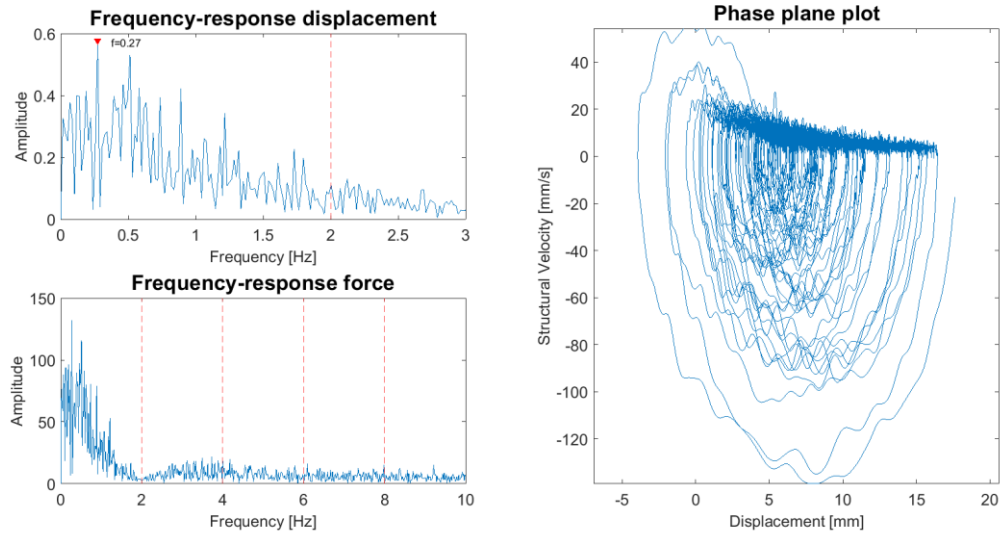
Test: SDOF-6. Fn: 2 Hz. V = 50 mm/s



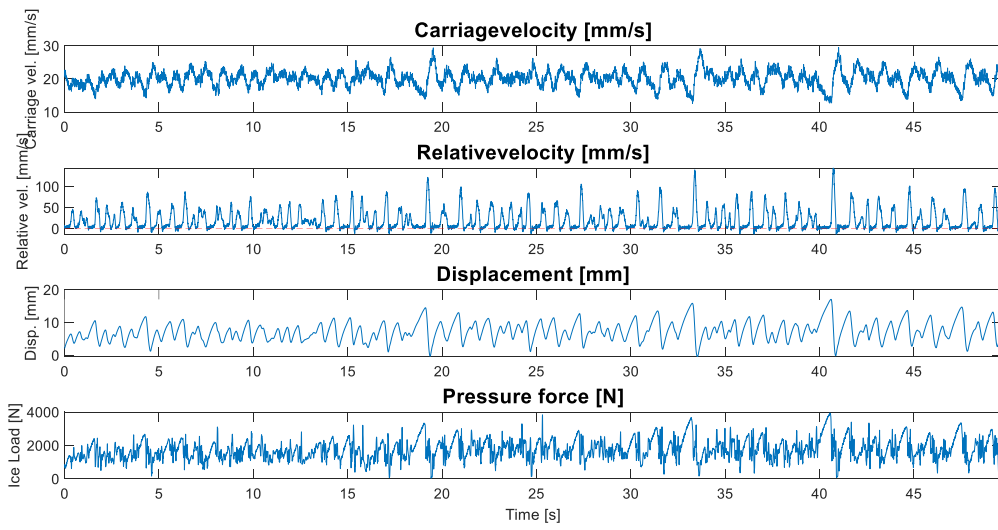
Test: SDOF-7. Fn: 2 Hz. V = 10 mm/s



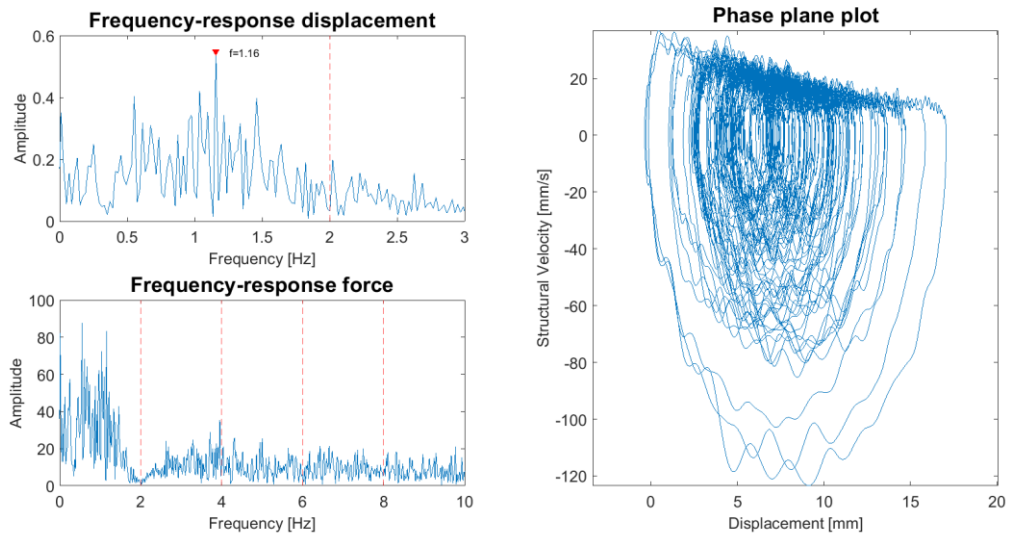
Test: SDOF-7. Fn: 2 Hz. V = 10 mm/s



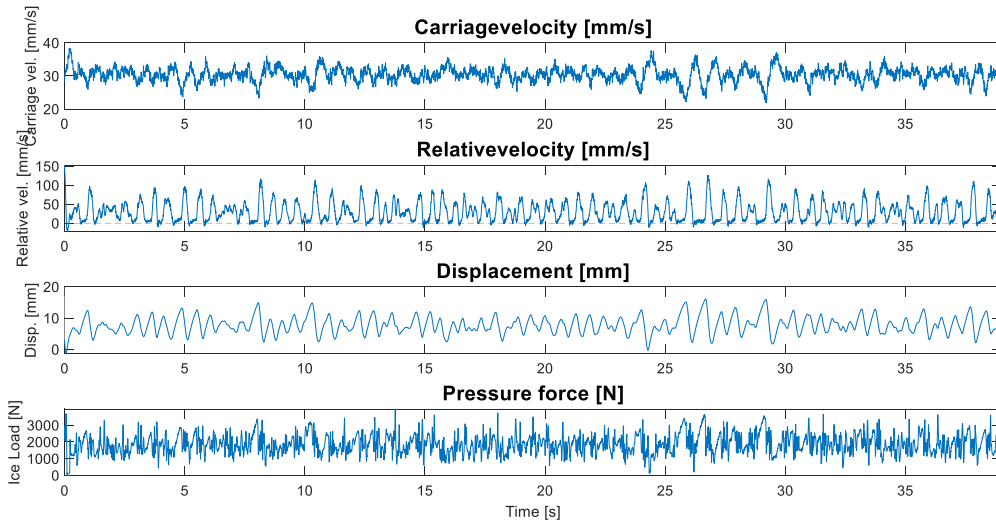
Test: SDOF-7. Fn: 2 Hz. V = 20 mm/s



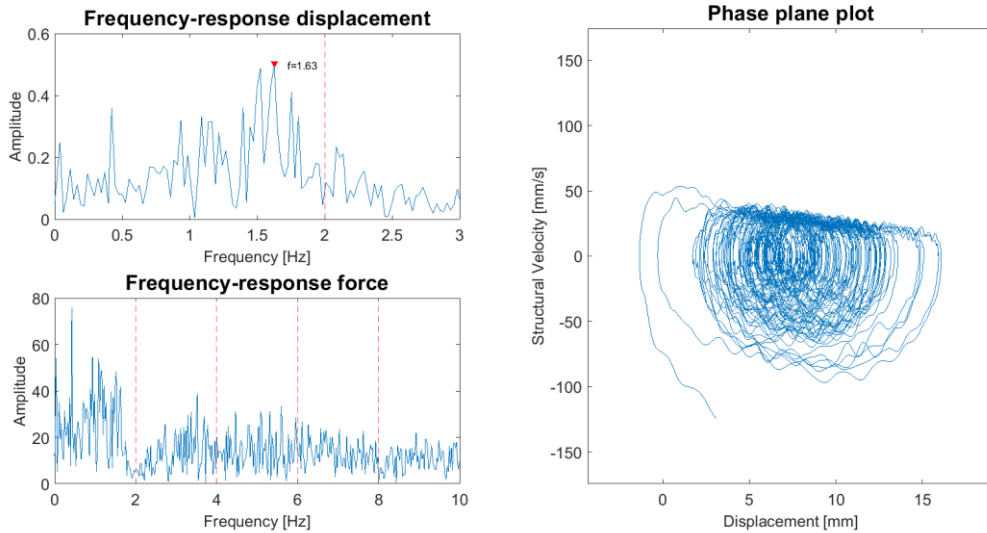
Test: SDOF-7. Fn: 2 Hz. V = 20 mm/s



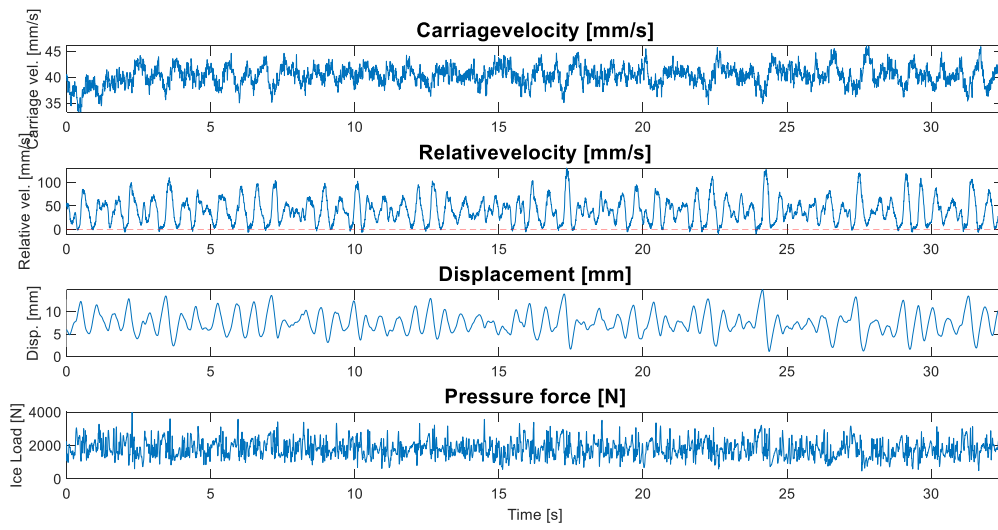
Test: SDOF-7. Fn: 2 Hz. V = 30 mm/s



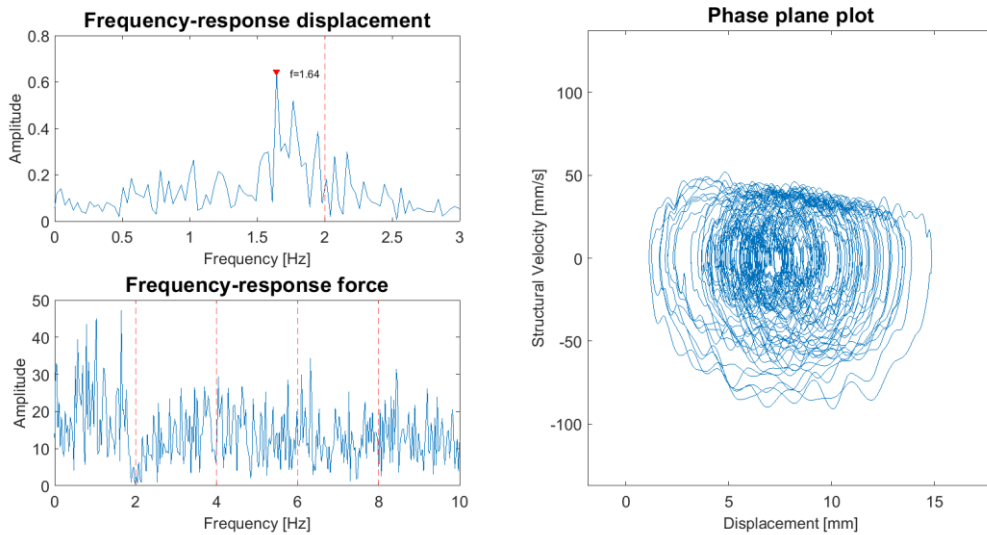
Test: SDOF-7. Fn: 2 Hz. V = 30 mm/s



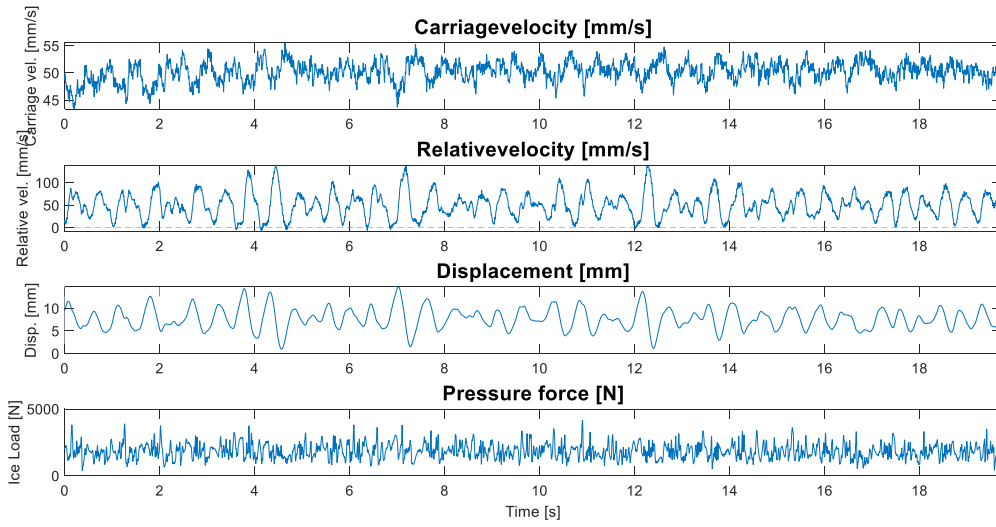
Test: SDOF-7. Fn: 2 Hz. V = 40 mm/s



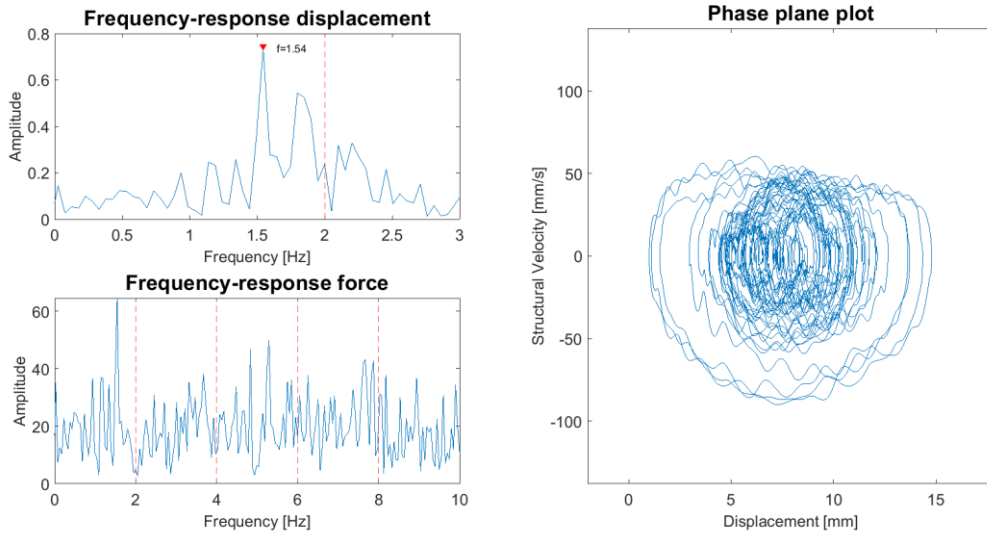
Test: SDOF-7. Fn: 2 Hz. V = 40 mm/s



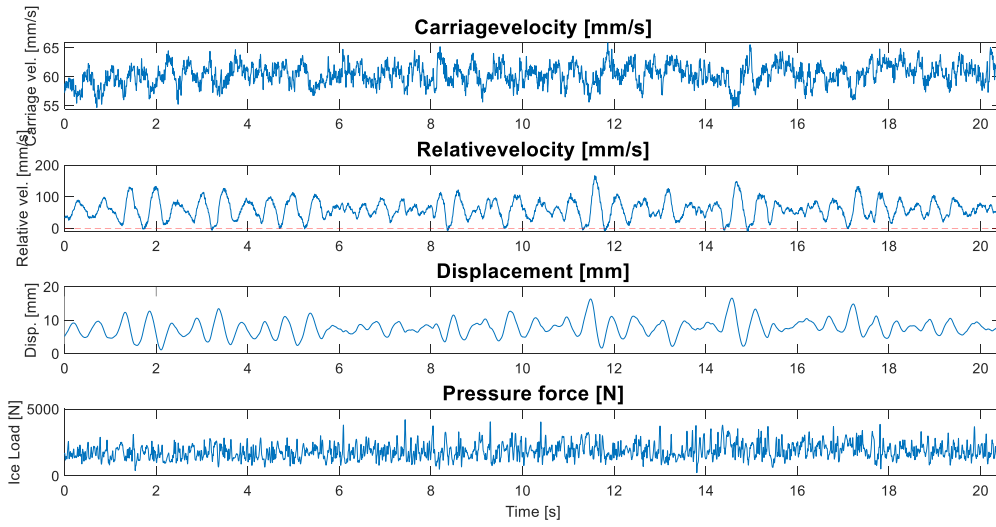
Test: SDOF-7. Fn: 2 Hz. V = 50 mm/s



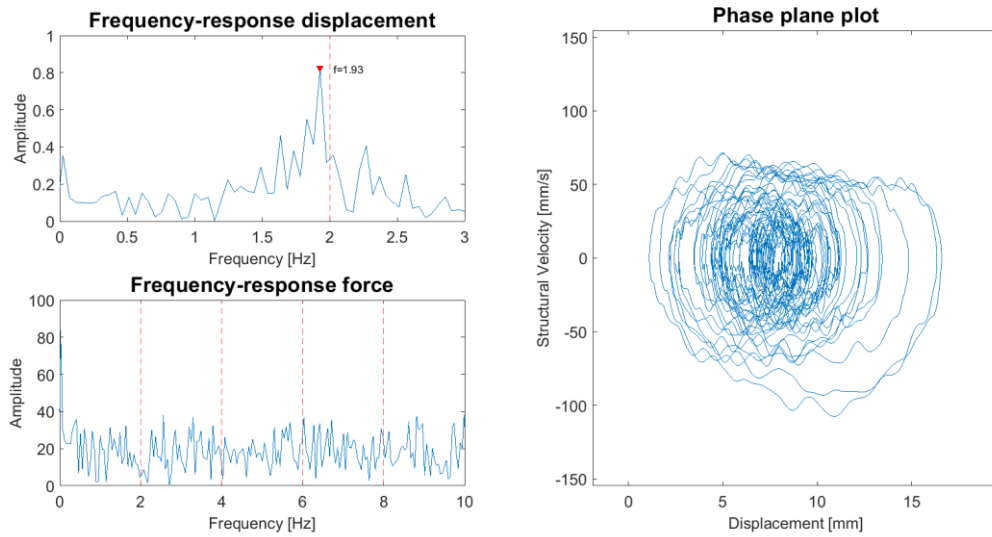
Test: SDOF-7. Fn: 2 Hz. V = 50 mm/s



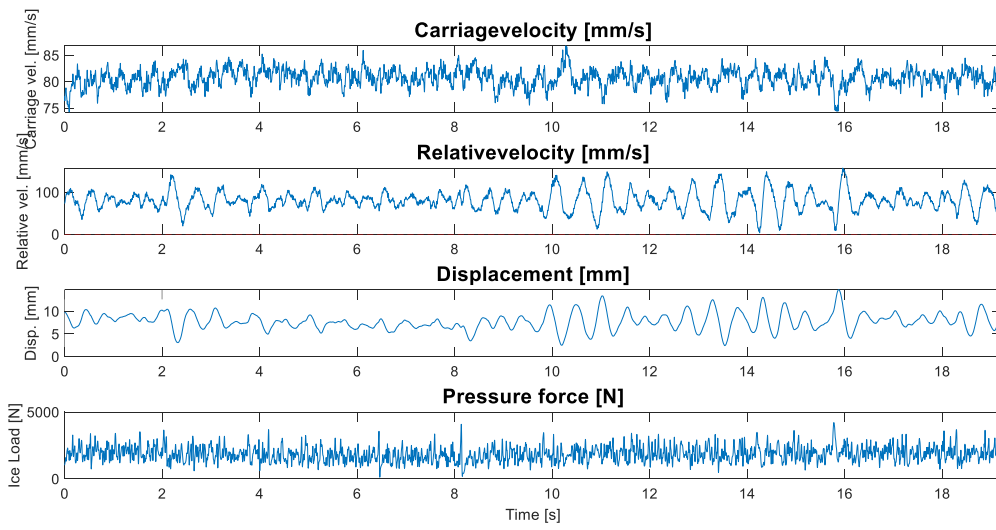
Test: SDOF-7. Fn: 2 Hz. V = 60 mm/s



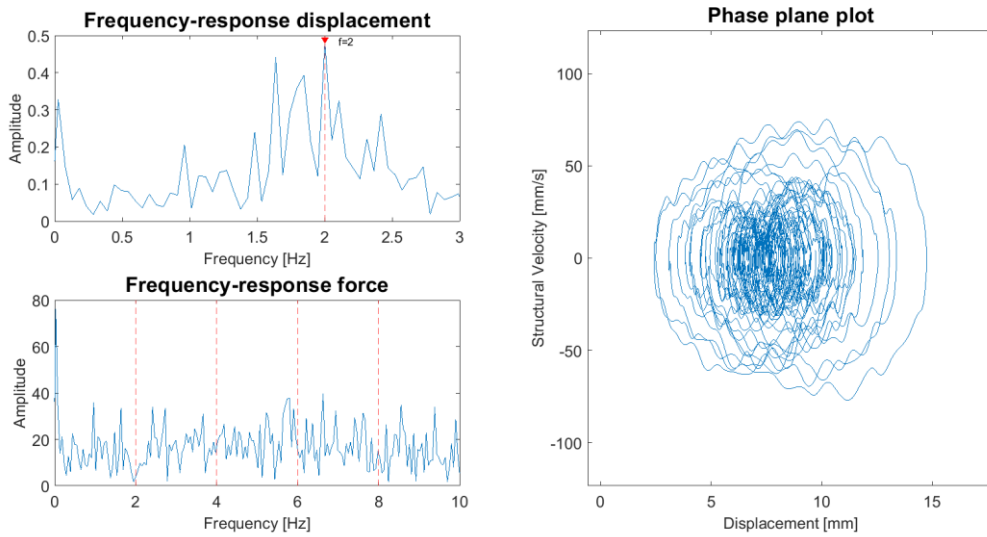
Test: SDOF-7. Fn: 2 Hz. V = 60 mm/s



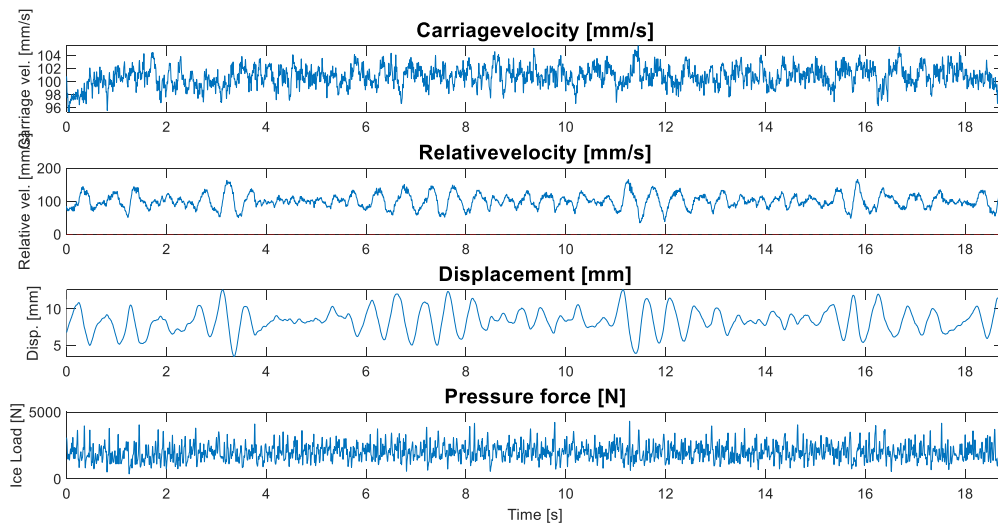
Test: SDOF-7. Fn: 2 Hz. V = 80 mm/s



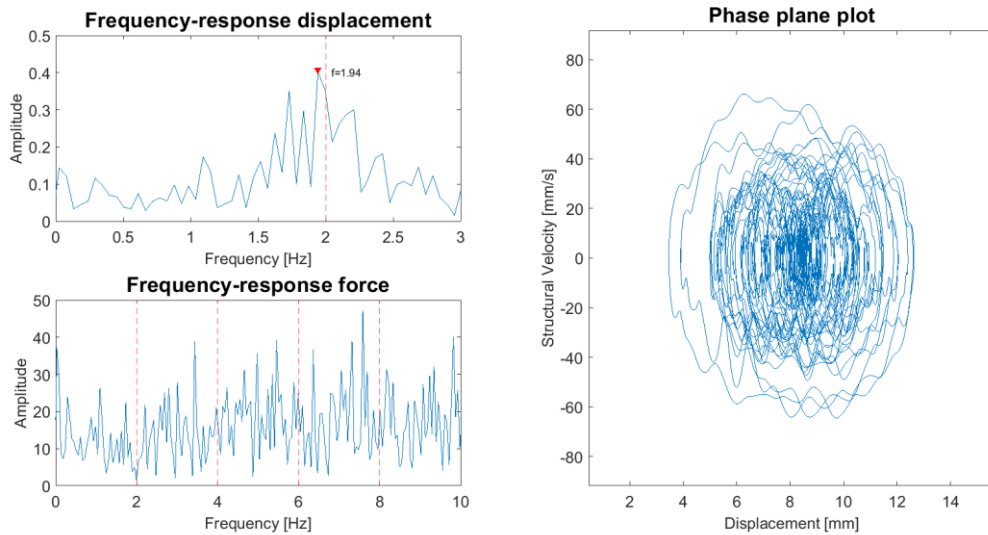
Test: SDOF-7. Fn: 2 Hz. V = 80 mm/s



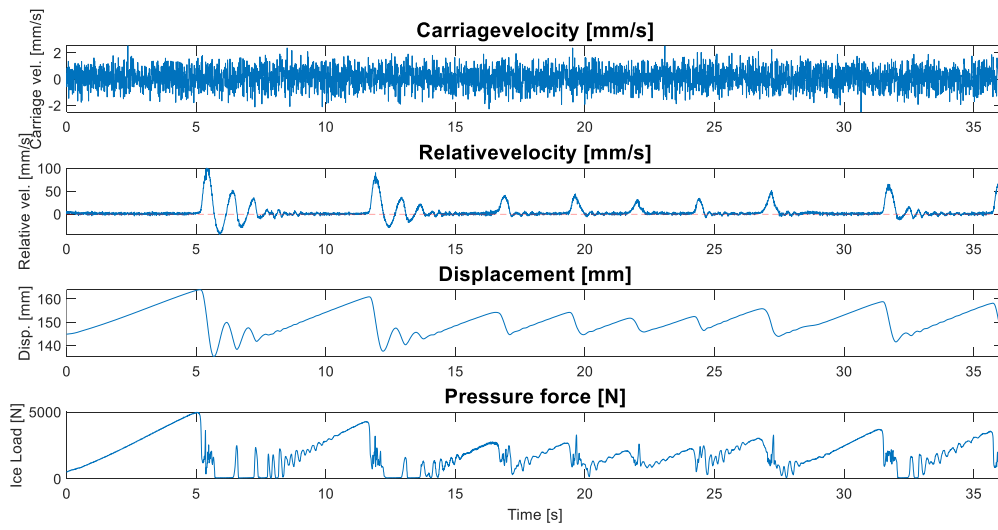
Test: SDOF-7. Fn: 2 Hz. V = 100 mm/s



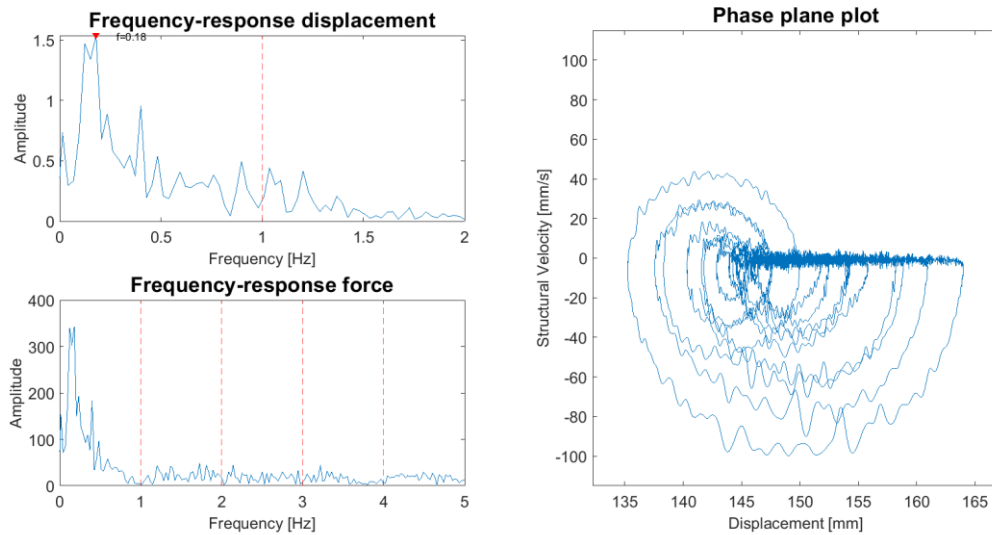
Test: SDOF-7. Fn: 2 Hz. V = 100 mm/s



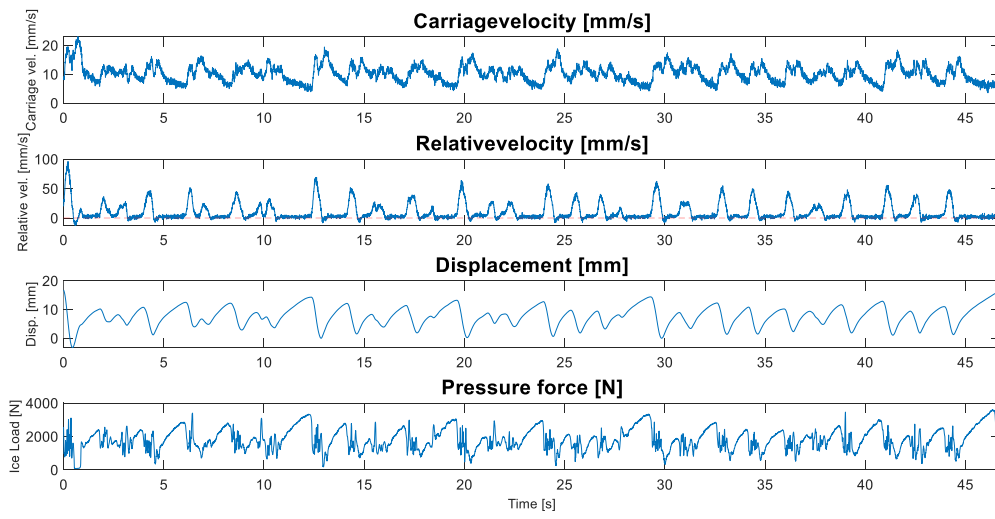
Test: SDOF-8. Fn: 1 Hz. V = 5 mm/s



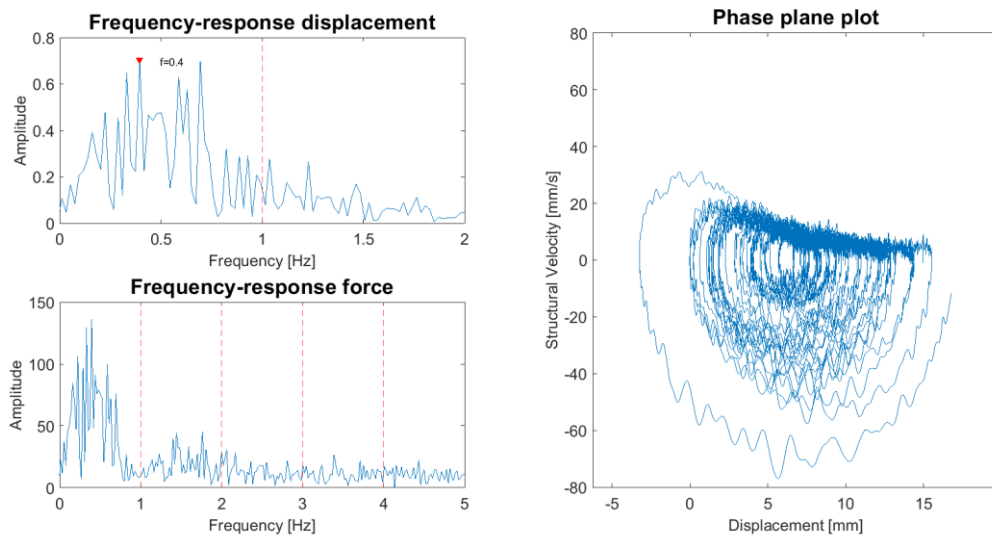
Test: SDOF-8. Fn: 1 Hz. V = 5 mm/s



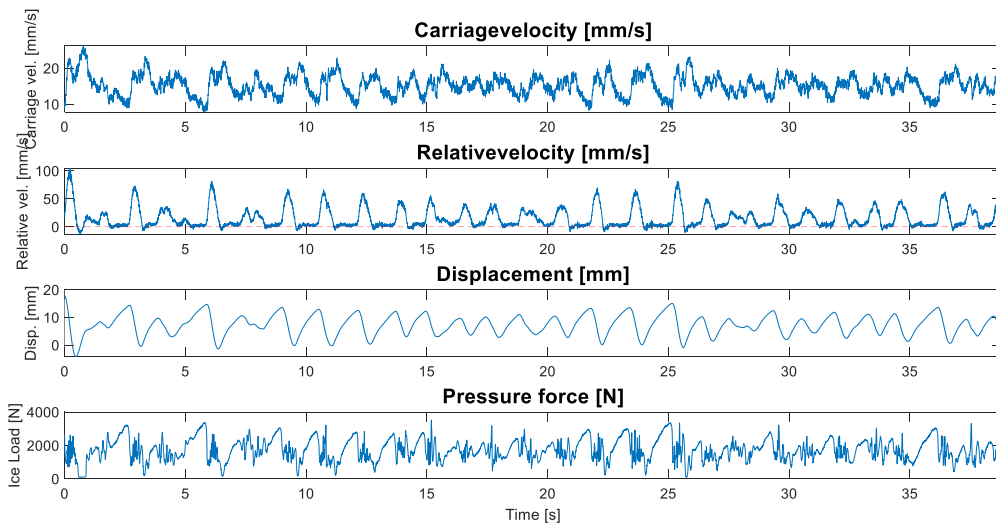
Test: SDOF-8. Fn: 1 Hz. V = 10 mm/s



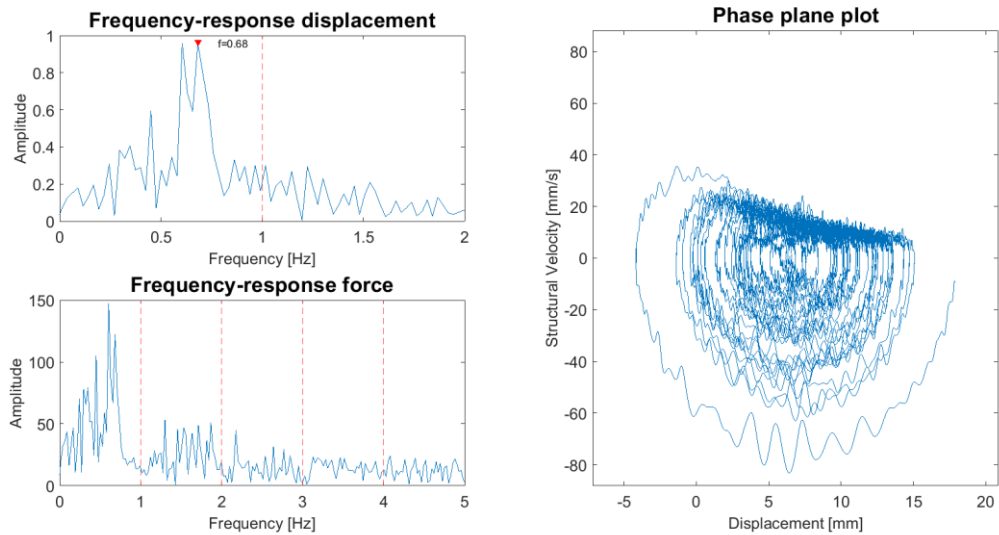
Test: SDOF-8. Fn: 1 Hz. V = 10 mm/s



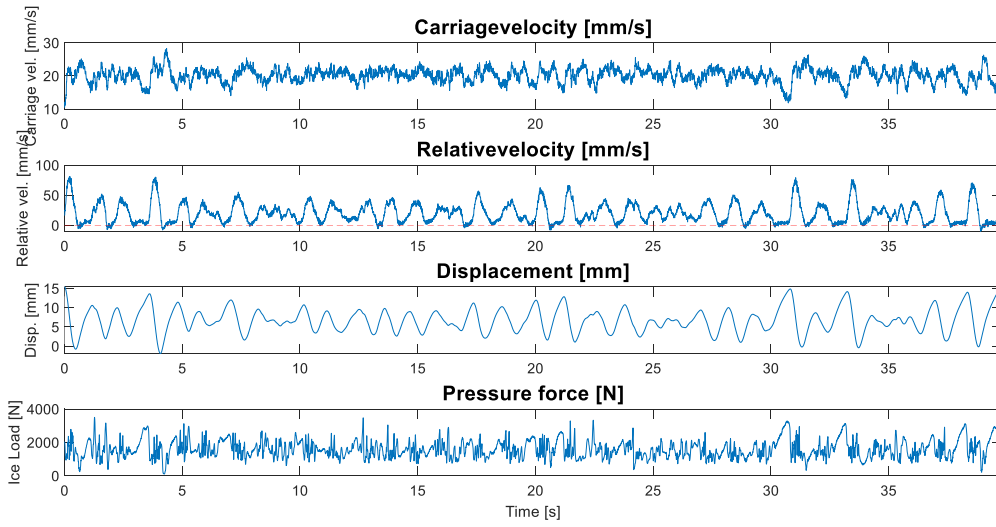
Test: SDOF-8. Fn: 1 Hz. V = 15 mm/s



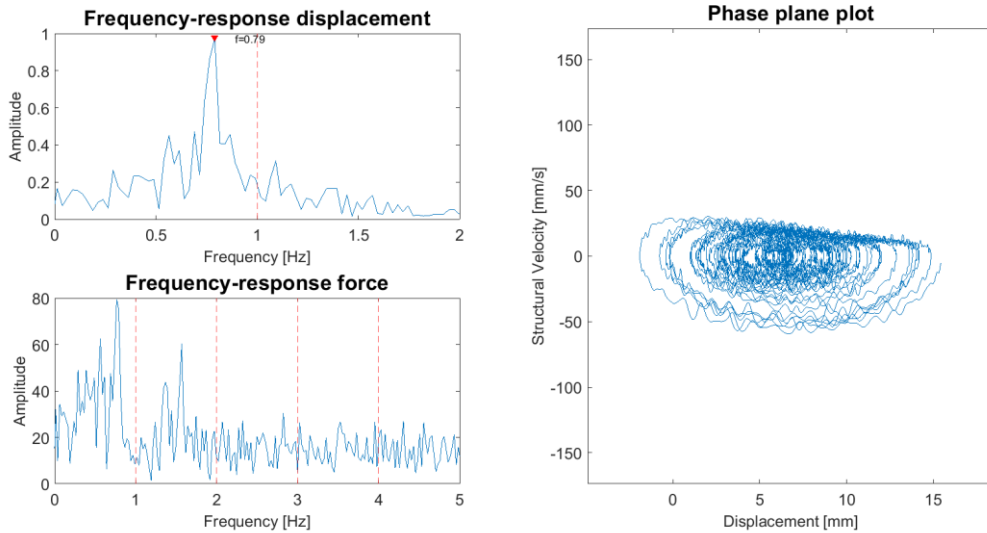
Test: SDOF-8. Fn: 1 Hz. V = 15 mm/s



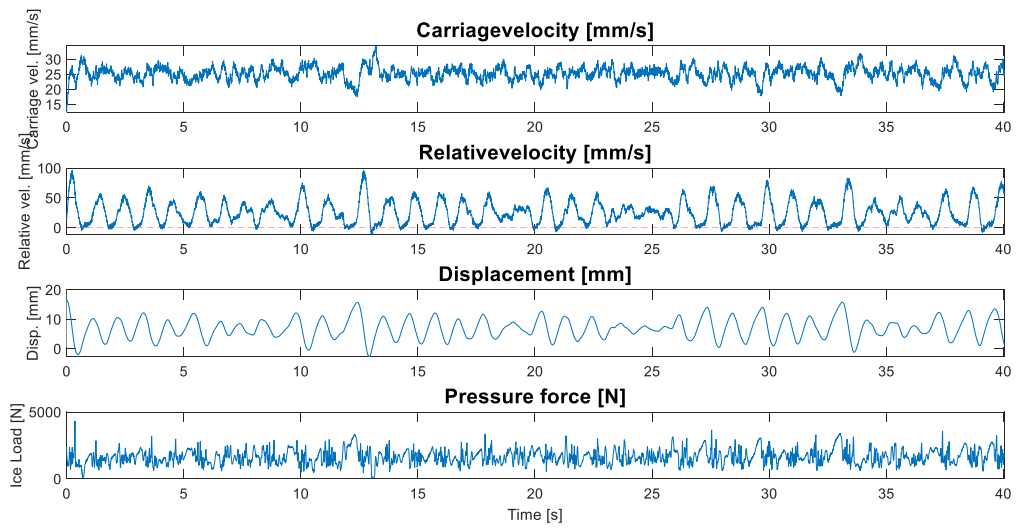
Test: SDOF-8. Fn: 1 Hz. V = 20 mm/s



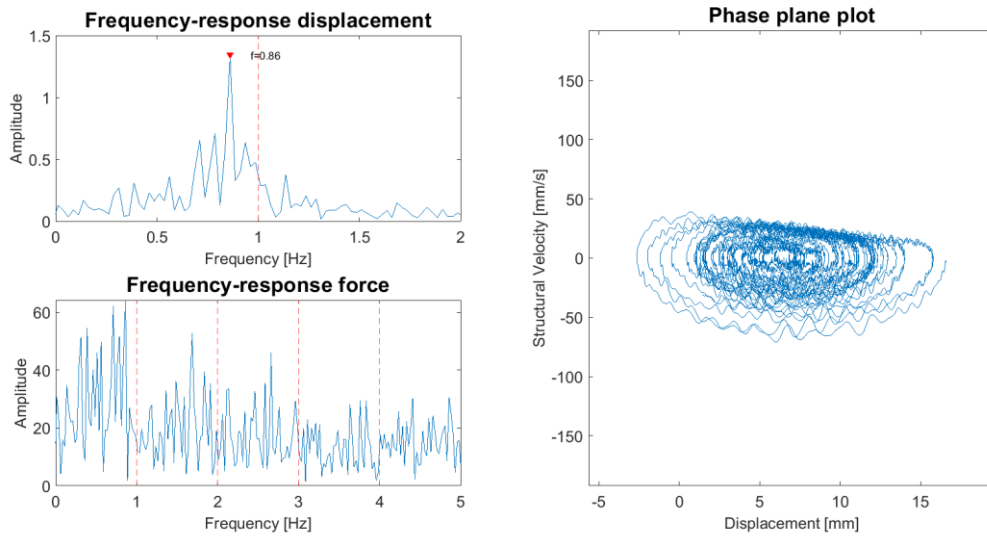
Test: SDOF-8. Fn: 1 Hz. V = 20 mm/s



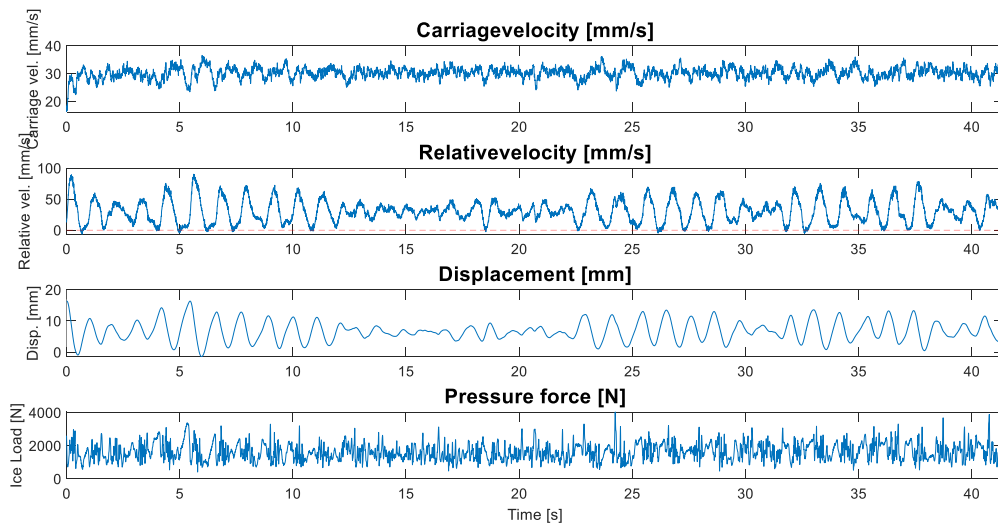
Test: SDOF-8. Fn: 1 Hz. V = 25 mm/s



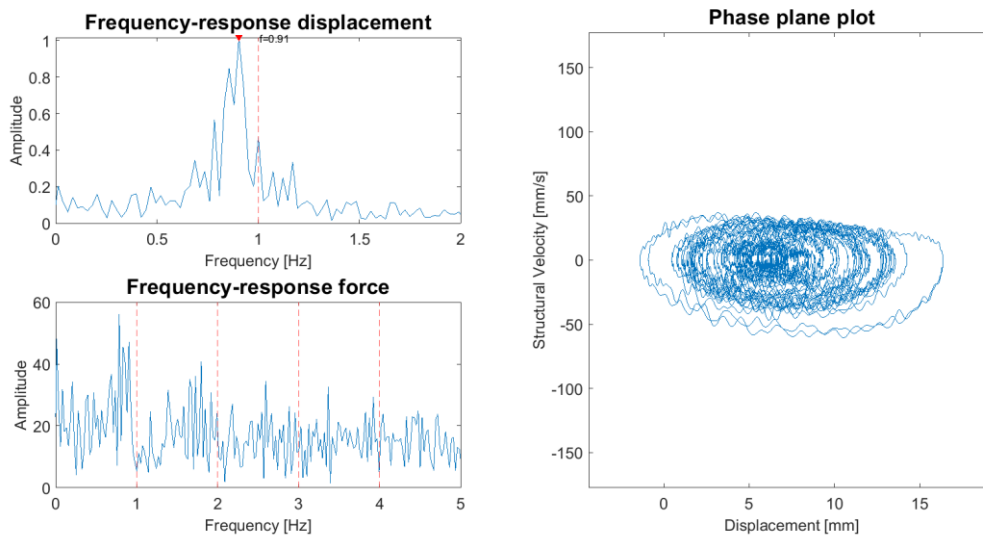
Test: SDOF-8. Fn: 1 Hz. V = 25 mm/s



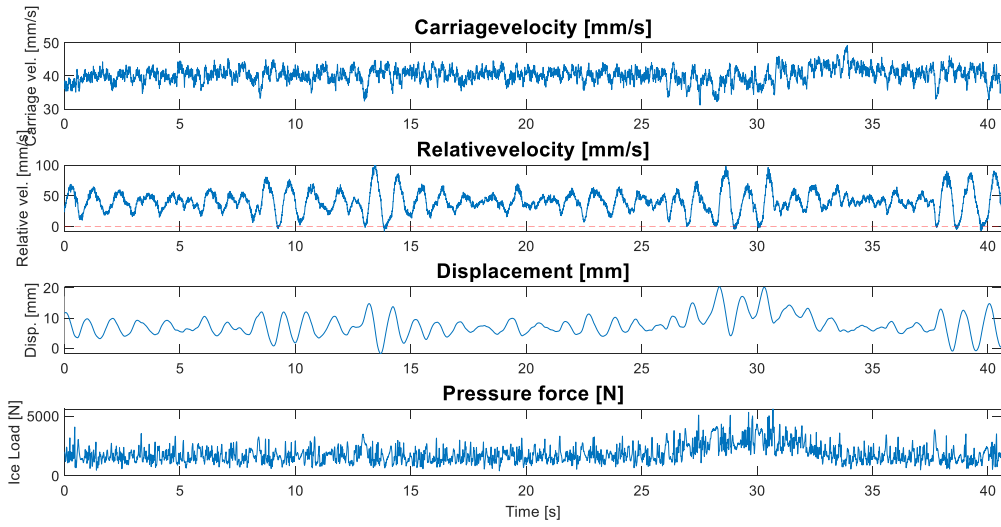
Test: SDOF-8. Fn: 1 Hz. V = 30 mm/s



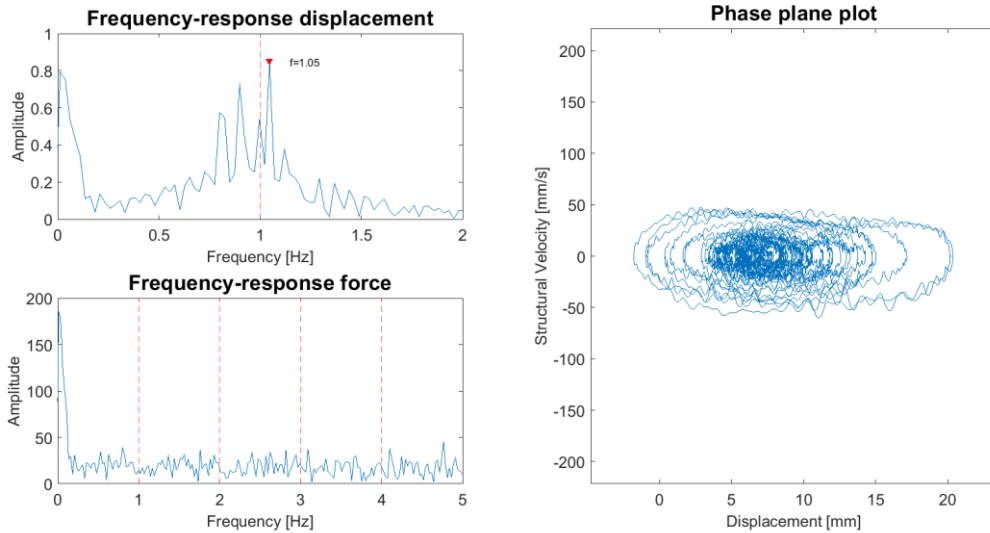
Test: SDOF-8. Fn: 1 Hz. V = 30 mm/s



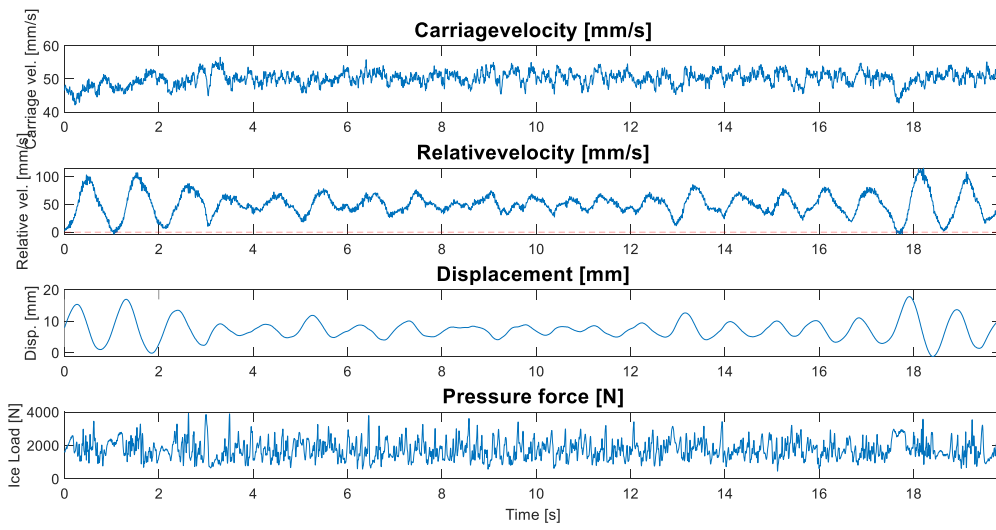
Test: SDOF-8. Fn: 1 Hz. V = 40 mm/s



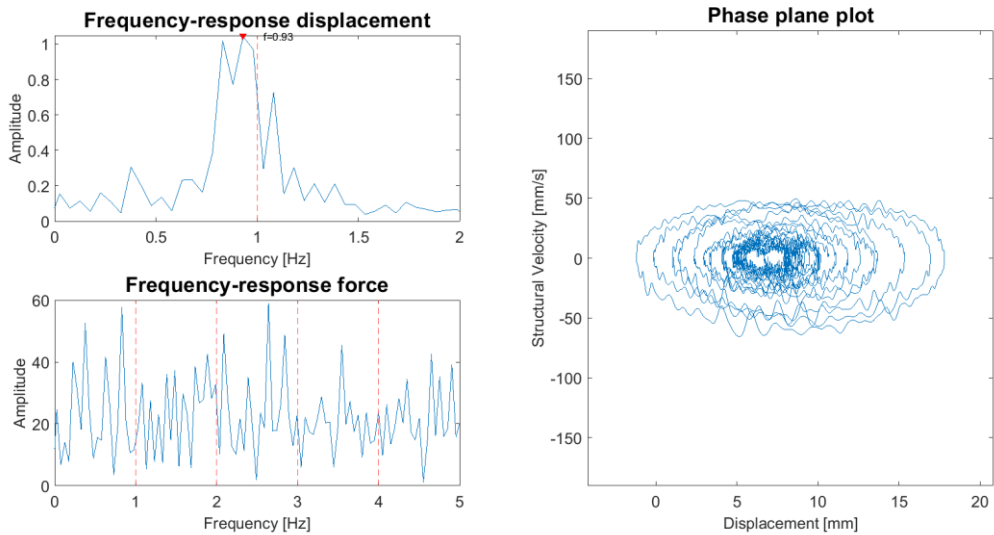
Test: SDOF-8. Fn: 1 Hz. V = 40 mm/s



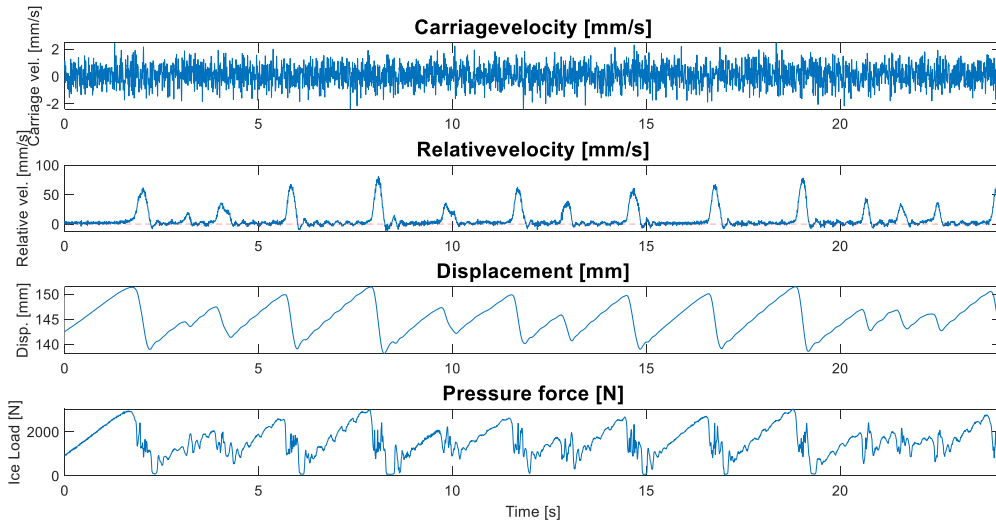
Test: SDOF-8. Fn: 1 Hz. V = 50 mm/s



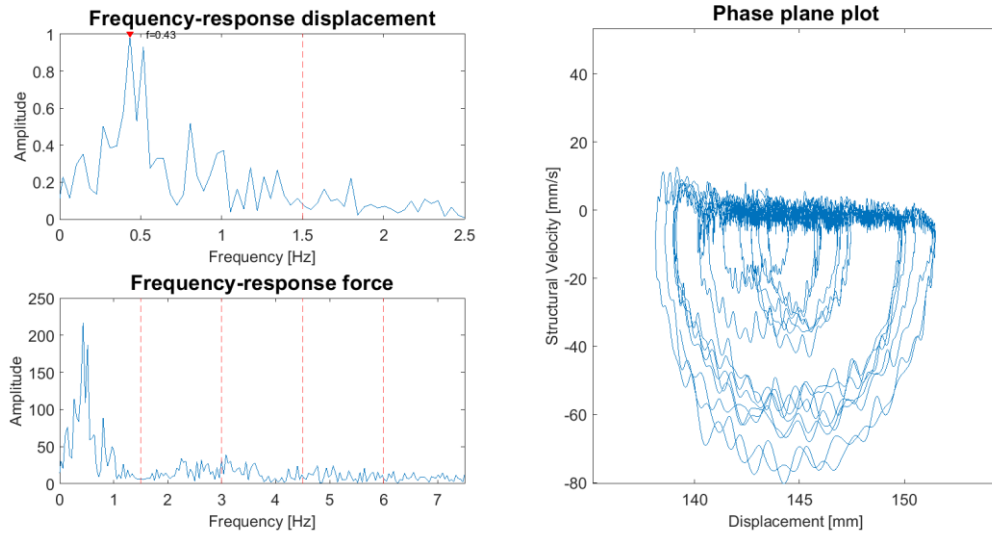
Test: SDOF-8. Fn: 1 Hz. V = 50 mm/s



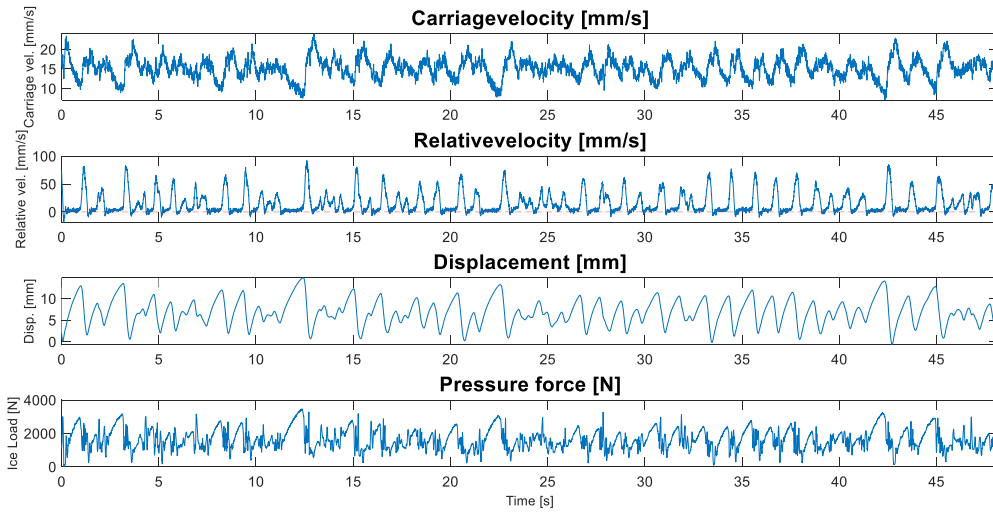
Test: SDOF-9. Fn: 1.5 Hz. V = 7.5 mm/s



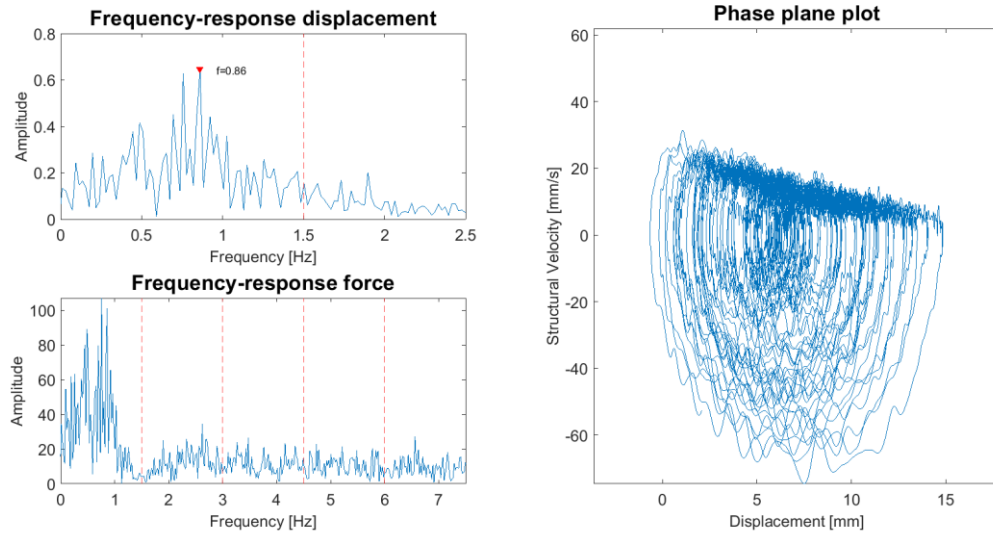
Test: SDOF-9. Fn: 1.5 Hz. V = 7.5 mm/s



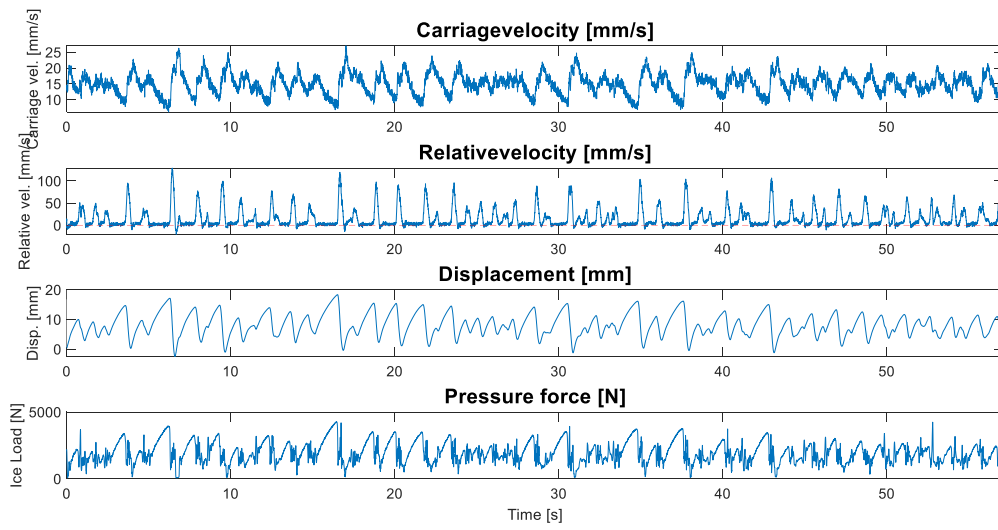
Test: SDOF-9. Fn: 1.5 Hz. V = 15 mm/s



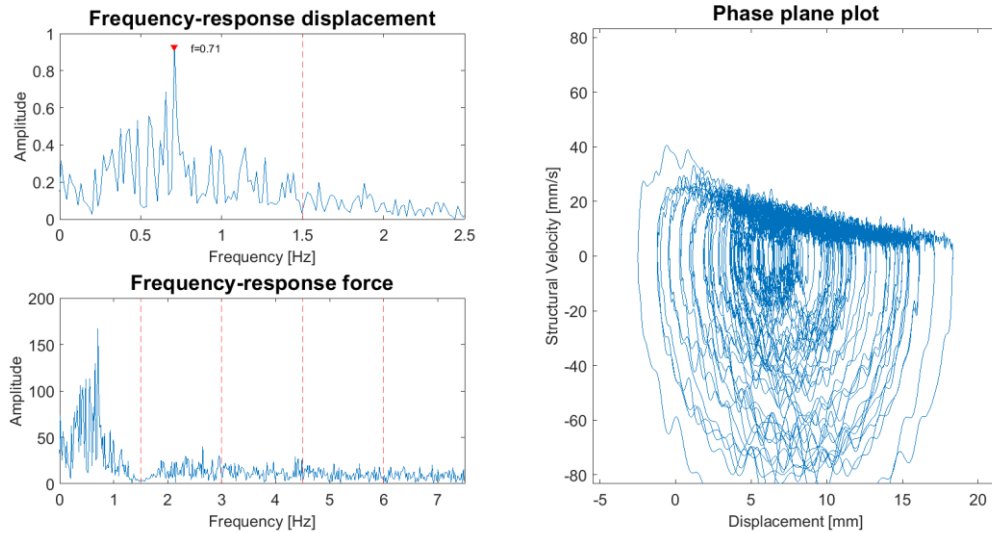
Test: SDOF-9. Fn: 1.5 Hz. V = 15 mm/s



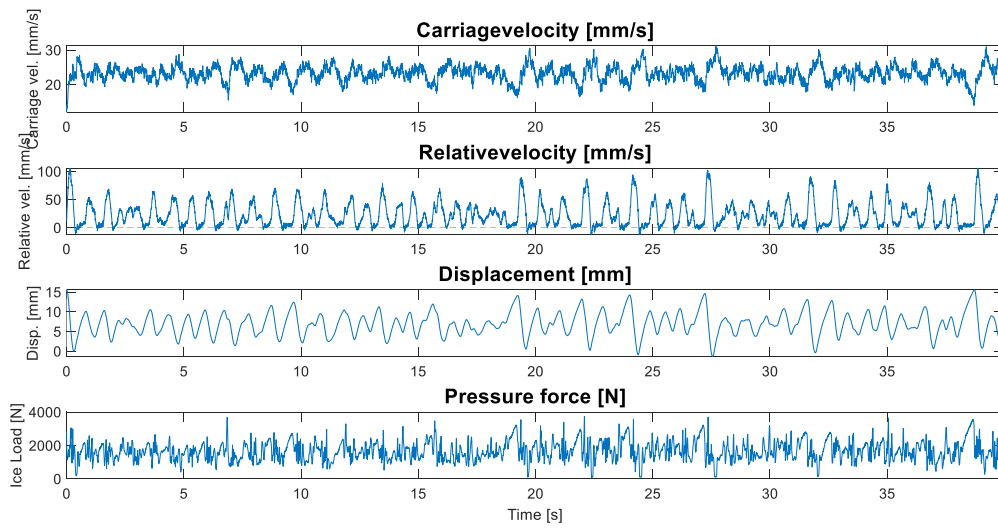
Test: SDOF-9. Fn: 1.5 Hz. V = 15 mm/s



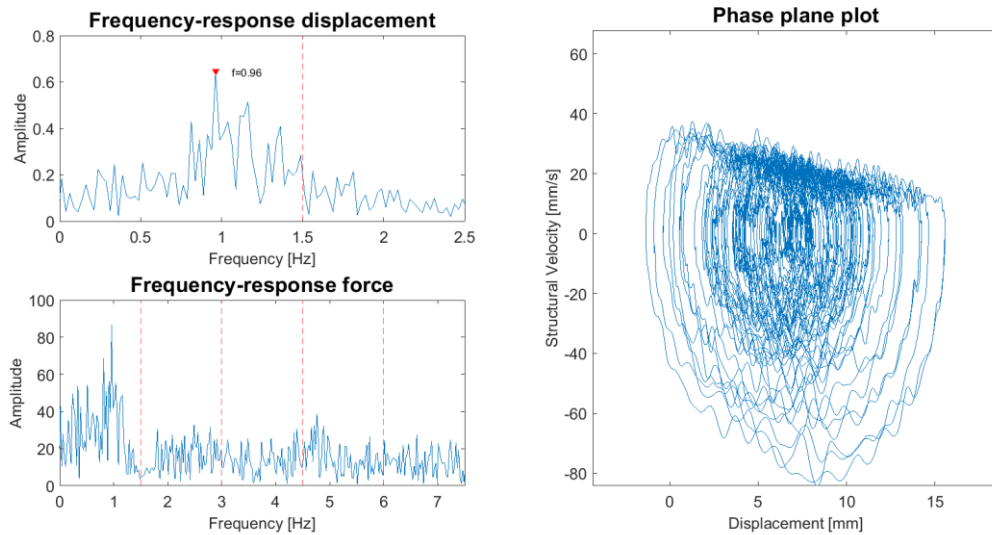
Test: SDOF-9. Fn: 1.5 Hz. V = 15 mm/s



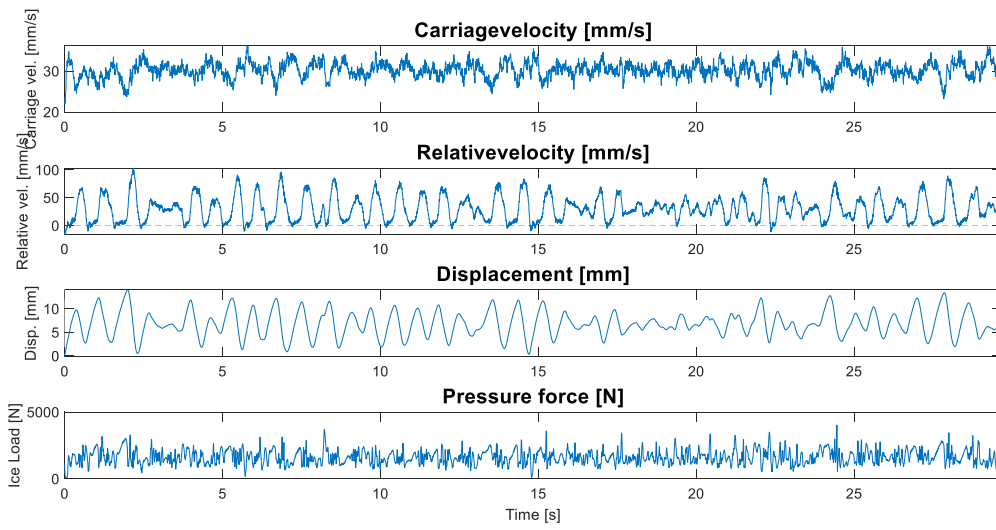
Test: SDOF-9. Fn: 1.5 Hz. V = 22.5 mm/s



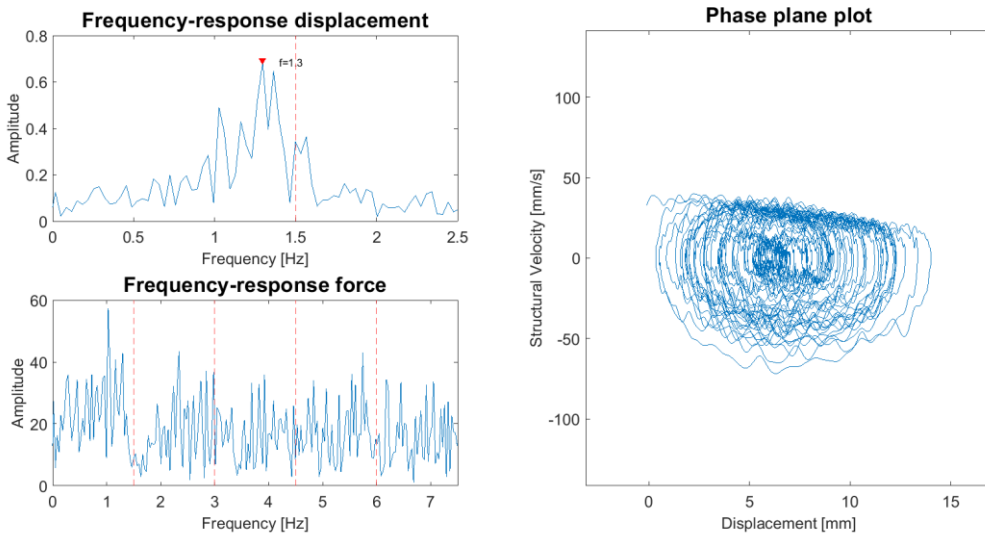
Test: SDOF-9. Fn: 1.5 Hz. V = 22.5 mm/s



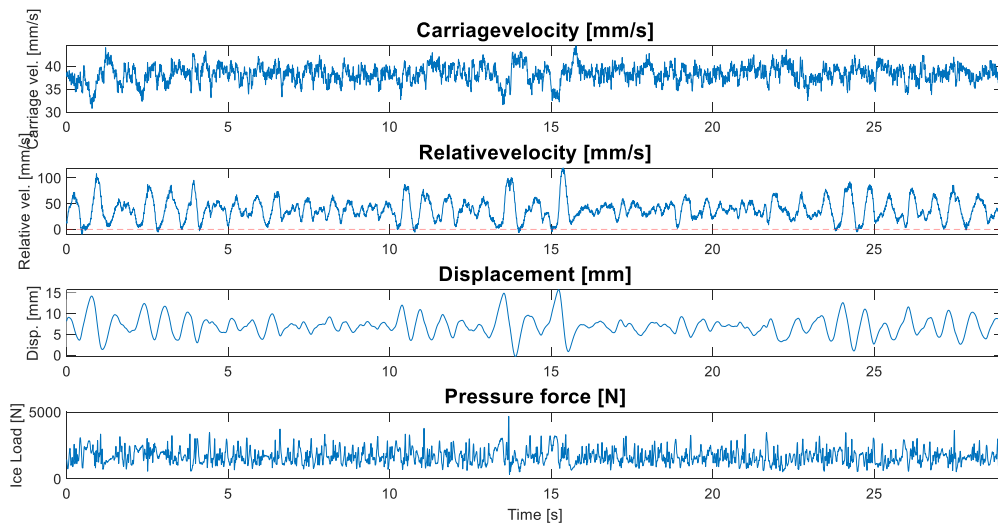
Test: SDOF-9. Fn: 1.5 Hz. V = 30 mm/s



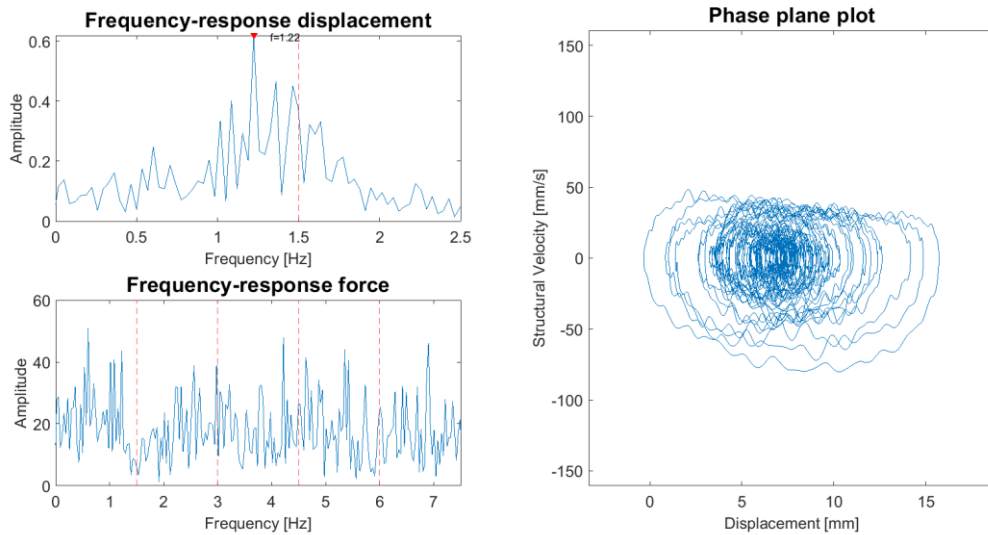
Test: SDOF-9. Fn: 1.5 Hz. V = 30 mm/s



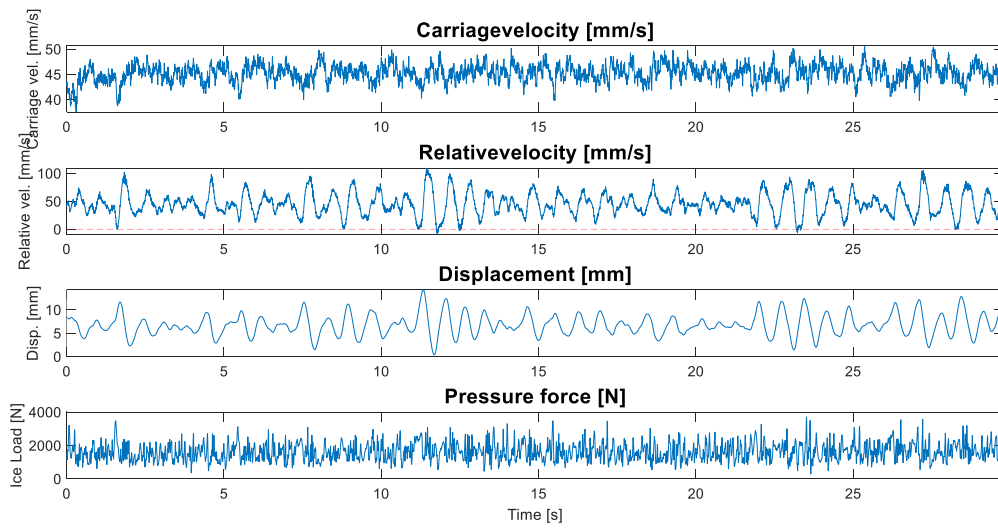
Test: SDOF-9. Fn: 1.5 Hz. V = 37.5 mm/s



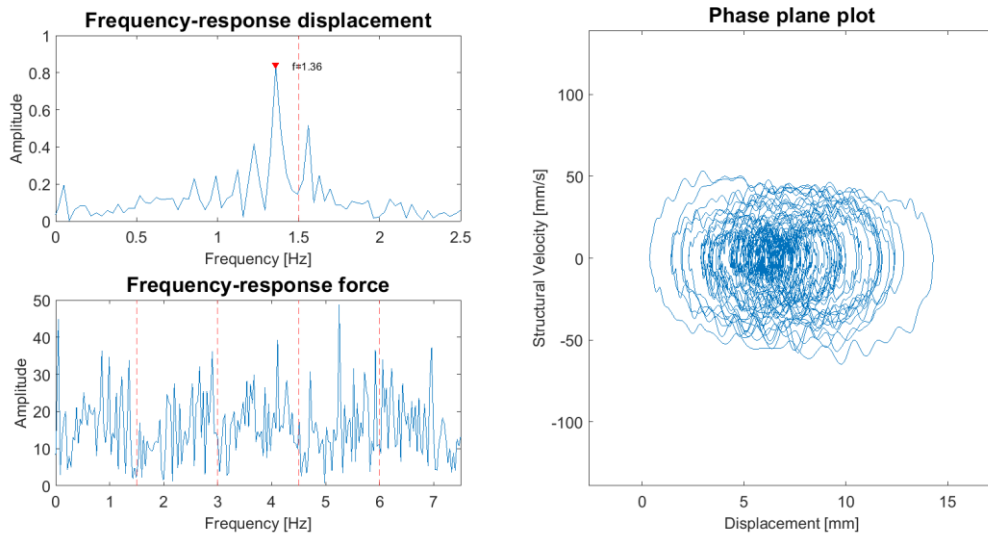
Test: SDOF-9. Fn: 1.5 Hz. V = 37.5 mm/s



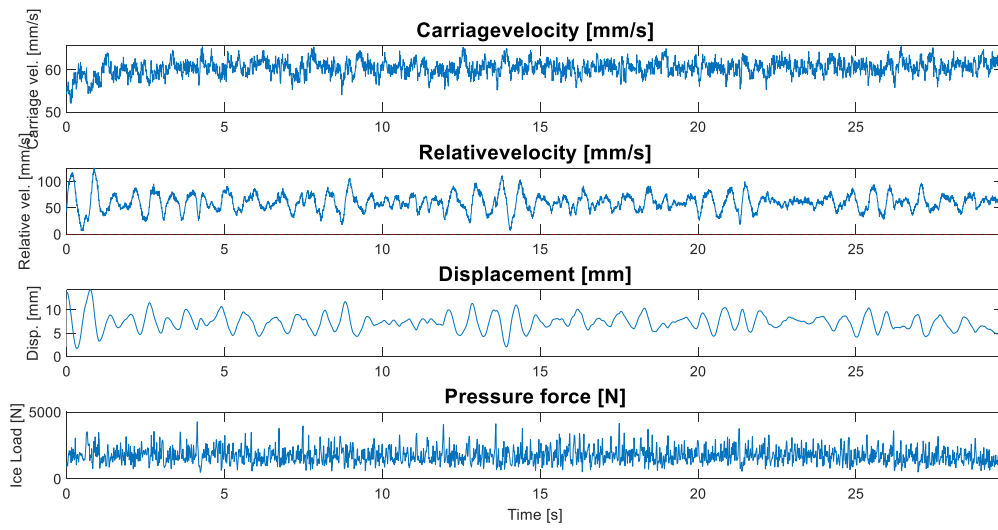
Test: SDOF-9. Fn: 1.5 Hz. V = 45 mm/s



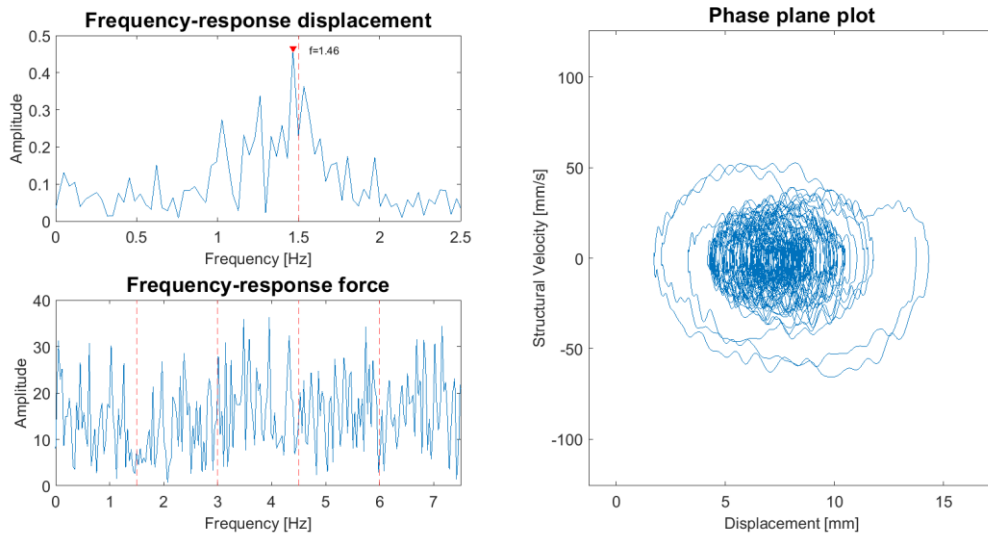
Test: SDOF-9. Fn: 1.5 Hz. V = 45 mm/s



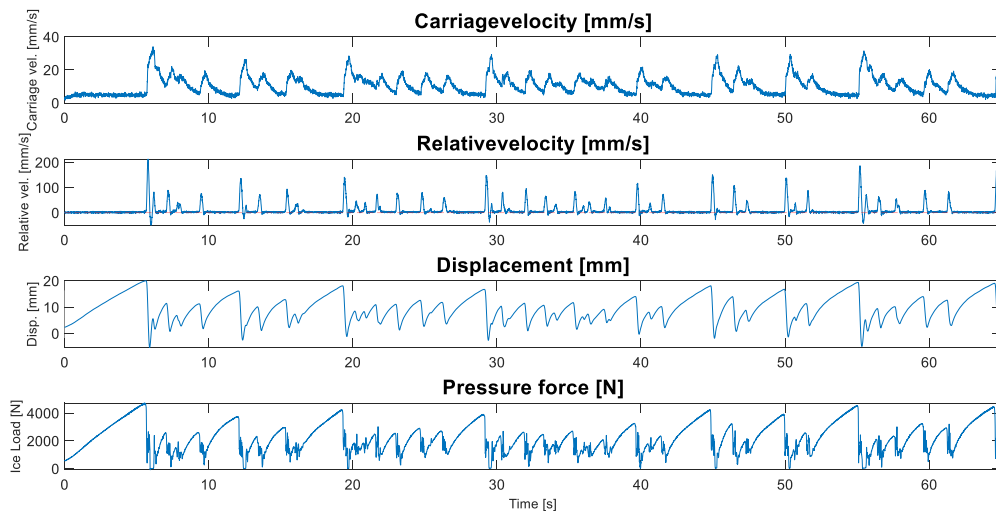
Test: SDOF-9. Fn: 1.5 Hz. V = 60 mm/s



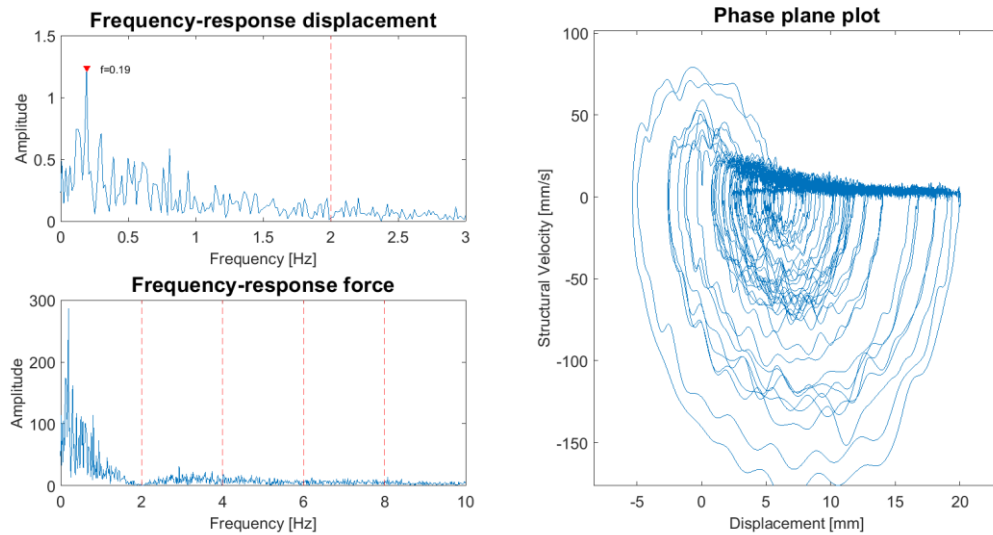
Test: SDOF-9. Fn: 1.5 Hz. V = 60 mm/s



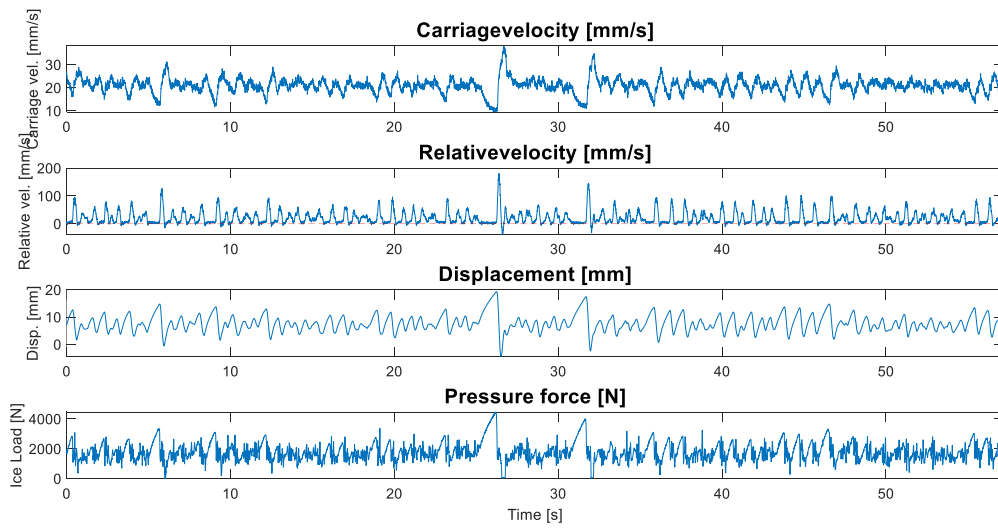
Test: SDOF-10. Fn: 2 Hz. V = 10 mm/s



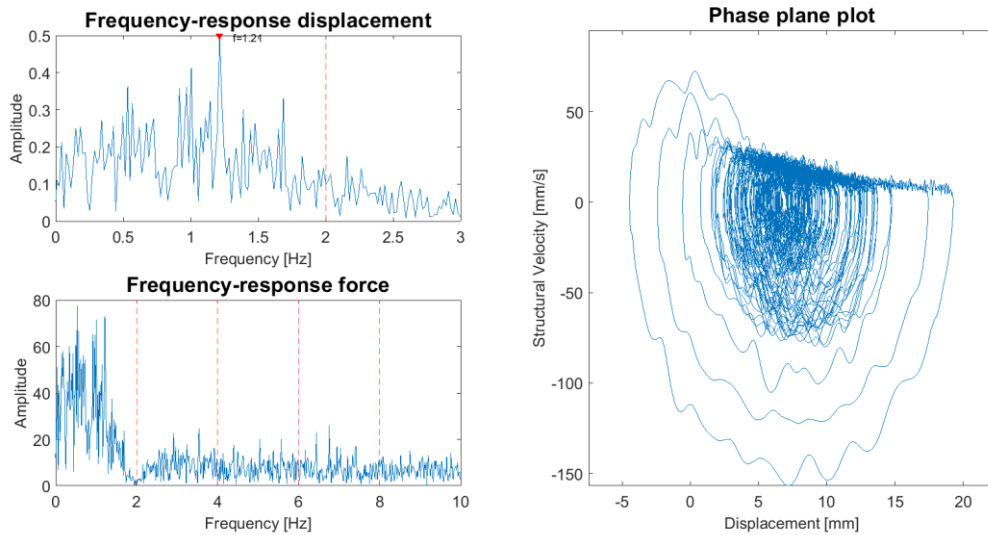
Test: SDOF-10. Fn: 2 Hz. V = 10 mm/s



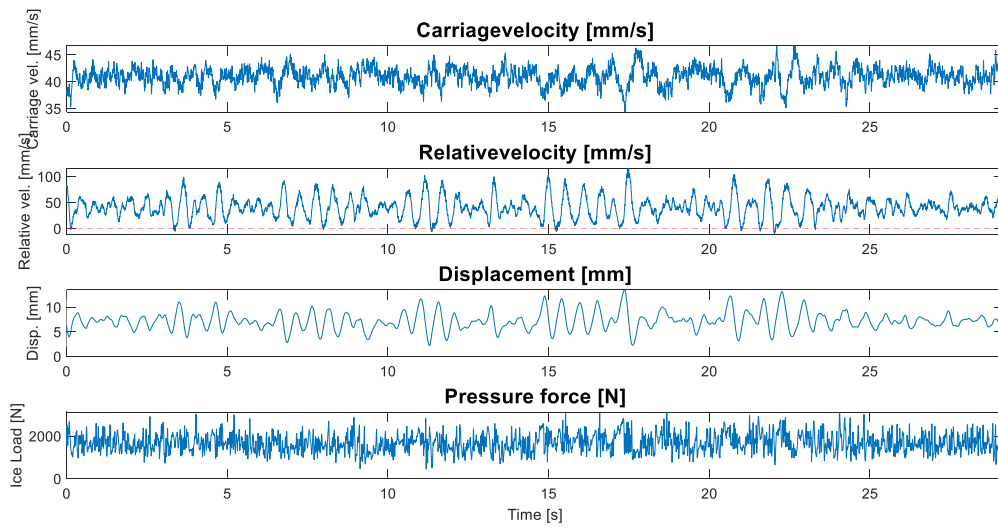
Test: SDOF-10. Fn: 2 Hz. V = 20 mm/s



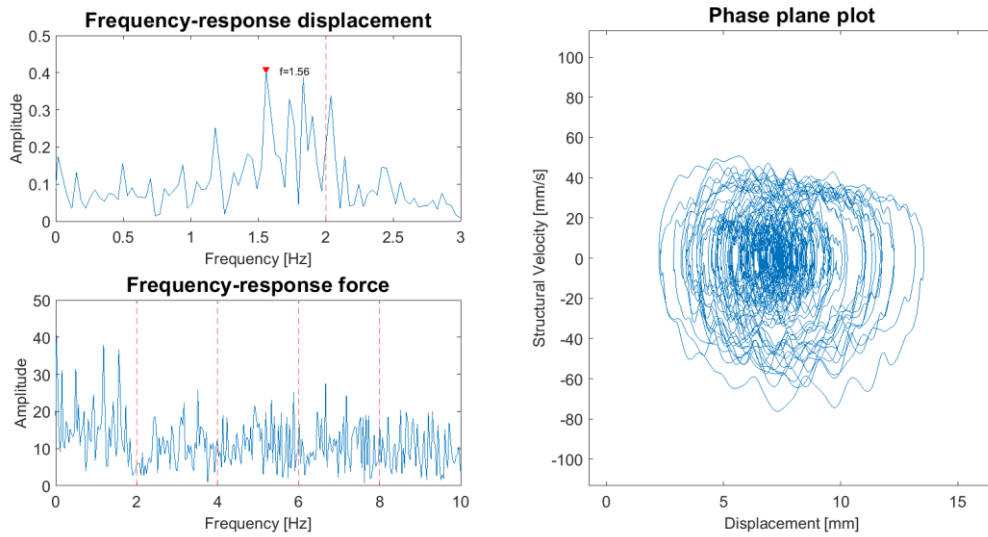
Test: SDOF-10. Fn: 2 Hz. V = 20 mm/s



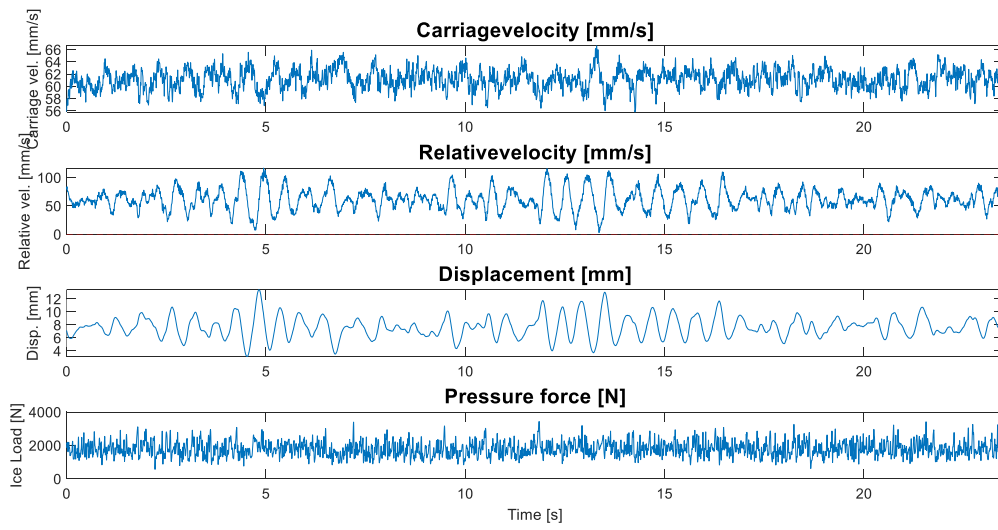
Test: SDOF-10. Fn: 2 Hz. V = 40 mm/s



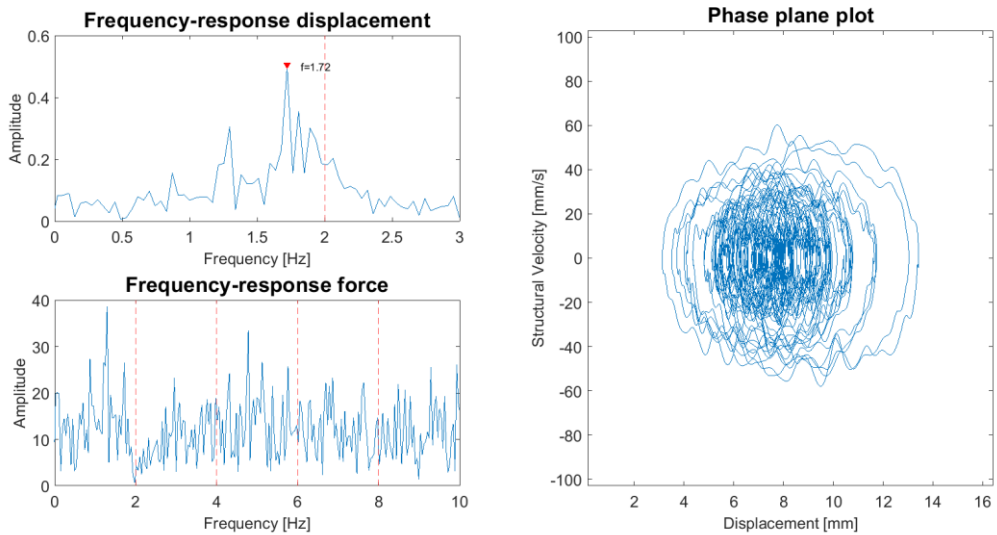
Test: SDOF-10. Fn: 2 Hz. V = 40 mm/s



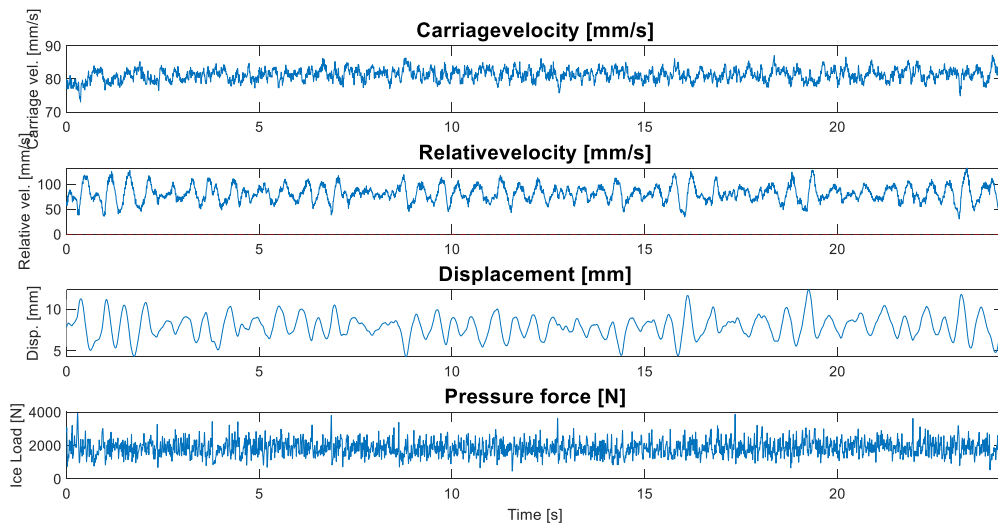
Test: SDOF-10. Fn: 2 Hz. V = 60 mm/s



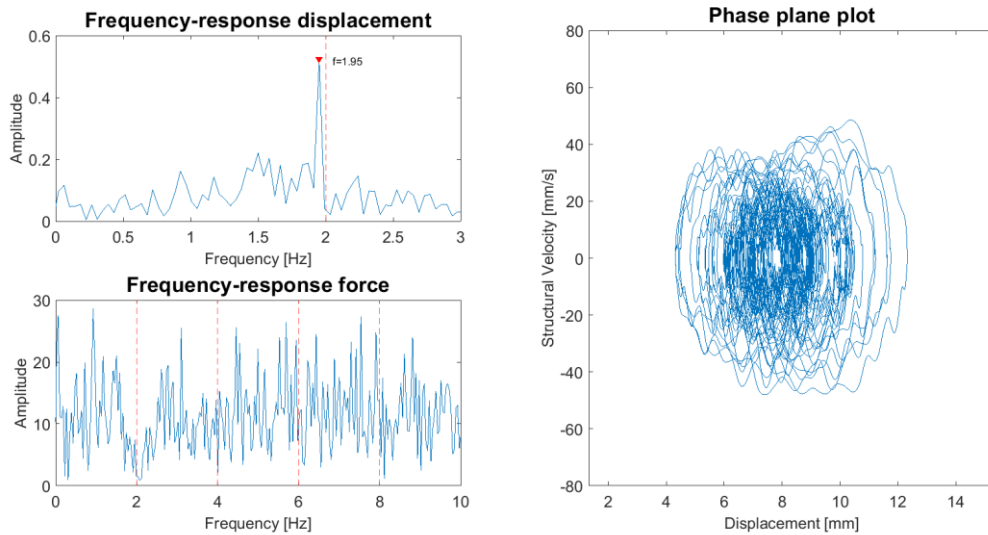
Test: SDOF-10. Fn: 2 Hz. V = 60 mm/s



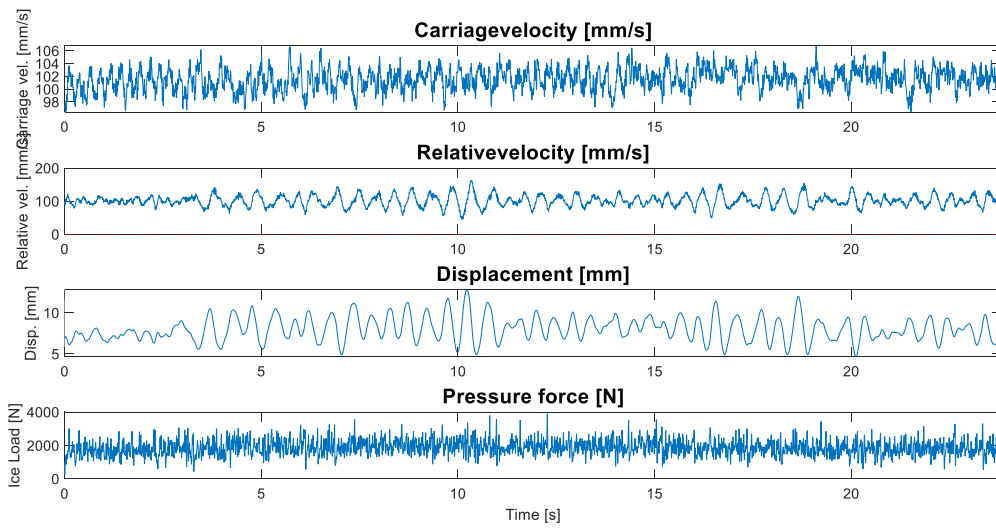
Test: SDOF-10. Fn: 2 Hz. V = 80 mm/s



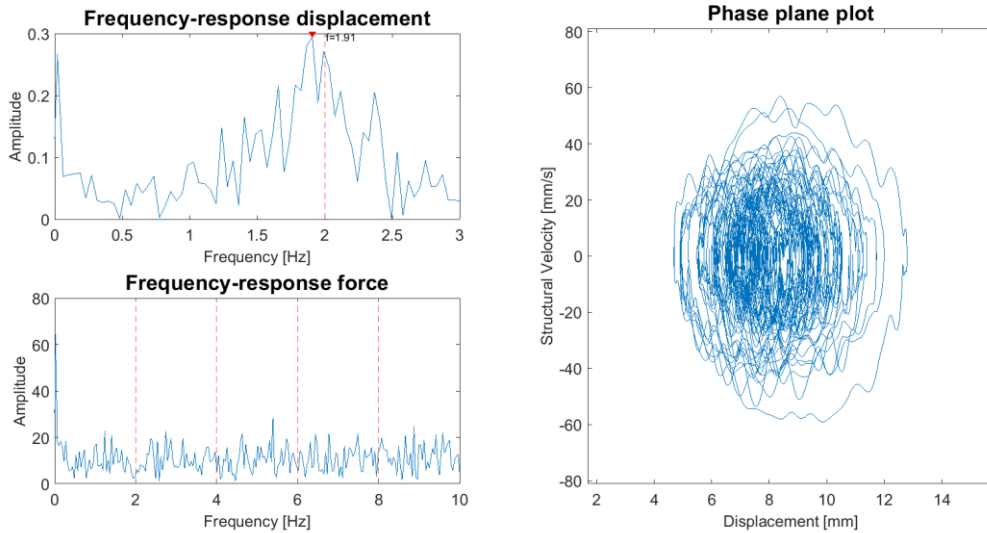
Test: SDOF-10. Fn: 2 Hz. V = 80 mm/s



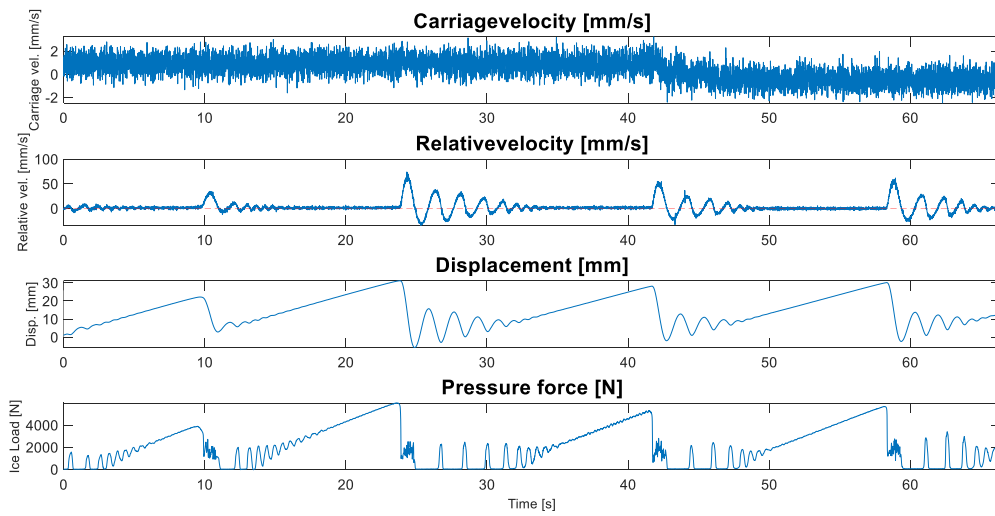
Test: SDOF-10. Fn: 2 Hz. V = 100 mm/s



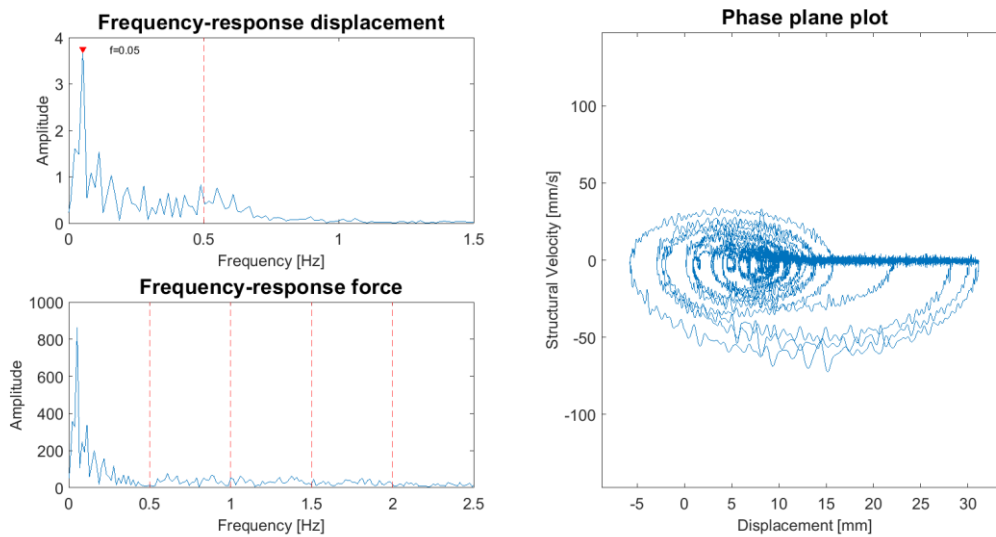
Test: SDOF-10. Fn: 2 Hz. V = 100 mm/s



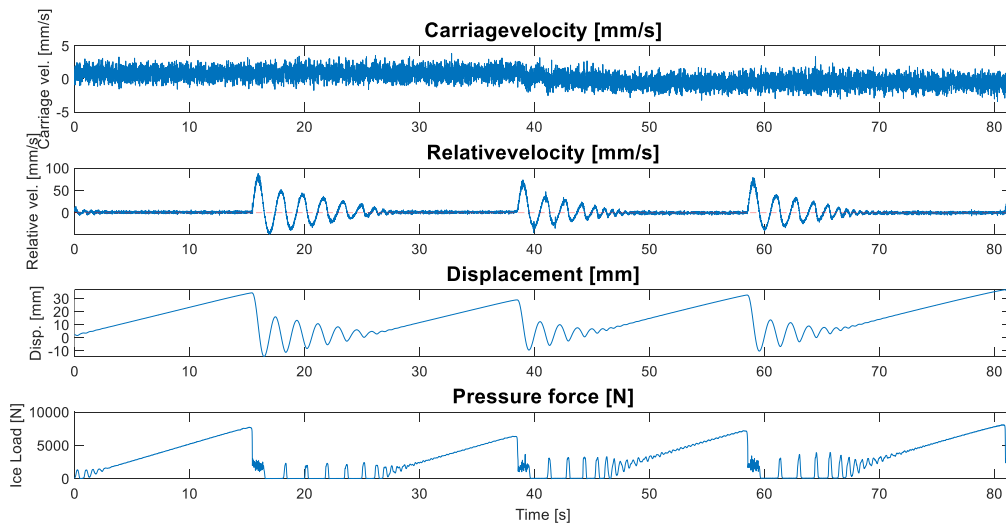
Test: SDOF-11. Fn: 0.5 Hz. V = 2.5 mm/s



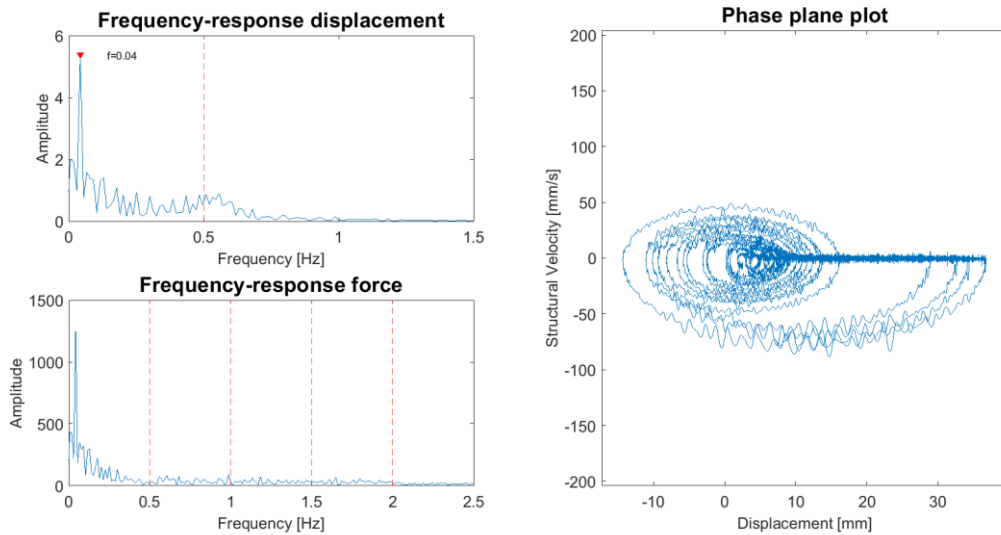
Test: SDOF-11. Fn: 0.5 Hz. V = 2.5 mm/s



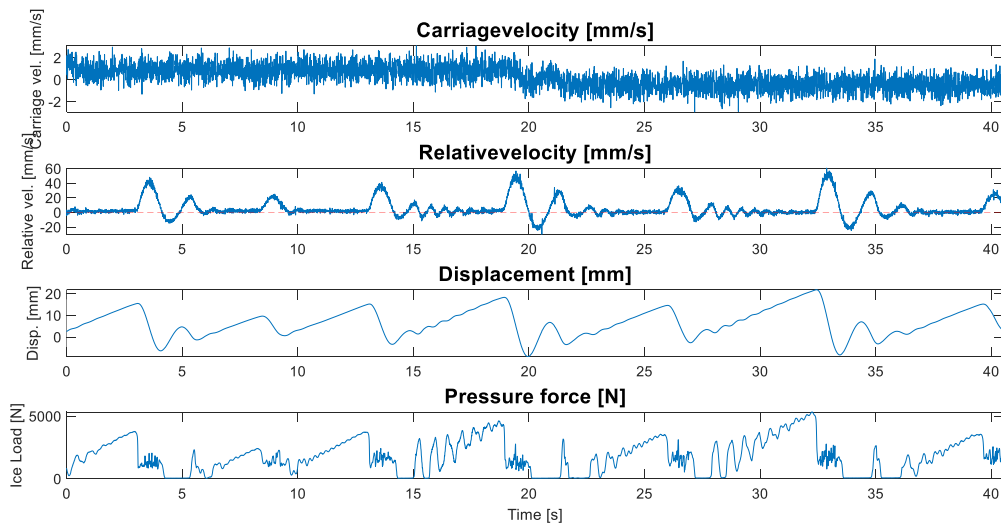
Test: SDOF-11. Fn: 0.5 Hz. V = 2.5 mm/s



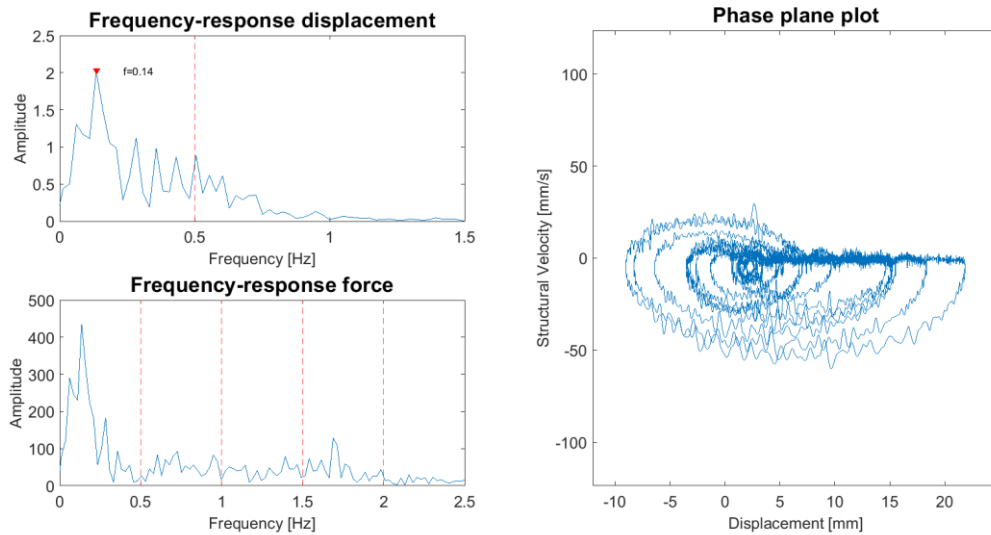
Test: SDOF-11. Fn: 0.5 Hz. V = 2.5 mm/s



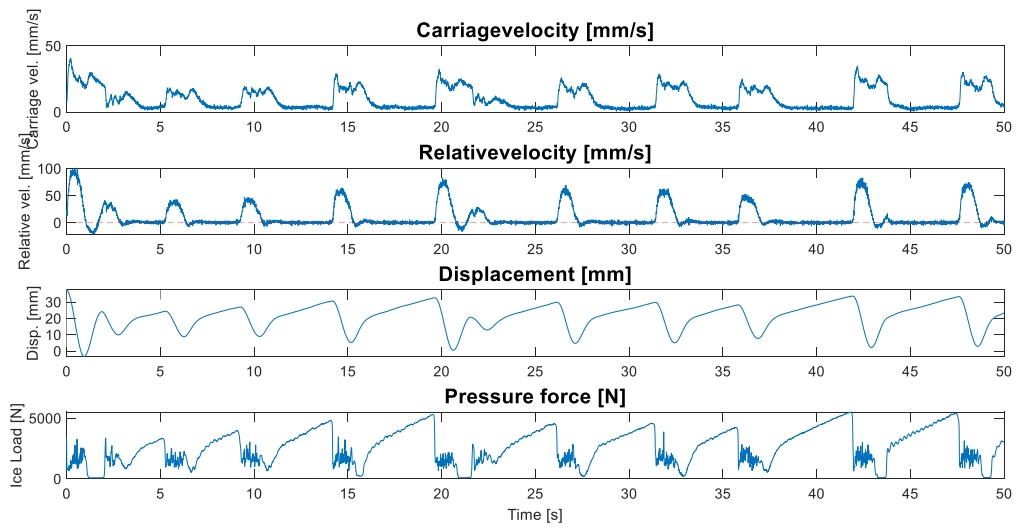
Test: SDOF-11. Fn: 0.5 Hz. V = 5 mm/s



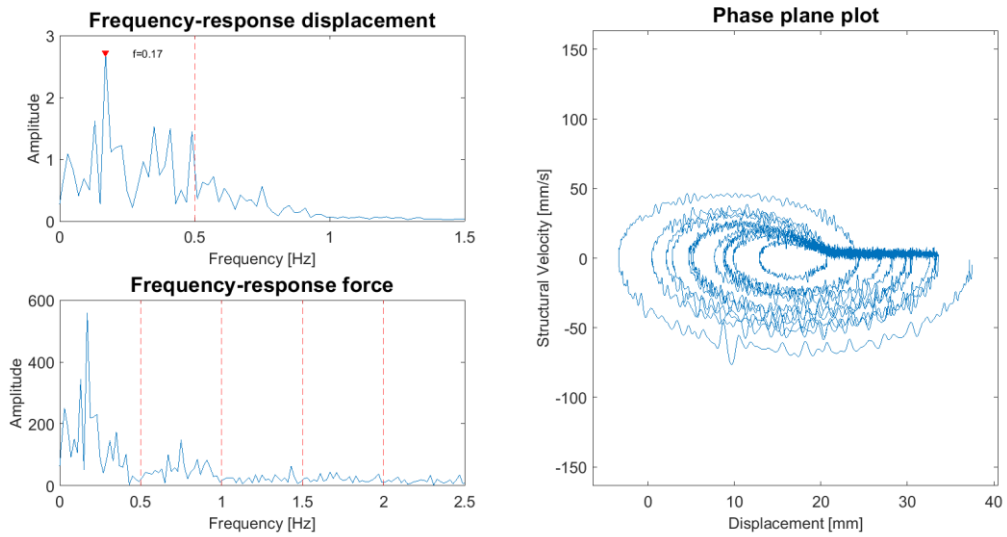
Test: SDOF-11. Fn: 0.5 Hz. V = 5 mm/s



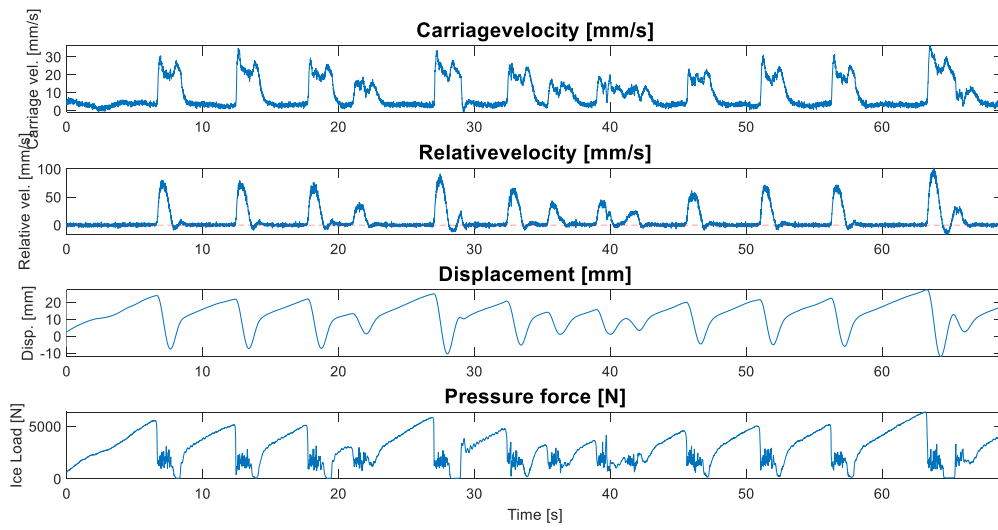
Test: SDOF-11. Fn: 0.5 Hz. V = 10 mm/s



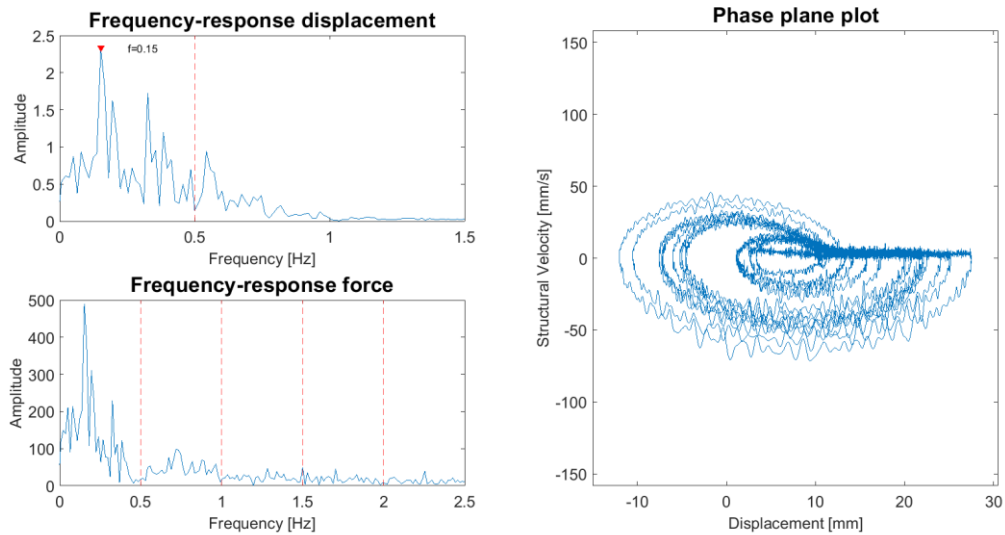
Test: SDOF-11. Fn: 0.5 Hz. V = 10 mm/s



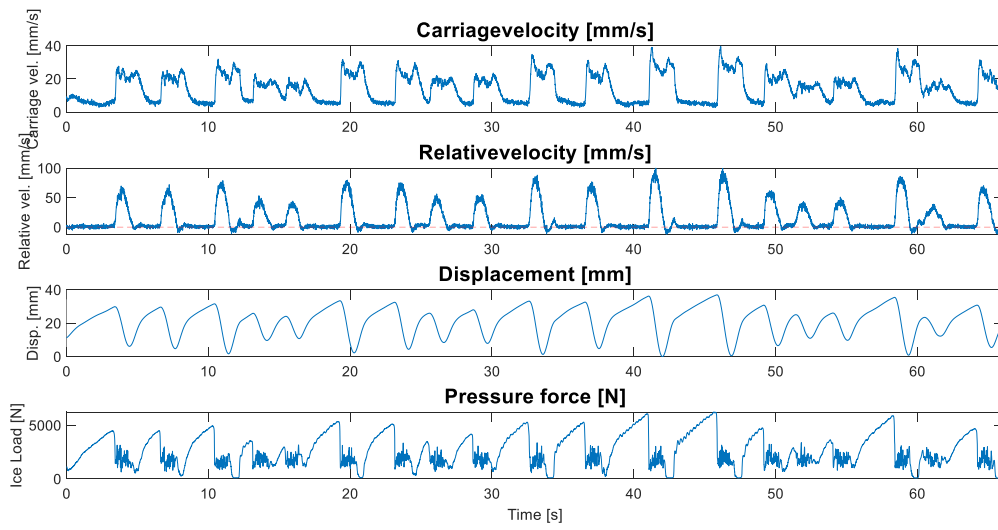
Test: SDOF-11. Fn: 0.5 Hz. V = 10 mm/s



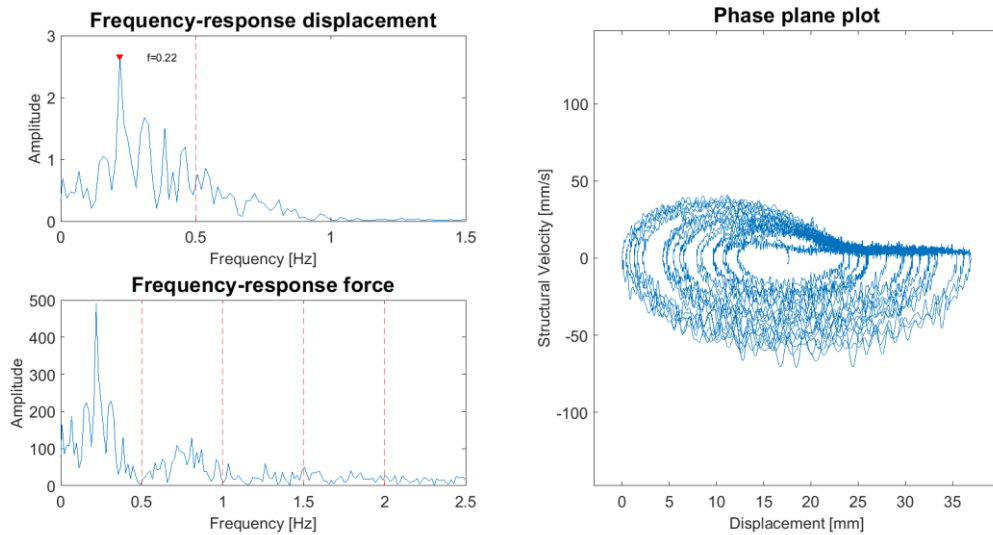
Test: SDOF-11. Fn: 0.5 Hz. V = 10 mm/s



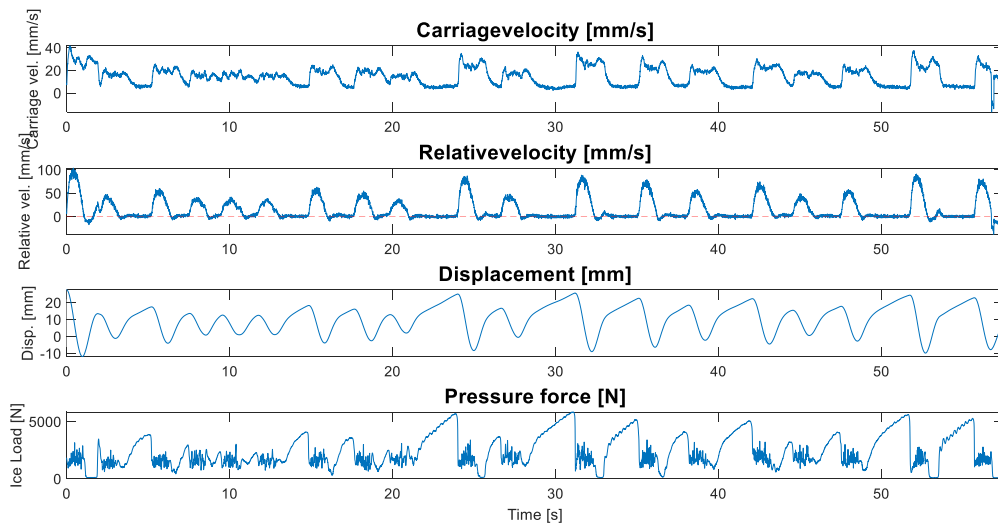
Test: SDOF-11. Fn: 0.5 Hz. V = 15 mm/s



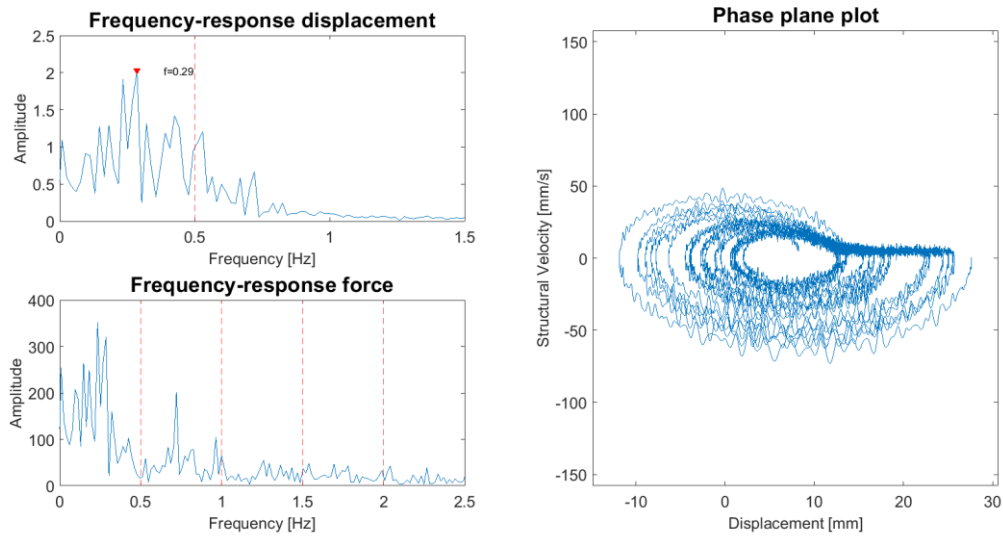
Test: SDOF-11. Fn: 0.5 Hz. V = 15 mm/s



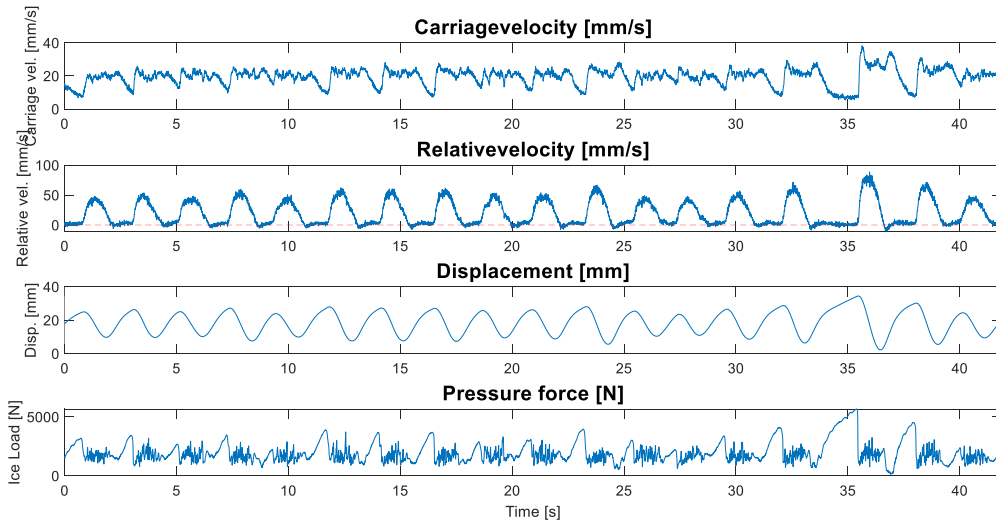
Test: SDOF-11. Fn: 0.5 Hz. V = 15 mm/s



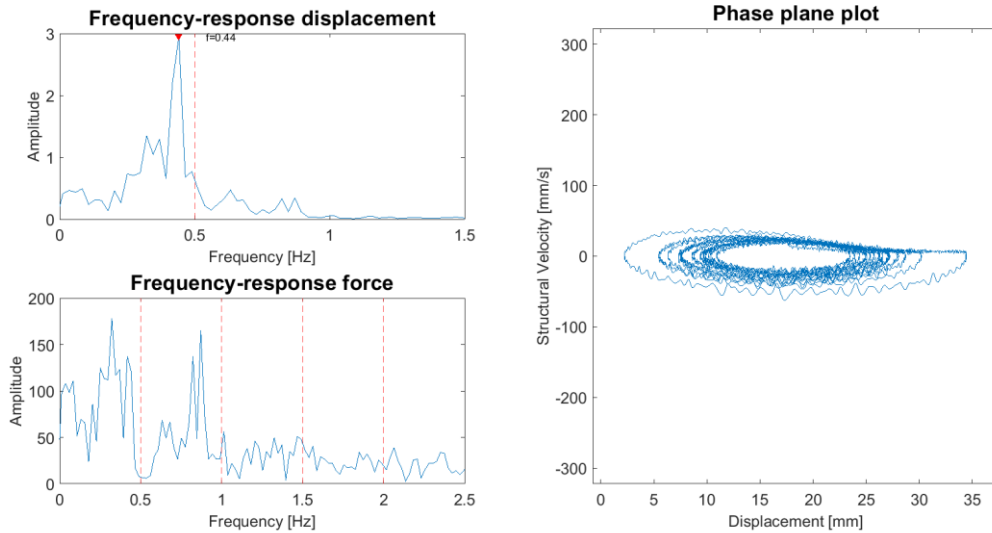
Test: SDOF-11. Fn: 0.5 Hz. V = 15 mm/s



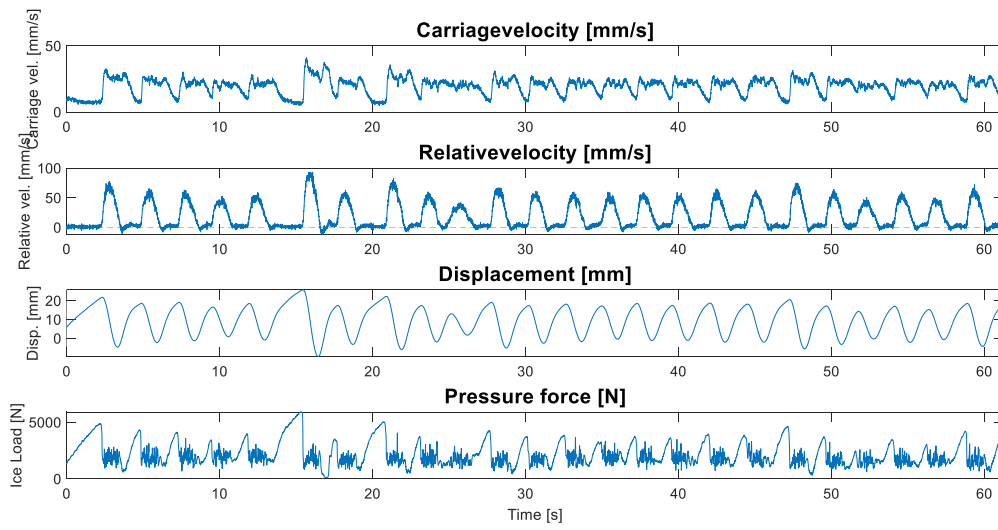
Test: SDOF-11. Fn: 0.5 Hz. V = 20 mm/s



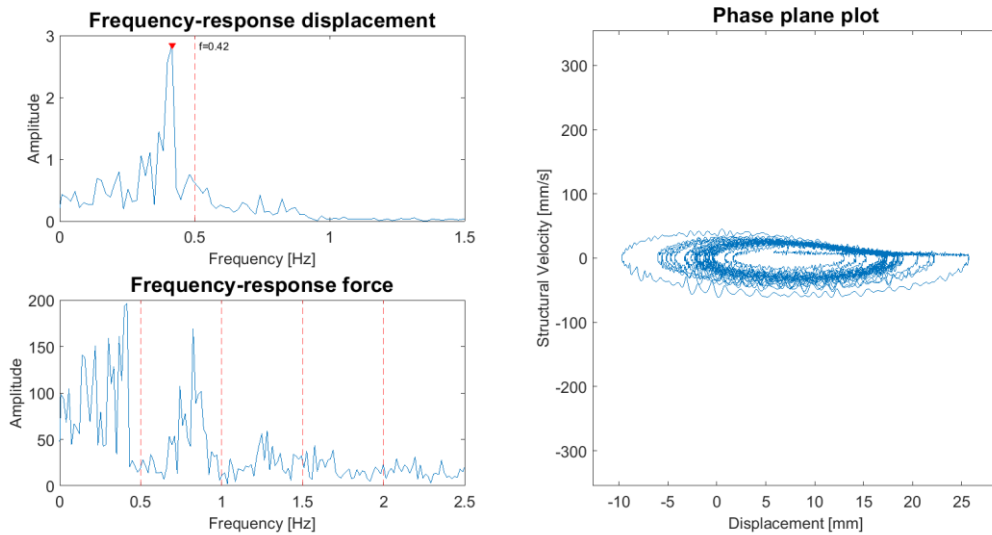
Test: SDOF-11. Fn: 0.5 Hz. V = 20 mm/s



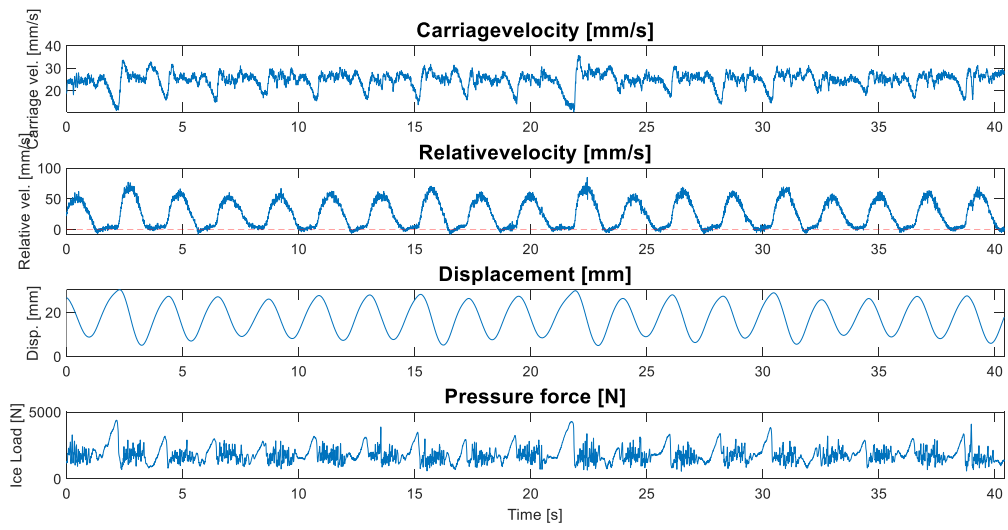
Test: SDOF-11. Fn: 0.5 Hz. V = 20 mm/s



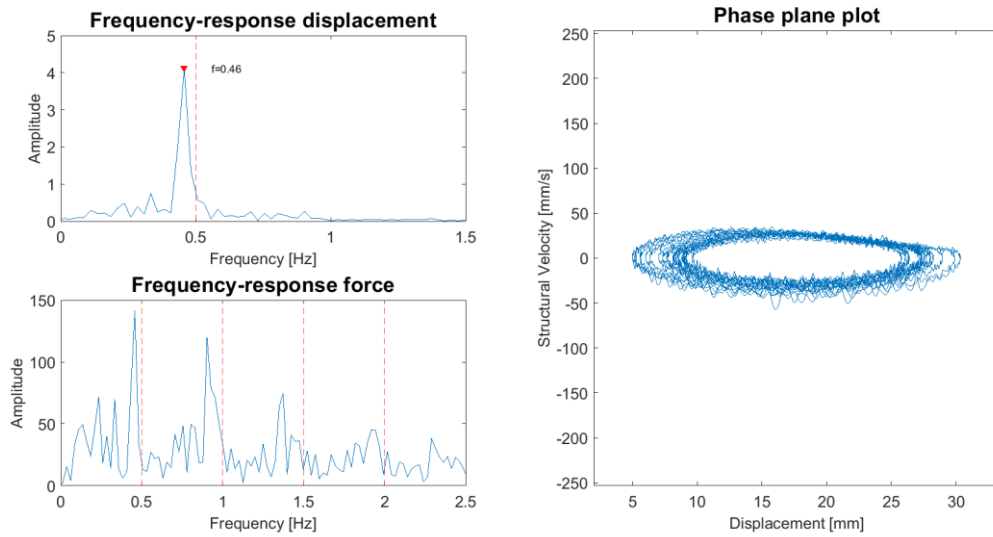
Test: SDOF-11. Fn: 0.5 Hz. V = 20 mm/s



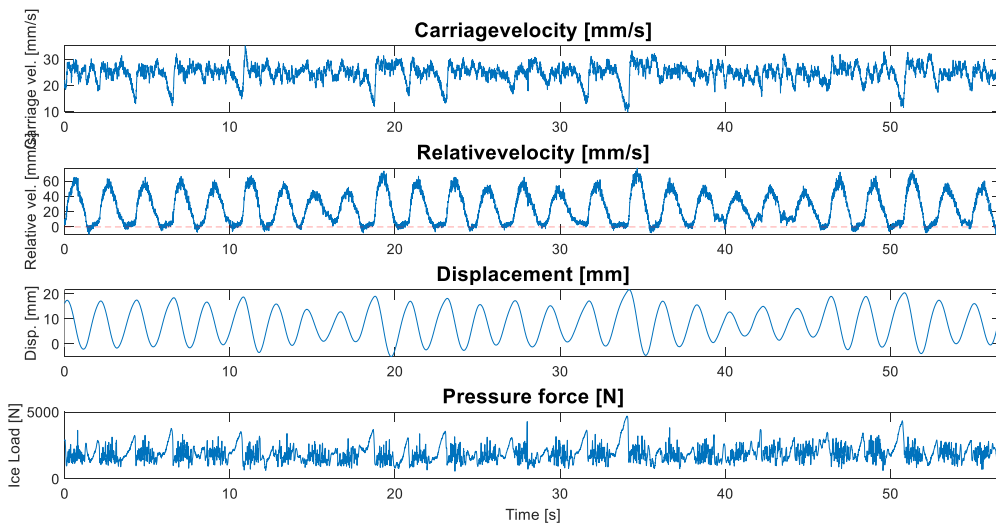
Test: SDOF-11. Fn: 0.5 Hz. V = 25 mm/s



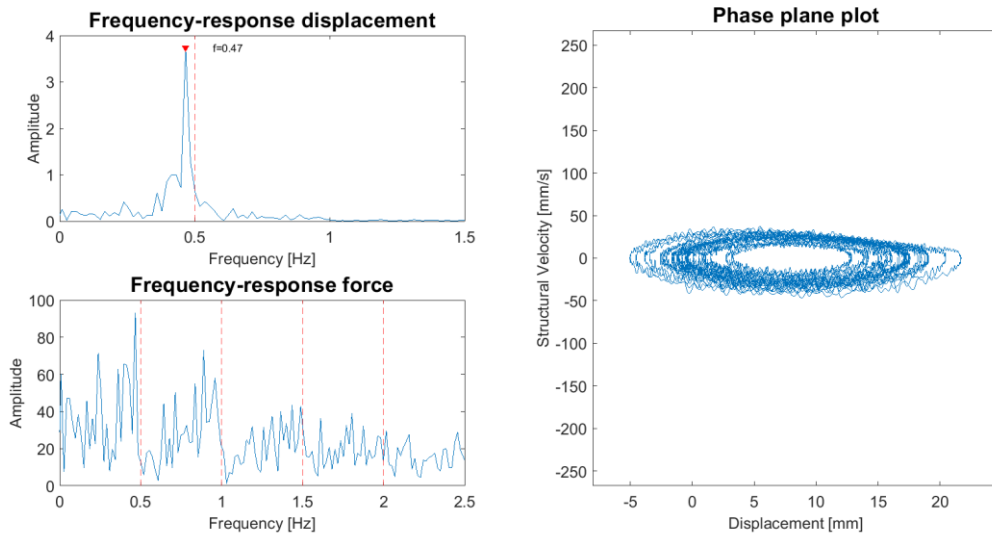
Test: SDOF-11. Fn: 0.5 Hz. V = 25 mm/s



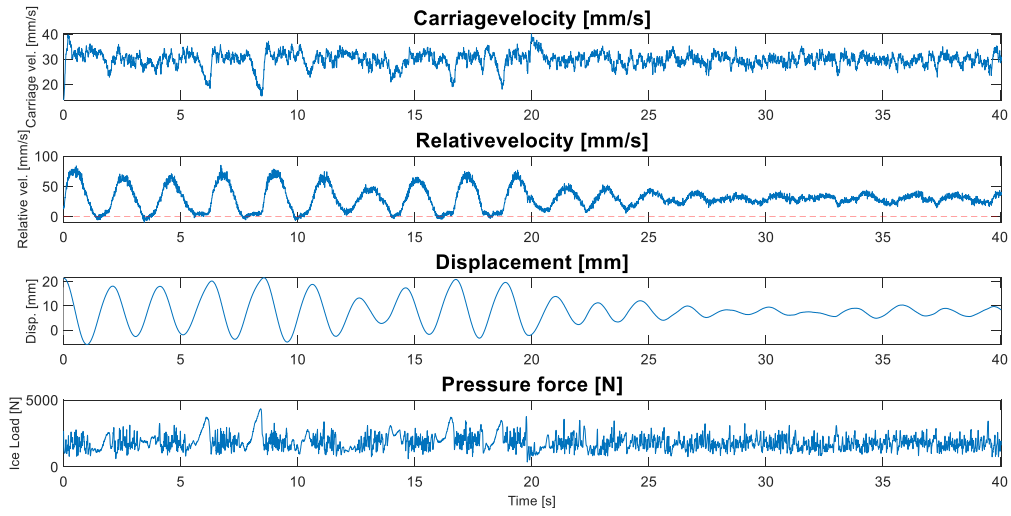
Test: SDOF-11. Fn: 0.5 Hz. V = 25 mm/s



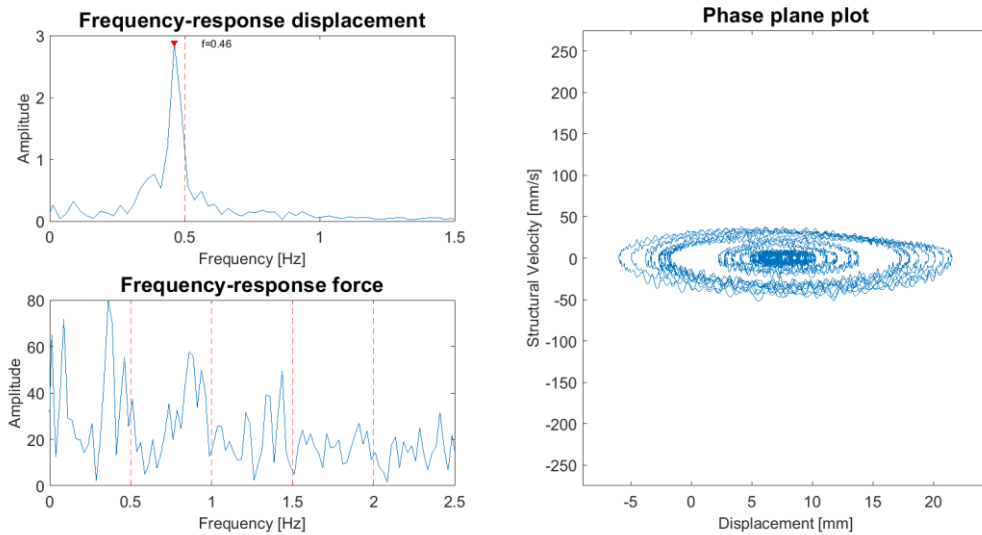
Test: SDOF-11. Fn: 0.5 Hz. V = 25 mm/s



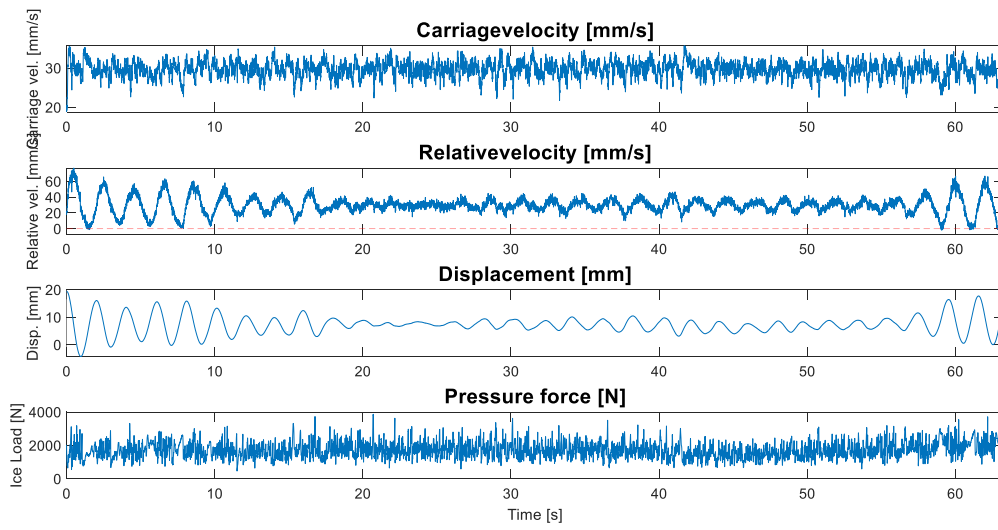
Test: SDOF-11. Fn: 0.5 Hz. V = 30 mm/s



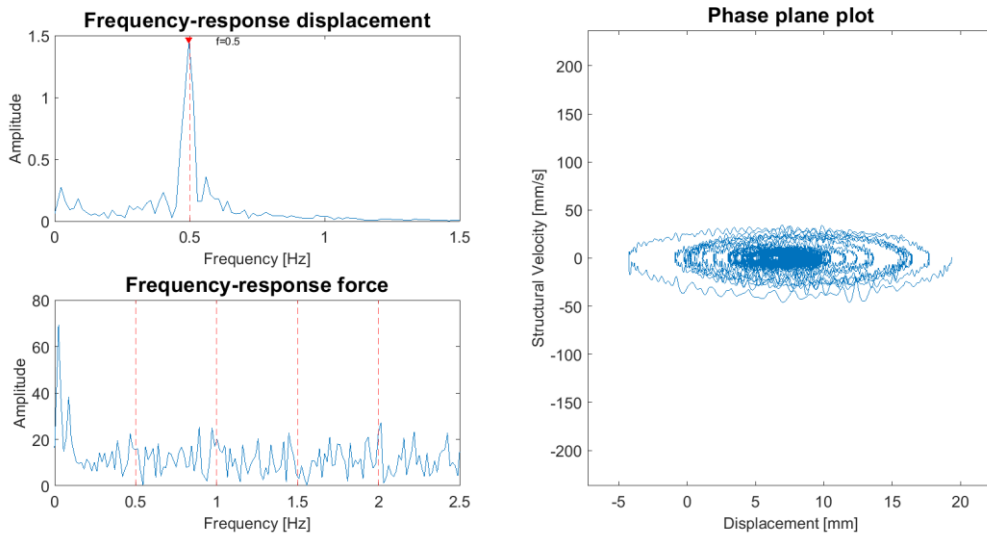
Test: SDOF-11. Fn: 0.5 Hz. V = 30 mm/s



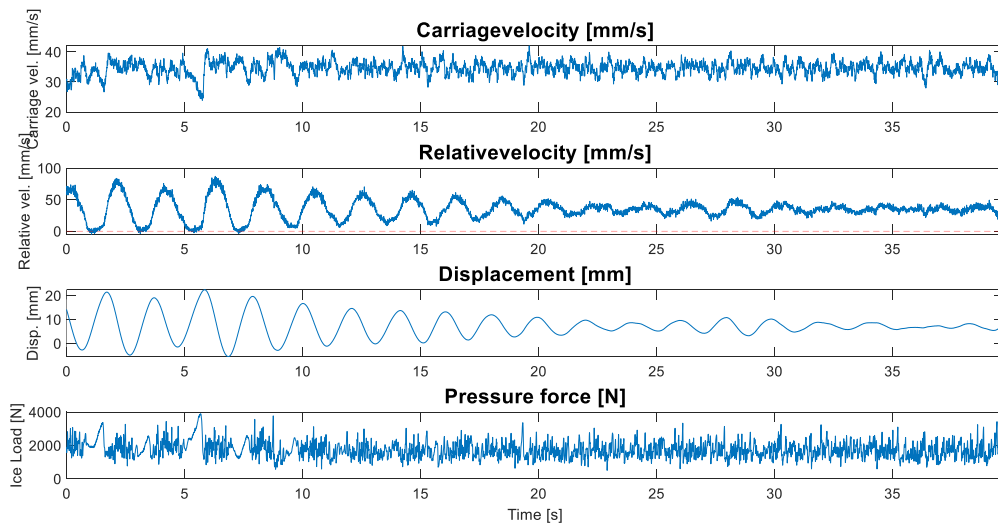
Test: SDOF-11. Fn: 0.5 Hz. V = 30 mm/s



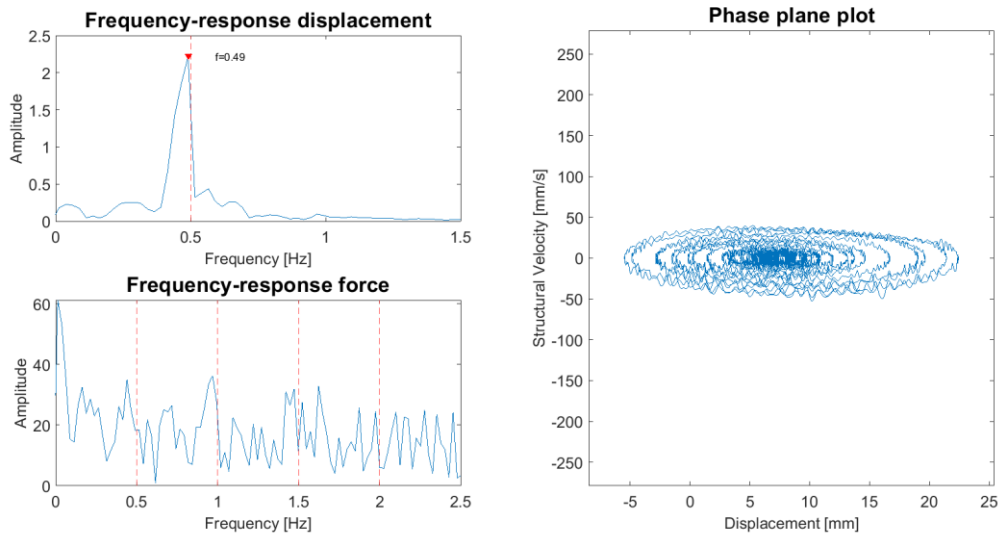
Test: SDOF-11. Fn: 0.5 Hz. V = 30 mm/s



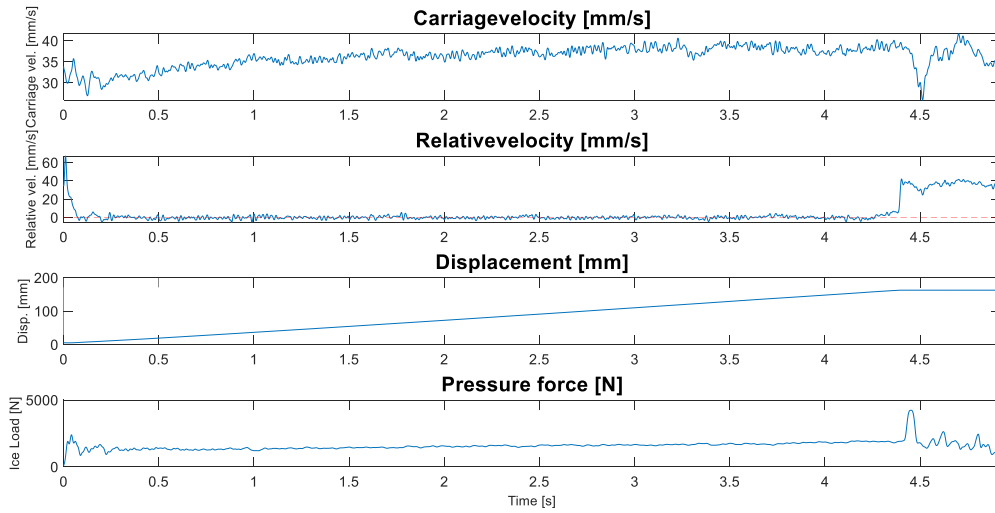
Test: SDOF-11. Fn: 0.5 Hz. V = 35 mm/s



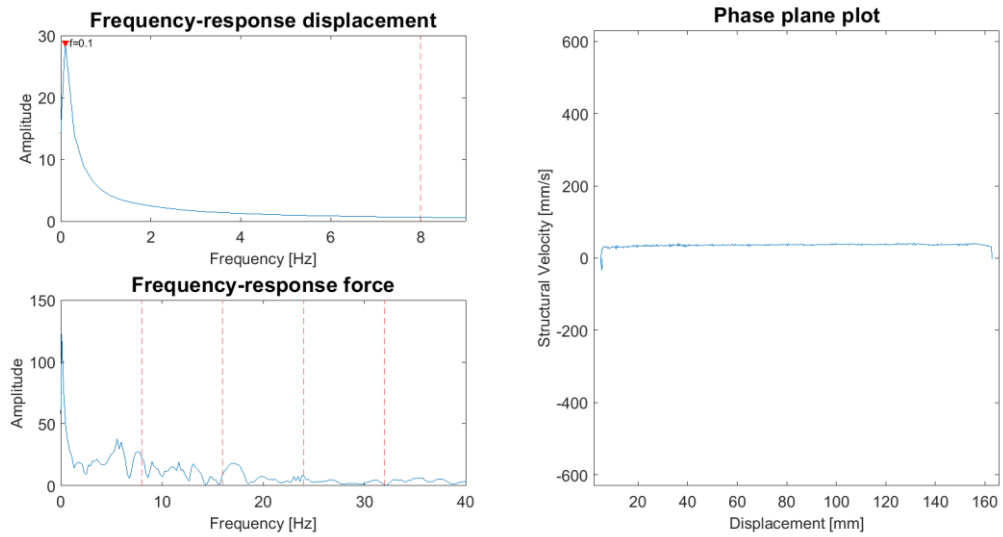
Test: SDOF-11. Fn: 0.5 Hz. V = 35 mm/s



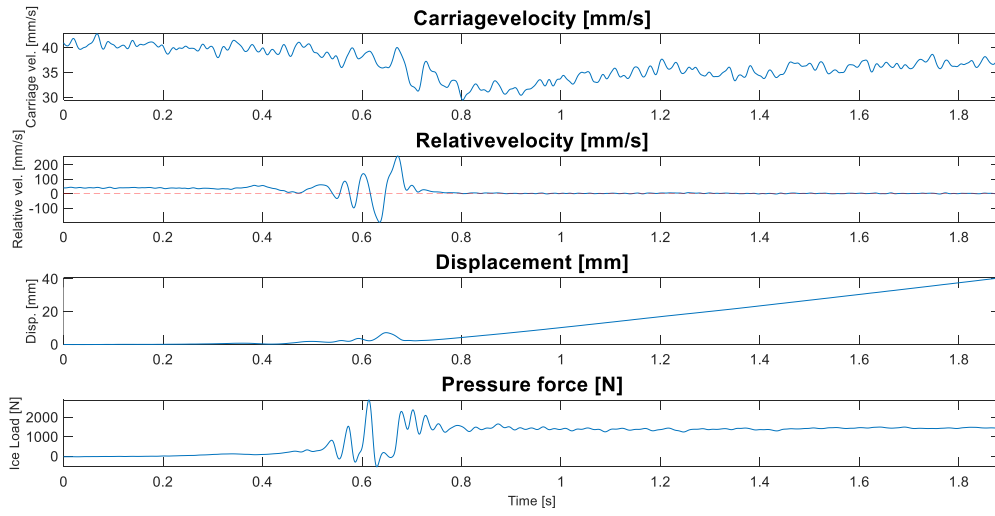
Test: SDOF-12. Fn: 8 Hz. V = 40 mm/s



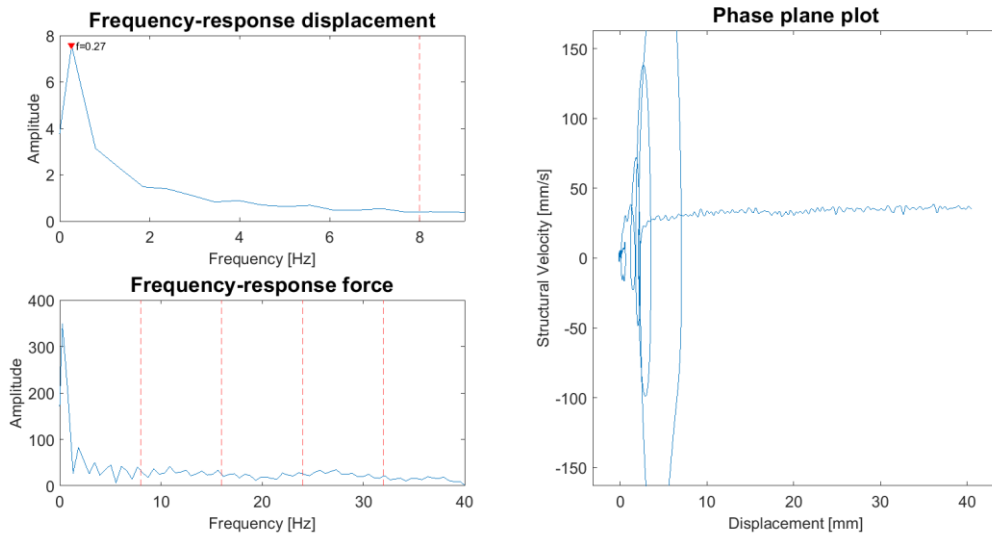
Test: SDOF-12. Fn: 8 Hz. V = 40 mm/s



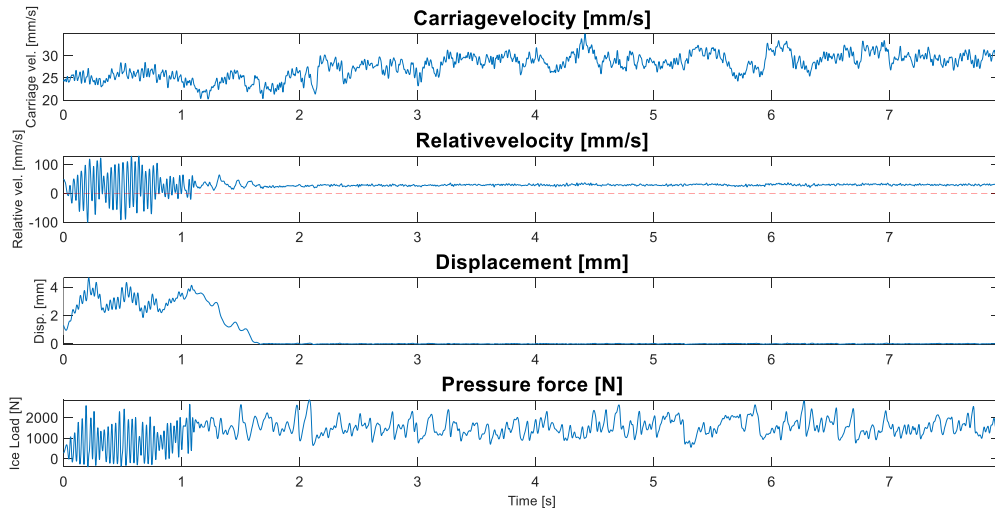
Test: SDOF-12. Fn: 8 Hz. V = 40 mm/s



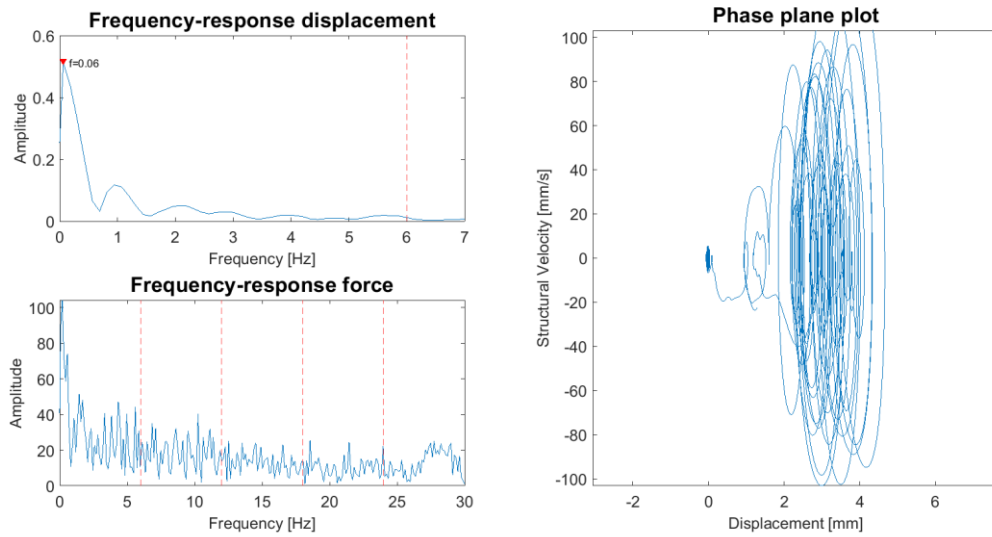
Test: SDOF-12. Fn: 8 Hz. V = 40 mm/s



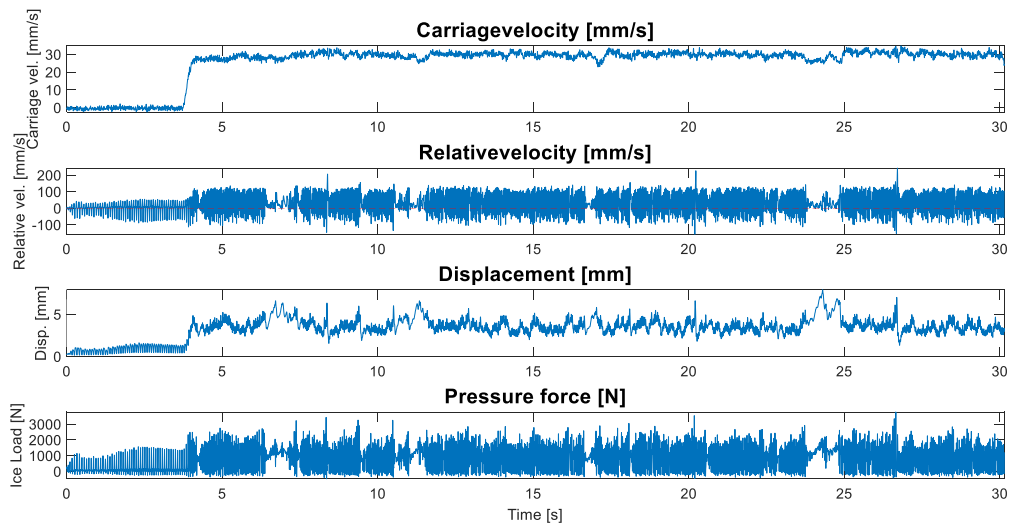
Test: SDOF-13. Fn: 6 Hz. V = 30 mm/s



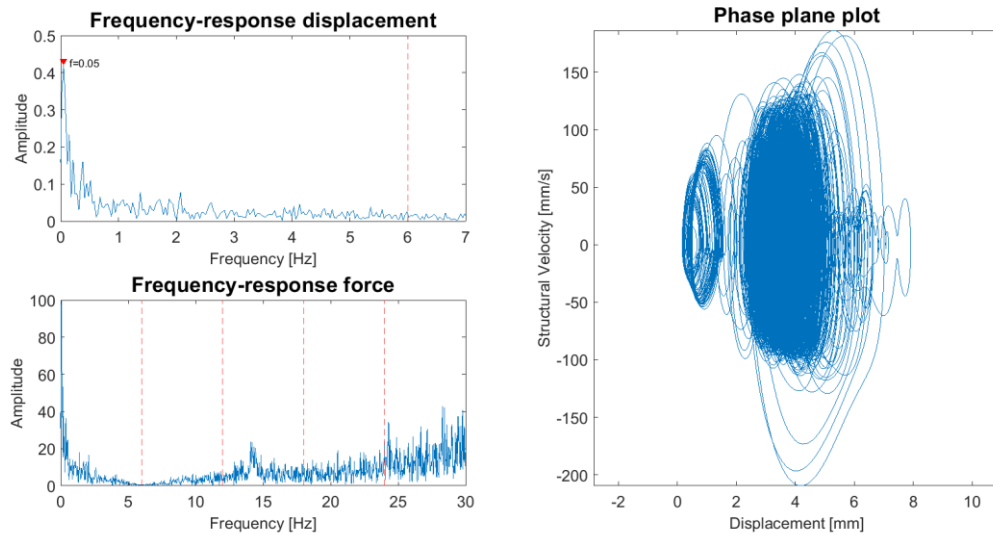
Test: SDOF-13. Fn: 6 Hz. V = 30 mm/s



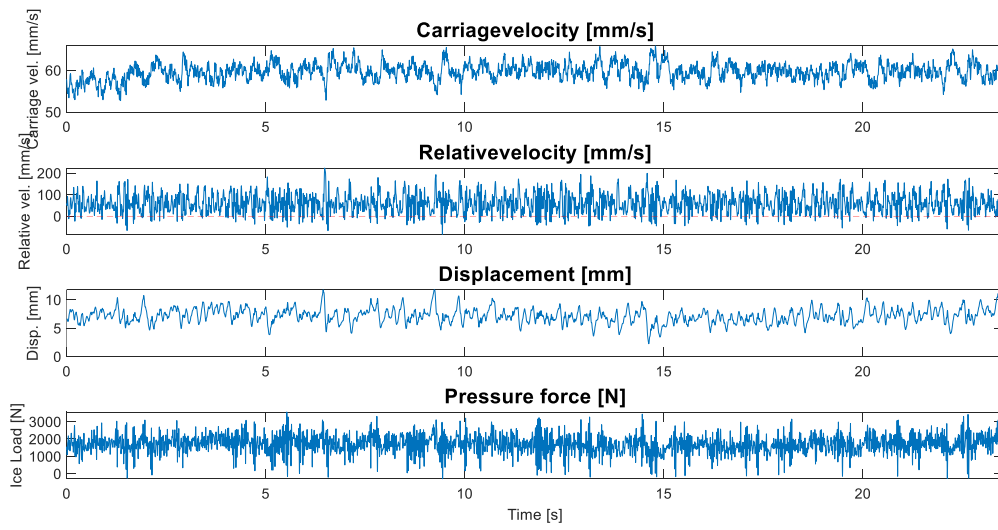
Test: SDOF-13. Fn: 6 Hz. V = 30 mm/s



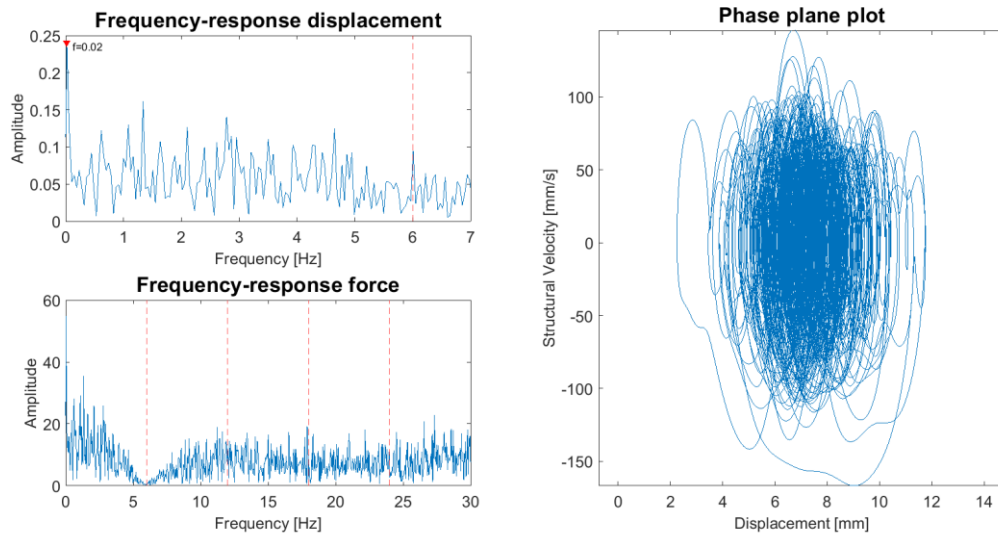
Test: SDOF-13. Fn: 6 Hz. V = 30 mm/s



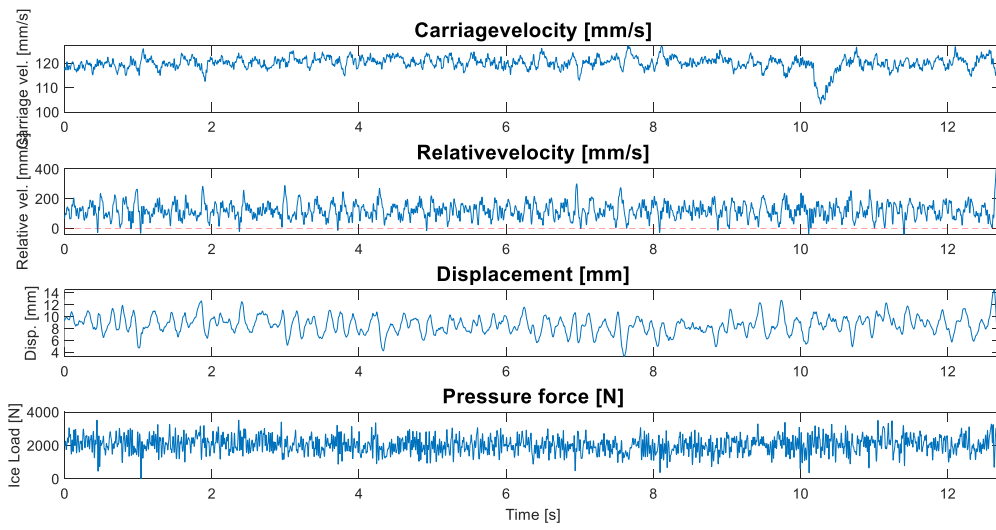
Test: SDOF-13. Fn: 6 Hz. V = 60 mm/s



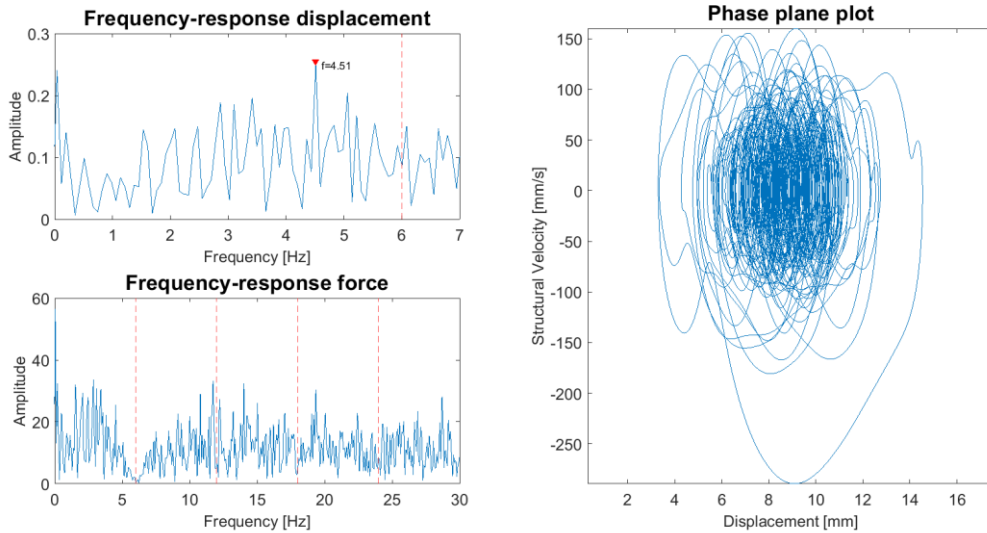
Test: SDOF-13. Fn: 6 Hz. V = 60 mm/s



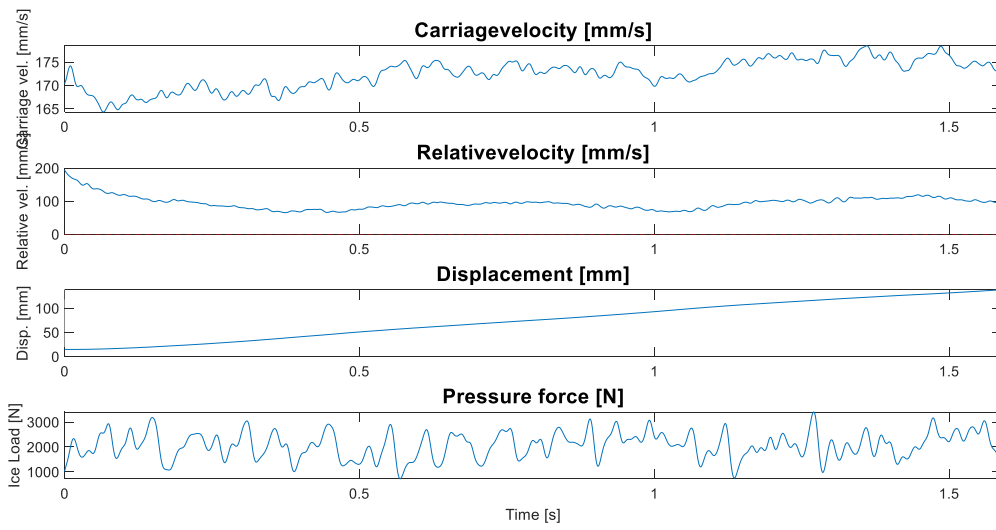
Test: SDOF-13. Fn: 6 Hz. V = 120 mm/s



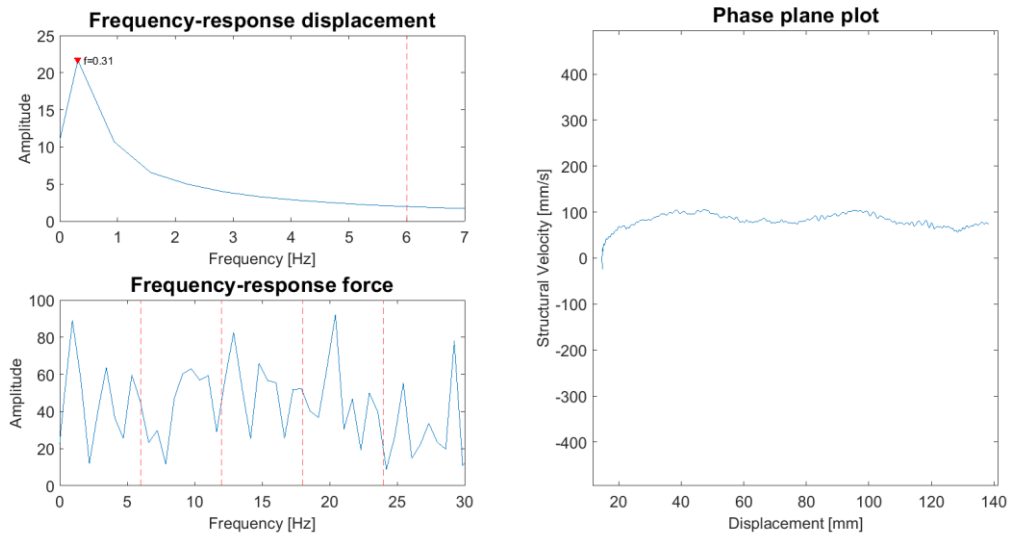
Test: SDOF-13. Fn: 6 Hz. V = 120 mm/s



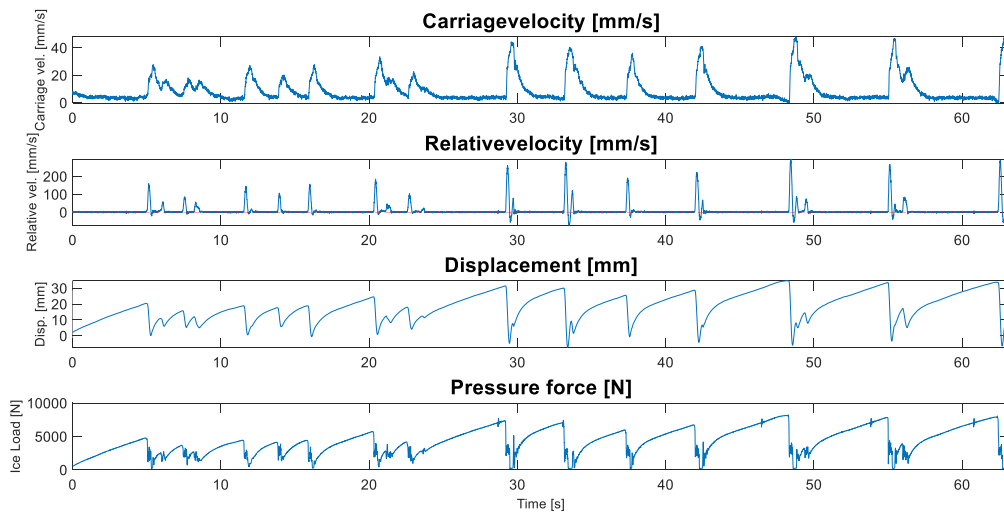
Test: SDOF-13. Fn: 6 Hz. V = 180 mm/s



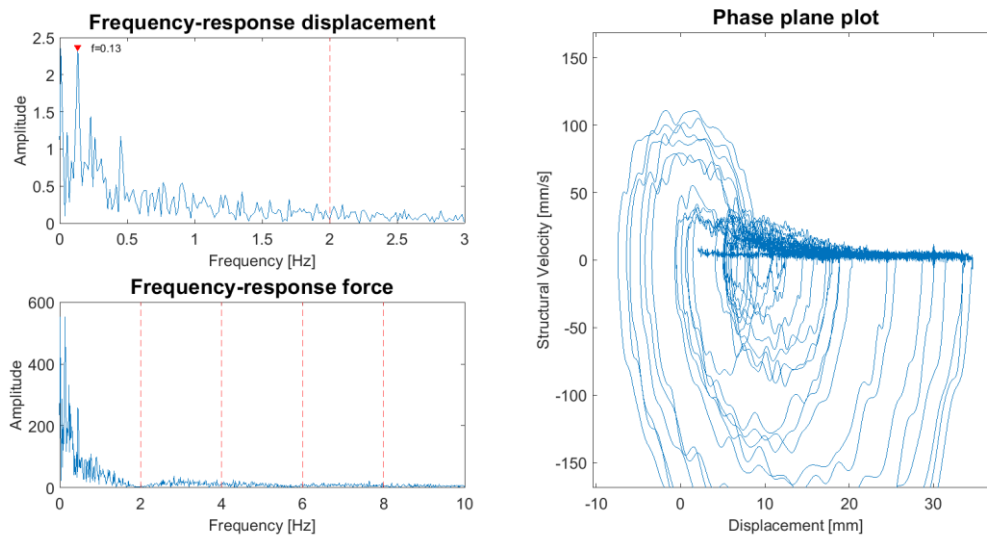
Test: SDOF-13. Fn: 6 Hz. V = 180 mm/s



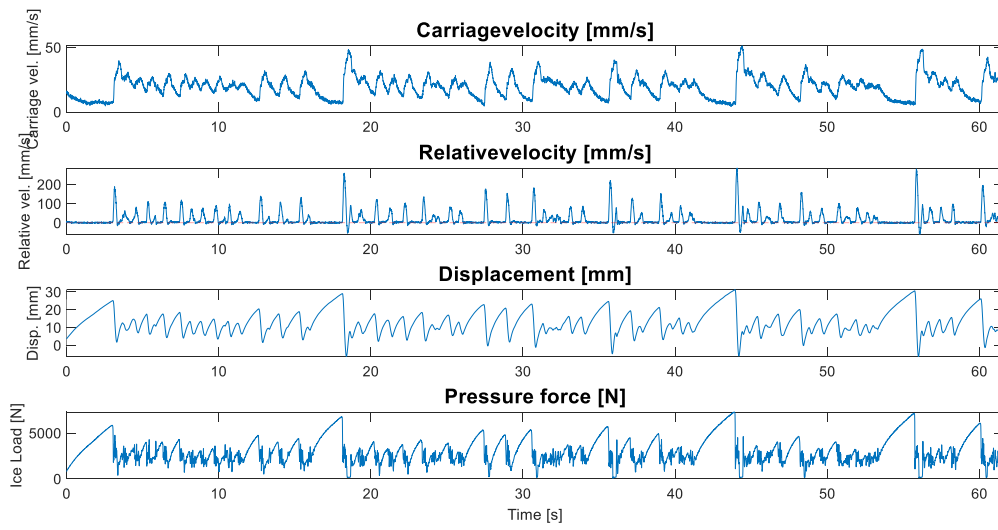
Test: SDOF-14. Fn: 2 Hz. V = 10 mm/s



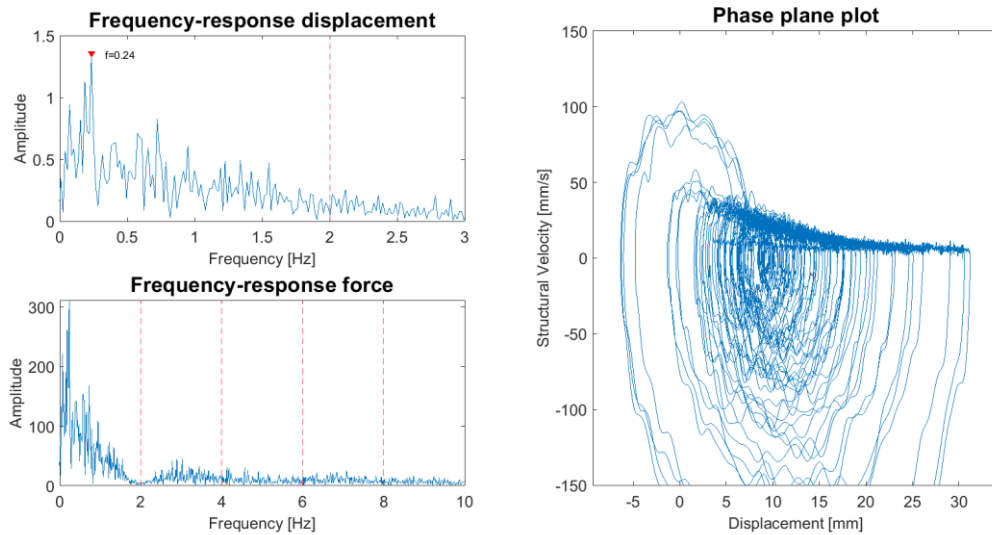
Test: SDOF-14. Fn: 2 Hz. V = 10 mm/s



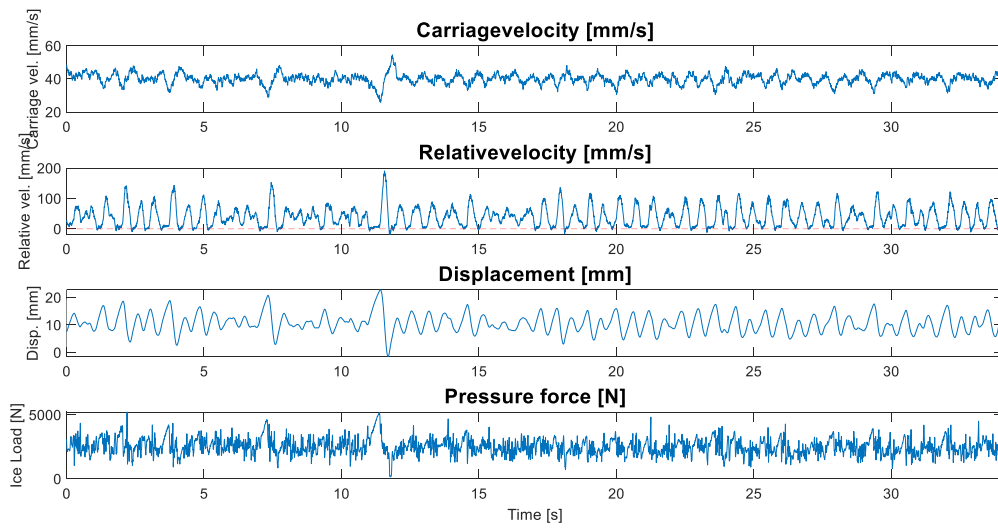
Test: SDOF-14. Fn: 2 Hz. V = 20 mm/s



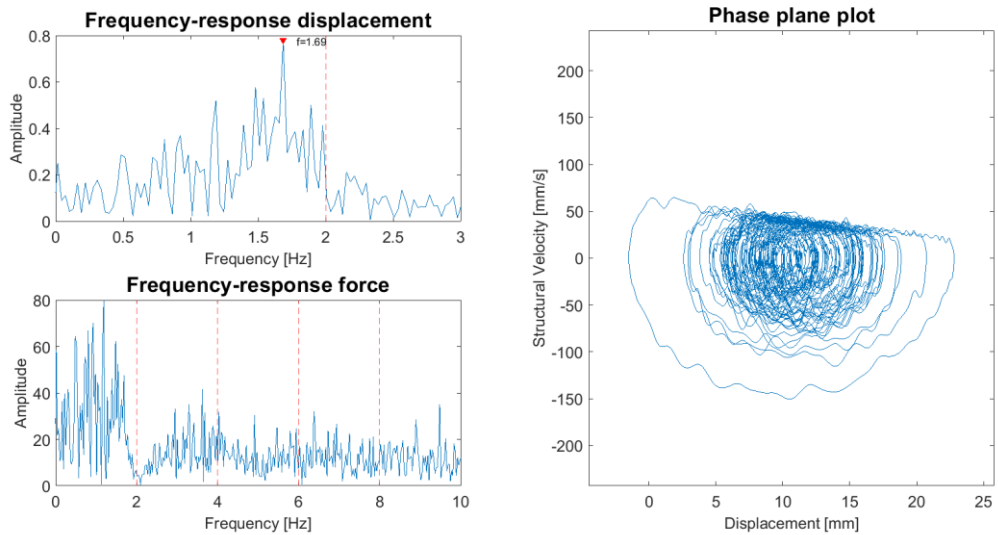
Test: SDOF-14. Fn: 2 Hz. V = 20 mm/s



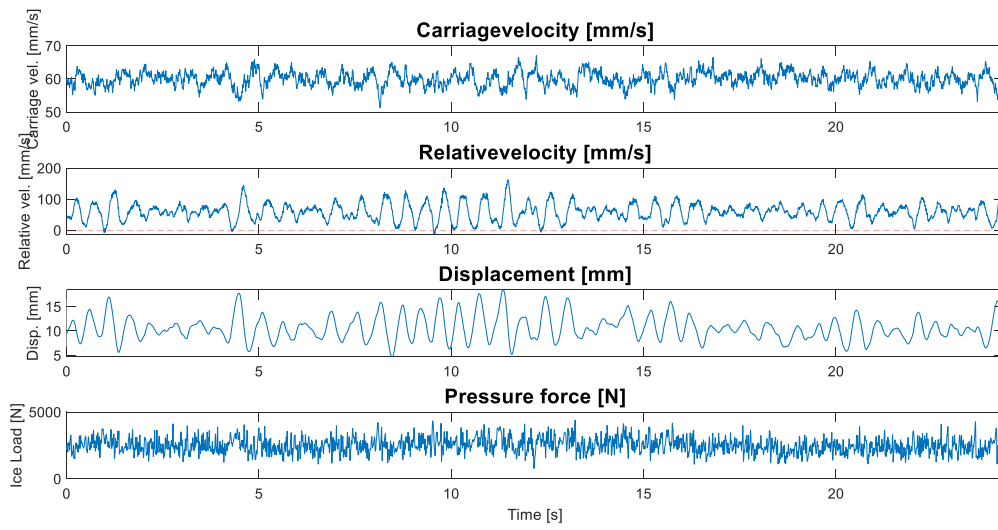
Test: SDOF-14. Fn: 2 Hz. V = 40 mm/s



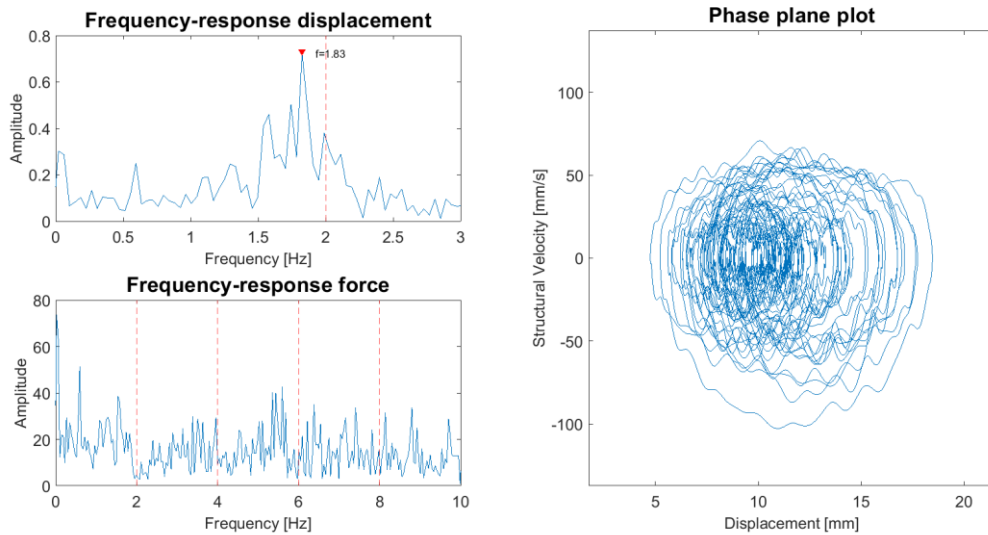
Test: SDOF-14. Fn: 2 Hz. V = 40 mm/s



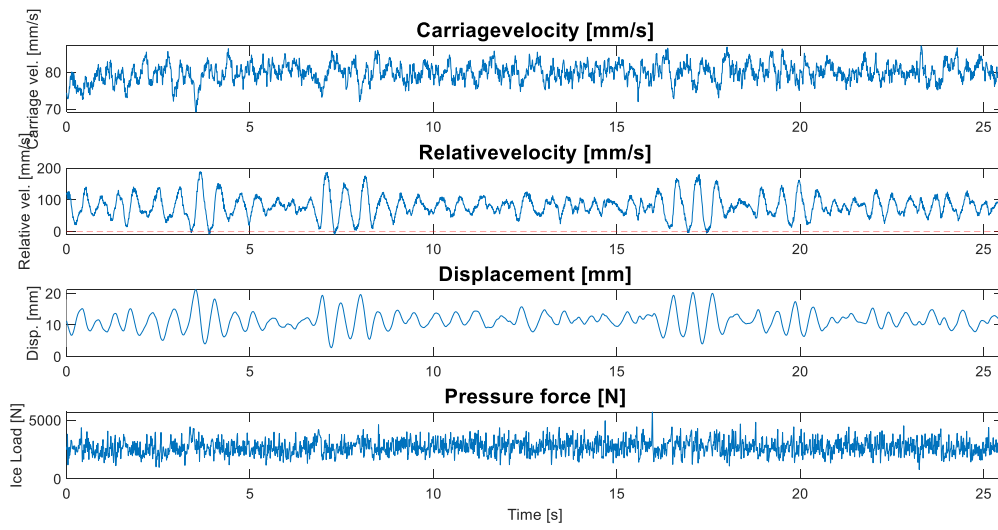
Test: SDOF-14. Fn: 2 Hz. V = 60 mm/s



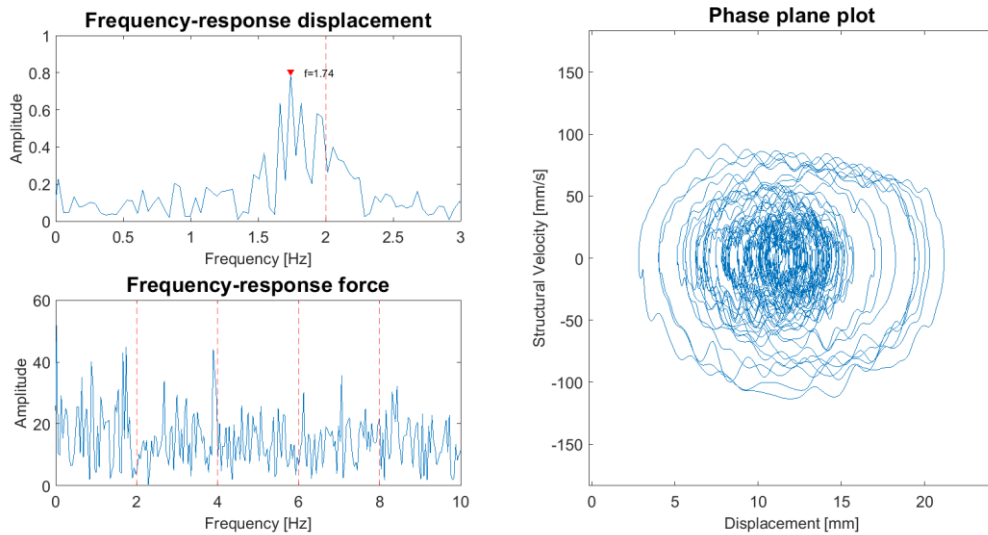
Test: SDOF-14. Fn: 2 Hz. V = 60 mm/s



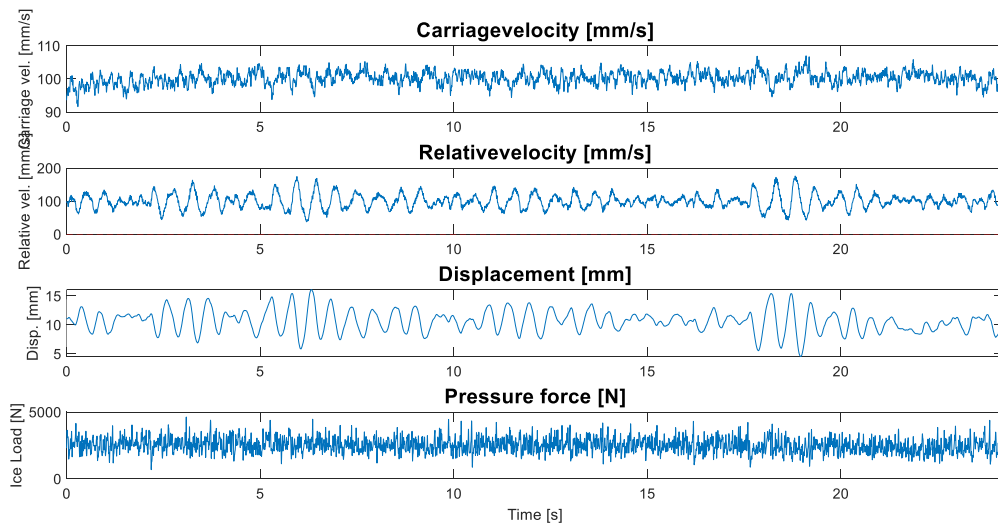
Test: SDOF-14. Fn: 2 Hz. V = 80 mm/s



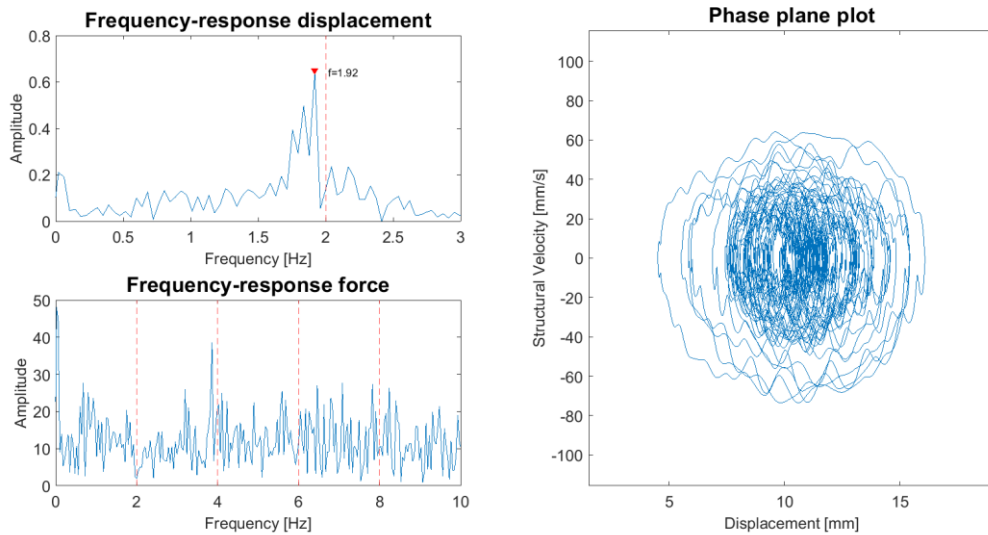
Test: SDOF-14. Fn: 2 Hz. V = 80 mm/s



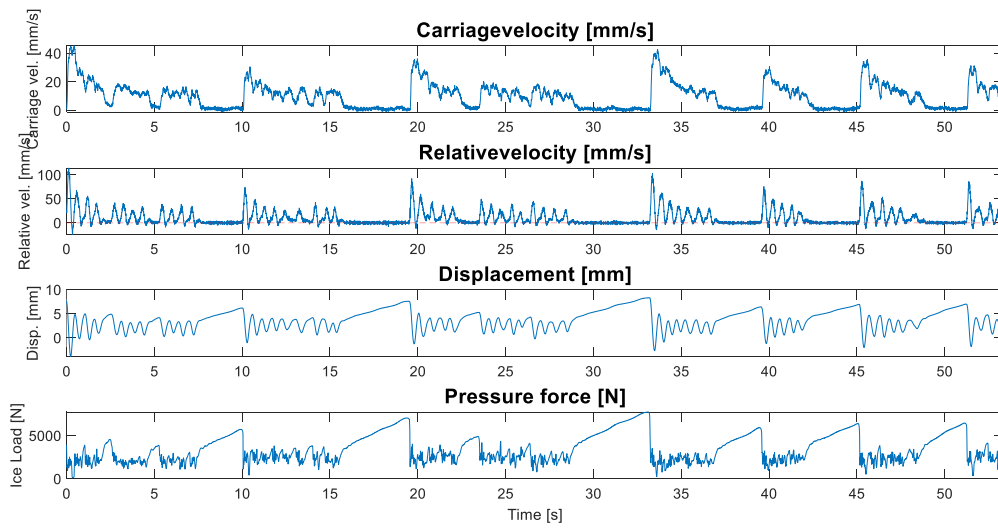
Test: SDOF-14. Fn: 2 Hz. V = 100 mm/s



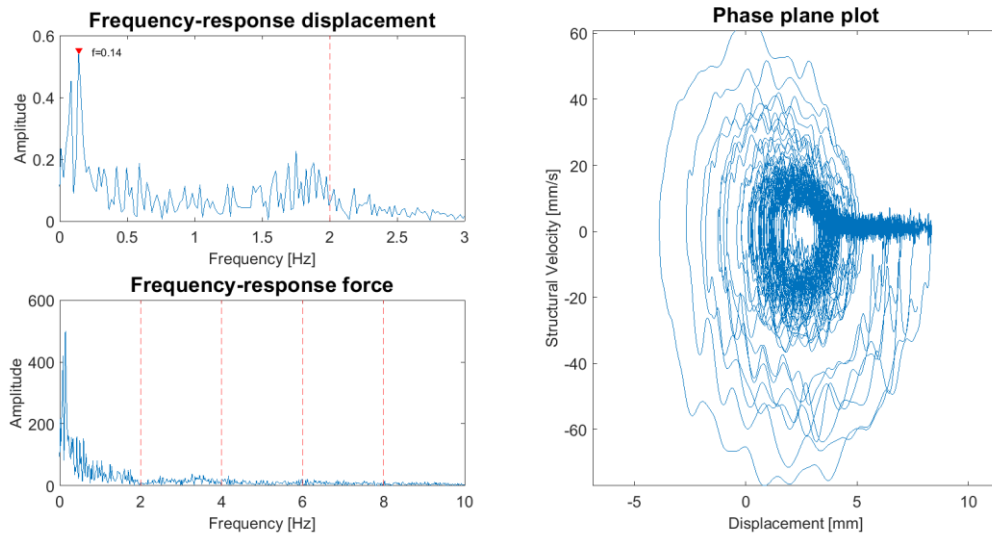
Test: SDOF-14. Fn: 2 Hz. V = 100 mm/s



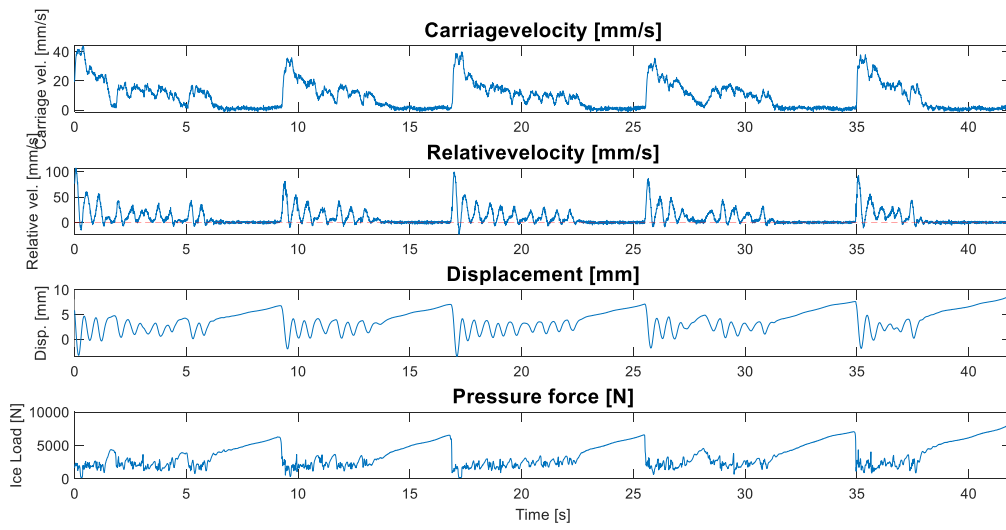
Test: SDOF-15. Fn: 2 Hz. V = 10 mm/s



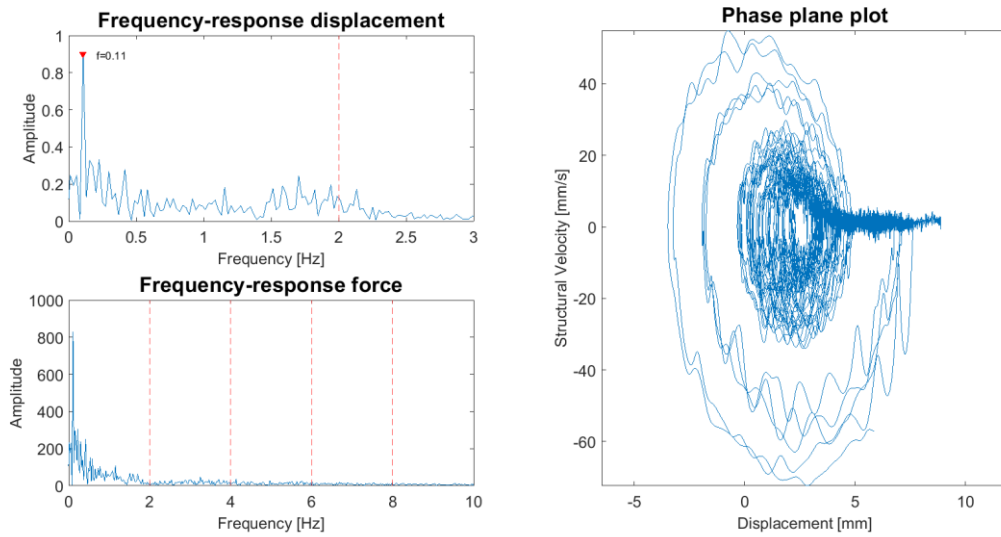
Test: SDOF-15. Fn: 2 Hz. V = 10 mm/s



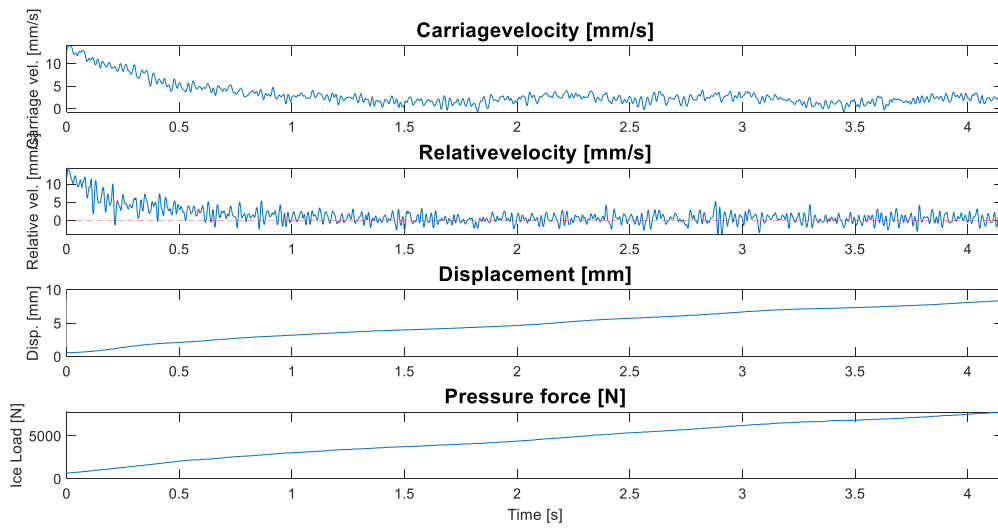
Test: SDOF-15. Fn: 2 Hz. V = 10 mm/s



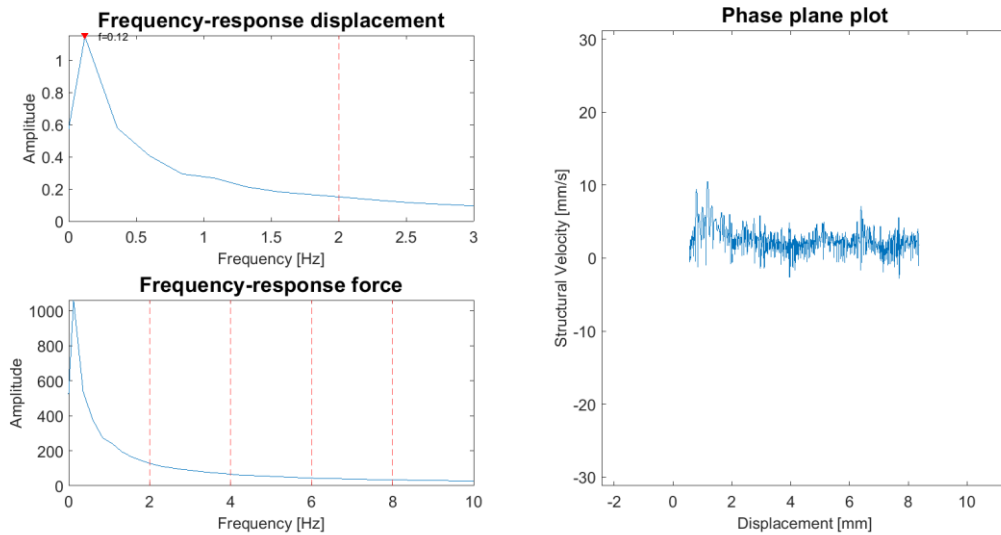
Test: SDOF-15. Fn: 2 Hz. V = 10 mm/s



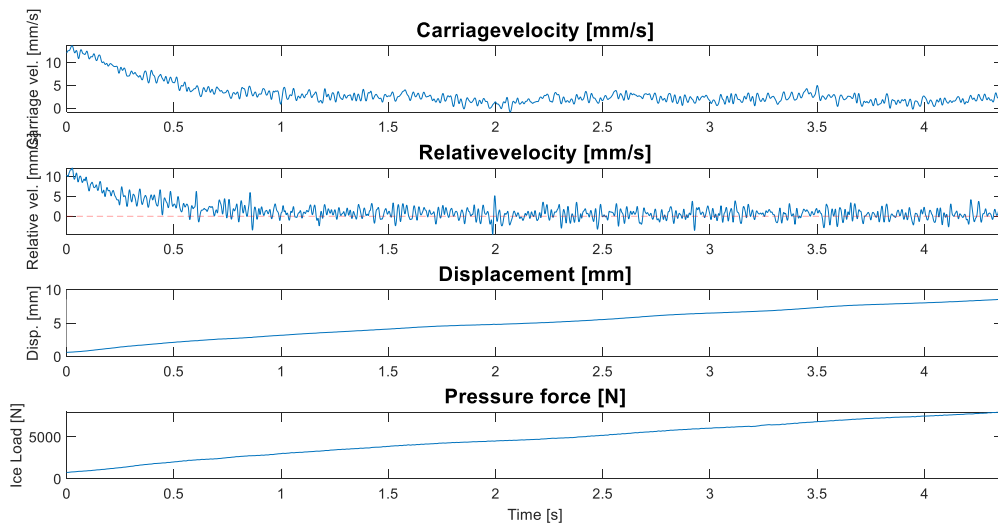
Test: SDOF-15. Fn: 2 Hz. V = 15 mm/s



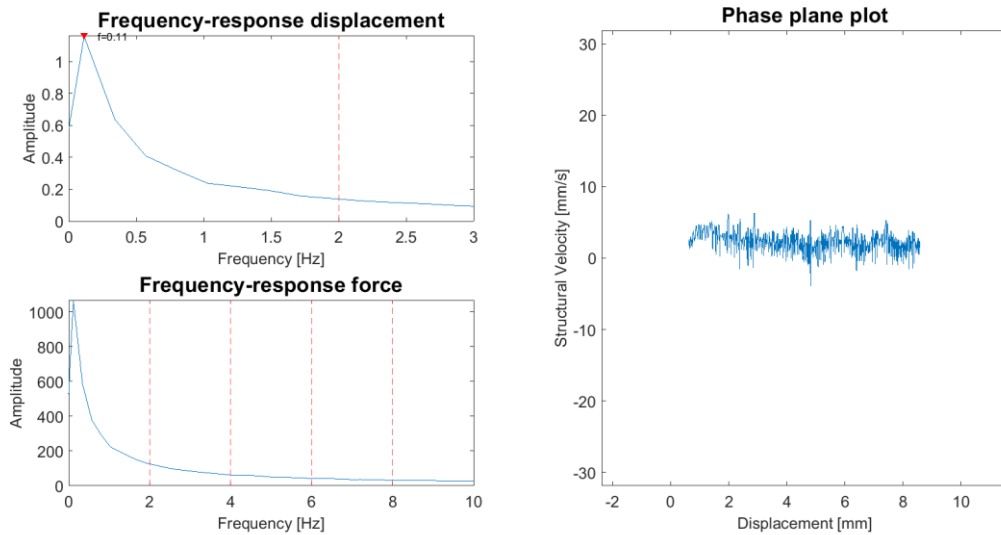
Test: SDOF-15. Fn: 2 Hz. V = 15 mm/s



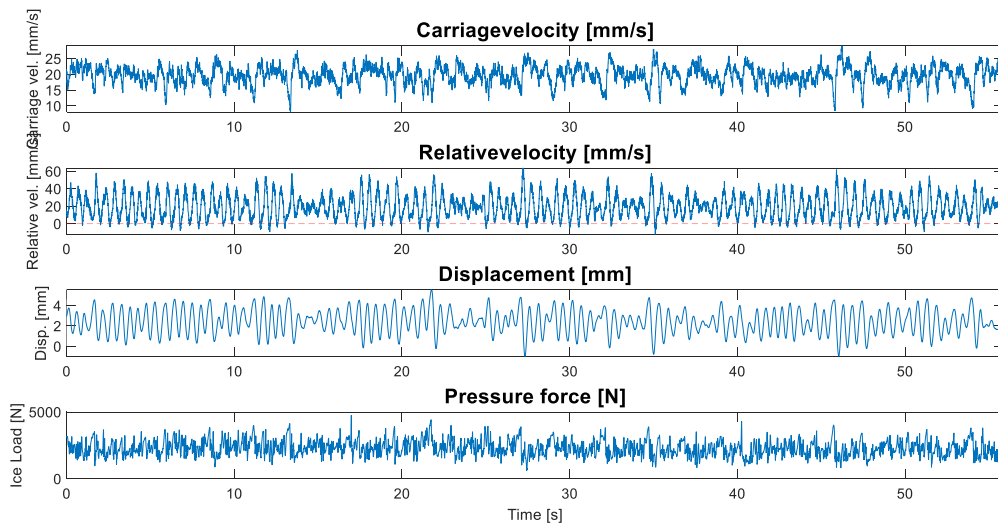
Test: SDOF-15. Fn: 2 Hz. V = 15 mm/s



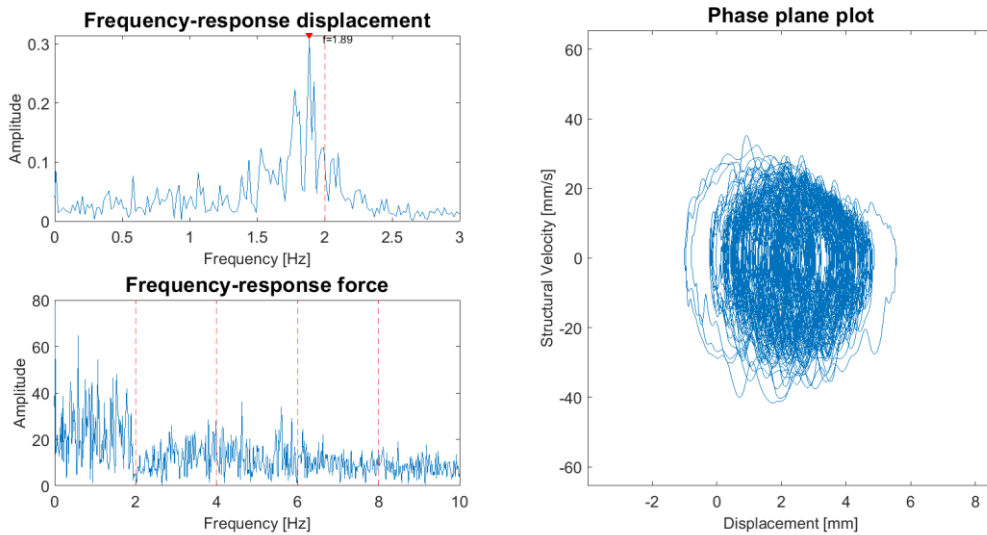
Test: SDOF-15. Fn: 2 Hz. V = 15 mm/s



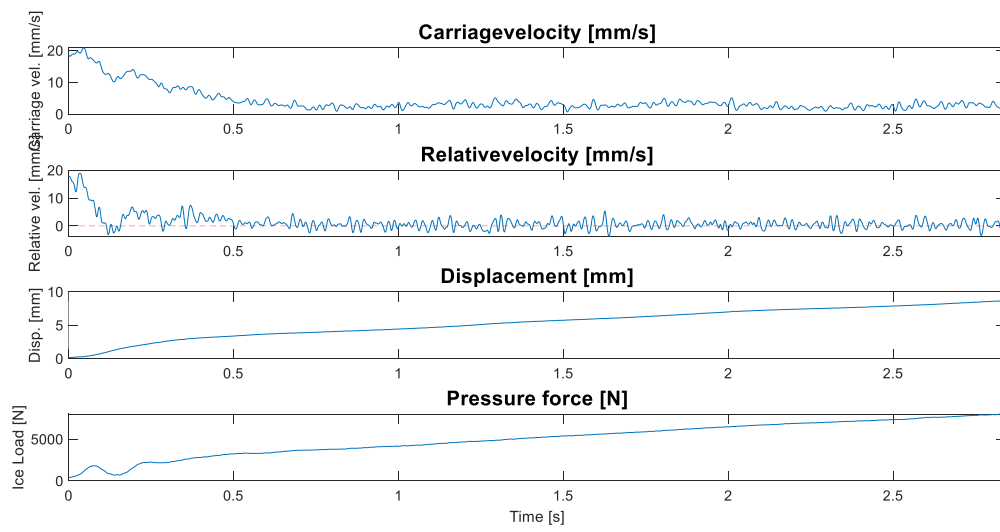
Test: SDOF-15. Fn: 2 Hz. V = 20 mm/s



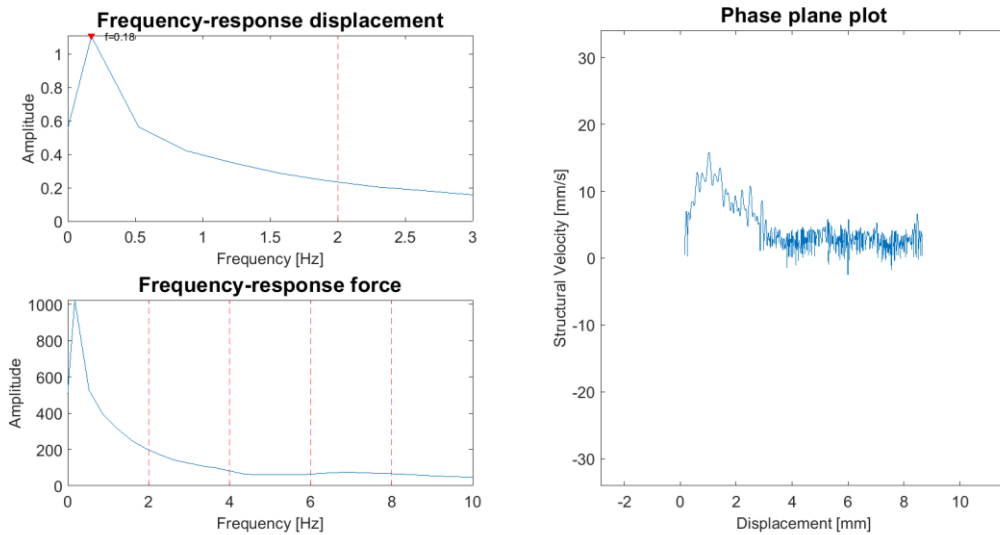
Test: SDOF-15. Fn: 2 Hz. V = 20 mm/s



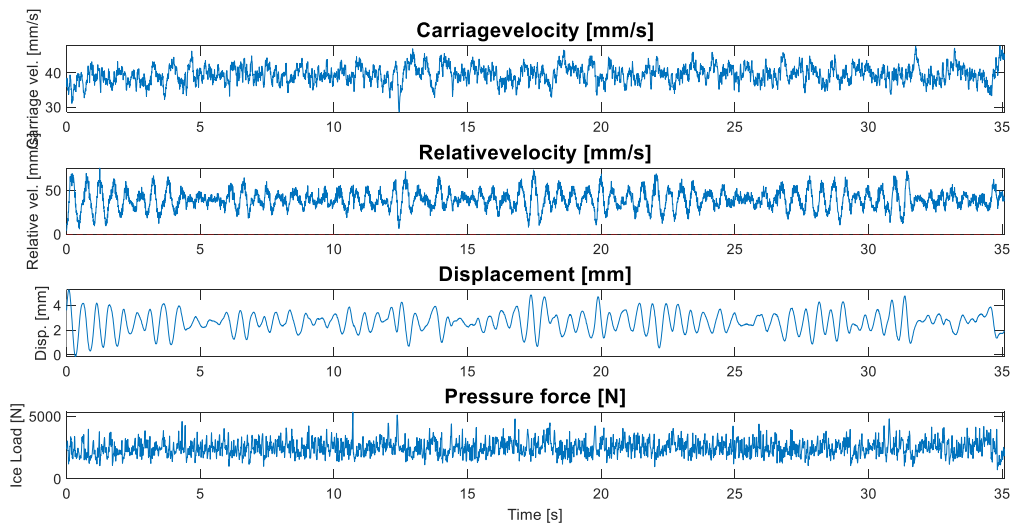
Test: SDOF-15. Fn: 2 Hz. V = 20 mm/s



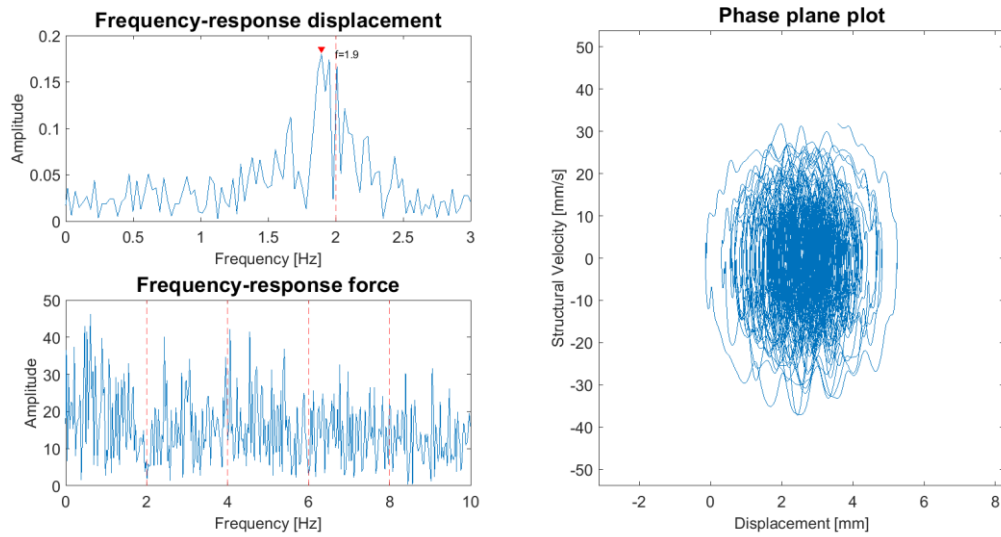
Test: SDOF-15. Fn: 2 Hz. V = 20 mm/s



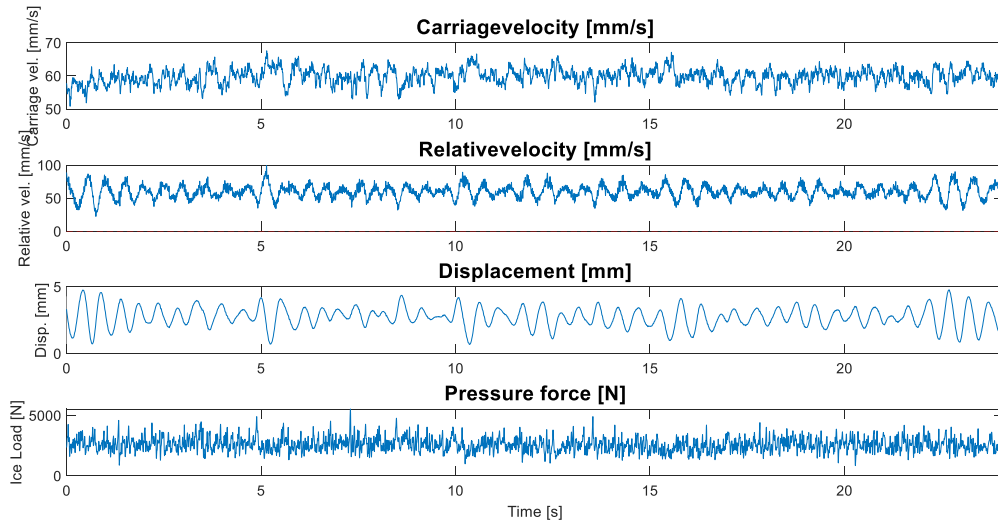
Test: SDOF-15. Fn: 2 Hz. V = 40 mm/s



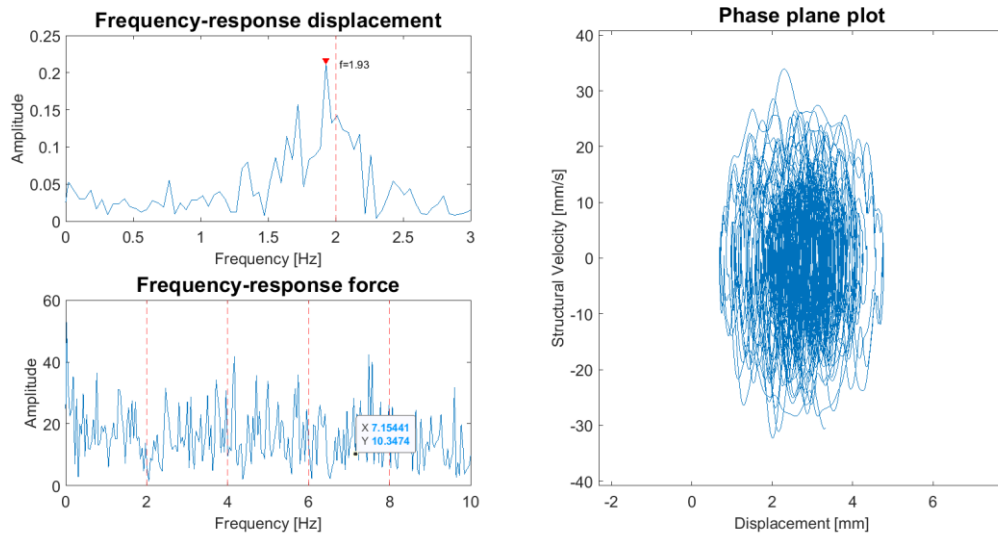
Test: SDOF-15. Fn: 2 Hz. V = 40 mm/s



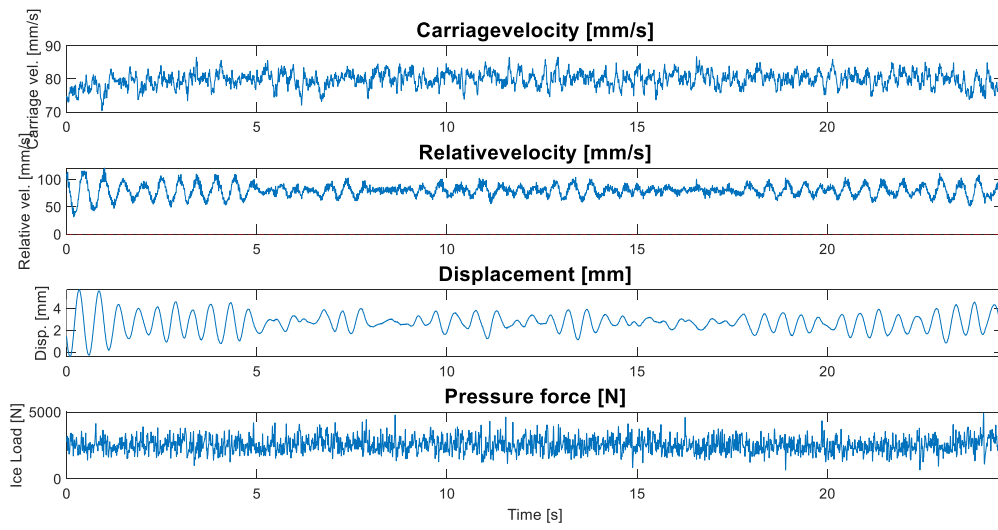
Test: SDOF-15. Fn: 2 Hz. V = 60 mm/s



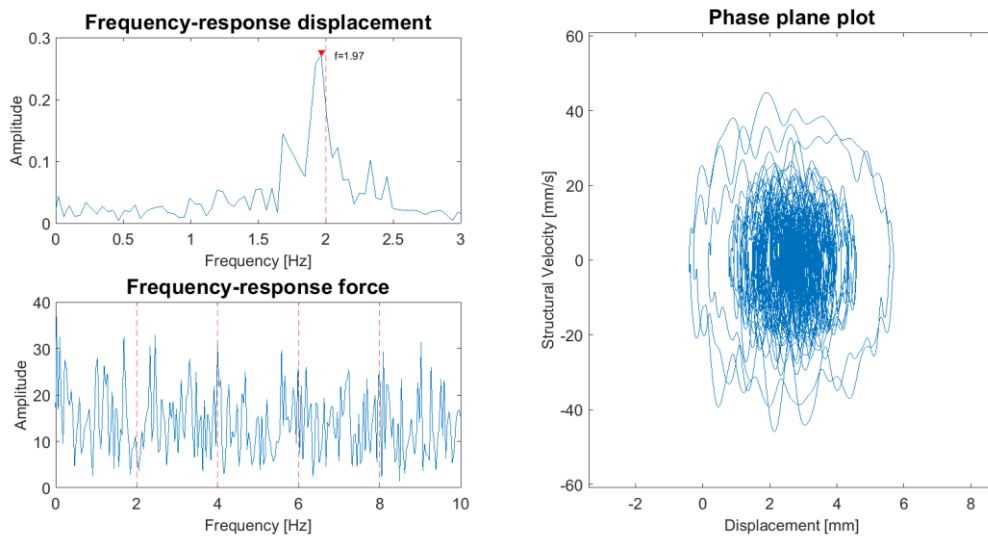
Test: SDOF-15. Fn: 2 Hz. V = 60 mm/s



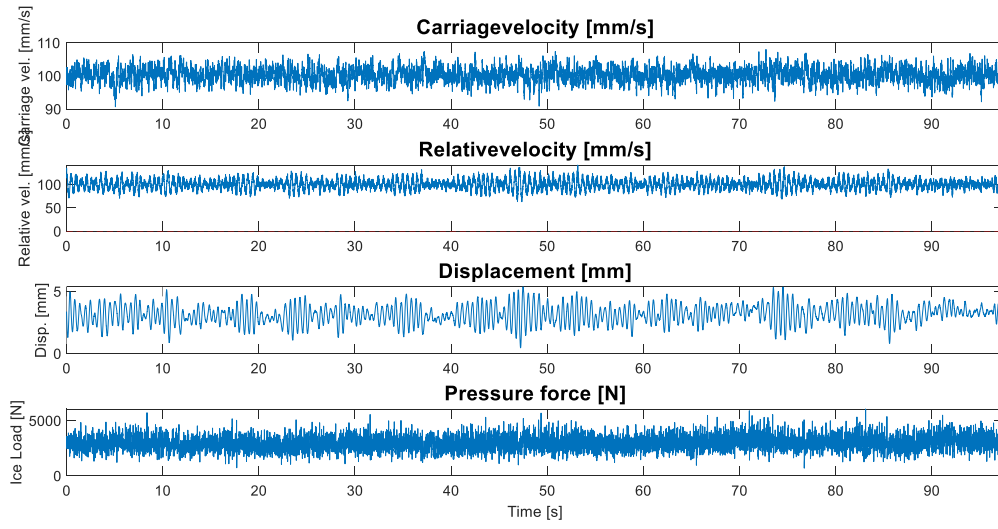
Test: SDOF-15. Fn: 2 Hz. V = 80 mm/s



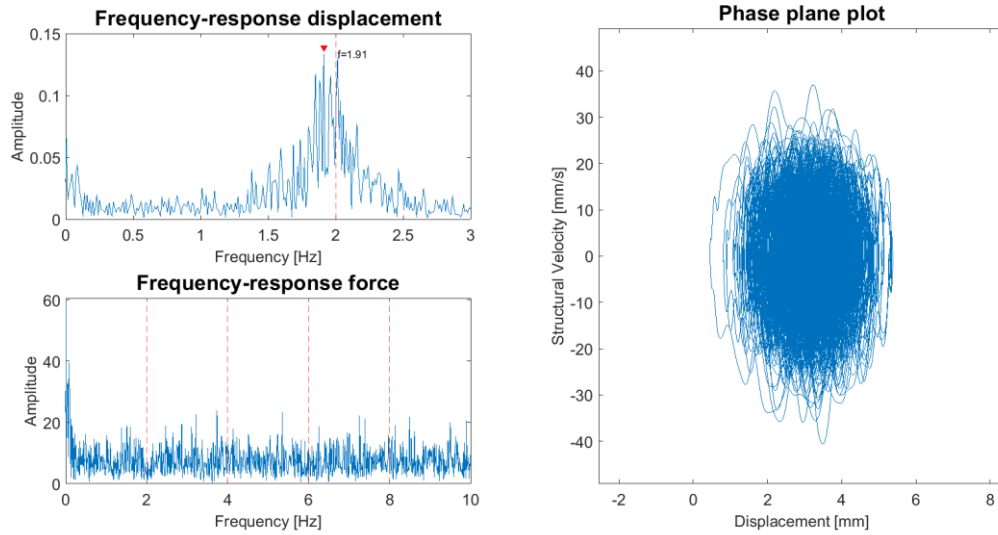
Test: SDOF-15. Fn: 2 Hz. V = 80 mm/s



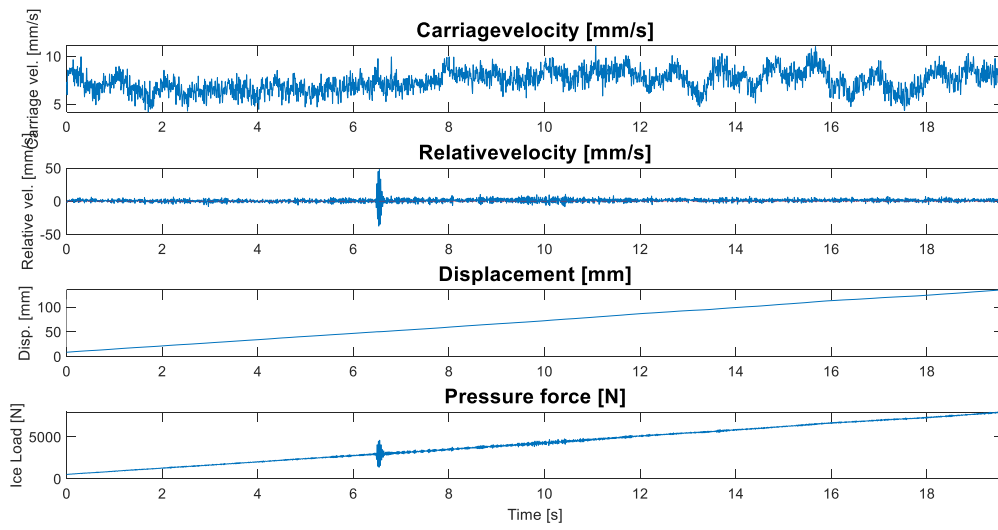
Test: SDOF-15. Fn: 2 Hz. V = 100 mm/s



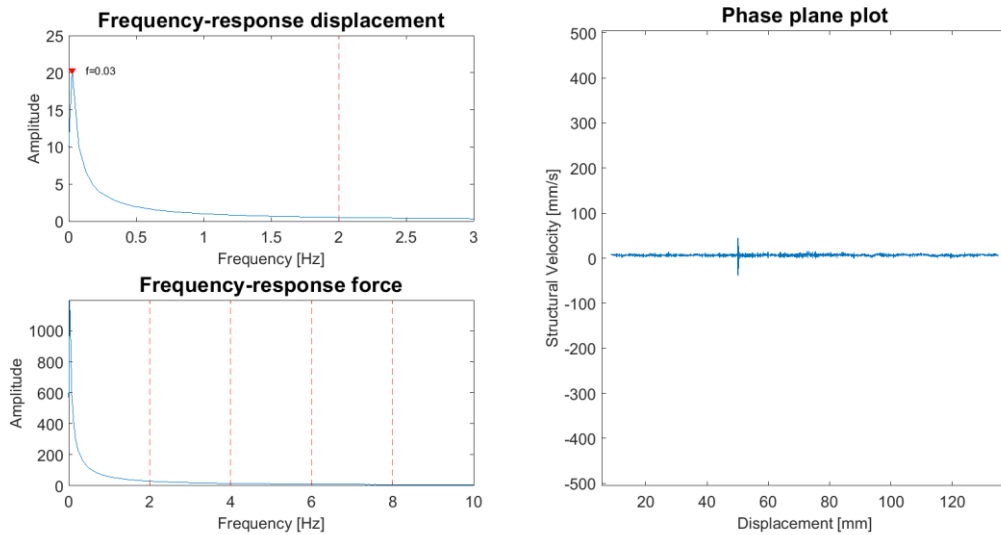
Test: SDOF-15. Fn: 2 Hz. V = 100 mm/s



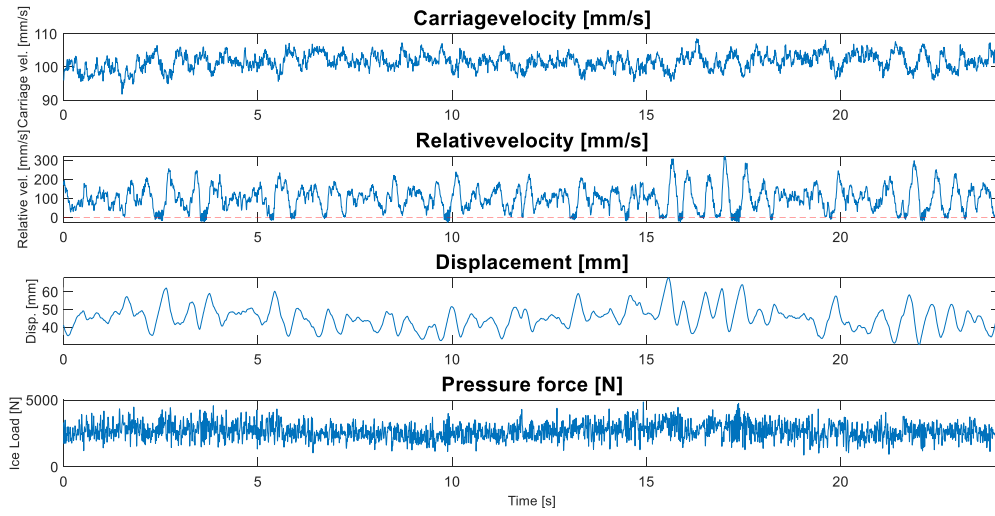
Test: SDOF-16. Fn: 2 Hz. V = 10 mm/s



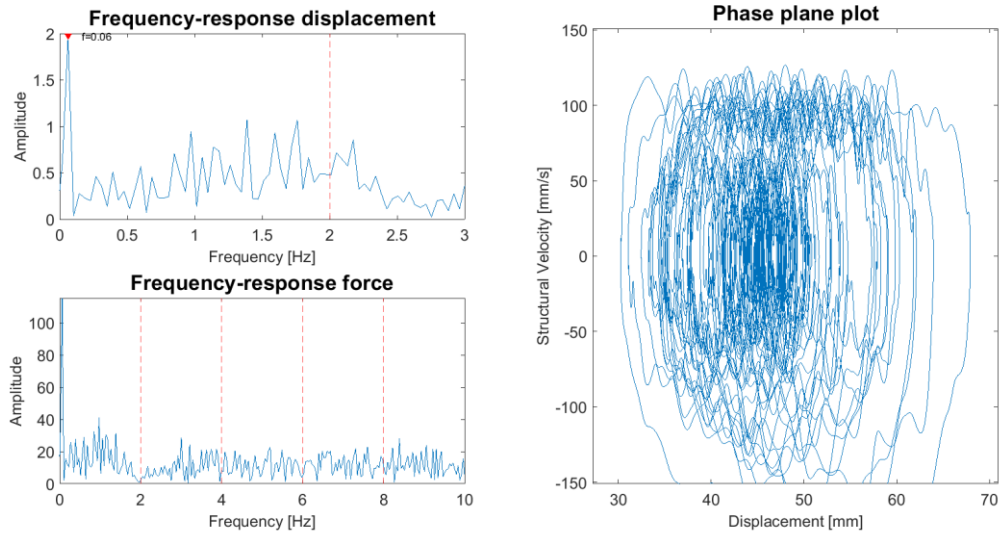
Test: SDOF-16. Fn: 2 Hz. V = 10 mm/s



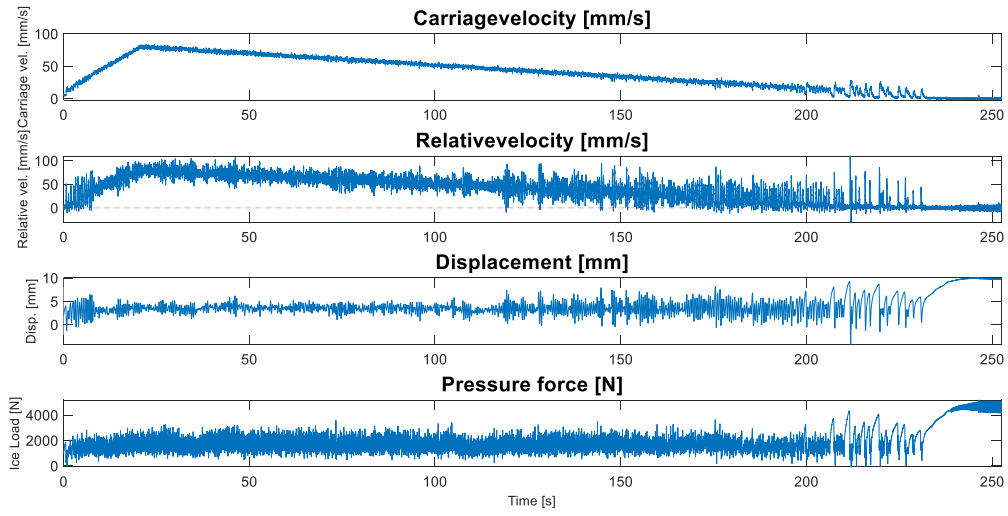
Test: SDOF-16. Fn: 2 Hz. V = 100 mm/s



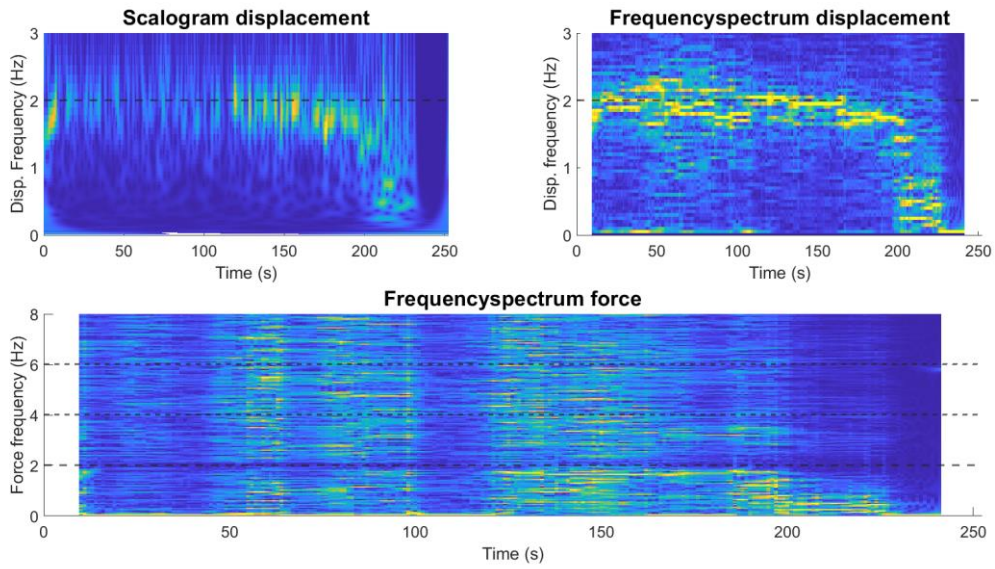
Test: SDOF-16. Fn: 2 Hz. V = 100 mm/s



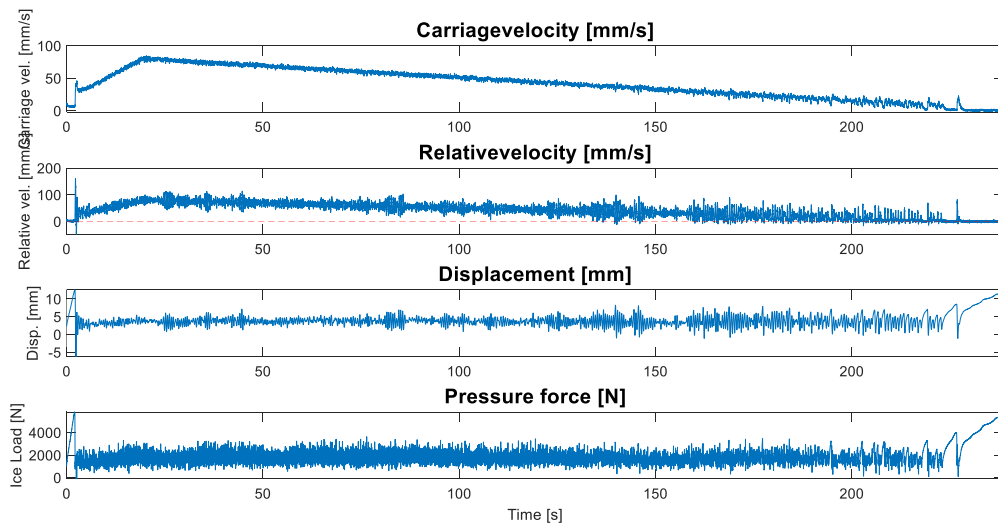
Test: SDOF-17. Fn: 2 Hz.



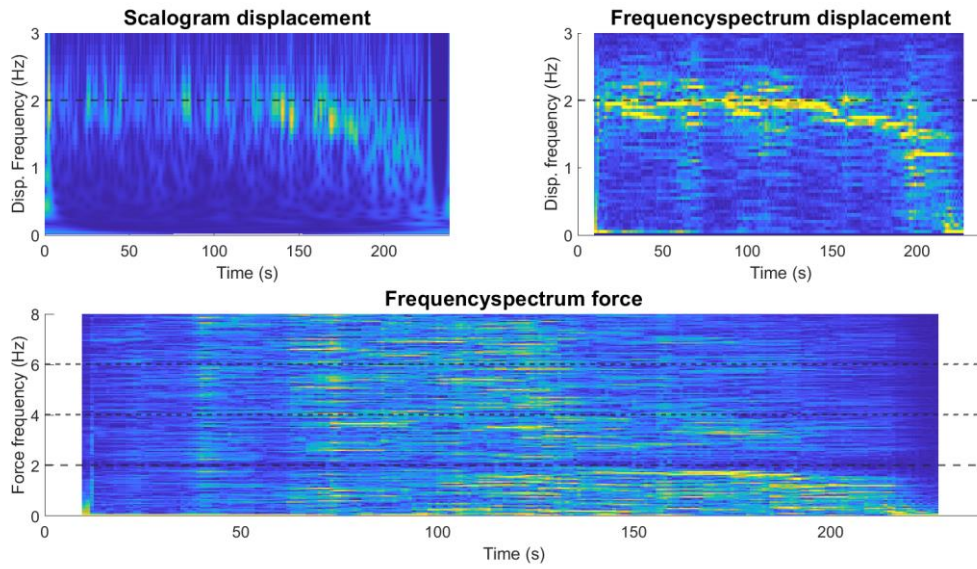
Test: SDOF-17. Fn: 2 Hz.



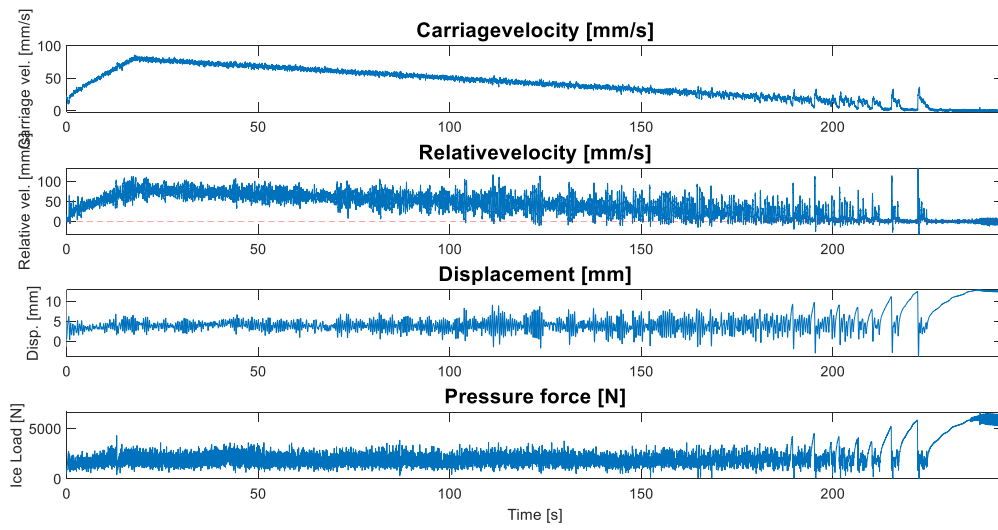
Test: SDOF-18. Fn: 2 Hz.



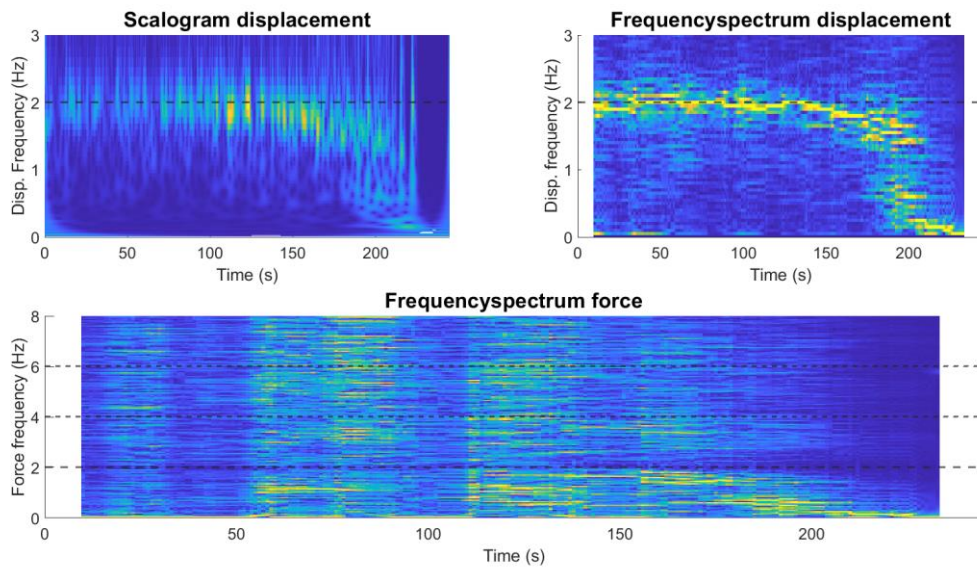
Test: SDOF-18. Fn: 2 Hz.



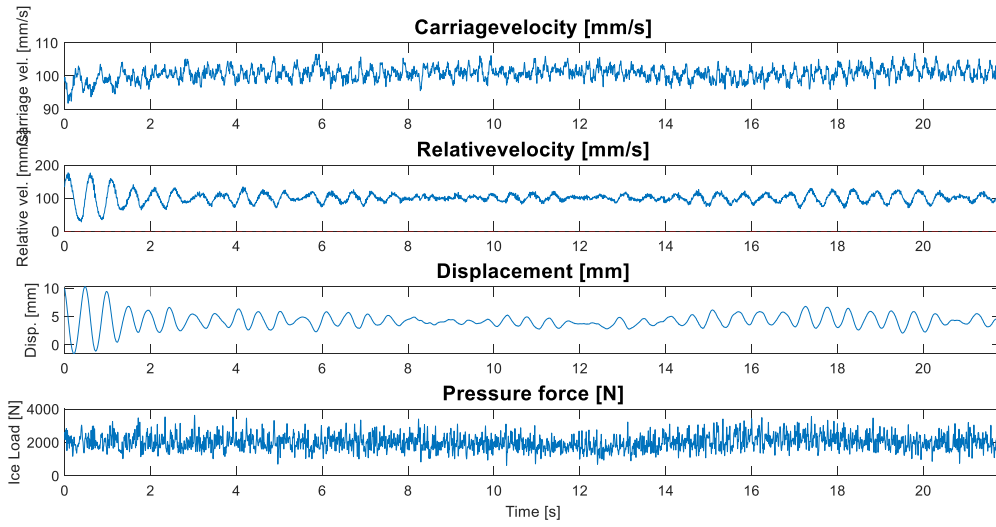
Test: SDOF-19. Fn: 2 Hz.



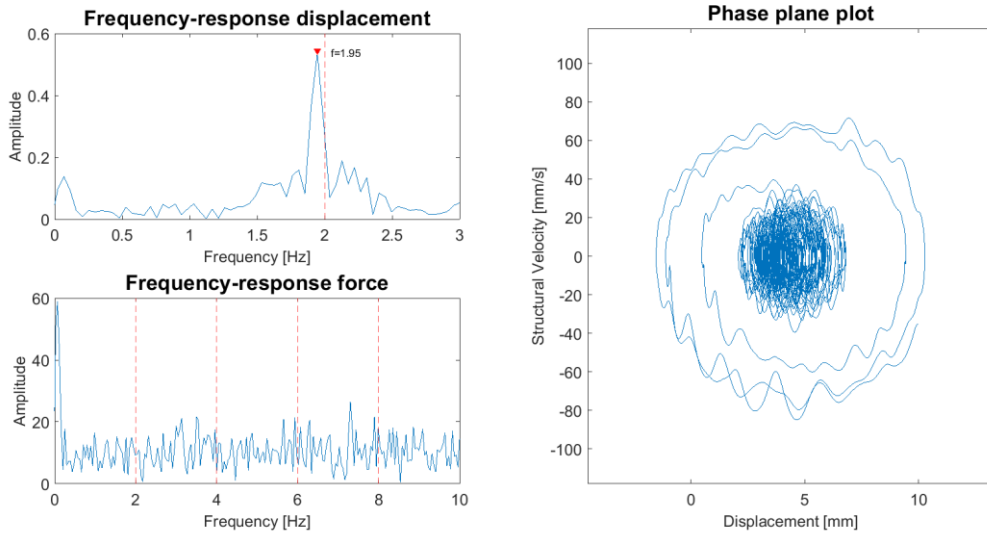
Test: SDOF-19. Fn: 2 Hz.



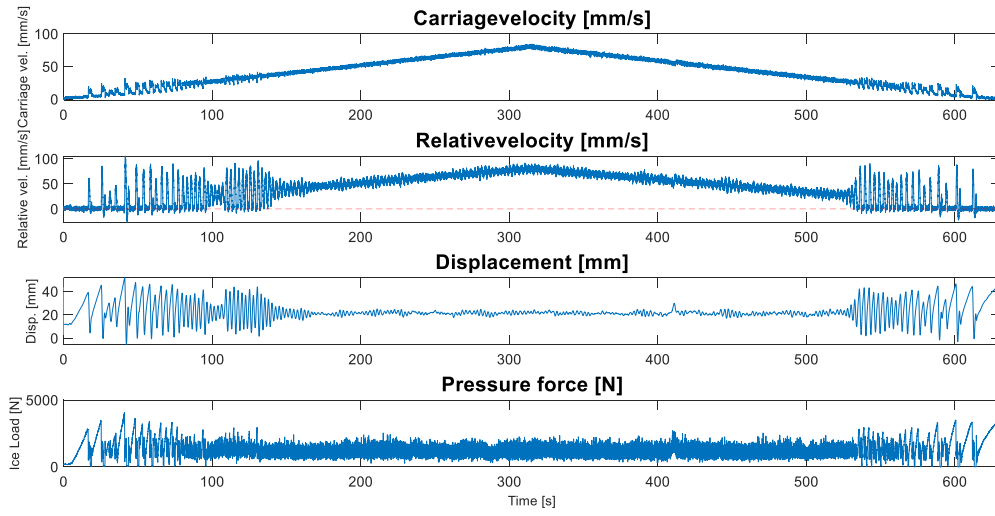
Test: SDOF-19. Fn: 2 Hz. V = 100 mm/s



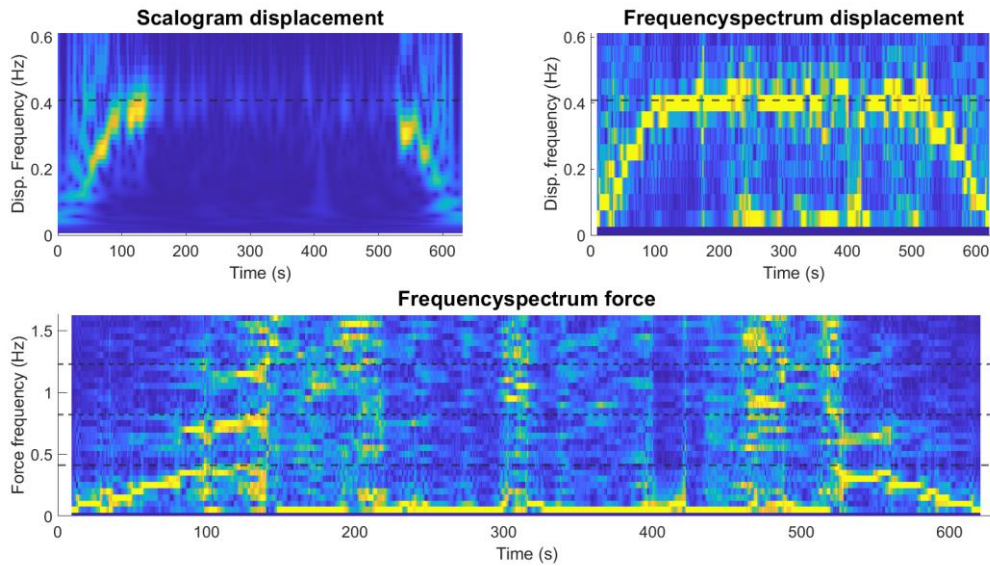
Test: SDOF-19. Fn: 2 Hz. V = 100 mm/s



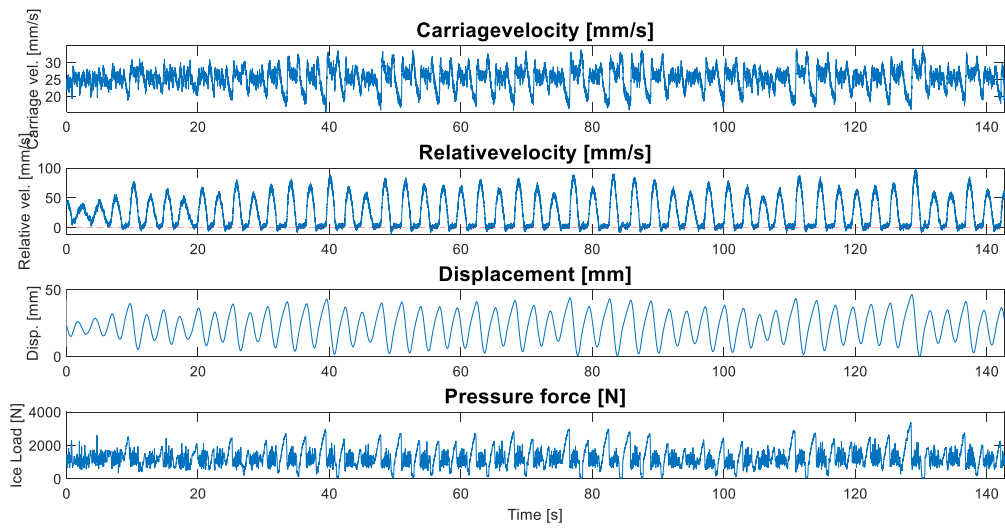
Test: SDOF-20. Fn: 0.40825 Hz.



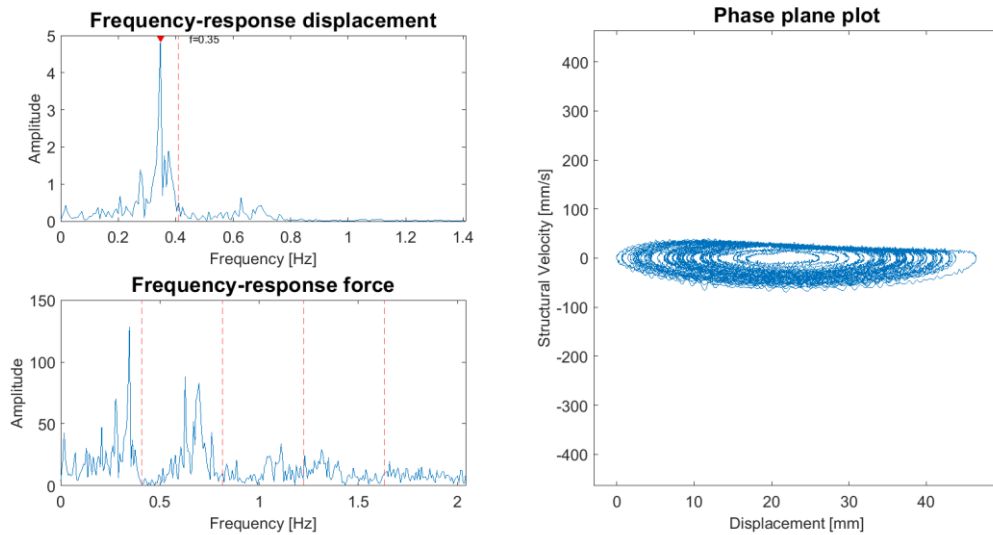
Test: SDOF-20. Fn: 0.40825 Hz.



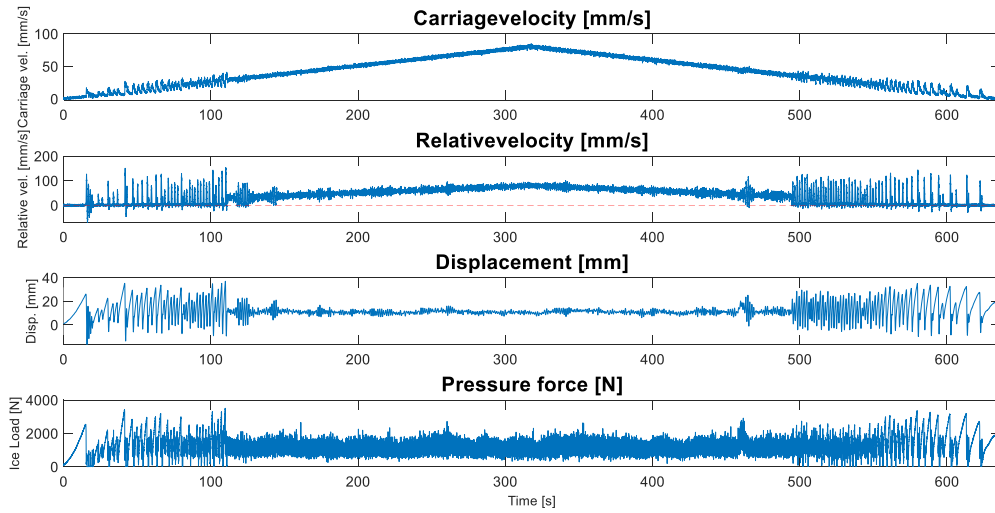
Test: SDOF-20. Fn: 0.40825 Hz. V = 25 mm/s



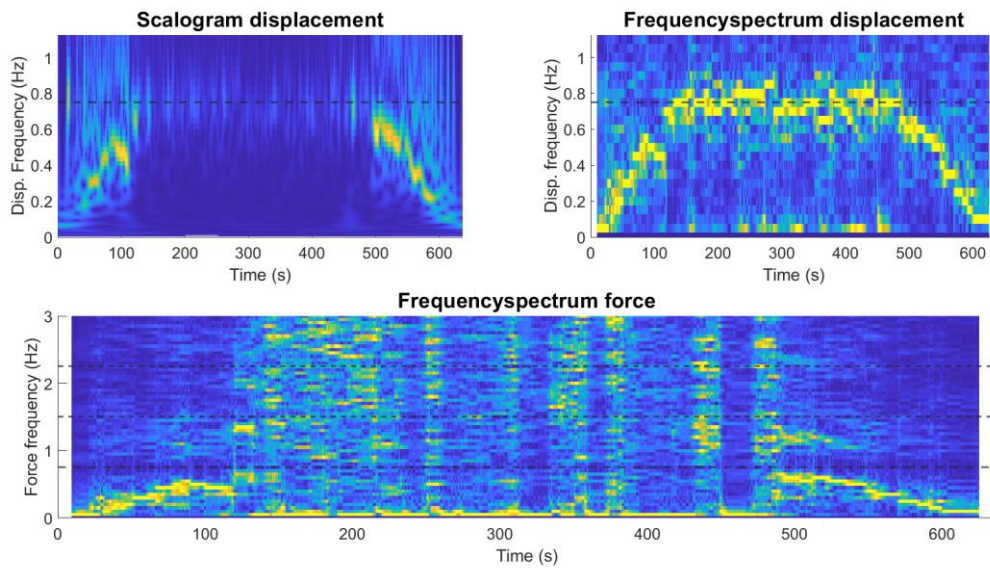
Test: SDOF-20. Fn: 0.40825 Hz. V = 25 mm/s



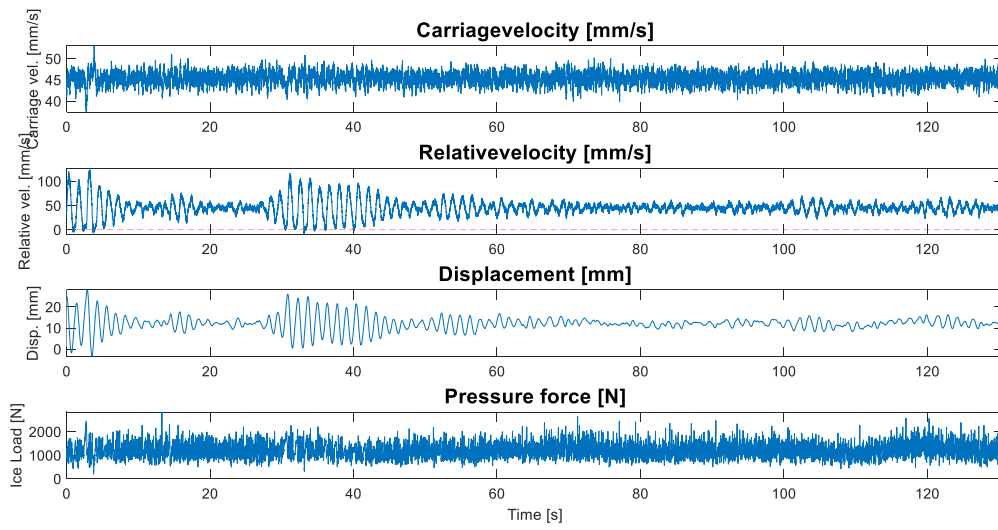
Test: SDOF-21. Fn: 0.75 Hz.



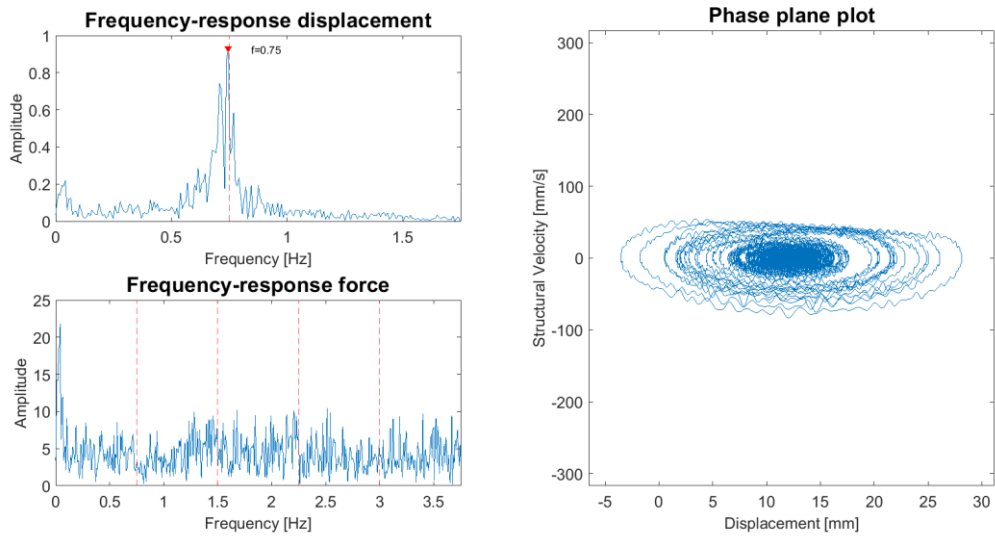
Test: SDOF-21. Fn: 0.75 Hz.



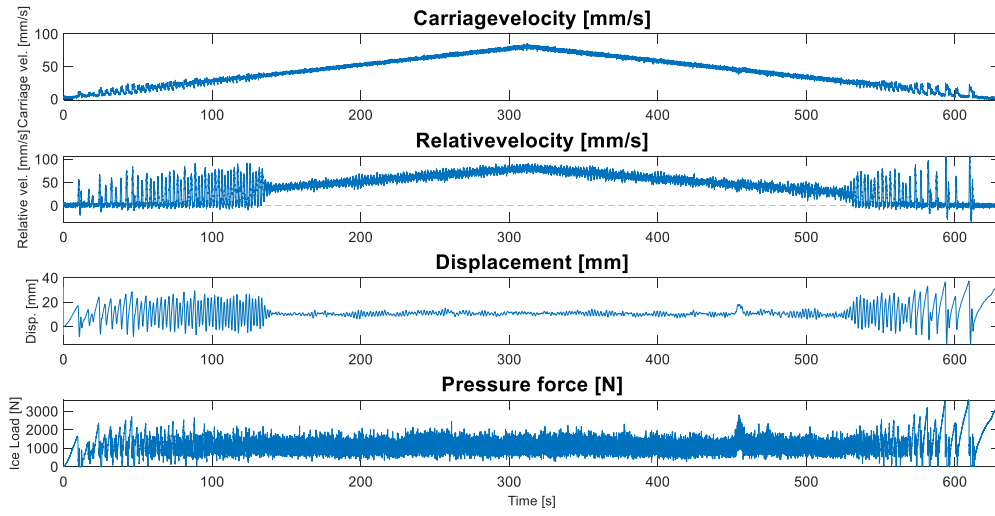
Test: SDOF-21. Fn: 0.75 Hz. V = 45 mm/s



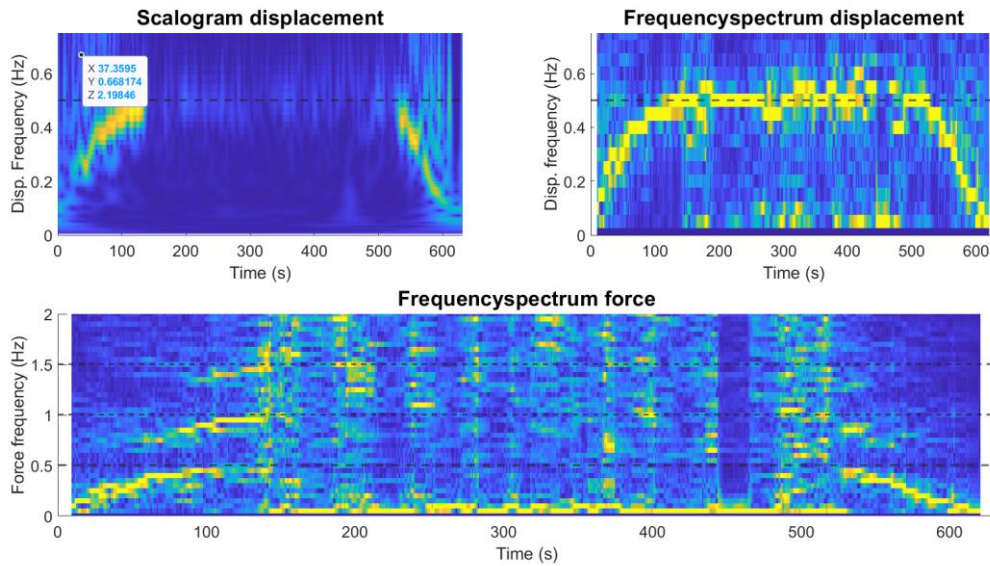
Test: SDOF-21. Fn: 0.75 Hz. V = 45 mm/s



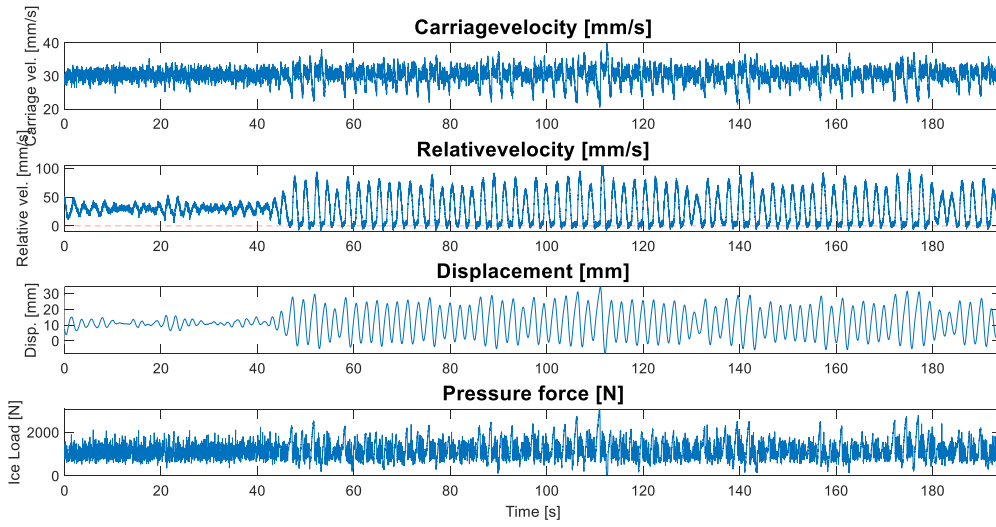
Test: SDOF-22. Fn: 0.5 Hz.



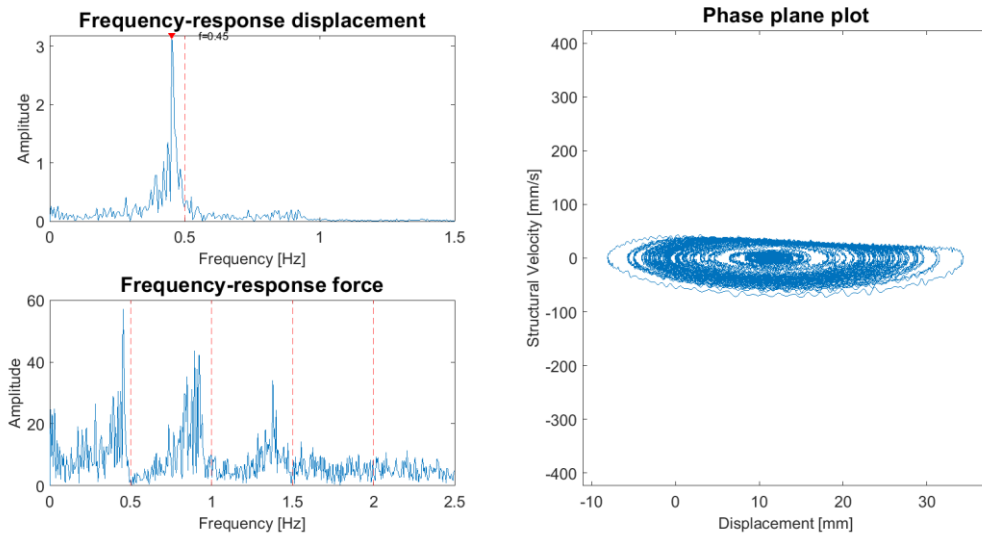
Test: SDOF-22. Fn: 0.5 Hz.



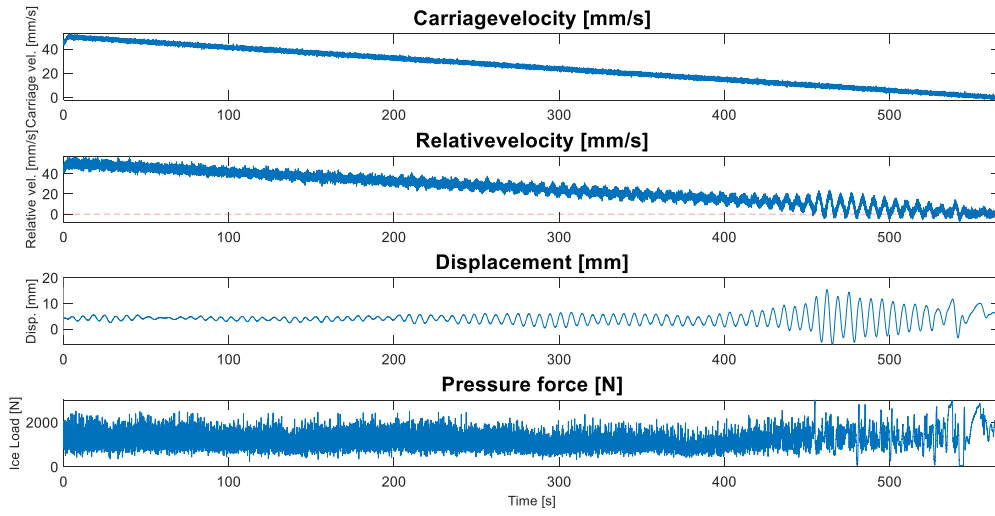
Test: SDOF-22. Fn: 0.5 Hz. V = 30 mm/s



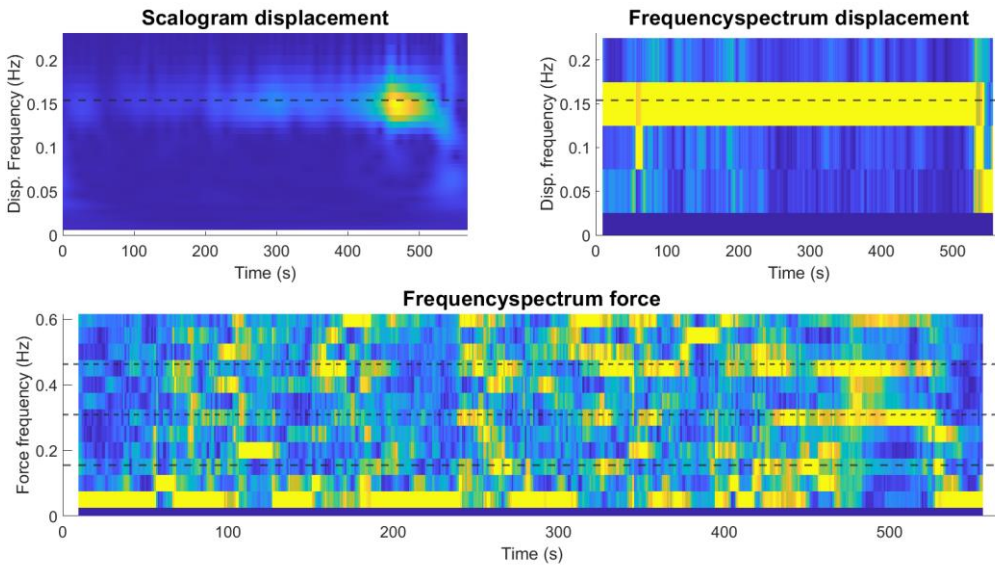
Test: SDOF-22. Fn: 0.5 Hz. V = 30 mm/s



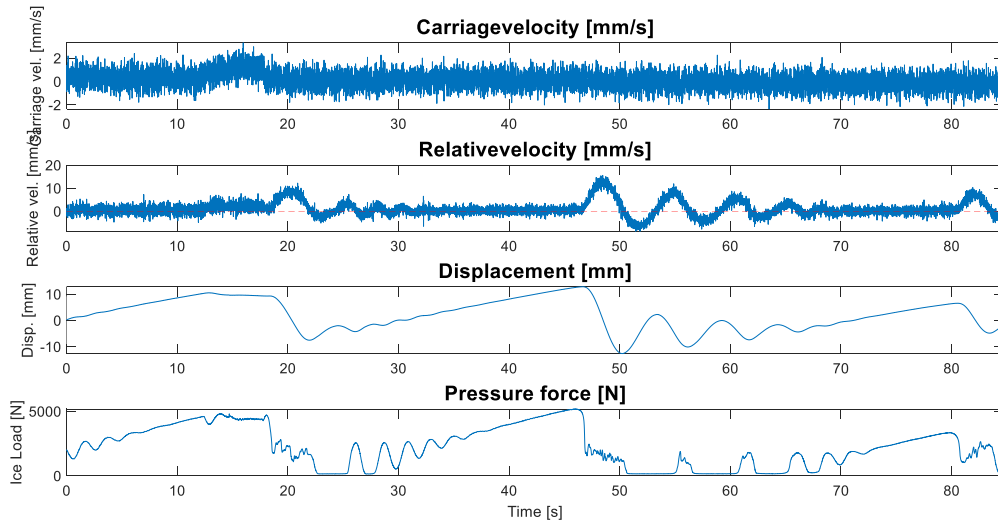
Test: SDOF-23. Fn: 0.154 Hz.



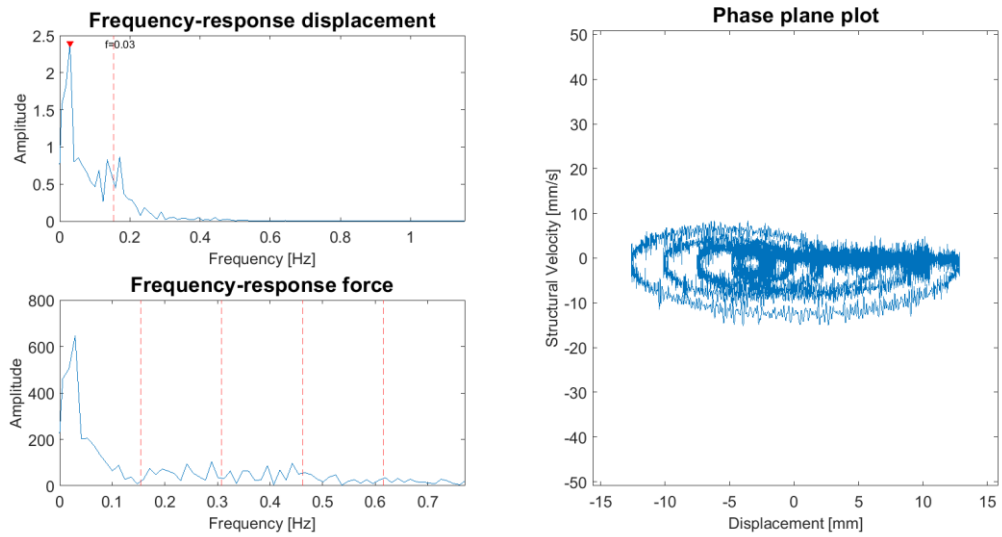
Test: SDOF-23. Fn: 0.154 Hz.



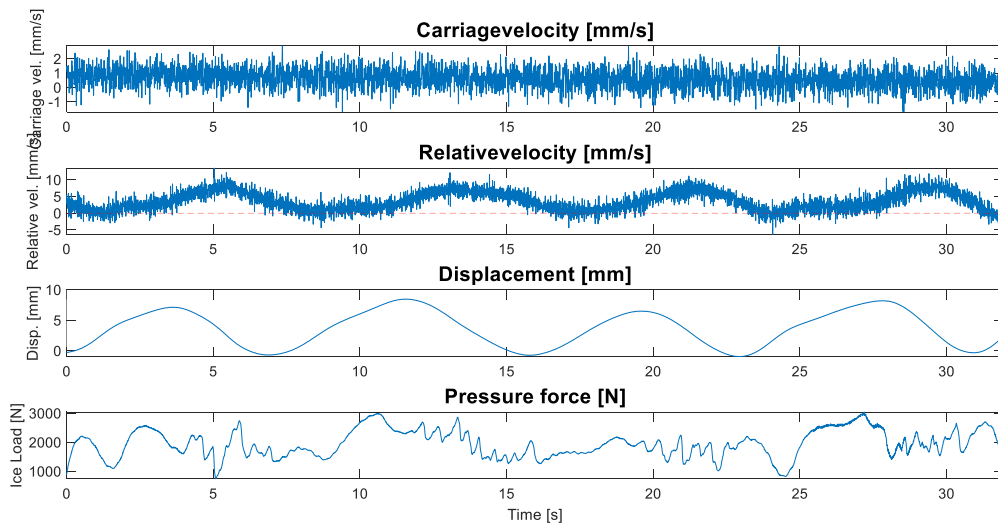
Test: SDOF-23. Fn: 0.154 Hz. V = 1 mm/s



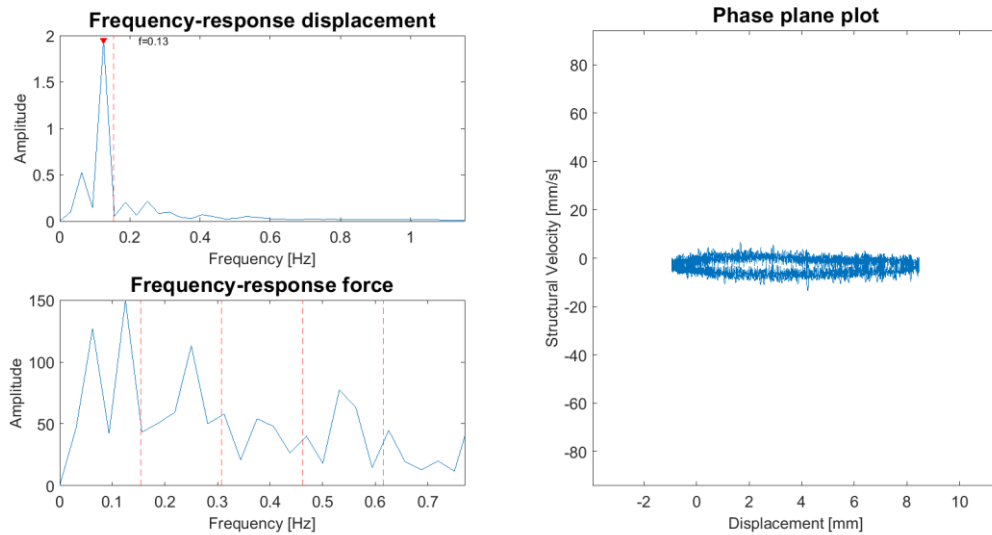
Test: SDOF-23. Fn: 0.154 Hz. V = 1 mm/s



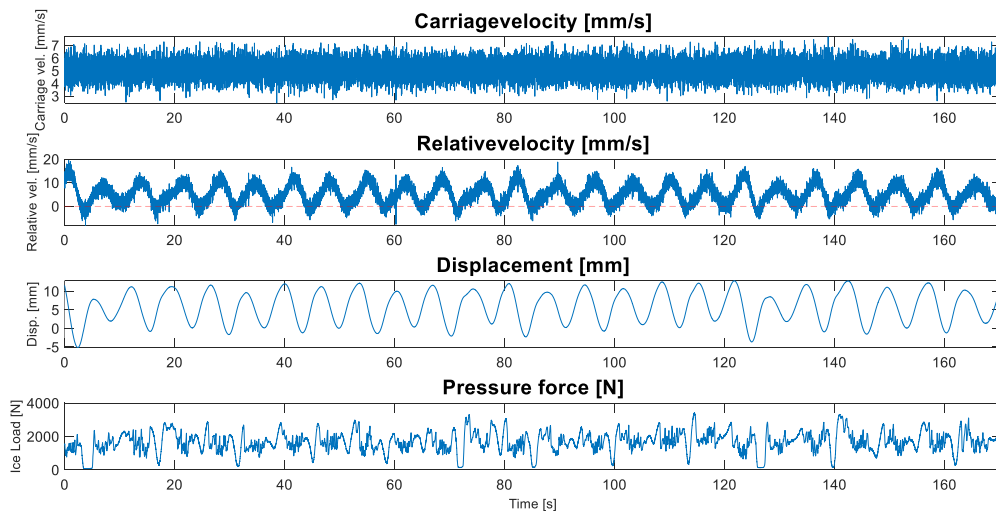
Test: SDOF-23. Fn: 0.154 Hz. V = 3 mm/s



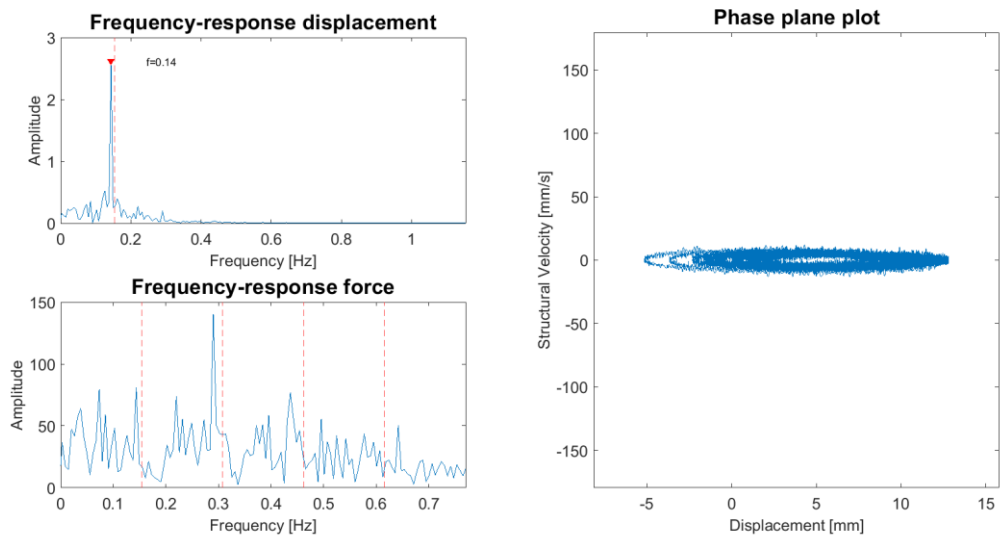
Test: SDOF-23. Fn: 0.154 Hz. V = 3 mm/s



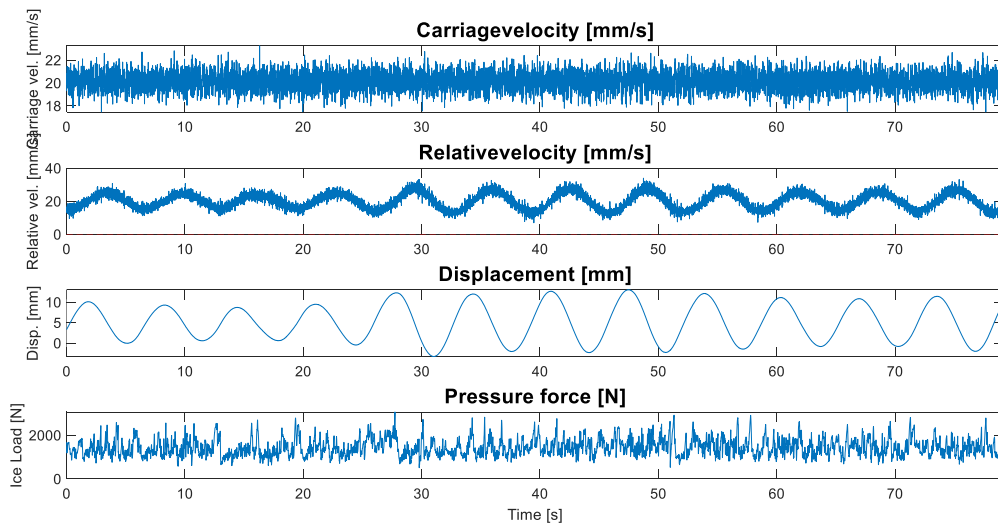
Test: SDOF-23. Fn: 0.154 Hz. V = 5 mm/s



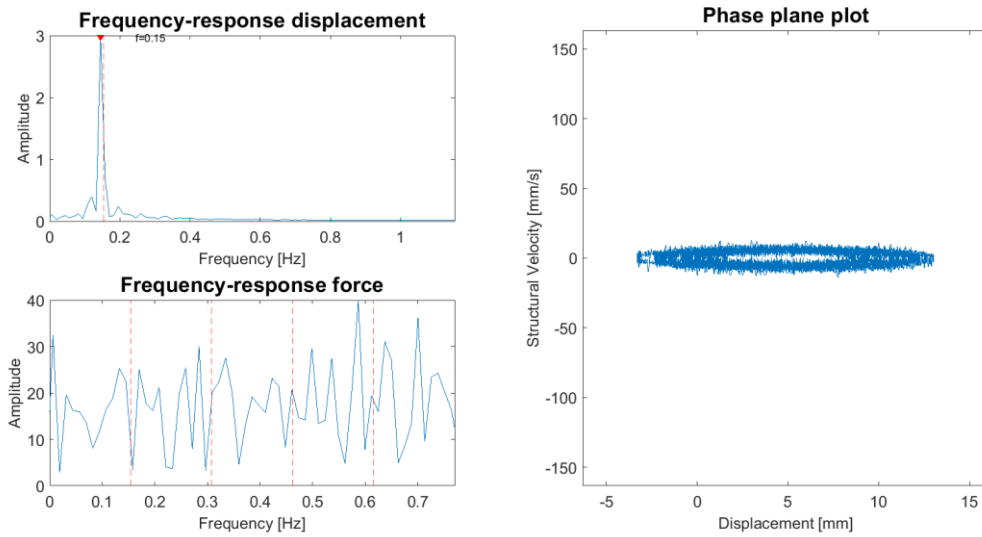
Test: SDOF-23. Fn: 0.154 Hz. V = 5 mm/s



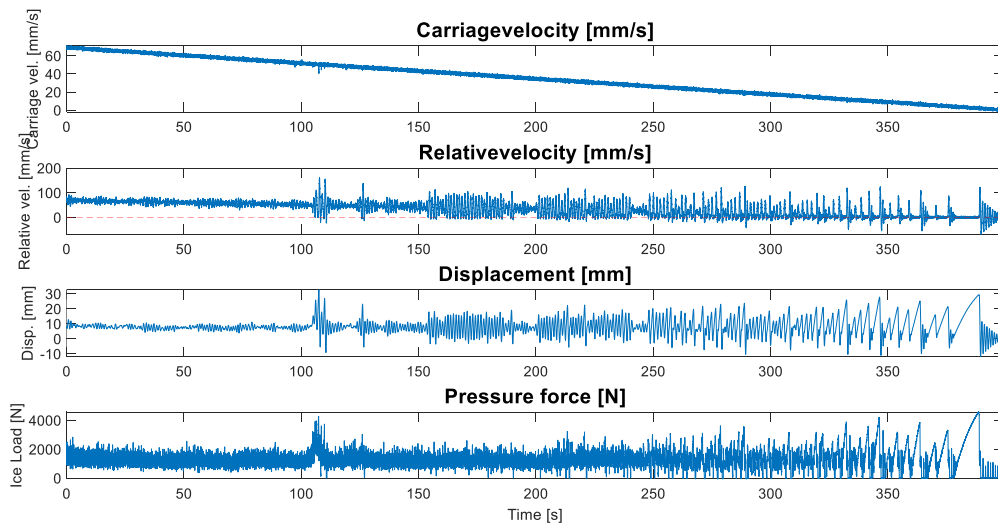
Test: SDOF-23. Fn: 0.154 Hz. V = 20 mm/s



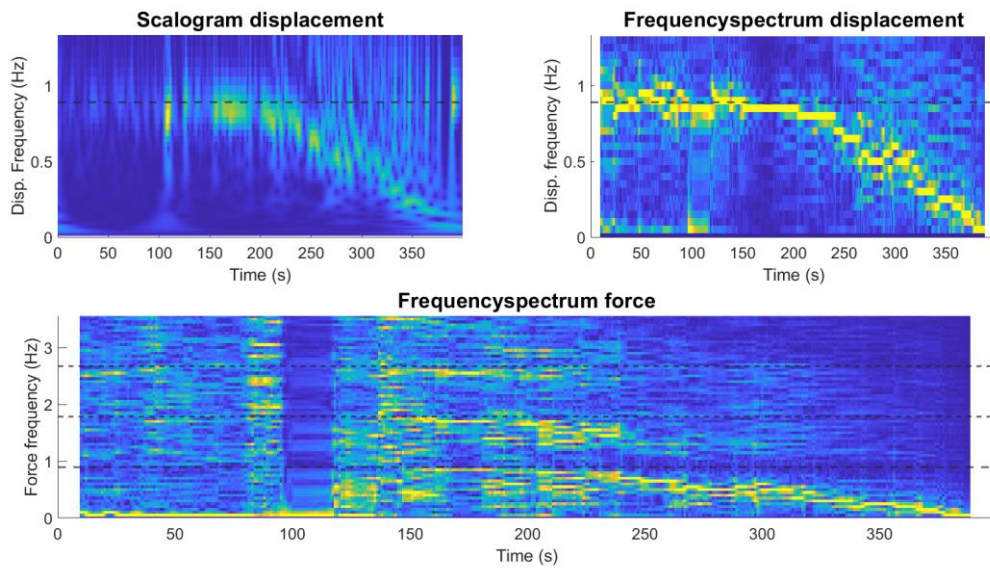
Test: SDOF-23. Fn: 0.154 Hz. V = 20 mm/s



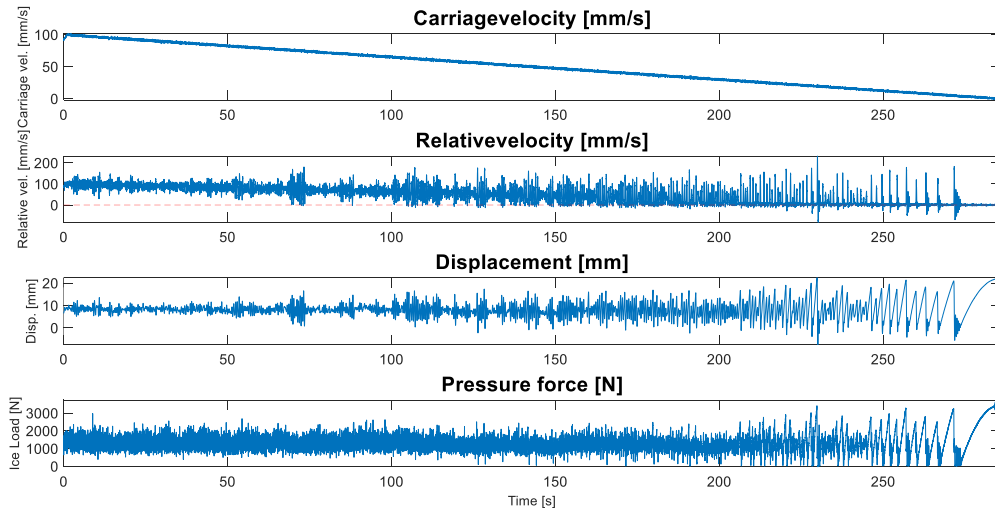
Test: SDOF-24. Fn: 0.889 Hz.



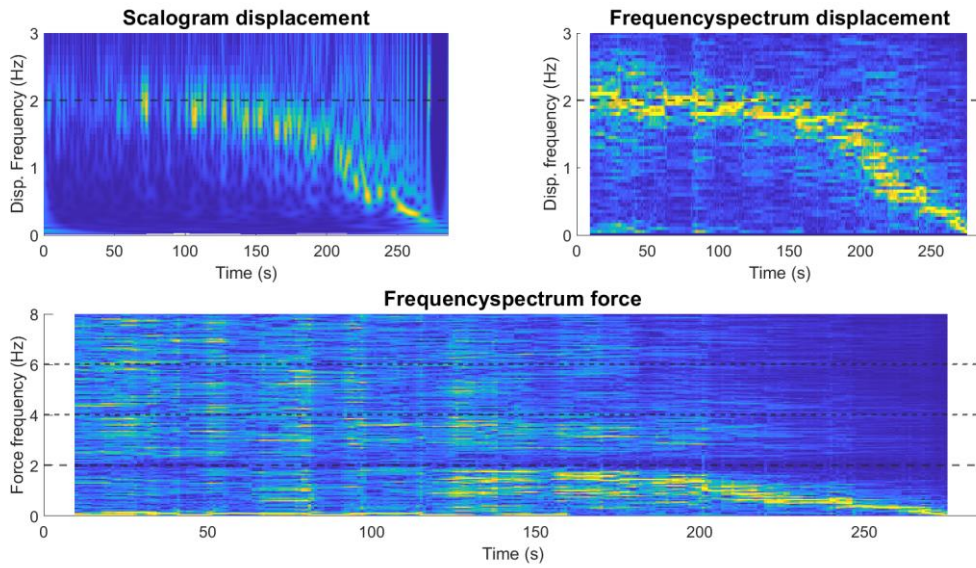
Test: SDOF-24. Fn: 0.889 Hz.



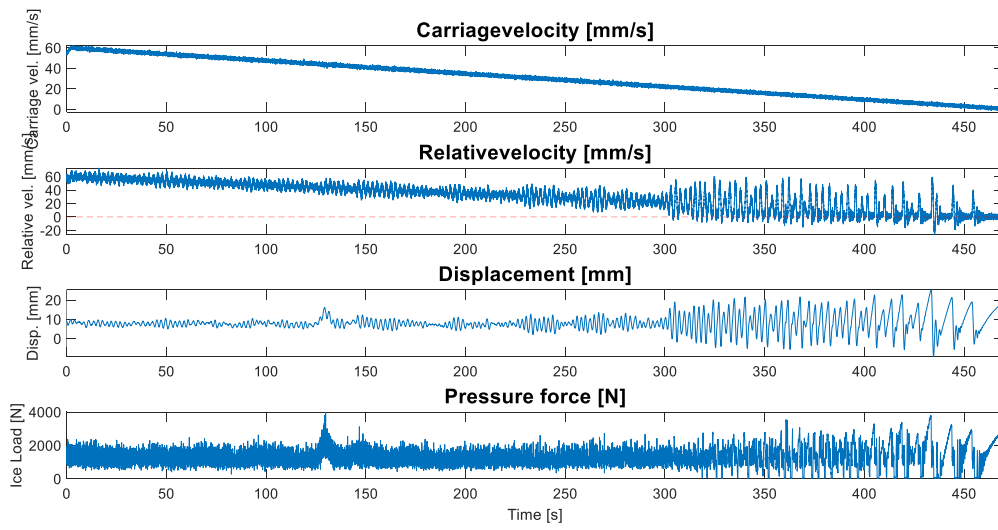
Test: SDOF-25. Fn: 2 Hz.



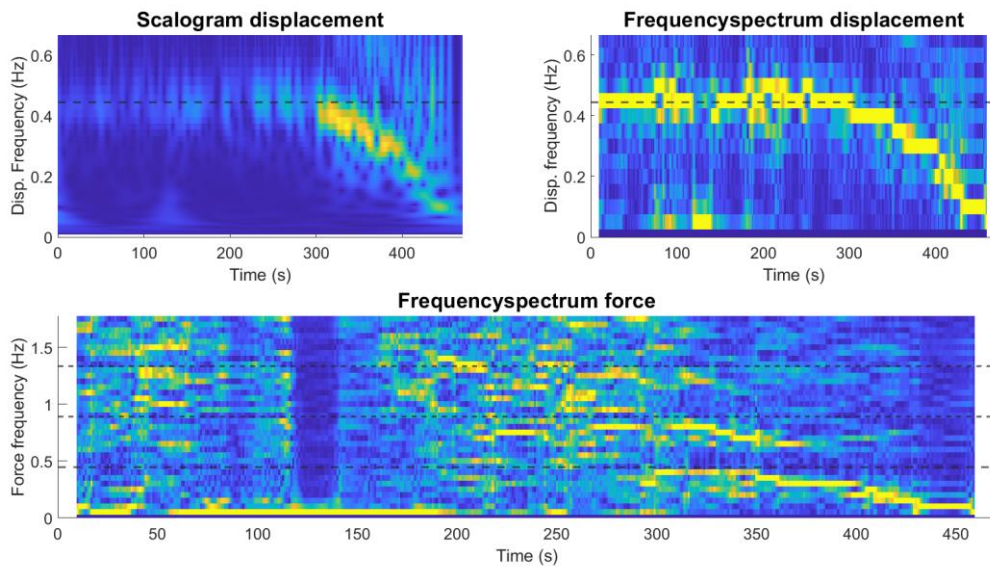
Test: SDOF-25. Fn: 2 Hz.



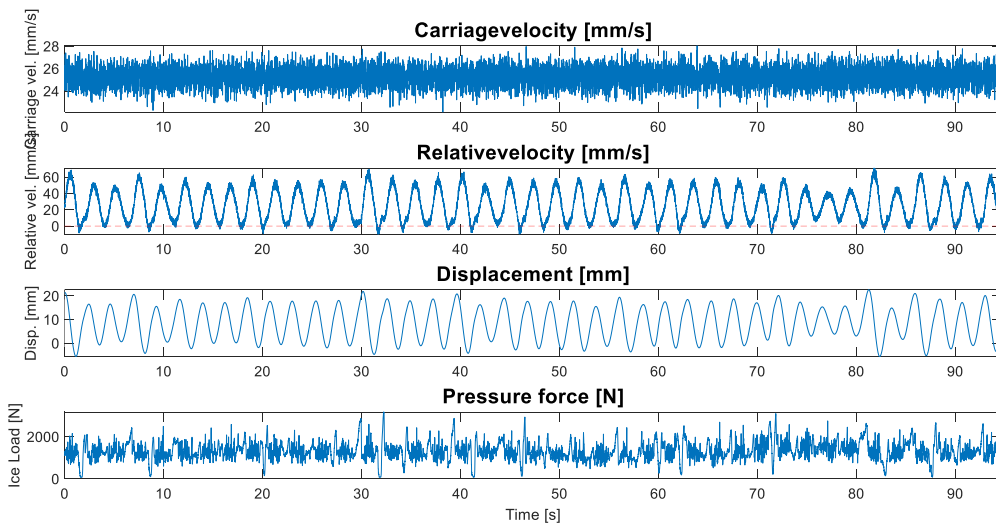
Test: SDOF-26. Fn: 0.444 Hz.



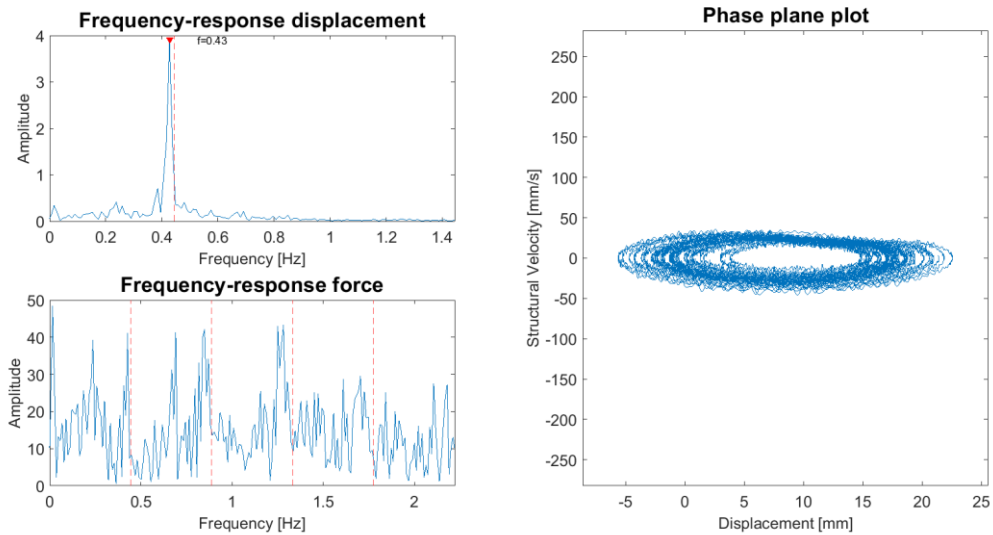
Test: SDOF-26. Fn: 0.444 Hz.



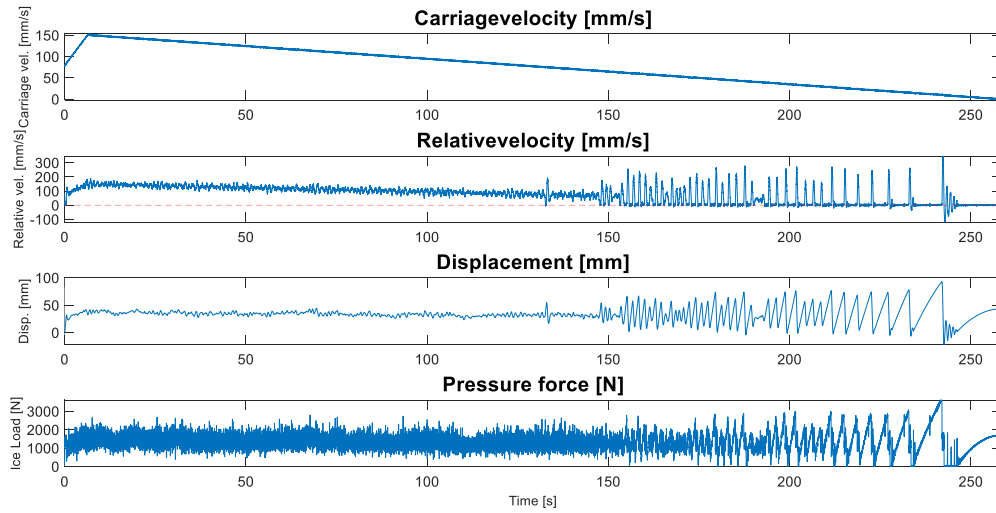
Test: SDOF-26. Fn: 0.444 Hz. V = 25 mm/s



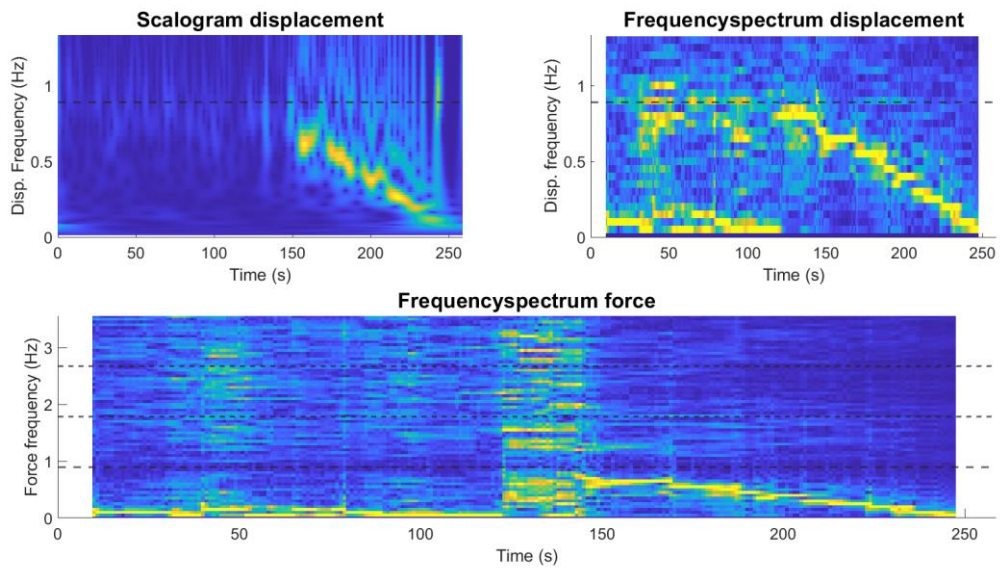
Test: SDOF-26. Fn: 0.444 Hz. V = 25 mm/s



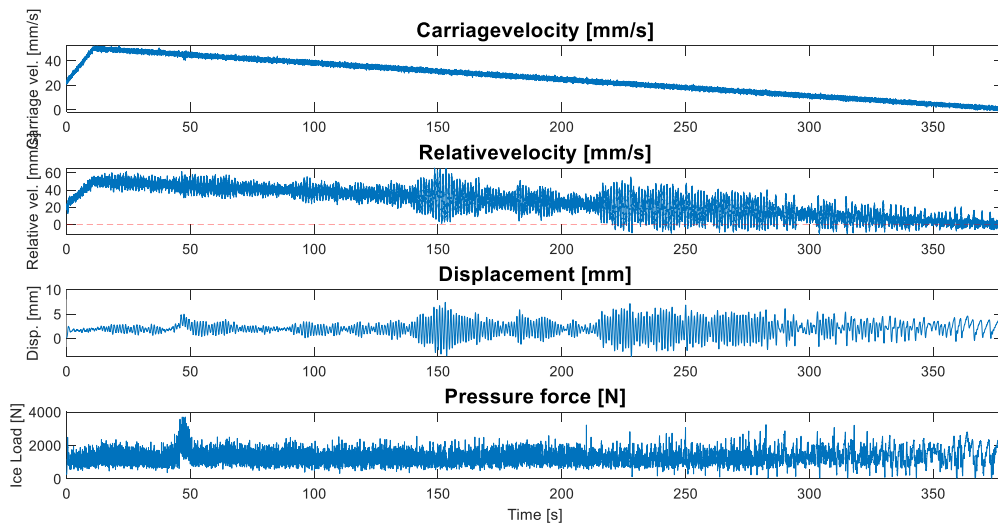
Test: SDOF-27. Fn: 0.889 Hz.



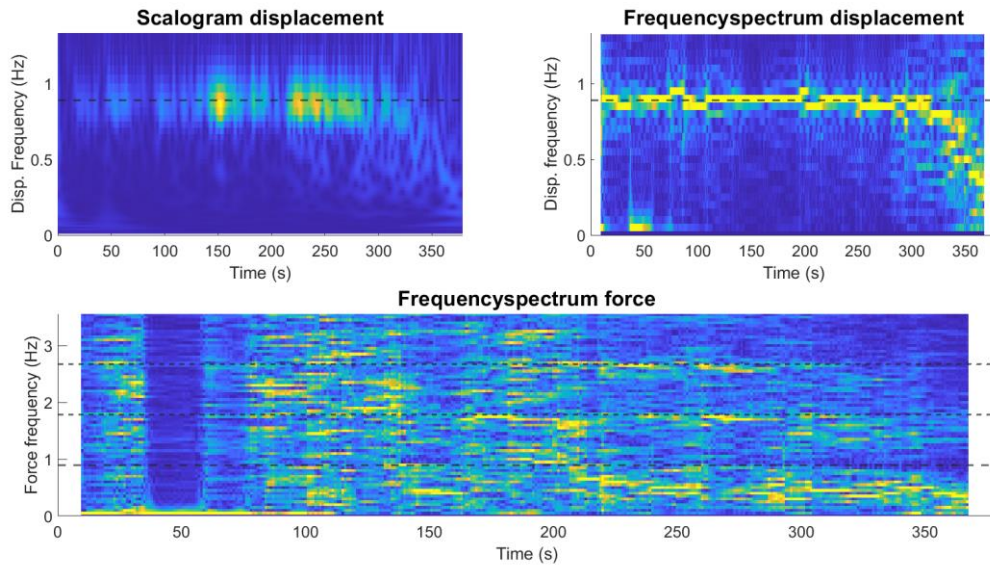
Test: SDOF-27. Fn: 0.889 Hz.



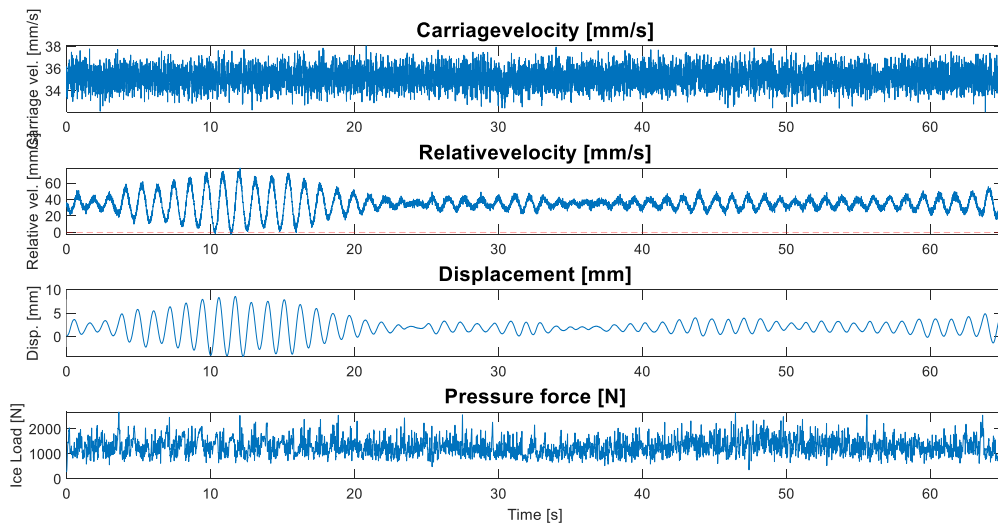
Test: SDOF-28. Fn: 0.889 Hz.



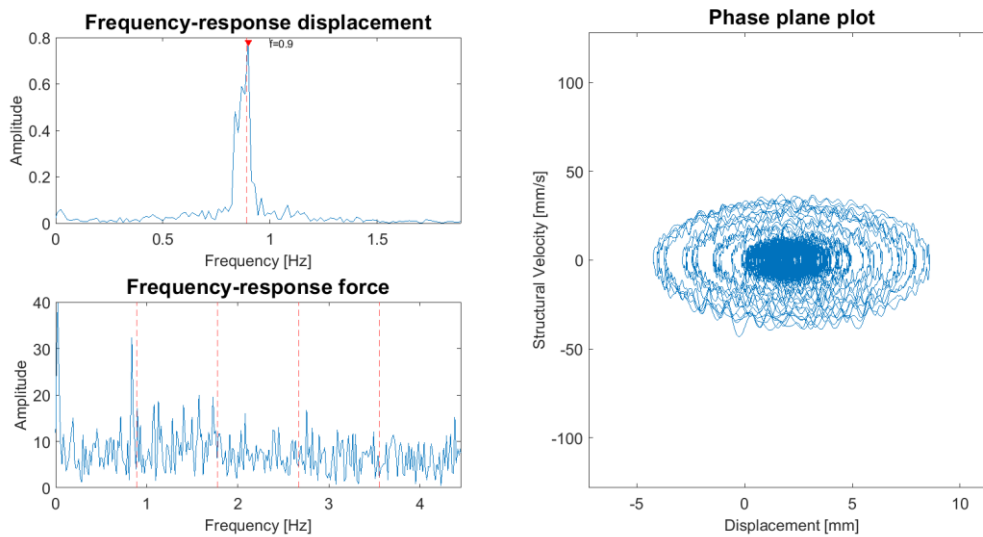
Test: SDOF-28. Fn: 0.889 Hz.



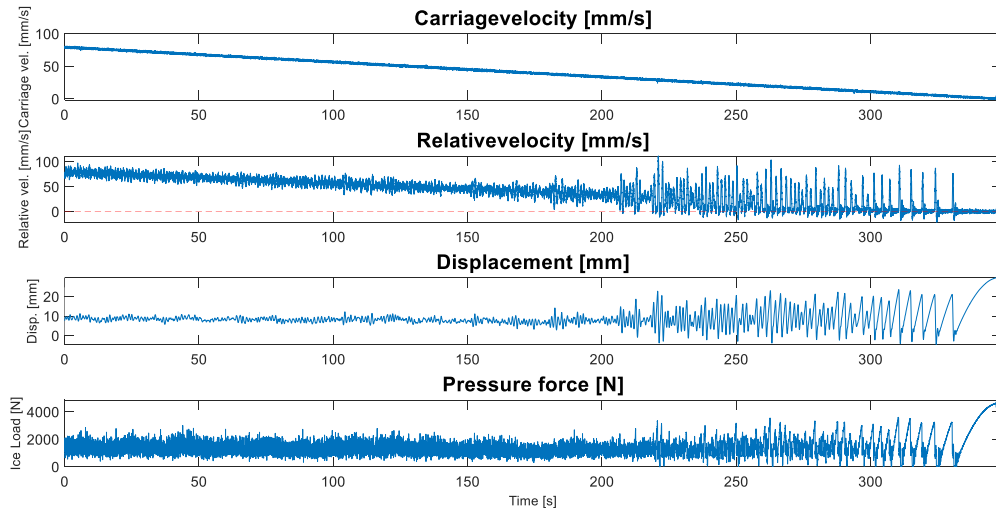
Test: SDOF-28. Fn: 0.889 Hz. V = 35 mm/s



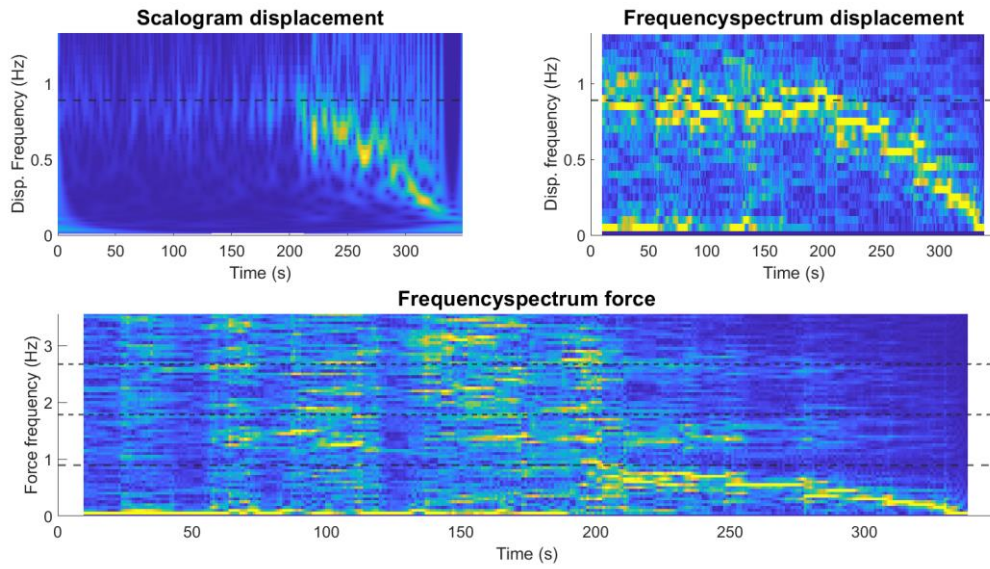
Test: SDOF-28. Fn: 0.889 Hz. V = 35 mm/s



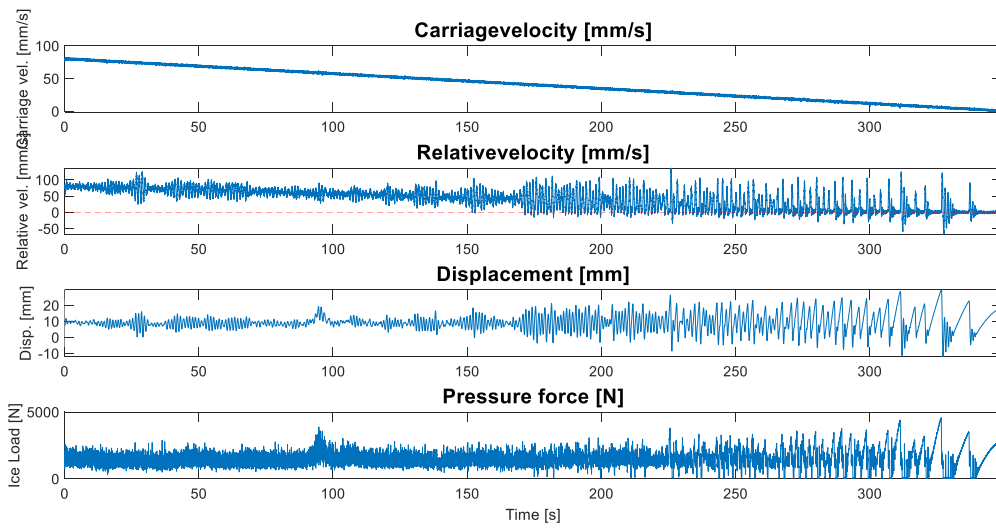
Test: SDOF-29. Fn: 0.889 Hz.



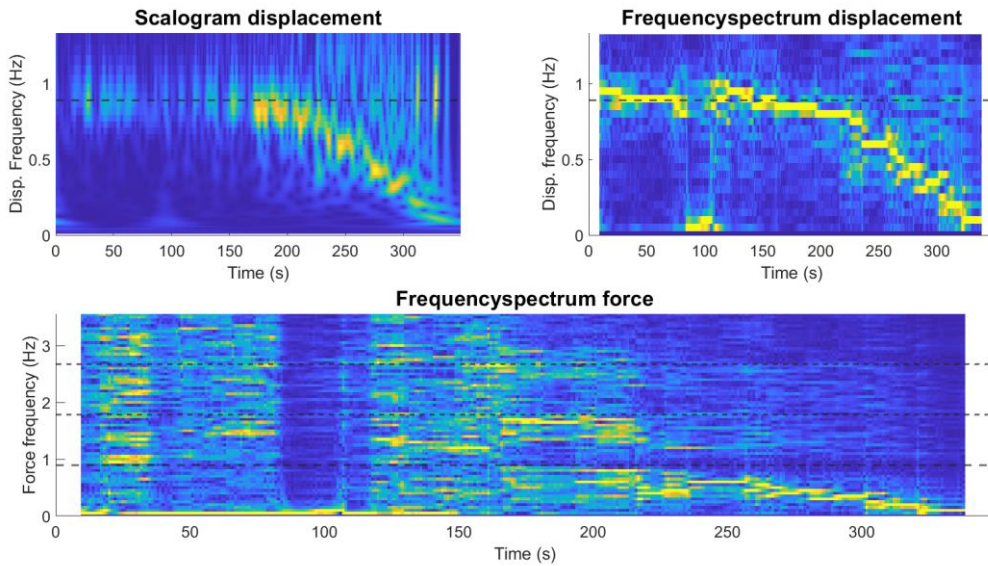
Test: SDOF-29. Fn: 0.889 Hz.



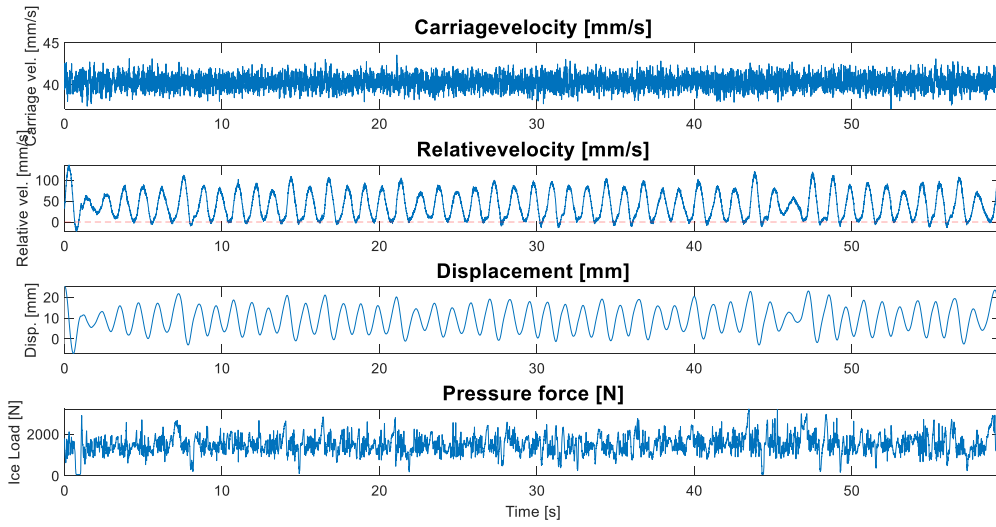
Test: SDOF-30. Fn: 0.889 Hz.



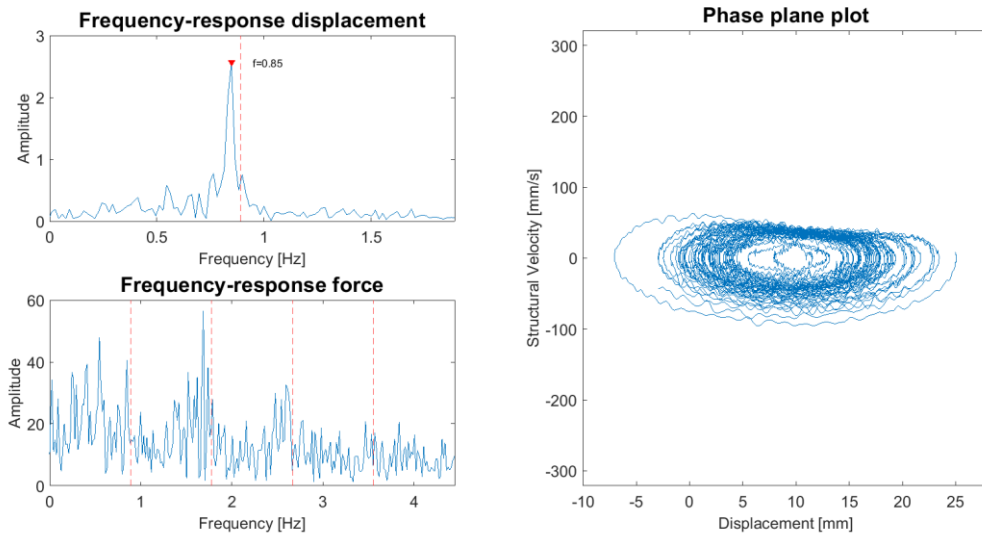
Test: SDOF-30. Fn: 0.889 Hz.



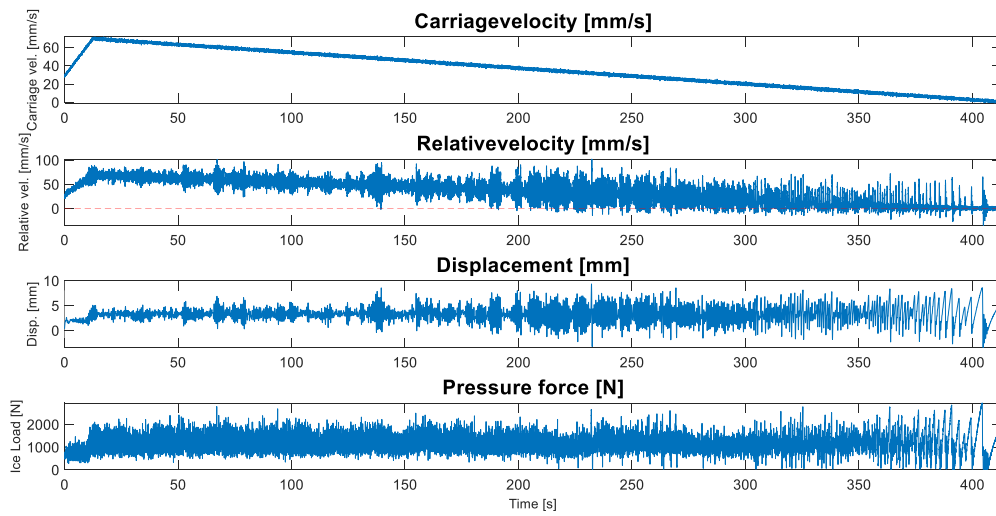
Test: SDOF-30. Fn: 0.889 Hz. V = 40 mm/s



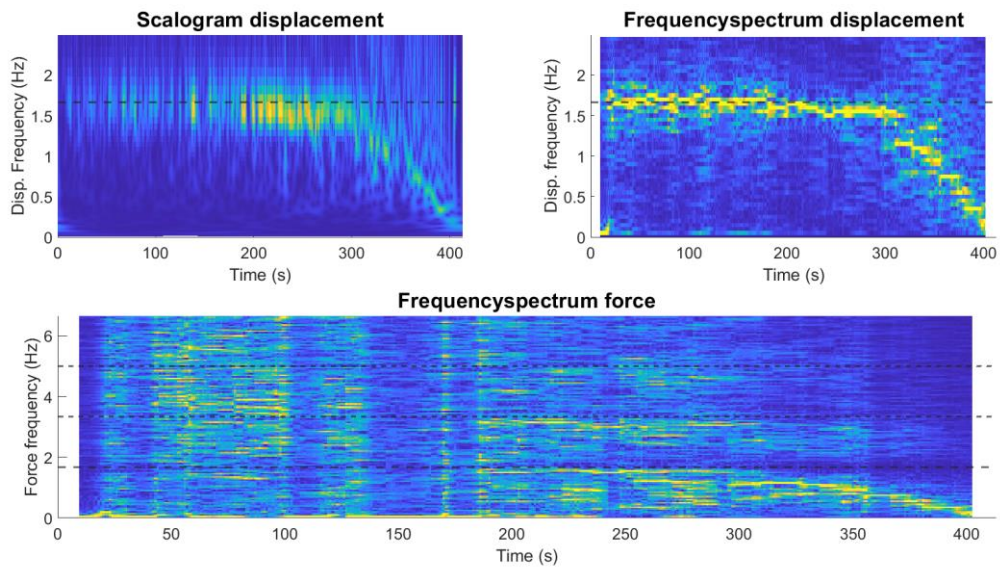
Test: SDOF-30. Fn: 0.889 Hz. V = 40 mm/s



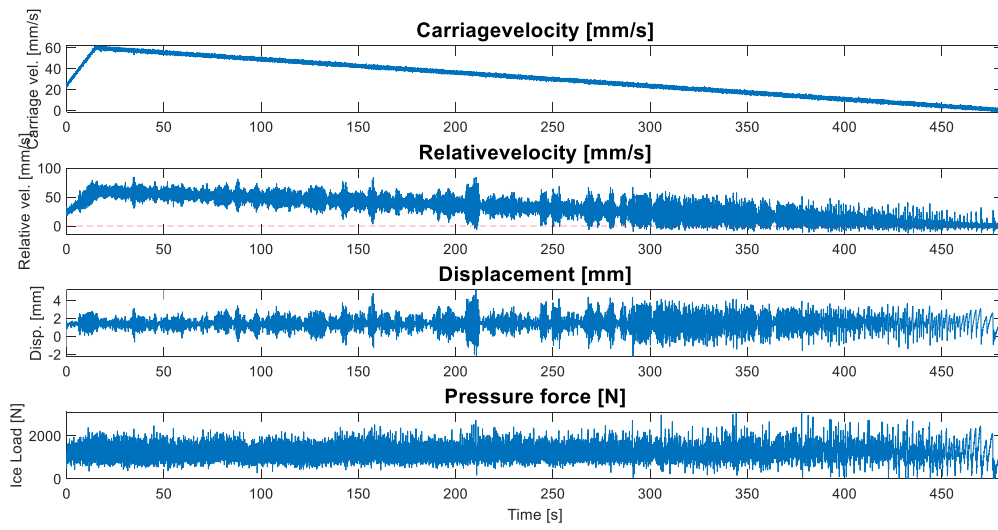
Test: SDOF-31. Fn: 1.663 Hz.



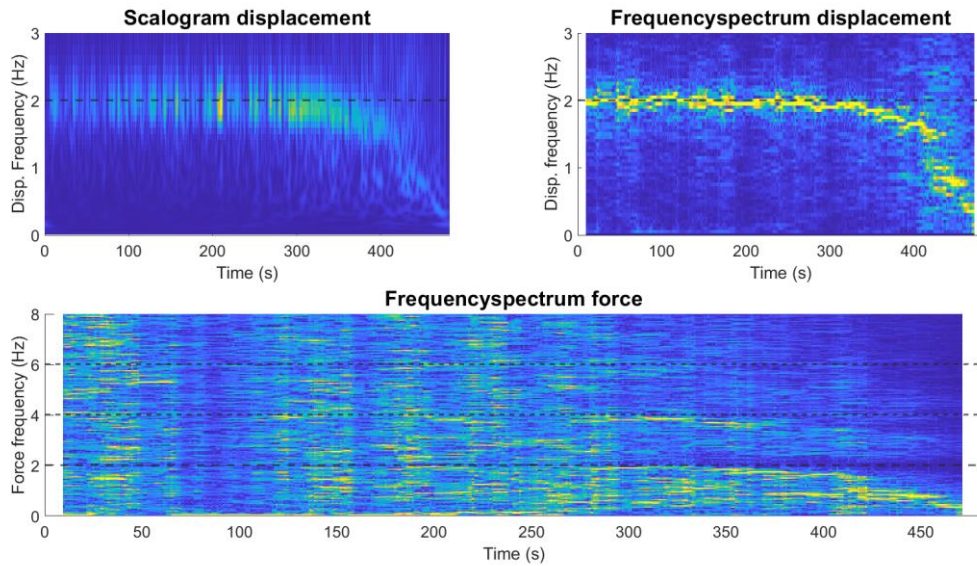
Test: SDOF-31. Fn: 1.663 Hz.



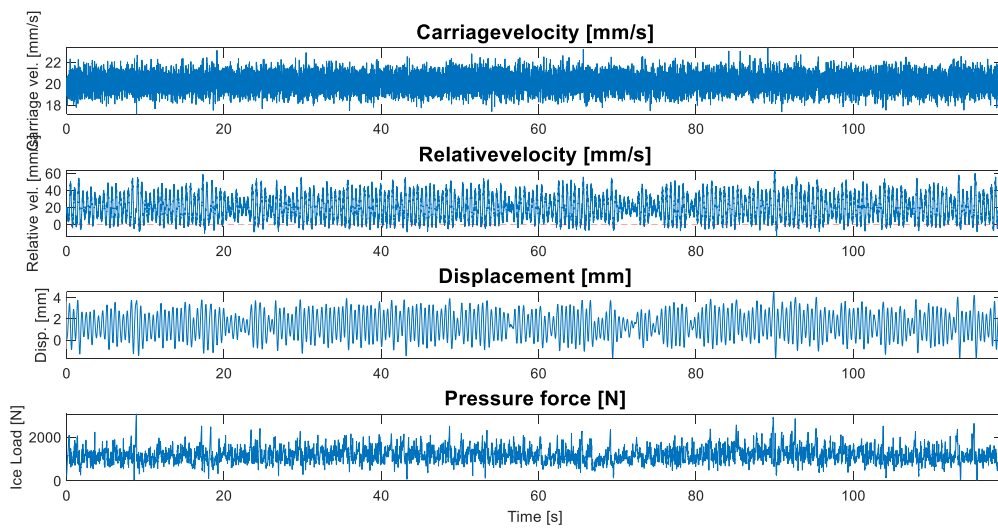
Test: SDOF-32. Fn: 2 Hz.



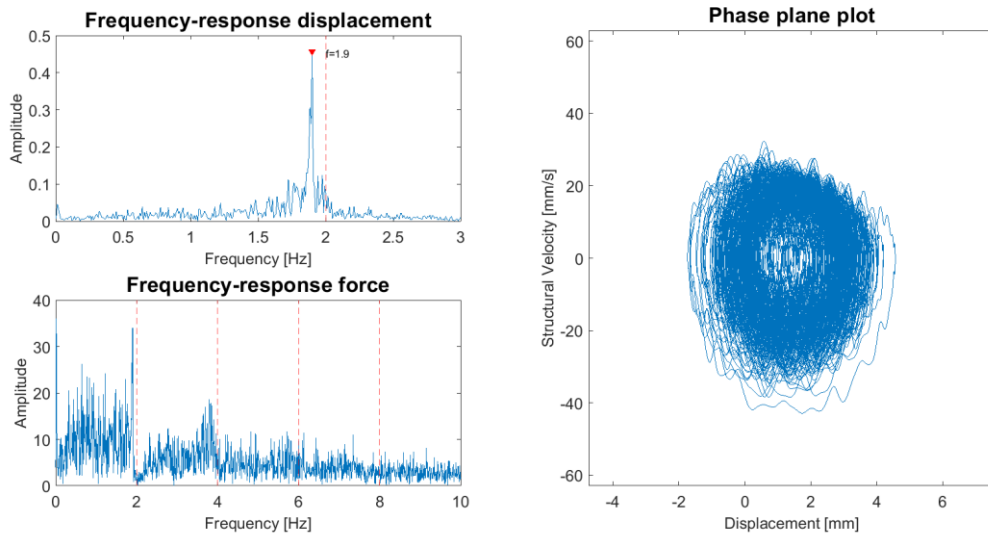
Test: SDOF-32. Fn: 2 Hz.



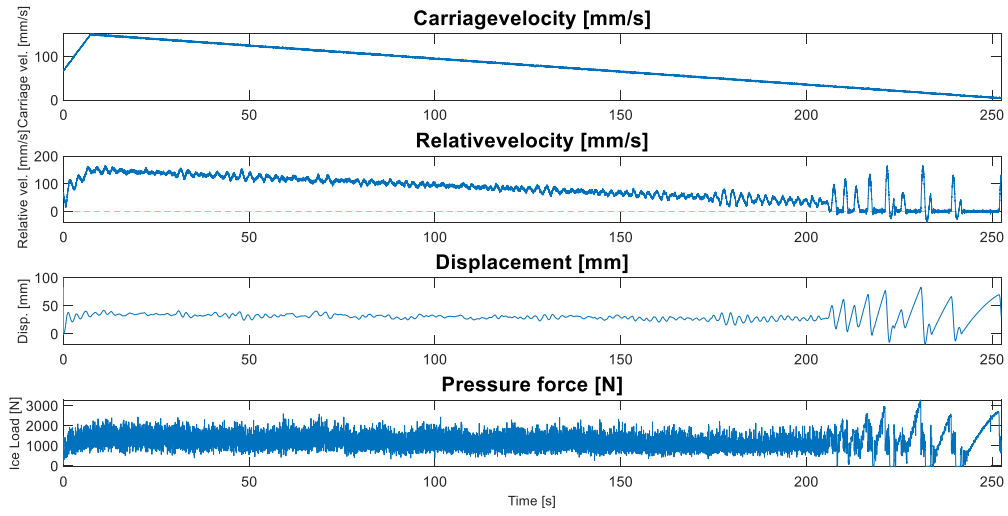
Test: SDOF-32. Fn: 2 Hz. V = 20 mm/s



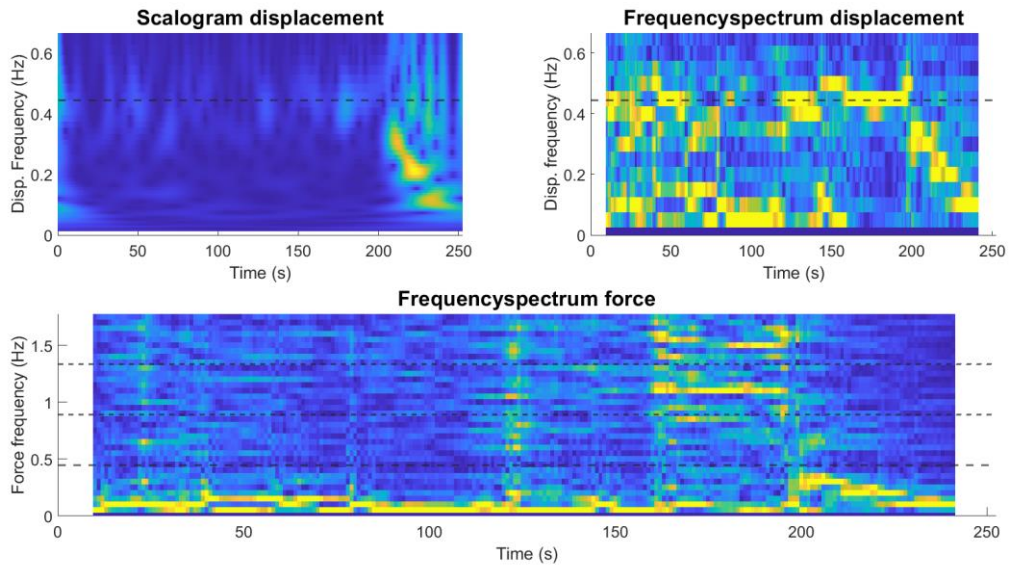
Test: SDOF-32. Fn: 2 Hz. V = 20 mm/s



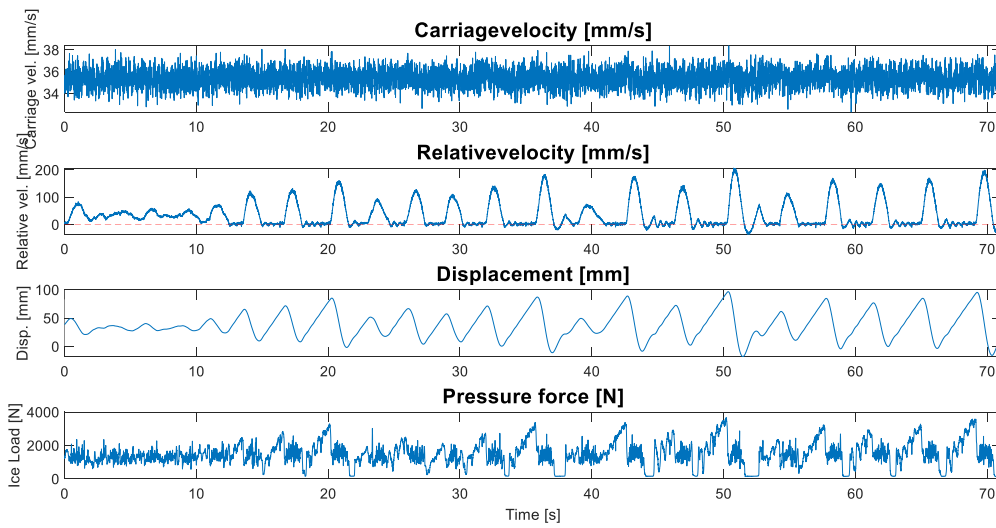
Test: SDOF-33. Fn: 0.444 Hz.



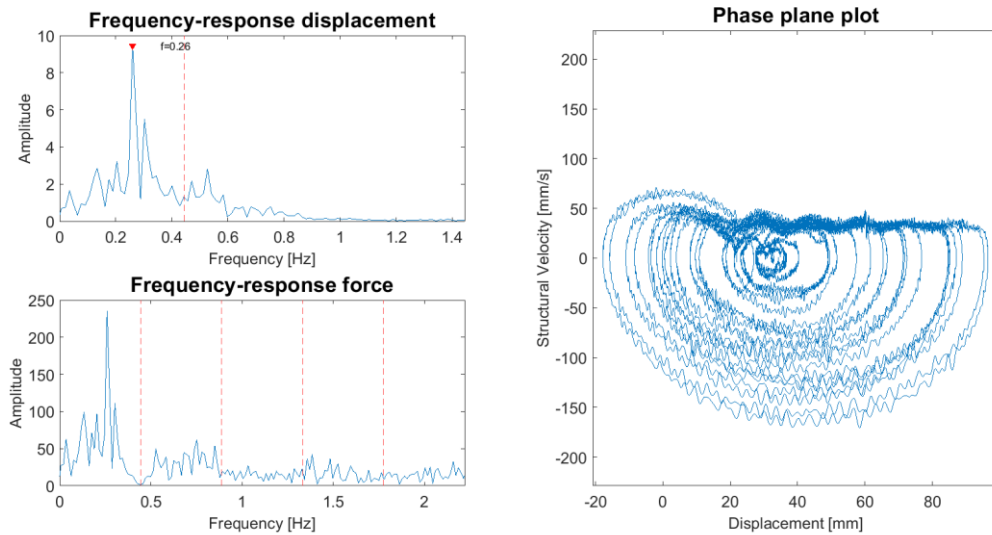
Test: SDOF-33. Fn: 0.444 Hz.



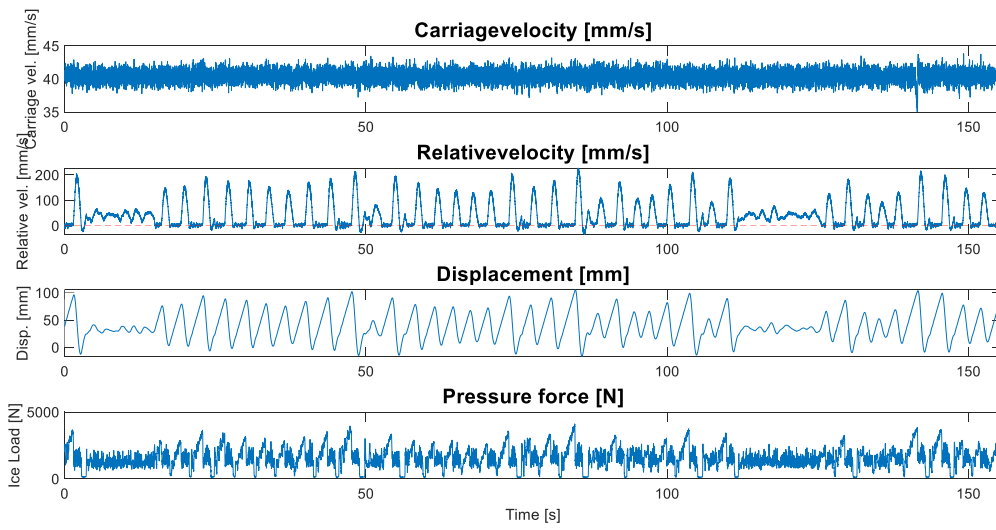
Test: SDOF-33. Fn: 0.444 Hz. V = 35 mm/s



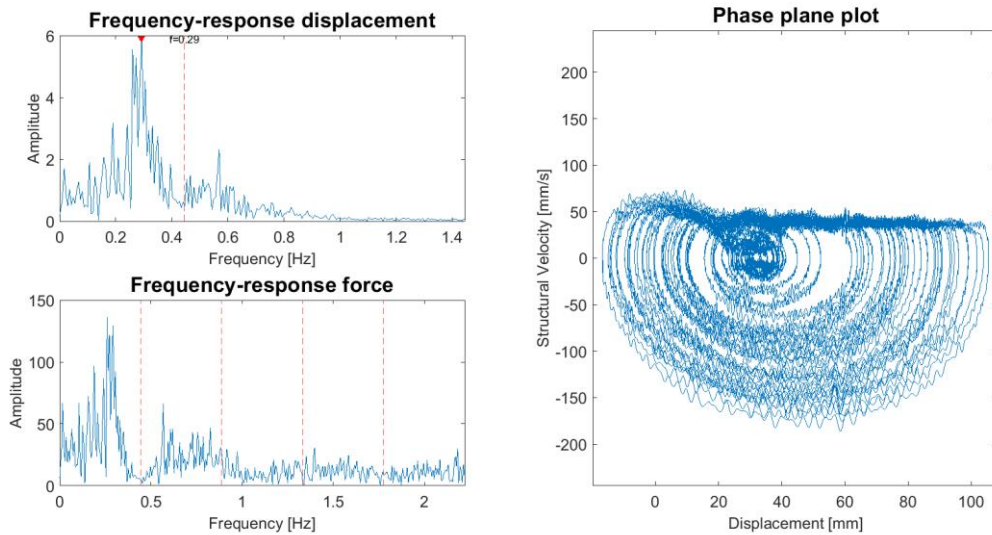
Test: SDOF-33. Fn: 0.444 Hz. V = 35 mm/s



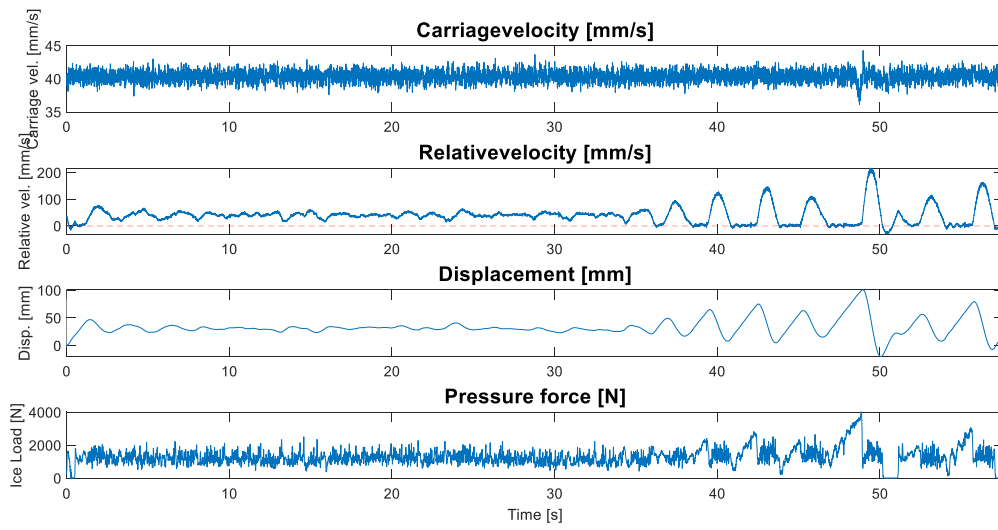
Test: SDOF-33. Fn: 0.444 Hz. V = 40 mm/s



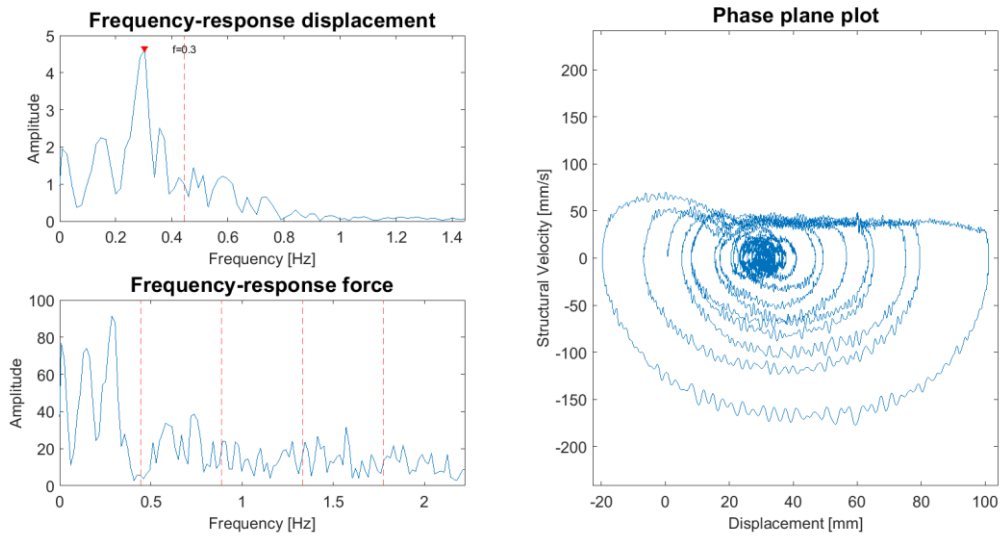
Test: SDOF-33. Fn: 0.444 Hz. V = 40 mm/s



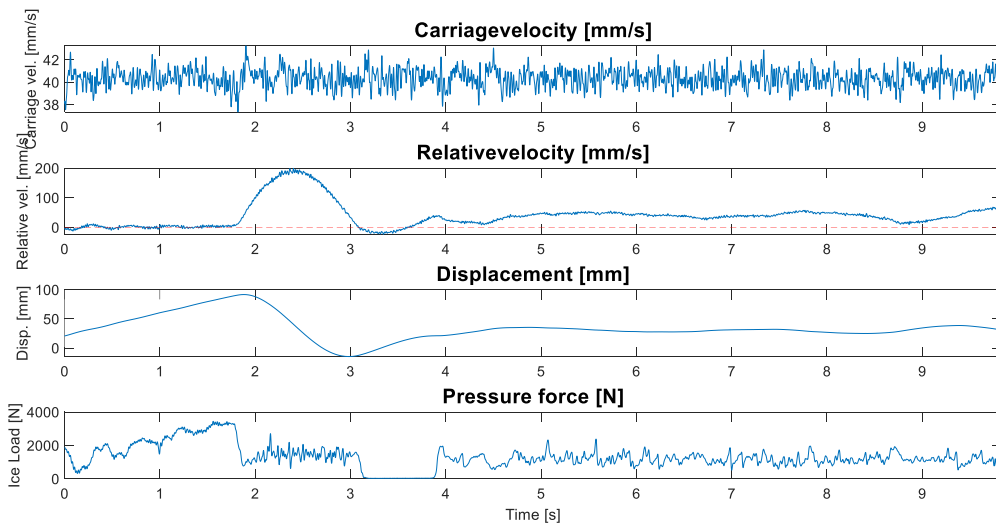
Test: SDOF-33. Fn: 0.444 Hz. V = 40 mm/s



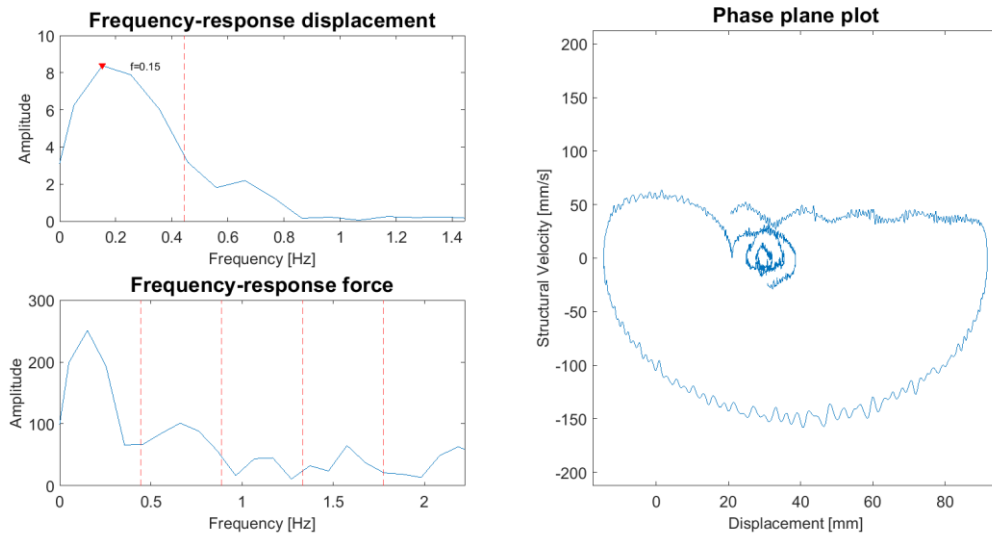
Test: SDOF-33. Fn: 0.444 Hz. V = 40 mm/s



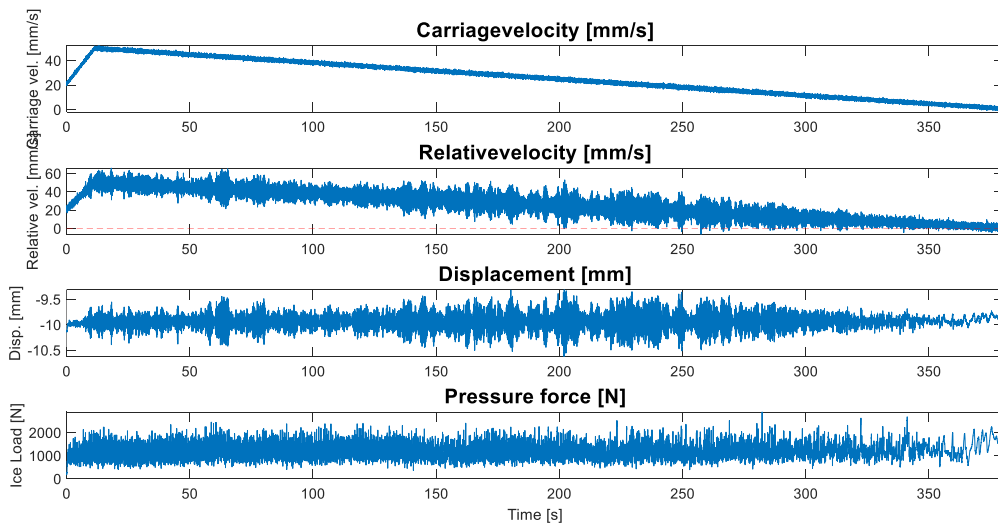
Test: SDOF-33. Fn: 0.444 Hz. V = 40 mm/s



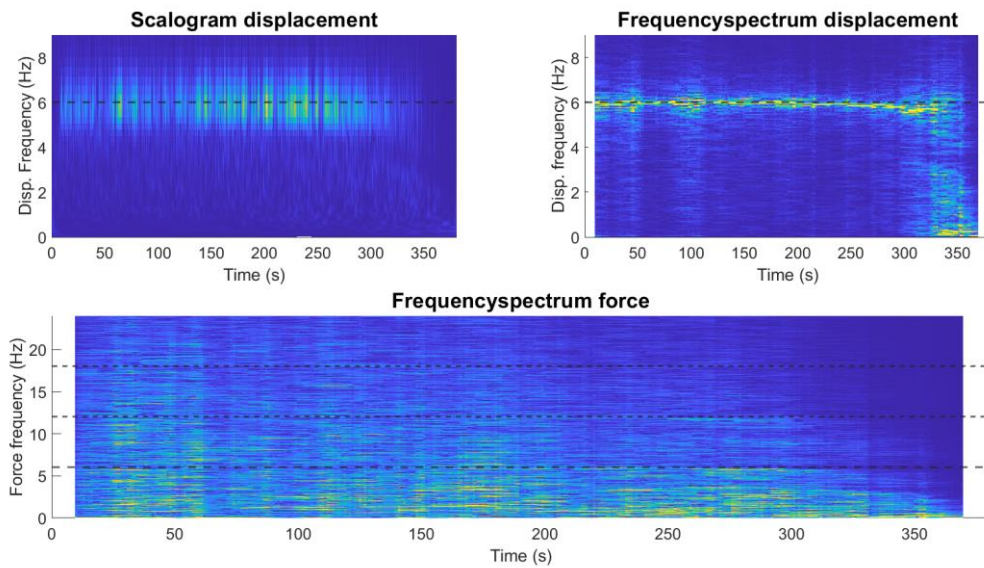
Test: SDOF-33. Fn: 0.444 Hz. V = 40 mm/s



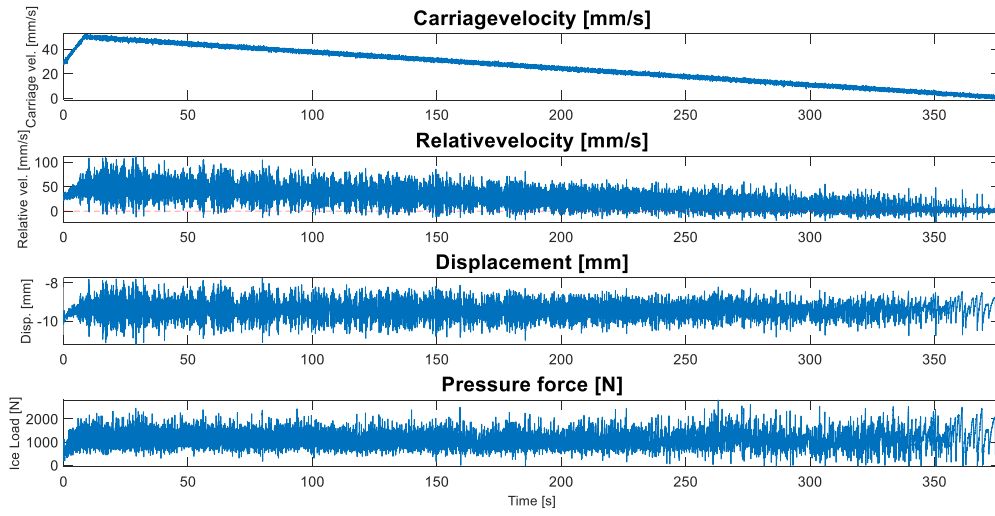
Test: SDOF-34. Fn: 6 Hz.



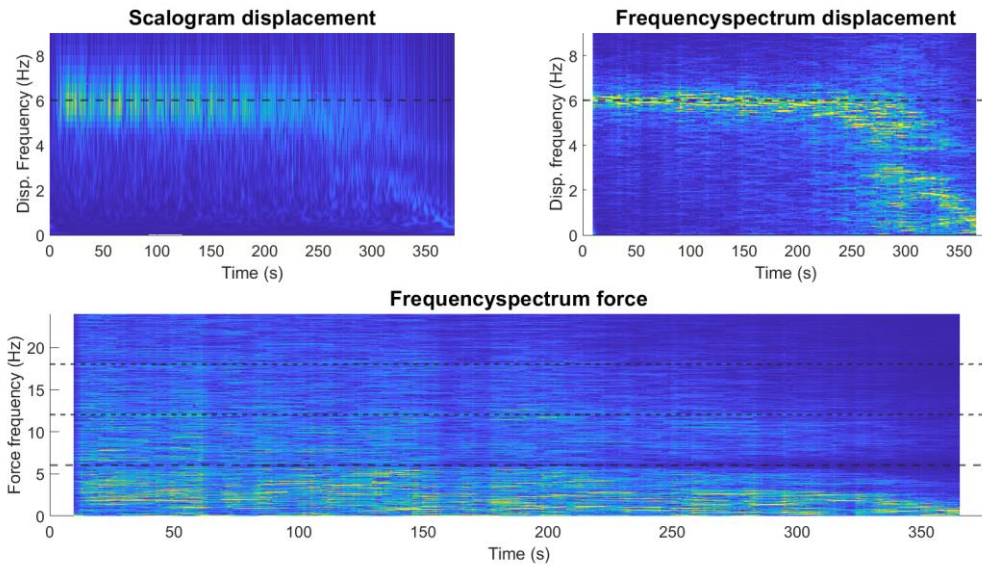
Test: SDOF-34. Fn: 6 Hz.



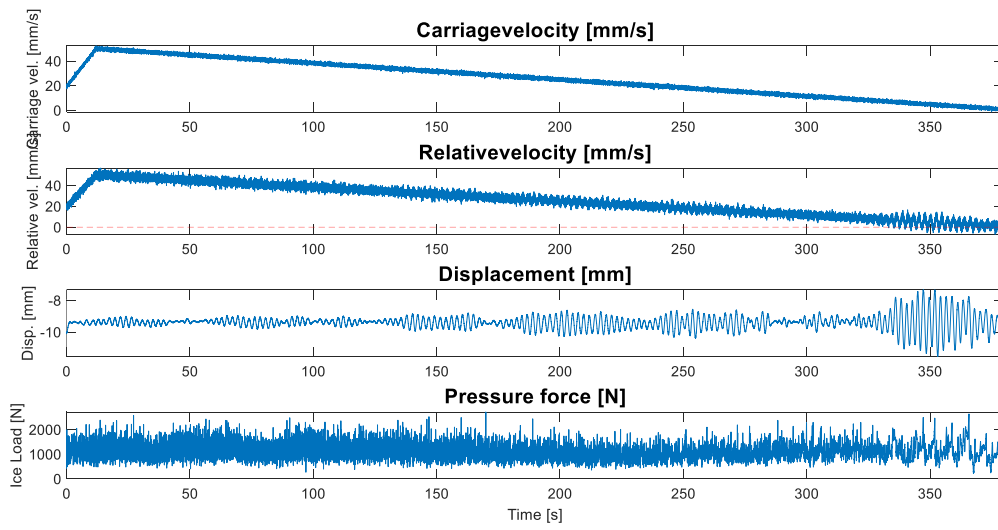
Test: SDOF-35. Fn: 6 Hz.



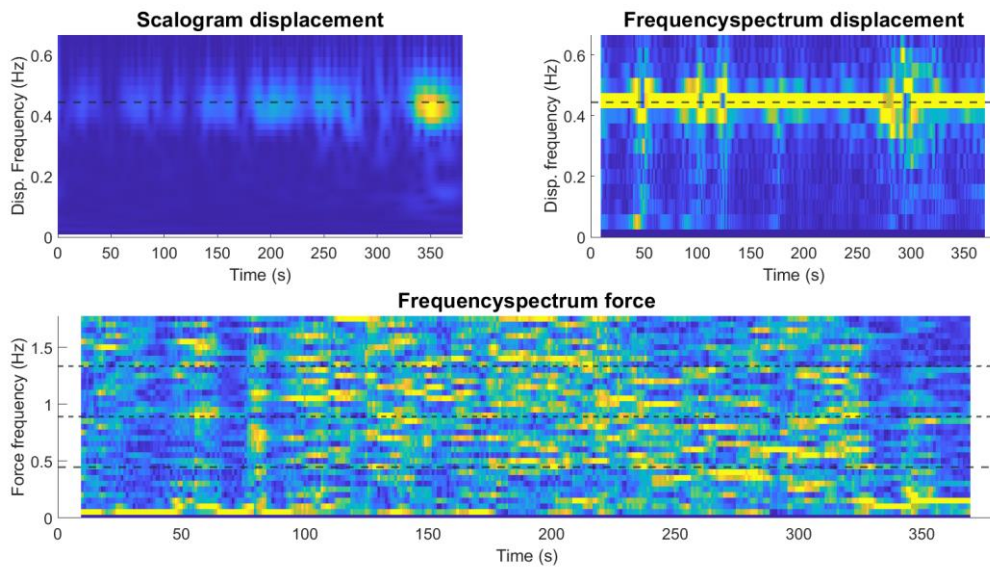
Test: SDOF-35. Fn: 6 Hz.



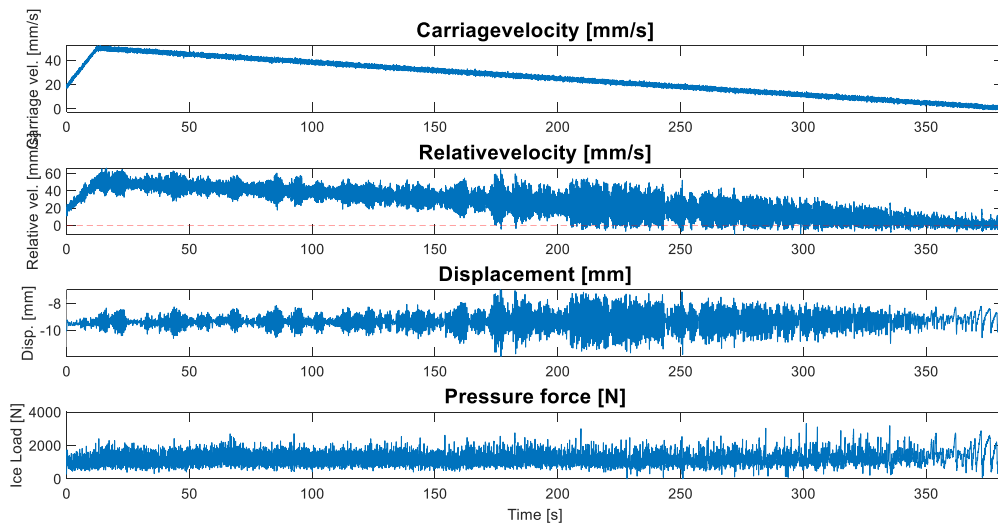
Test: SDOF-36. Fn: 0.444 Hz.



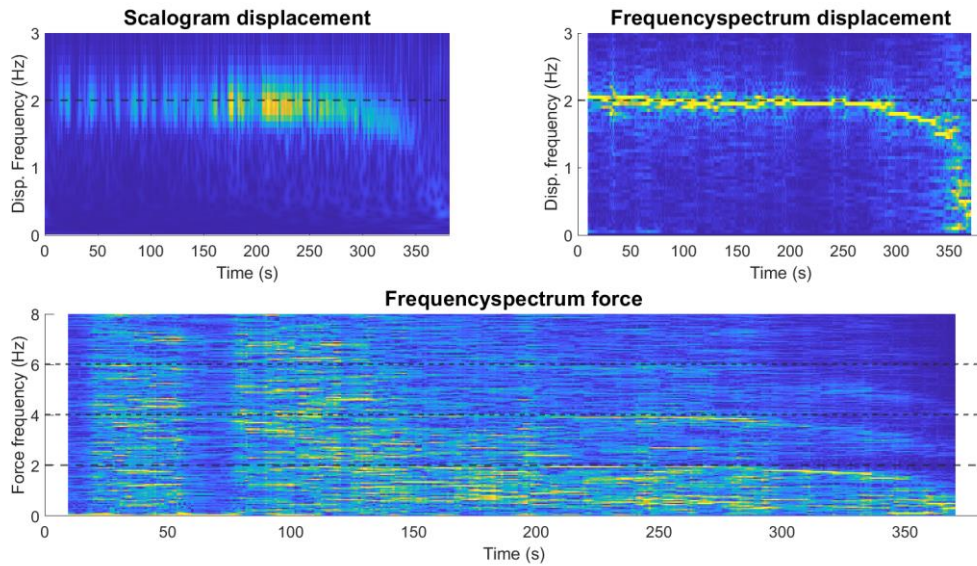
Test: SDOF-36. Fn: 0.444 Hz.



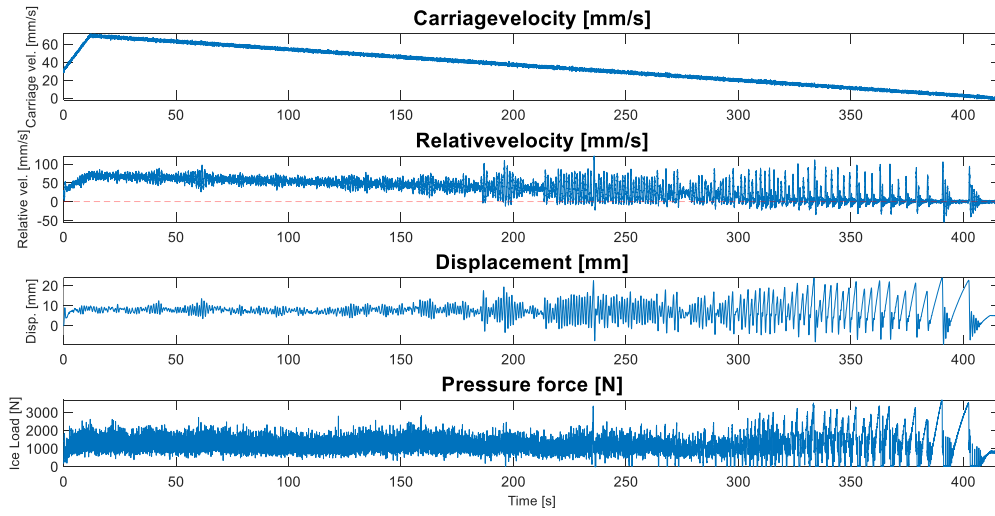
Test: SDOF-37. Fn: 2 Hz.



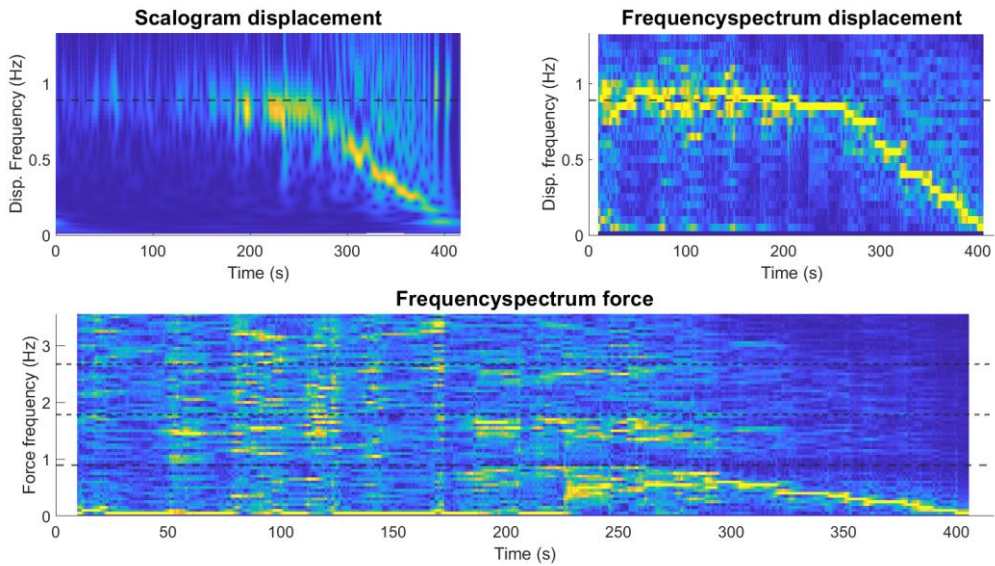
Test: SDOF-37. Fn: 2 Hz.



Test: SDOF-38. Fn: 0.889 Hz.



Test: SDOF-38. Fn: 0.889 Hz.



---

## Bibliography

- [1] WindEurope, "Significant developments on offshore wind in the Baltic Sea," 7 January 2021. [Online]. Available: <https://windeurope.org/newsroom/significant-developments-on-offshore-wind-in-the-baltic-sea>. [Accessed 18 2021].
- [2] Equinor, "Breakthrough for Equinor in Polish offshore wind," 5 May 2021. [Online]. Available: <https://www.equinor.com/en/news/20210412-breakthrough-polish-wind.html>. [Accessed 2 September 2021].
- [3] "Denmark Moves Forward with Energy Islands," 23 November 2020. [Online]. Available: <https://www.offshorewind.biz/2020/11/23/denmark-moves-forward-with-energy-islands/>. [Accessed 2 September 2021].
- [4] Xinhua, "Latvia, Estonia to jointly build offshore wind farm in Baltic Sea," 12 May 2021. [Online]. Available: [http://www.xinhuanet.com/english/europe/2021-05/12/c\\_139939408.htm](http://www.xinhuanet.com/english/europe/2021-05/12/c_139939408.htm). [Accessed 2 September 2021].
- [5] Wikipedia, "List of offshore wind farms in the Baltic Sea," 8 June 2021. [Online]. Available: [https://en.wikipedia.org/wiki/List\\_of\\_offshore\\_wind\\_farms\\_in\\_the\\_Baltic\\_Sea](https://en.wikipedia.org/wiki/List_of_offshore_wind_farms_in_the_Baltic_Sea). [Accessed 2 September 2021].
- [6] H. Hendrikse, *Seminar 8: Dynamic ice-structure interaction, lecture slides, Arctic Engineering OE44115*, Technical University Delft, 2020.
- [7] D. A. Bouzid, S. Bhattacharya and L. Otsmane, "Assessment of natural frequency of installed offshore wind turbines using nonlinear finite element model considering soil-monopile interaction," *Journal of Rock Mechanics and Geotechnical Engineering*, no. 10, pp. 333-346, 2018.
- [8] H. Hendrikse, "Ice-induced vibrations of vertically sided offshore structures," 2017.
- [9] S. Singh, G. W. Timco, R. M. W. Frederking and L. J. Jordaan, "Tests of ice crushing on a flexible structure," *Proceedings of the 9th Offshore Mechanics and Arctic Engineering Symposium*, vol. IV, pp. 89-94, 1990.

- [10] K. Izumiyama and S. Uto, "Ice loading on a compliant indenter," *Proceedings of the 16th International Conference on Offshore Mechanics and Arctic Engineering*, vol. IV, pp. 431-436, 1997.
- [11] Q. Yue, F. Guo and S. Chu, "Laboratory test of ice induced structure vibrations," *Proceedings of the 18th IAHR International Symposium on ice*, pp. 191-198, 2006.
- [12] A. Palmer, Y. Qianjin and F. Guo, "Ice-induced vibrations and scaling," *Cold Regions Science and Technology journal*, vol. 60, pp. 189-192, 2010.
- [13] F. Guo, Q. Yue, X. Bi and Y. Liu, "Model test of ice-structure interaction," *Proceedings of the 28th International Conference on Ocean, Offshore and Arctic Engineering*, 2009.
- [14] Q. Yue, F. Guo and T. Kärnä, "Dynamic ice forces of slender vertical structures due to ice crushing," *Cold Regions Science and Technology journal*, vol. 56, pp. 77-83, 2009.
- [15] K. Yap and A. Palmer, "A model test on ice-induced vibrations: Structure response characteristics and scaling of the lock-in phenomenon," *Proceedings of the 22nd International Conferences on Port and Ocean Engineering under Arctic Conditions*, 2013.
- [16] G. Ziemer and P. Hinse, "Relation of maximum structural velocity and ice drift speed during frequency lock-in," June 2017.
- [17] Y. Huang, Q. Shi and A. Song, "Model test study of the interaction between ice and a compliant vertical narrow structure," *Cold Regions Science and Technology*, no. 49, pp. 151-160, 2007.
- [18] K. Izumiyama, M. Irani and G. Timco, "Influence of compliance of structure on ice load," in *IAHR Ice Symposium*, Trondheim, 1994.
- [19] Y. Toyama, T. Senu, M. Minami and N. Yashima, "Model tests on ice-induced self-excited vibration of cylindrical structures," in *Poac 83, Seventh Int. Conf. on Port & Ocean Engng. Under Arctic Conditions*, Espoo, 1983.
- [20] G. Timco, M. B. Irani, J. Tseng, L. Liu and C. Zheng, "Model tests of dynamic ice loading on the Chinese JZ-20-2 jacket platform," *Canadian Journal of Civil Engineering*, no. 19, pp. 819-823, 1992.
- [21] K. Yap, "Level ice-vertical structure interaction: Steady-state self-excited vibration of structures," August 2011.
- [22] C. Owen and H. Hendrikse, "A study of the transition of ice speed from intermittent crushing to frequency lock-in vibrations based on model-scale experiments," *Proceedings of the 25th International Conference on Port and Ocean Engineering under Arctic Conditions*, June 2019.
- [23] M. Tsuchiya, S. Kanie, K. Ikejiri, A. Yoshida and H. Saeki, "An Experimental Study on Ice-Structure Interaction," in *17th Annual Offshore Technology Conference*, Texas, 1985.
- [24] S. Sodhi, "Ice - Structure Interaction During Indentation Tests," 1991.

- [25] T. Kärnä, K. Kolari, P. Jochmann, K.-U. Evers, B. Xiangjun, M. Määttänen and P. Martonen, "Ice action on compliant structures. Laboratory indentation test," *VTT Tiedotteita*, 2003.
- [26] M. Määttänen, "Laboratory tests for dynamic ice-structure interaction," in *Proceedings of the Port and Ocean Engineering under Arctic Conditions 79*, Trondheim, 1979.
- [27] K. Yap and A. Palmer, "A model test on ice-induced vibrations: structures response characteristics and scaling of the lock-in phenomenon," Espoo, 2013.
- [28] D. Blanchet, A. Churcher, J. Fitzpatrick and P. Badra-Blanchet, "An analysis of observed failure mechanisms for laboratory, first-year and multi-year ice," in *IAHR Ice Symposium*, Sapporo, 1988.
- [29] G. Timco, "Ice Forces on Structures: Physical Modelling Techniques," vol. IV, 1984.
- [30] J. Dempsey, A. Palmer and D. Sodhi, "High pressure zone formation during compressive ice failure," *Engineering Fracture Mechanics*, no. 68, pp. 1961-1974, 2001.
- [31] A. Palmer and J. Dempsey, "Models of large-scale crushing and spalling related to high-pressure zones," in *Proceedings on 16th IAHR Symposium on Ice*, Dunedin, 2002.
- [32] A. Palmer, J. Dempsey and D. Masterson, "A revised pressure-area curve and a fracture mechanics explanation," *Cold Regions Science and Technology*, no. 56, pp. 73-76, 2009.
- [33] Britannica, The Editors of Encyclopedia, "Pi theorem," October 2016. [Online]. Available: <https://www.britannica.com/science/pi-theorem>. [Accessed 18 May 2021].
- [34] T. Hammer, K. v. Beek, J. Koning and H. Hendrikse, "A 2D test setup for scaled real-time hybrid tests of dynamic ice-structure interaction," in *Proceedings of the 26th International Conference on Port and Ocean Engineering under Arctic Conditions*, Moscow, 2021.
- [35] A. Cromer, "Stable solutions using the Euler approximation," *American Journal of Physics*, no. 49, p. 455, 1981.
- [36] MathWorks, "cwt," The MathWorks, Inc., [Online]. Available: <https://nl.mathworks.com/help/wavelet/ref/cwt.html>. [Accessed 22 8 2021].
- [37] D. Sodhi and C. Morris, "Ice forces on rigid, vertical, cylindrical structures," Hanover, 1984.
- [38] A. Muhonen, T. Kärnä, E. Eranti, K. Riska, E. Järvinen and E. Lehmus, "Laboratory indentation tests with thick freshwater ice; Volume I," Valtion teknillinen tutkimuskeskus (VTT), Espoo, 1992.
- [39] D. Finn, S. Jones and I. Jordaan, "Vertical and inclined edge-indentation of freshwater ice sheets," *Cold Regions Science and Technology*, no. 22, pp. 1-18, 1993.
- [40] K. Kamesaki, Y. Yamauchi and T. Kärnä, "Ice force as a function of structural compliance," in *Proceeding to 13th IAHR Ice symposium*, Beijing, 1996.
- [41] A. Barker, G. Timco, H. Gravesen and P. Volund, "Ice loading on Danish wind turbines Part 1: Dynamic model tests," *Cold regions science and technology*, no. 41, pp. 1-23, 2005.

- [42] Y. Qianjin, G. Fengwei and S. Chu, "Laboratory tests of ice induced structure vibrations," in *Proceedings on the 18th IAHR International Symposium on Ice*, 2006.
- [43] T. S. Nord, "Deciphering of Ice Induced Vibration (DIIV)," 2012.
- [44] T. Nord, E.-M. Lourens, M. Määttänen, O. Oiseth and K. V. Hoyland, "Laboratory experiments to study ice-induced vibrations of scaled model structures during their interaction with level ice at different ice velocities," *Cold Regions Science and Technology*, no. 119, pp. 1-15, 2015.
- [45] M. Määttänen, S. Loset, A. Matrikine, K.-U. Evers, H. Hendrikse, C. Lonoy, I. Metrikin, T. Nord and S. Sukhorukov, "Novel Ice Induced Vibration Testing in a Large-scale Facility: Deciphering Ice Induced Vibrations, Part 1," in *21st IAHR International Symposium on Ice*, Dalian, 2012.
- [46] B. O' Rourke, I. Jordaan, R. Taylor and A. Gürtner, "Experimental investigation of oscillation of loads in ice high-pressure zones, part 1: Single indenter system," *Cold Regions Science and Technology*, no. 124, pp. 25-39, 2016.
- [47] B. O' Rourke, I. Jordaan, R. Taylor and A. Gürtner, "Experimental investigation of oscillation of loads in ice high-pressure zones, part 2: Double indenter system - Coupling and synchronization of high-pressure zones," *Cold Regions Science and Technology*, no. 124, pp. 11-24, 2016.
- [48] H. Hendrikse, G. Ziemer and C. Owen, "Experimental validation of a model for prediction of dynamic ice-structure interaction," *Cold Regions Science and Technology*, no. 151, pp. 345-358, 2018.